CRANFIELD UNIVERSITY

SCHOOL OF APPLIED SCIENCES

PhD

Academic Year 2011- 2012

WOJCIECH JERZY SUDER

Study of fundamental parameters in hybrid laser welding

Supervisor: Professor Stewart Williams

December 2011

This thesis is submitted in fulfilment of the requirements for the degree of PhD

ABSTRACT

This thesis undertakes a study of laser welding in terms of basic laser material interaction parameters. This includes power density, interaction time and specific point energy. A detailed study of the correlation between the laser material interaction parameters and the observed weld bead profiles is carried out. The results show that the power density and the specific point energy control the depth of penetration, whilst the interaction time controls the weld width. These parameters uniquely characterise the response of the material to the imposed laser energy profile, which is independent of the laser system. It is demonstrated that by studying the laser welding with respect to the basic laser material interaction parameters also helps explain some phenomenological phenomena in laser welding, such as the effect of beam diameter on the weld profile.

In addition a new approach for parameter selection in laser and hybrid laser welding is investigated. A phenomenological model allowing achievement of a particular laser weld on different laser systems is developed. In the proposed method the user specifies the required weld profile, according to the quality requirements and then the model provides combination of laser parameters, which lead to this particular weld on a given laser system. This approach can be potentially used to transfer laser data between different laser systems with different beam diameters.

An extensive study of residual stains in laser and hybrid laser welding is carried out. Both processes are compared either at a constant total heat input or at conditions required to achieve the same depth of penetration. The results demonstrate that there is a trade-off between the fit-up tolerance and the residual stress-induced distortion. Hybrid laser welding provides better ability to bridge gaps than the laser welding, but for the price of increased residual stress and distortion. Additionally, industrial study of the sensitivity to fit-up of hybrid laser welding with high deposition rate MIG sources is carried out.

This thesis is a part of NEGLAP (Next Generation Laser Processing) project sponsored by EPSRC (Engineering and Physical Sciences Research Council) and Tata Steel. The main objective is to understand the process fundamentals and exploit the usefulness of laser technology in pipe industry.

ACKNOWLEDGEMENTS

The results presented in this doctoral thesis were achieved as a part of NEGLAP Project (Next Generation Laser Processing) supported by EPSRC (Engineering and Physical Science Research Council) through Cranfield IMRC (Innovative Manufacturing Research Centres) and Tata Steel.

I would like to express my deep appreciation to my supervisor Professor Stewart Williams for his support and encouragement. His experience and enthusiasm were the main driving forces of this project.

I would also like to thank to all academic staff from Welding Engineering and Laser Processing Centre, in particular Dr. Paul Colegrove, Dr. Supriyo Ganguly and Mr. David Yapp for their kindness, friendly atmosphere and constructive discussion and advice.

Thanks to the technical staff, especially to Flemming Nielsen and Brian Brooks for their patience, tolerance and willingness of solving various engineering issues, as well as for being good friends.

I also appreciate technical advice and input of the industrial partners, particularly Alan Thompson and Chris Heason from Tata Steel.

To all my fellow colleagues from Welding Engineering and Laser Processing Centre for their friendship and cheerful attitude, in particular Matthew Rush, Pedro Almeida, Eurico Assuncao, Nuno Pepe, Tamas Nagy, Gil Lopes, Wang Hua, Matyas Benke, Filomeno Martina, Luis Cozzolino, Harry Coules, Goncalo Rodrigues, Sonia Martins, Ibrahim Nuruddin, Ofem Usani Unoh, Stephan Herbst and Craig Pickin. I am also grateful to Anna Paradowska neutron scientist from ENGIN-X for help with residual stress measurement.

Special thanks to my fiancée Ewa (Joanna) Palacz for taking care of me during hard times, huge support, encouragement, as well as help in graphical design. I would also like to thank my family for their patience and support.

TABLE OF CONTENTS

LIST OF FIGURES

LIST OF TABLES

LIST OF EQUATIONS

NOMENCLATURE

A_s cross sectional area of laser spot on the surface

a_0 lattice parameter from stress free reference sample

$a_{L,N,T}$ lattice parameter in longitudinal, normal, transverse direction

α thermal diffusivity

B brightness

BPP beam parameter product

CW continuous wave

CTWD contact-to-workpiece-distance (stick out in MIG welding)

CO_2 laser carbon dioxide laser

DOF depth of focus

D diameter of collimated beam

E_d energy density

E_{ut} energy per unit thickness

d_{waist} diameter of laser beam at the laser source

d_f diameter of laser beam at the focal point

d diameter of beam on the surface of workpiece

DC direct current

E_{SP} specific point energy

$\varepsilon_{L,N,T}$ residual strain in longitudinal, normal, transverse direction

F focal length

GMAW Gas Metal Arc Welding

h plate thickness

HI heat input per unit length

JE joining efficiency

k thermal conductivity

λ wavelength

M^2 definition of beam diameter

MA melting area (cross sectional area of melt zone from macrographs)

ME melting efficiency

MIG metal inert gas

Nd:YAG laser neodymium yttrium aluminium garnet laser

P_{AI} instantaneous arc power

P_{AV} average arc power

Pe Peclet number

PD depth of penetration

P_F power factor

P_L laser power

P_r recoil pressure

q_p power density

r_b beam radius

S heat function

$\sigma_{L,N,T}$ residual stress in longitudinal, normal, transverse direction

T temperature

TC thermocouple

τ_i interaction time

TIG	tungsten inert gas
T_S	surface temperature
θ	divergence angle
v	travel speed
w	weld width measured at the top
WFS	wire feed speed
X	normalised power input
Y	normalised speed-weld width

Chapter 1. Introduction

The rapid development of technology in last few decades could only be possible thanks to new materials and methods of joining them. Welding and other joining techniques are deeply embedded in every engineering field to such an extent that it would not have been possible to realise any of the great modern achievements, such as cars, buildings, and transport infrastructure without it. The first step in technological breakthrough happened when the welding technology replaced riveting. This allowed for an improvement in efficiency, productivity, weight reduction and aesthetic perception of built goods. Modern joining processes, such as laser, ultrasound and electro-beam welding allow more advanced materials to be used, which enable further exploration of new ideas. Nowadays laser technology is revolutionising manufacturing due to its versatility and non-contact character of the processing.

Lasers have great potential to be widely used in heavy industry welding applications. This is due to their capability to be narrowly focussed, which leads to a deep penetration, high productivity and low distortion. These benefits are particularly useful when combined with an arc-based welding source into hybrid welding. However, the full benefit of high productivity can be used only if high quality is also achieved. Many research works have demonstrated the high complexity of laser and hybrid laser welding. To develop a reliable welding process a comprehensive understanding of fundamental laser material interaction phenomena is required.

In spite of many potential benefits of laser technology, heavy industry is still reluctant in using it, seeing lasers as complicated, energy consuming and unreliable. This is particularly due to the high sensitivity of the process to the variation of gap between joined faces, the difficulties with achieving consistent mechanical properties and the high level of complexity. Laser welding is often attributed with the complicated phenomena that occur during the interaction of laser beam with matter, control of which can be cumbersome.

One of the biggest advantages of lasers is their flexibility in terms of the energy conditions delivered to the workpiece. The energy can be applied with different

combinations of power density and interaction time and different temporal modes. For example it can be focused to a large beam diameter, providing a moderate power density and a large processing area for surface treatment or brazing. Alternatively, it can be focused to a very small beam diameter of tens of microns, providing a high power density and causing an intense evaporation of material. This is required in processes such as laser keyhole welding or cutting. The same laser beam can interact with materials in different ways, which depends on many parameters, such as absorption conditions and energy density. This, on one hand, demonstrates the versatility of lasers and allows them to be used in many processes, such as micro-joining, marking, hardening, brazing, deep penetration welding and cutting [1]. On the other hand, the amount of variables, which can affect the resultant welds, makes the process difficult to control.

Laser welding offers the possibility to achieve joints with relatively deep penetrations, as compared to the traditional arc-based processes. The depth of penetration is the main parameter that users wish to control, in order to accommodate a particular thickness. Typically the depth in laser welding varies between a fraction of millimetre and tens of millimetres, depending on the applied conditions. Since many parameters can affect the achieved depth of penetration, a lot of effort is required to select optimum parameters for a particular process or to maintain a stable process. If we consider laser power and travel speed, the same depth of penetration can be achieved with many combinations of these parameters, as demonstrated by the horizontal dashed line in Fig.1.1. However, each combination of the travel speed and the laser power will result in different weld profiles, despite the same depths of penetration. Weld on the left in Fig.1 is significantly wider, with a thicker heat affected zone and a coarser microstructure, as compared to the weld on the right. This will result in different mechanical properties between the presented welds and also will affect other properties, such as distortions. Thus it can be deducted that the applied laser parameters are directly reflected on the mechanical properties of the resultant welds, which should be considered when selecting parameters for a particular application.

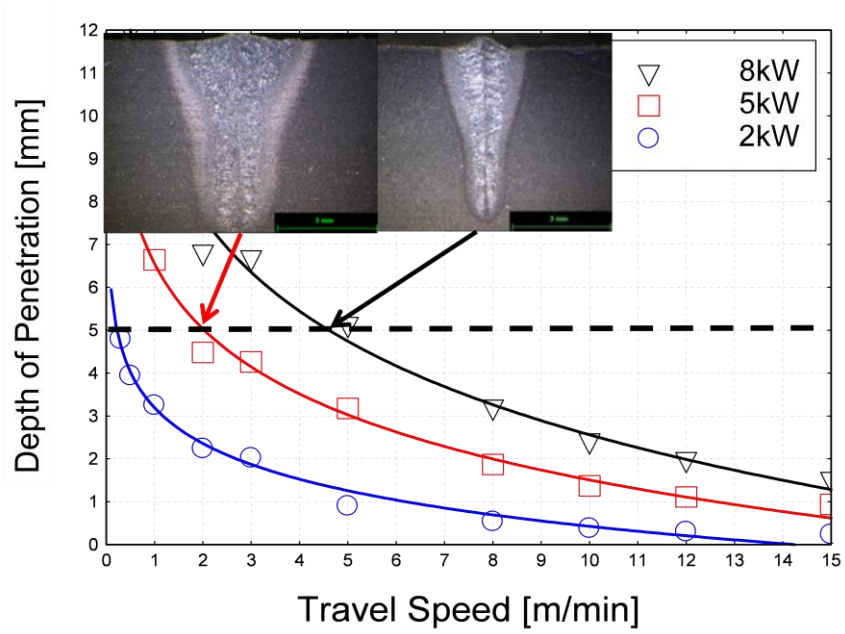

***Figure 1.1**: Effect of welding parameters on weld profile for the same weld depth.*

The parameter selection procedure is even more complicated due to the effect of beam diameter. The same combination of laser power and travel speed applied on different beam diameters will result in different welds. This implies that the graphs similar to that presented in Fig.1 are unique for a particular laser system with a particular beam diameter. Therefore, specifying the laser welding based on the laser power and the travel speed, which is common amongst laser practitioners, makes every case unique. This can impede a comparison or transfer of the results between the laser systems.

The final beam diameter is determined, among other properties, by the characteristics of the optical cavity and the delivery system, the quality of the optics and the precision of assembly. There are many different laser systems available on the market, which can be combined with various optical systems. The beam properties of a particular laser system can also change with time, due to the degradation of the sensitive optics or interference of contamination. This makes almost every laser system unique in terms of delivered beam diameter. The unique beam diameter gives a unique combination of the laser material interaction parameters, which cannot be easily replicated on other laser systems. This

demonstrates the need of developing a system of parameters which would enable us to specify the laser processing independent of the laser system.

Hybrid laser welding consists of two very different heat sources, a laser beam and an electric arc, which if properly controlled can complement each other. However, the demand of high productivity, which is required from hybrid laser welding, requires extremely high deposition rates of the filler metal from the arc source. In Fig.1.2 the effect of travel speed on the size of the reinforcement at a constant deposition rate of 7.3 kg/h is shown. This demonstrates that to maintain the high quality joints and achieve sufficient gap bridging ability (good tolerance to fit-up) of the process at high travel speeds, high melting rate of filler wire is required.

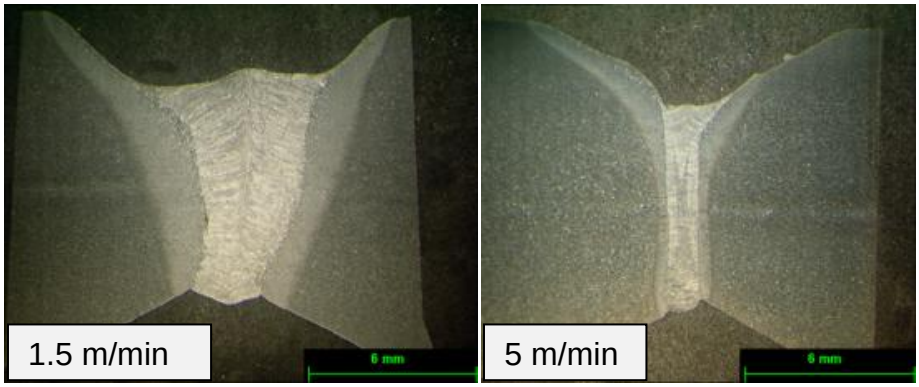

Figure 1.2*: Influence of welding speed of hybrid laser/MIG welding on fit-up tolerance*

High currents, associated with high deposition rate arc processes, are usually problematic to achieve a stable metal transfer without spatter and defects. The electric arc column with its strong electromagnetic field, plasma and accelerated droplets of molten filler wire can induce a strong force on the melt pool [2]. This can be particularly problematic in hybrid laser welding where the arc interacts in a close proximity of the laser interaction point. An example of laser-induced melt pool is shown in Fig.1.3. Improperly selected arc conditions, in such a case, can easily lead to excessive spatter and instabilities.

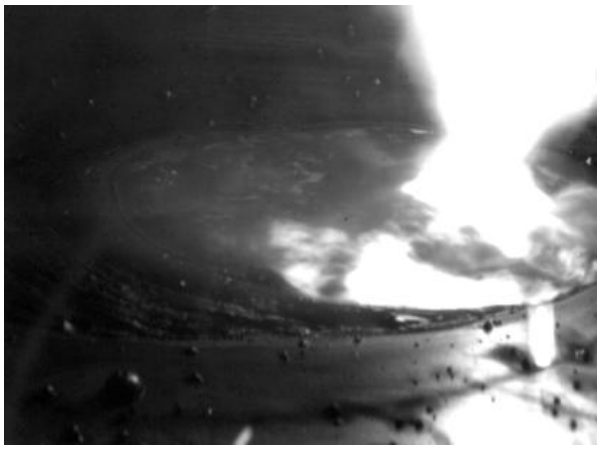

***Figure 1.3**: Laser interaction point*

Hybrid laser welding process can be very efficient way of joining materials, however, to fully utilise its benefits, some issues have to be resolved. This includes poor data transferability between different laser systems, lack of criteria for selection of parameters for a particular joint conditions and undefined limits of the tolerance to fit-up. The following project attempts to address these issues.

The thesis is structured in the following manner. The literature review in Chapter 2 is divided into eight sections. A short description of hybrid laser welding process shown in Section 2.1 is followed by an evaluation of benefits of high brightness lasers in welding, which is made in Section 2.2. Since the ability to measure the beam diameter and other propagation properties of lasers was the necessary condition for this research, a short summary of measuring methods and definitions of beam diameters are presented in Section 2.3. One of the main aims of this project is to find parameters which control the depth of penetration in laser welding. Therefore in Section 2.4 an extensive review of all forces affecting the depth of the keyhole in laser processing is shown. There are many phenomena which occur when a high power laser beam irradiates a surface: absorption, multiple reflection, heat conduction, vaporisation-induced drilling, attenuation of laser beam in the vapour/plasma, melt flow. To look at the net effect of some of these physical phenomena the most interesting studies of the temporal evolution of keyhole, using X-ray imaging or acquired from welding of transparent materials, found in the literature are summarized. Also some studies of laser welding in vacuum, which show the effect of vaporisation temperature of the material on the process, are reviewed.

Then in Section 2.5 a summary of alternative parameters, which were previously used to attempt the laser system-independent characterisation of laser welding is presented. Next, in order to understand the hybrid laser process, the interactions between the laser beam and the electric arc column are discussed in Section 2.6. Finally, some findings from literature regarding the ability of hybrid laser welding to bridge large gaps are shown in Section 2.7. The literature review section is summed-up by concluding remarks, which led to formulation of the aims and objectives of this thesis in Section 2.8.

The experimental part is presented as a chapter structure, with introduction, methodology, results and discussion sections in every chapter. In Chapter 3 the experimental set-up, such as the laser system and the power sources, as well as materials and consumables used throughout this thesis are listed. Chapter 4 includes characterisation of the fibre laser in the perspective of heavy industry applications, such as measurement of its stability and evaluation of drawbacks. Chapter 5 is focused on the study of basic laser material interaction parameters in laser welding. This includes study of the effect of laser energy on the achieved weld profiles, evaluation of the influence of beam diameter, divergence angle and the optical set-up on welding conditions. It also explains many phenomena observed in laser welding. Chapter 6 looks into the parameter selection criteria and the issue of data transferability between different laser systems. Chapter 7 is focused on residual strains caused by the heat effects in laser and hybrid laser welding. Chapter 8 demonstrates industrial study of the sensitivity of laser and hybrid laser welding to fit-up. The thesis is closed-up by a short critical discussion in Chapter 9, which summarizes the most important findings of this project, followed by conclusions and suggestions for future work, shown in Chapter 10.

Chapter 2. Literature review

2.1. Hybrid laser welding – process description and advantages

In hybrid laser welding a laser beam and an arc-based welding process are focused in to the same point, simultaneously creating one melt pool. Thanks to such a combination the advantages of both processes are magnified and drawbacks are compromised. Laser welding has a poor fit-up tolerance, as a result of focused energy and therefore requires costly preparation of joined edges prior to welding. Furthermore, a fast cooling rate and deep and narrow character of fusion zone can result in undesired microstructures. The situation is hardly improved with the filler wire due to difficulties with spreading the alloying elements uniformly through the depth, in case of thick sections [3]. Any arc-based welding process, on the other hand, is relatively slow and exerts a high heat input, which causes distortion. If both sources are combined in to the hybrid process, the laser beam with its high energy density enables a deep penetration and fast processing speeds, whilst the arc source widens the melt pool, reduces the cooling rate and provides filler metal to bridge the gap. A typical interaction zone of hybrid laser MIG (Metal Inert Gas) is shown in Fig.2.1. The main phenomena include, keyhole and vapour plume induced by the laser beam and droplets of molten filler wire deposited by the MIG source. Faster travel speeds, as compared to the arc welding result in a reduction of distortion, whereas lower cooling rates, as compared to the laser welding have a positive effect on microstructure, reduction of hardness [4, 5] and suppression of defects, such as porosity [6] and cracks [7]. A comparison of macrographs of typical MIG, laser and hybrid welds is shown in Fig.2.2. Note that the laser tandem MIG hybrid process refers to the combination of laser with twin-wire MIG source in the same melt pool.

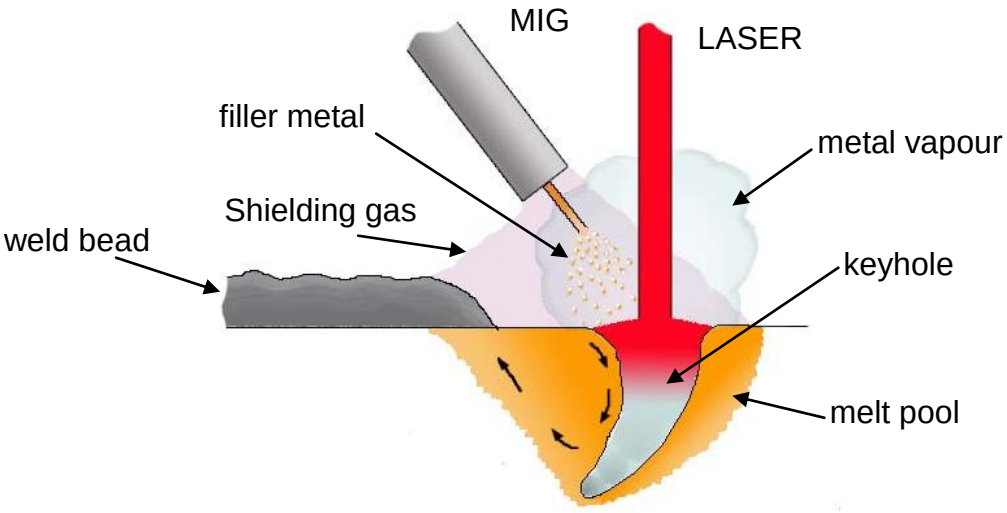

***Figure 2.1**: Interactions in laser MIG hybrid welding.*

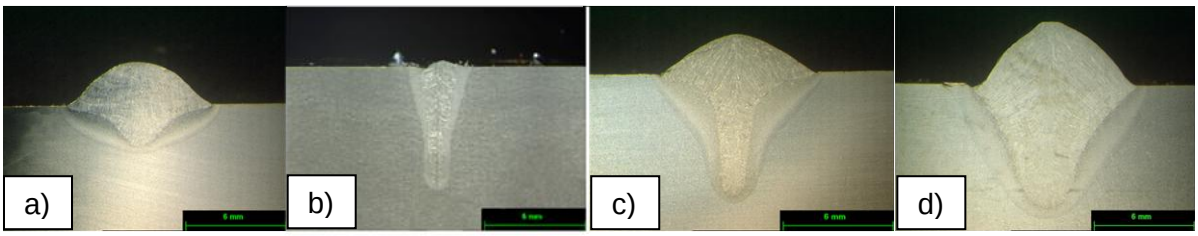

***Figure 2.2**: Comparison of weld bead profiles: **a)** MIG; **b)** autogenous laser; **c)** laser/MIG hybrid; **d)** laser/tandem MIG hybrid.*

There are many kinds of hybrid laser welding, which compile use of laser with various heat sources, such as plasma arc welding [8-10], submerged arc welding [11, 12], tungsten inert gas TIG and metal inert gas welding MIG. However, the most popular is laser/MIG hybrid process due to the incorporated filler wire. This process enables thick sections to be welded with high productivity, low distortion and good tolerance to fit-up. Another advantage of hybrid laser welding is the high ability to control the bead shape. The depth of penetration is mainly determined by the laser, whereas the bead reinforcement is controlled by the arc source. Thus the bead shape can be flexibly altered by changing the energy ratio between the laser and the arc, whilst the microstructure can be controlled by the appropriate cooling rate and filler wire [13, 14].

2.2. High brightness lasers

Application of any new technology is dependent on its advantages over existing technology, cost efficiency and reliability. Although Steen and Eboo [15] published the first work regarding hybrid laser welding in the eighties, this process started to be widely used only in the last decade. The situation was mainly caused by costly and unreliable lasers. In that period only the carbon dioxide (CO_2) and neodymium-ytterbium-aluminium-garnet (Nd:YAG) lasers had enough output power required for industrial applications, such as welding or cutting. The low efficiency and beam stability of Nd:YAG lasers and the high maintenance cost and difficulties with the optical system of CO_2 lasers, as well as the significant absorption of laser by plasma, contributed to the reluctance of heavy industry to the laser technology.

Nowadays developments of fibre, disc and direct diode lasers have resulted in a wide range of new laser sources, characterised by high efficiency, excellent beam quality and stability. Also the shorter wavelength of solid state lasers makes them less susceptible for plasma absorption, as compared to CO_2 lasers. The fibre laser in particular, in which several meters long and tens of microns thick glass fibre is used as the optical cavity is advantages due to the simple construction and the maintenance-free optical cavity. The specific dimensions of the cavity enable a wave guiding effect, which leads to the excellent beam quality of the fibre lasers. A new technique of coupling several pumping units allowed scaling up the output power to any practical level. The continuous development of pumping diodes improves the lifetime, compactness, efficiency and stability, as well as lowers the price of modern laser sources. Also the low wavelength of new solid state lasers allows them to be delivered through optical delivery fibres, which simplifies the automation.

Despite of many advantages of the new generation solid state lasers their benefits are often overestimated. A great source of controversy is for example the benefits from the genuine beam quality. Advantages of the high brightness lasers in welding processes are investigated in this section.

2.2.1. Beam quality

In order to define laser light uniquely, many parameters have to be specified, such as transverse electromagnetic mode, polarisation, coherence, brightness, divergence, intensity etc. Unfortunately a universal definition of beam quality, which would take into account all of these properties, does not exist. Instead the divergence (Fig.2.3), which describes the propagation of a particular ray of light throughout the space, is often considered to be an important property of a laser beam. There are two definitions of beam quality based on the divergence angle, commonly used [1]:

- M^2

$$M^2 = \frac{\pi d_{waist} \cdot \Theta}{4\lambda} \qquad 2.1$$

- Beam parameter product (BPP)

$$BPP = M^2 \frac{\lambda}{\pi} = \frac{d_{waist} \cdot \Theta}{4} [mm \cdot mrad] \qquad 2.2$$

d_{waist} – beam diameter in waist, Θ – full divergence angle, λ – wavelength

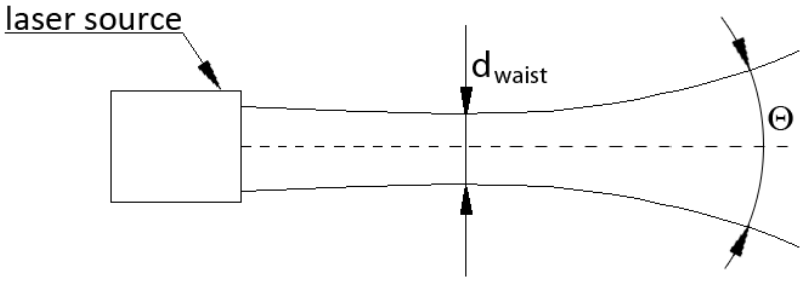

***Figure 2.3**: Beam divergence.*

The M^2 definition of the beam quality is usually used for comparison of lasers with different wavelengths. It corresponds to the quality of a particular laser beam

relatively to a perfect beam, referred to as the diffraction limit. For example a laser characterised by M^2 value of 1.2 will provide a beam diameter larger by 20%, as compared to a laser with perfect beam (M^2=1) [1]. This is demonstrated in Fig.2.4. Note that a 20% increase in beam diameter is equivalent to a 44% increase in beam cross sectional area on the surface and corresponds to a 30% reduction in power density.

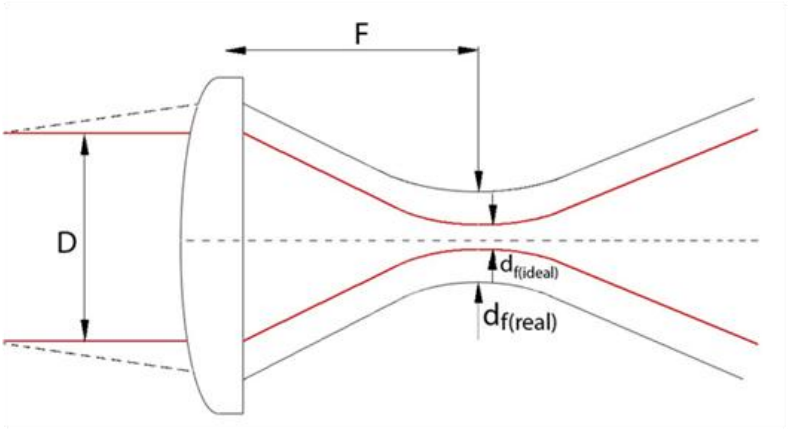

$$d_{f(ideal)} = \frac{4\lambda F}{\pi D}$$

$$d_{f(real)} = (M^2)\frac{4\lambda F}{\pi D}$$

***Figure 2.4**: Definition of M^2.*

Beam parameter product (BPP) is used to describe the focus-ability of a particular laser system. A practical meaning of the beam parameter product was demonstrated by O'Neill [16] as shown in Fig.2.5. The lower the BPP of a particular laser the greater the depth of focus.

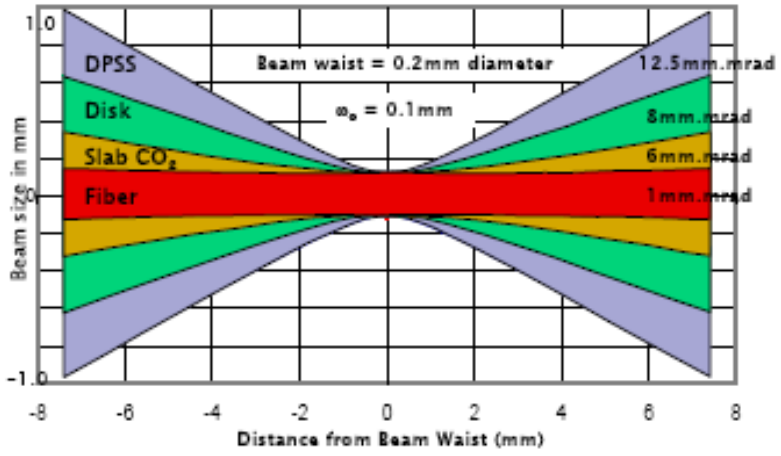

***Figure 2.5**: Effect of beam parameter product (BPP) on beam caustic [16].*

The focus-ability of a laser beam is also proportional to the beam quality. The lower the BPP the smaller beam diameter is achieved with a given optic. The smallest beam diameter that can be obtained with a particular laser system is dependent on the optical set-up and the BPP of a laser beam, and is given by Equation 2.3 [1]:

$$d_f = 4\frac{F}{D}BPP \qquad 2.3$$

Since the beam diameter is also dependent on the focusing optics, a longer focal length lens can be used to achieve the same beam diameter when BPP decreases, which has practical advantages. This can be beneficial in some applications where a long working distance is required, such as remote welding. Furthermore, a high beam quality enables a reduction of the dimensions of the optics, which minimises the inertia forces of the processing head, allowing a faster movement of the optical head.

The dependence of beam diameter and power density with BPP is shown in Fig.2.6. There are many benefits resulting from a higher beam quality (low BPP). A reduction of beam parameter product by a factor of two results in a decrease of beam diameter by a factor of two, for the same optical set-up. This corresponds to an increase of power density by a factor of four. Thus lasers with a lower BPP can be operated at lower powers to achieve the same power density.

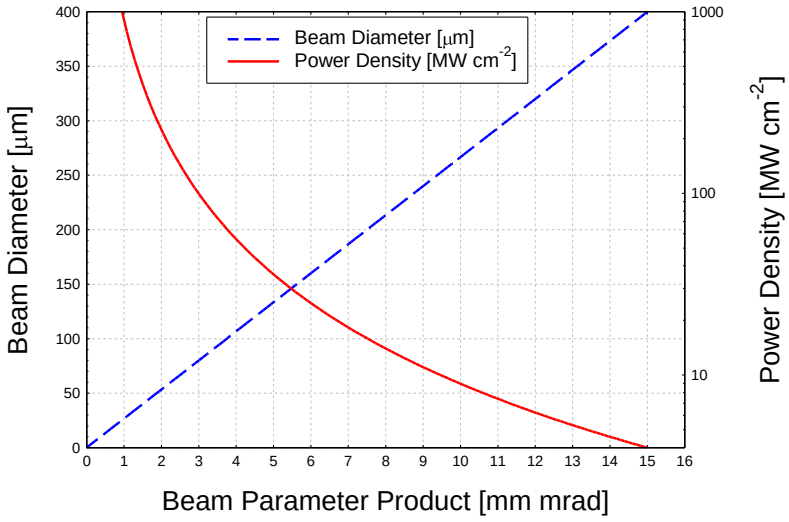

***Figure 2.6**: Effect of beam parameter product (BPP) on beam diameter and power density*

The beam quality is one of the most important arguments when comparing CO_2 lasers with fibre lasers. Modern CO_2 lasers have the beam qualities approaching the diffraction limit, which corresponds to values of M^2 close to the unity. However, because the focus-ability is also dependent on the wavelength, CO_2 lasers are significantly limited, as compared to the fibre laser. Thus despite the M^2 of CO_2 lasers being low, their focus-ability is compromised by the fundamental limit of the wavelength. The effect of the wavelength of laser radiation on the minimum achievable beam diameter as a function of M^2 is shown in Fig.2.7. The fundamental advantage of the lower wavelength of fibre laser is exhibited by a smaller beam diameter.

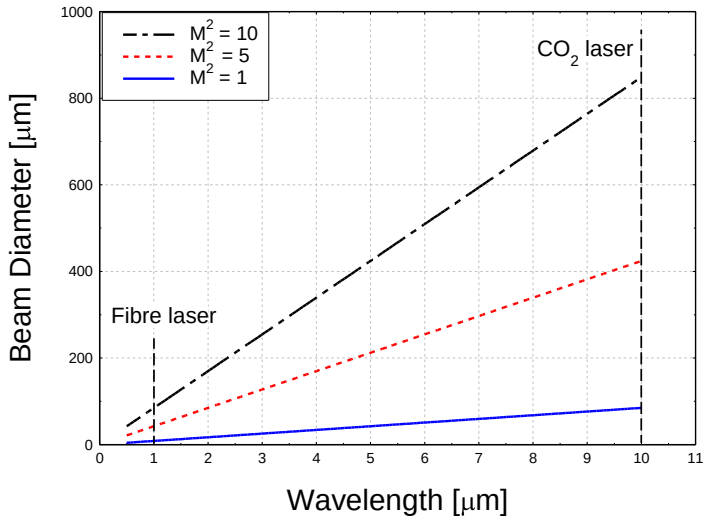

***Figure 2.7**: Effect of wavelength of laser radiation on minimum achievable beam diameter.*

The excellent beam quality of the fibre laser, resulting from the character of the optical cavity and wavelength has to be quantified. Namely fibre lasers with a BPP close to the diffraction limit are available with a limited power. A maximum power of a single mode fibre laser with BPP <1.07 is approximately 1 kW [17]. In order to increase the output power, much thicker fibres with a double cladding have to be used. Thus there is a trade-off between the beam quality and the output power. The multimode fibres can be coupled with a greater amount of pumping units, which increases the output power, but the bigger diameter allows more fundamental modes to propagate, hence the beam quality is compromised. This is also manifested by a

uniform top hat intensity distribution of the multimode fibre lasers. The parameter, which characterise laser source in terms of beam quality and output power is brightness, which is given by [18]:

$$B = \frac{P_L}{\left(\pi \frac{d_f^{\,2}}{4}\right)\pi\Theta^2} \quad [W \cdot sr^{-1} \cdot cm^{-2}] \qquad 2.4$$

A high brightness laser provides a high output power and at the same time enables achievement of a small beam diameter. Thus the brightness characterise a given laser in terms of its usefulness as a tool in real applications.

Many researchers reported an improved performance of fibre lasers in material processing, as compared to Nd:YAG and CO_2 lasers [16, 19-25]. The benefits of high beam quality and small beam diameter are the most profound in micro processing, such as micro-drilling and micro-welding. In contrast in macro-processing, a high brightness allows an increase in depth of penetration for a given travel speed or an increase in travel speed for the same depth of penetration. This leads to a reduction of weld size and heat affected zone. The high beam quality fibre lasers enable achievement of the same depth of penetration with a lower power, as compared to CO_2 lasers, which ensues in lower distortions [26]. Thus most of the advantages of fibre lasers result from the small beam diameter.

However, in contrary to all expectations, the level of improvement, which would be expected from the excellent beam quality and high power density of the fibre lasers in some applications, is low. The extremely narrow fusion zone has a poor fit-up tolerance. The small diameter of keyhole makes it prone to instabilities and porosity. The narrow melt pool and the high surface tension, resulting from the low heat input, makes the process susceptible for humping and formation of pearl-like shape in the root [27, 28]. Although it was possible to achieve a depth of penetration of approximately 1 mm at extremely high travel speeds up to 100 m/min, using a single mode fibre laser with 24 μm beam diameter and 1 kW of power, the operating window for high quality welds was very narrow. For example a severe humping occurred at travel speeds exceeding 10 m/min, whereas at speeds below 5 m/min, the keyhole perturbations, manifested as necking of the bottom part, were evident. This caused a variation of depth of penetration and porosity [20]. Also the high power

density and processing speed increase material losses due to the spatter, control of which is very difficult [29, 30].

A high power density applied on a small dimension optic can induce a thermal load, which in some cases can lead to focus shift [31-33] manifested as a relative change of the focal point during the emission time. According to the literature the focus shift is caused by the absorption of laser energy on optical components [34-36]. For instance the presence of residuals of OH- molecules in the glass used for the optics can lead to the absorption and thermal lensing effect [37]. It is believed that the main reason of focus shift is the change of refractive index with the temperature [38]. In reality it is difficult to predict how various optical components will behave when subjected to the heating of laser radiation [34, 35]. In addition, wrong design or inaccuracy in assembly and alignment of the processing heads may account for further focus shift [39]. Focus shift is strongly dependent on the purity and type of material used for the optics, as well as its cleanness [31, 32, 40, 41]. Also it is more severe for transmissive optics, due to the cooling difficulties. Some authors claim that a large focus shift can change the welding conditions by changing the beam diameter in the workpiece [31-33, 41]. Zhang et al. [42] visualised the beam profile before and after welding by making single spots in an acrylic resin. According to the authors, the difference between the spots and also the differences in weld profiles was significant. The influence of focus shift on welding conditions should be dependent on the proportion of the focus shift to the depth of focus of the optical system.

A great source of controversy is whether the higher beam quality of fibre lasers can improve the depth of penetration in laser welding. A laser beam with a low divergence can be focused to a small beam diameter providing a high power density. However, the gain of depth of penetration with these small beam diameters is incomparable lower than expected from the increase of power density [22, 24, 28, 42-44]. This is demonstrated in Fig.2.8 [28]. It was shown that when decreasing beam diameter at a constant power and travel speed the depth of penetration reached a plateau at a certain level and did not increase further, despite the beam diameter being continuously decreased [43-45]. This is shown in Fig.2.9 [43]. In some cases the depth of penetration even started to decrease with decreasing beam diameter [26, 46].

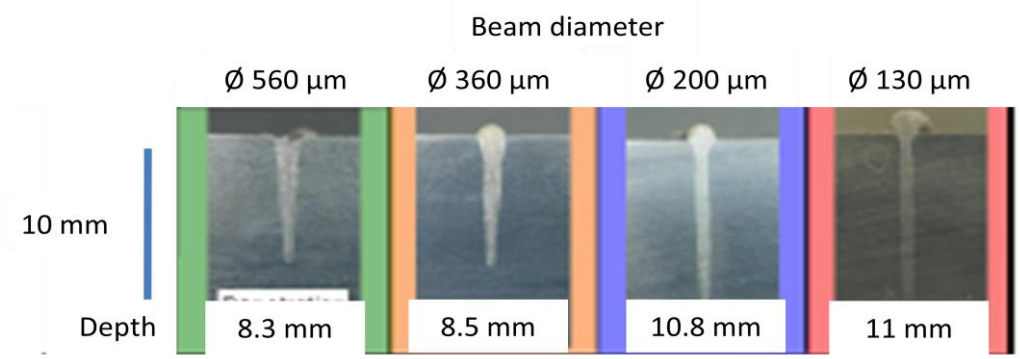

***Figure 2.8**: Effect of beam diameter on weld shape at constant power of 10 kW and travel speed of 4.5 m min^{-1} [28].*

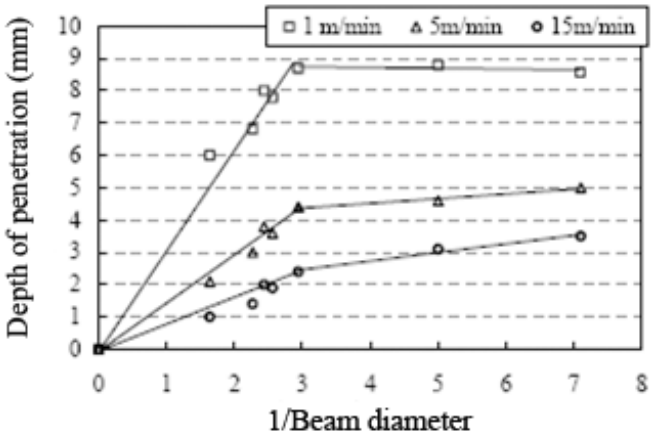

***Figure 2.9**: Depth of penetration as a function of inverse beam diameter for different travel speeds [43].*

Some researchers claim that when the beam diameter on the surface is smaller than 200 µm, the depth of penetration depends not only on the power density but also on the beam quality [24, 42, 45, 47]. Weberpals [48, 49] carried out laser welding with different optical set-ups in order to obtain the same beam diameter (100 µm) with various divergence angles. The results confirmed the influence of divergence angle on the depth of penetration when the beam diameter was reduced below 200 µm. However, it has to be mentioned that all the beams with high divergence angles, used in this experiment, had very low depth of focus (below 1 mm). This has a large effect on the tolerance of the practically achieved beam diameter on the surface, which could diminish the real effect of divergence angle on depth of penetration.

Alternative explanations of the plateau effect with low beam diameters, according to the literature are: attenuation of the laser beam in the vapour plasma, which is induced by these extremely high power densities [42, 43] or a strong closing force of the surface tension due to the narrow diameter of keyhole [20, 42].

A lot of effort was made to evaluate the potential benefits of fibre lasers in laser cutting, currently dominated by CO_2 lasers. It was expected in the past that the low wavelength combined with the excellent focus-ability and the large depth of focus of the new solid state lasers would improve the cutting performance, by reducing the thermal affected zone and increasing productivity [50, 51]. The reality however, is surprisingly different. A significant increase in cutting speed with fibre lasers is only evident in thin plates. As the sheet thickness exceeds approximately 6 mm the CO_2 laser is as efficient as the fibre laser. Moreover the cut quality, in terms of roughness and perpendicularity of the cut edges, achieved with CO_2 laser exceeds the quality of fibre laser cuts [52]. This low performance of fibre lasers, despite their high brightness is often attributed to Fresnel absorption [21, 53-55], which will be highlighted in Section 2.4.1.

The alternative hypothesis of the poor cut quality, achieved in thick sections with high brightness lasers, assume dependence of the quality on the width of the cut. A much lower roughness of the cut surface was achieved with defocused beam, which was attributed to the improved efficiency of the melt removal from the kerf [56, 57]. Olsen [58] points out that the high power density of fibre lasers induces a local evaporation on the cut front, which on one hand, increases the melt removal, but on the other hand, deteriorates the quality.

In summary the contemporary lasers offer much better features than it is required in many cases, particularly in terms of divergence and brightness. This makes the choice of an optimum laser system for a particular application a difficult task. The divergence angle of a laser beam mainly determines its focus-ability and depth of focus. Even though a large depth of focus is desired in welding and cutting, the excessively small beam diameters and resultant high power densities are not always beneficial. In majority of welding applications the parameters are selected based on quality requirements, such as fit-up tolerance or weld bead geometry rather than productivity only.

The effect of divergence angle on the seam dimension is often overestimated. Although it was shown that the seam width could be reduced by reducing the divergence and as a result the beam diameter [59, 60], but the effect was only profound at high processing speeds. At the travel speeds typically used in laser or hybrid laser welding, the heat conduction and fluid dynamic become dominant and the width of the seam is determined by the thermal properties of the material. It seems that the benefits of fibre lasers are fully utilised in remote processing, where the high quality laser sources allow small beam diameters to be achieved with long focal lengths optics or in micro welding where small beam diameters allow for better precision.

2.2.2. Wavelength

The wavelength of a particular light depends on energy levels of the species in the active medium and its ability to maintain the stimulated emission. All active mediums have diverse properties in terms of excitation energy, quantum efficiency and scalability. Molecules of carbon dioxide (CO_2) for instance produce a relatively long wavelength but the ability of using large volumes, combined with the ability of efficient cooling, enables a generation of high power CW laser action. Meanwhile other mediums, despite lower wavelength, can have other limitations which fundamentally or practically limit their value for laser emission [1]. Not so long ago laser users had to choose between the longer wavelength but higher output power of CO_2 laser and the shorter wavelength but lower power of Nd:YAG laser.

Wavelength defines the fundamental limits of a particular ray of light in terms of interaction with matter. The fibre laser has many advantages over CO_2 resulting from the shorter wavelength. First, the energy of photons is inversely proportional to the wavelength, which is beneficial in case of processing of non-metals. Second, more important for metals, the absorption of most metals is approximately few times greater for the fibre lasers than for CO_2 lasers, as shown in Fig.2.10 [61]. This is particularly important in conduction welding and all kind of surface treatment applications, as well as in processing of highly reflective materials such as copper.

Thanks to the relatively low wavelength of fibre, disc and Nd:YAG lasers they do not interact with silica glass, which enables them to be delivered through optical fibres.

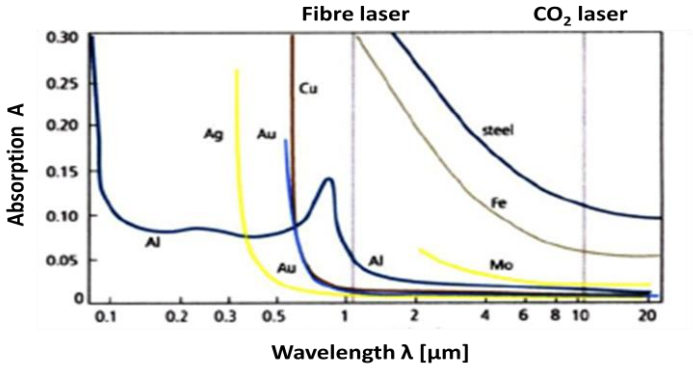

***Figure 2.10**: Absorption in metals as a function of wavelength of laser radiation [61].*

Lasers with shorter wavelengths do not interact with gases as easily as lasers with longer wavelength, which has practical advantages in material processing. When a workpiece is subjected to the interaction with a high power density laser beam, the arising vapour cloud can increase its ionisation state, due to heating by the incident laser beam. This may lead to a significant absorption of the laser energy in the plume [62]. The relatively long wavelength of CO_2 lasers makes them susceptible for interaction with plasma, which increases its ionisation. This is manifested by the appearance of bright plasma followed by a sudden decrease of depth of penetration when a high power density CO_2 laser interacts with workpice in the atmosphere of argon or nitrogen [63, 64]. Therefore helium with its high ionisation potential is recommended as the shielding medium for CO_2 laser processing.

The plasma absorption with fibre, disc or Nd:YAG laser should be less severe than in case of CO_2 laser [65, 66] as shown in Fig.2.11 [67]. In this case the laser beam does not increase the ionisation state of the vapour plume, which is therefore referred to as a hot gas. The shielding gas in this case is only used to protect the molten metal from the ambient atmosphere and since the ionisation potential is no longer important any inert shielding gas can be used. This allows the cheaper argon instead of helium to be used for 1 µm lasers. Despite the fact that some authors [68-75] claim that 1 µm laser radiation can also be efficiently absorbed by the plume, due to the scattering effect on vapour particles, however, this should be still easier to suppress than the plasma in case of CO_2 laser [63, 76].

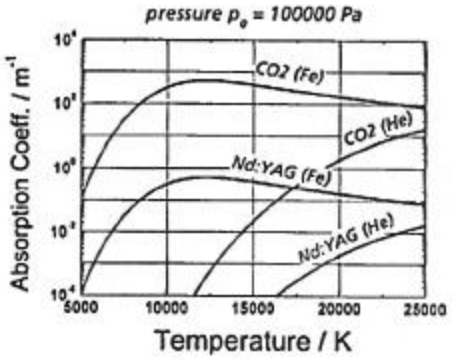

***Figure 2.11**: Plasma absorption coefficient as a function of temperature for different materials and laser types [67].*

The plasma absorption is also an important aspect in hybrid laser welding. It is known that helium can have an undesired effect on the arc source, due to its high ionisation potential. The droplet transfer becomes unstable when helium content increases over a certain range [77, 78]. In this case the fibre laser seems to be privileged over CO_2 laser due to its rather insensitive nature on the type of shielding gas. This allows a use of shielding medium in fibre laser hybrid laser welding, which is more preferable for the arc source.

2.3. Measuring methods of beam properties

In order to determine the usefulness of a laser beam as a processing tool, its basic properties have to be characterised. This includes the average output power, beam diameter and intensity distribution. In the past not only the unreliable laser sources contributed to the reluctance of industry to the laser technology, but also difficulties with measuring their properties. This resulted in several problems. First, the laser user was unaware of any fluctuation of laser properties, which could result from changes in the optical cavity, degradation of the optics or any kind of misalignment in the optical path. Second, the user had to rely on the assurance given by the laser manufacturer regarding the specification of the particular laser system. Thus the real beam diameter was unknown and the laser system had to be subjected to a series of parametrical studies before it could be employed into applications. Nowadays there are plenty of devices to characterise lasers in terms of output power and beam propagation properties. The possibility of measuring the most important parameters of laser beam was one of the necessary conditions to undertake this project.

2.3.1. Measurement of output power

There are several different types of power monitors available on the market [79-81]. Various measuring techniques of laser power differ in terms of response time, accuracy and damage threshold. The most accurate are devices equipped with photodiodes, which however, have a low damage threshold and are wavelength dependent [18]. Most power meters convert the optical power into the heat, which is then measured. In a low power range devices the power is derived from the temperature difference between a thermopile or a thermocouple and a reference point, at which the temperature is known, such as the casing of the power meter [18, 82]. These power meters can measure lasers operating in the continuous wave, as well as in a pulse mode [83]. The most common power meters used for high power CW lasers are calorimetric-based devices. They measure the temperature of a cooling medium, which attains the heat from the laser beam absorbed in a highly absorbing chamber [84]. The schematic of such a device is shown in Fig.2.12 [85].

These power meters can withstand high powers of continuous radiation, but they are not suitable for pulsed lasers, due to the low response time.

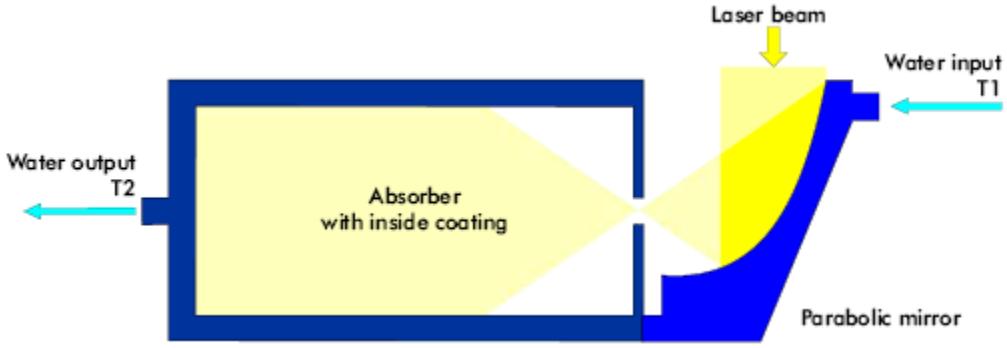

***Figure 2.12**: Schematic of calorimetric power meter [85].*

2.3.2. Measurement of beam diameter

A laser beam passes through several optical components on its way from the optical cavity to the workpiece. Each of these components is manufactured with a given quality which is never prefect. The quality of any lens for instance, is determined by the accuracy of its curvatures and dimensions, the purity and refractive indexes of the glass, as well as the quality of the coating. All these, combined with the difficulties with alignment of many optical components lead to the discrepancies between theoretical calculations made by laser designers and practically obtained beams. This affects the fundamental propagation properties, such as beam diameter at the focal point, focal length, divergence angle and intensity distribution. This became a motivation for development of various laser monitoring systems.

2.3.2.1. Measurement methods

Burn marks technique was the first and most intuitive procedure used for the evaluation of beam diameter. In this case the beam diameter is acquired from spots burned with a laser on a specially selected material. The main disadvantage of this method is the lack of information regarding the intensity distribution and the spatial properties of a laser. The accuracy of the measurement is strongly dependent on the operating parameters, such as power density and time of irradiation. A comparison of

this method with a commercially available beam profiler have shown that the diameter obtained from the burn marks on a polyimide film can approach a 99% of the actual laser beam after at least four shots of a pulsed laser to the same point [86].

In order to improve the accuracy and make possible to measure the spatial properties of laser beam, it is required to carry out the measurement on several planes along the propagation direction, according to ISO standard 11146 [87-89]. There are several methods of acquiring the optical intensity of a particular laser beam. Extensive overviews can be found elsewhere [90-92]. The most popular among these are camera based sensors, slit scanners, knife-edge scanners and pinhole scanners [93].

The camera based scanners work as a two dimensional matrix of pixels, which gives the instantaneous measurement of the intensity distribution at a measured plane. The main advantage of this technique is a high resolution and a short response time. It also gives a real two dimensional intensity distributions profile. The main drawback of these types of systems is a low damage threshold, which requires using beam splitters and filters to reduce a fraction of energy that reaches the sensor [18, 93].

Slit scanners, knife-edge scanners and pinhole scanners use a mechanical component, which scans the beam across the plane perpendicular to the beam propagation direction and records intensity with respect to the position of this mechanical component. The main advantage of these types of devices is the possibility of measuring high power laser beams directly [92, 93].

In the knife-edge method the power or intensity is analysed by means of a power meter or a photodiode, whilst the beam is sliced with a razor, as shown in Fig.2.13. First, as a reference the total energy is recorded when the entire beam reaches the detector. Next, the energy is recorded with respect to the position of the razor, which is continuously cutting-off the beam, until no energy can reach the sensor. Then the normalised sensor response is plotted as a function of razor position and the error function is fitted to the data points (Fig.2.14). Then the energy distribution is achieved by differentiating the fitted curve, as shown in Fig.2.14. Next, the slit or the razor is rotated by 90° along the propagation direction and the measurement is carried out in a perpendicular direction. This allows a two dimensional average power density profile to be obtained with the assumption of circular beam shape [94, 95]. The edge-

knife method does not give the exact profile of the intensity distribution, but the average integrated power, which is directly related to the effective power density of the evaluated beam. The main advantage of this method is its high versatility allowing all range of beam diameters to be measured. Unlike in the pinhole devices, the measurement error is independent of the size of the aperture [93, 96-98].

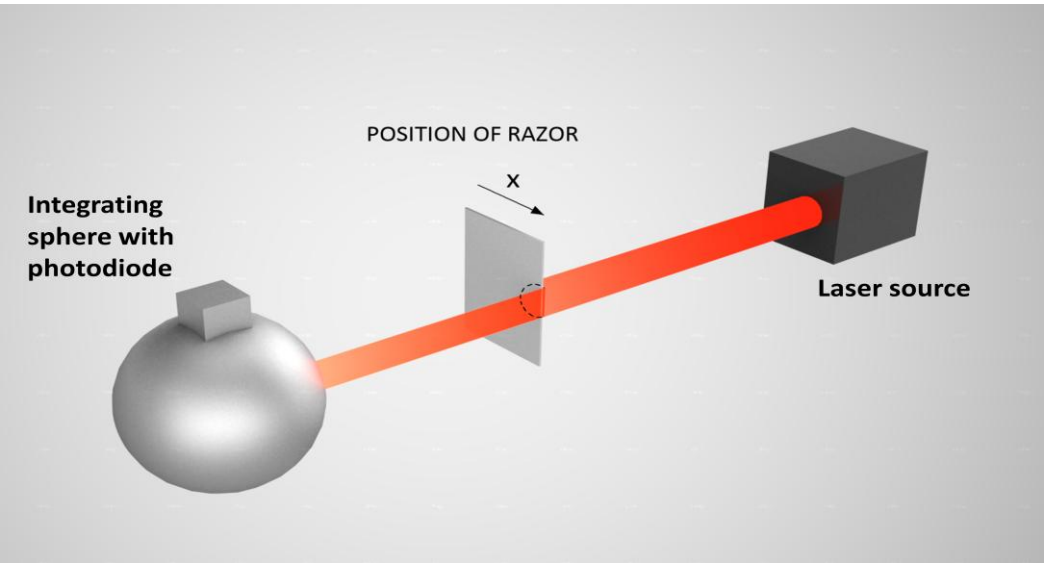

***Figure 2.13**: Principle of measurement of beam diameter with edge-knife technique.*

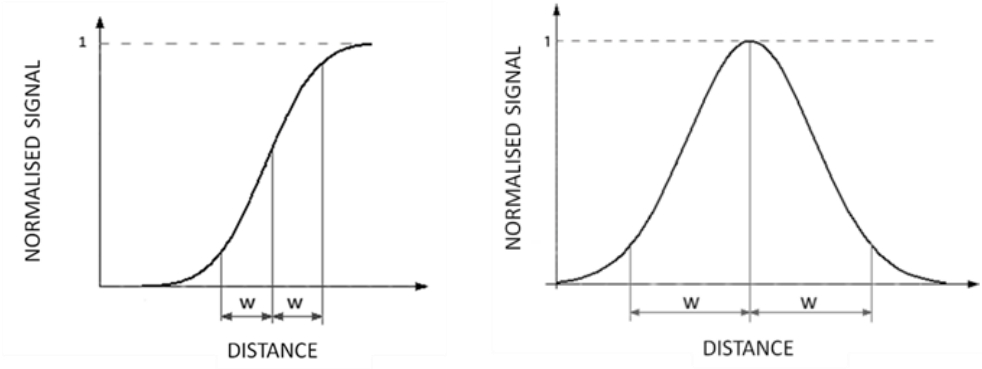

***Figure 2.14**: Edge-knife method: **a)** response as a function of razor position; **b)** differential*

Slit scanners use a scanning element with a long and narrow slit, which transmits the entire beam in a parallel direction and only a slice in a perpendicular direction. Then the subsequent procedure is similar as in the case of knife-edge method [93].

In pinhole devices the laser energy is transmitted through a pinhole, which is connected with a detector. The pinhole moves in x and y direction and collects the values of intensity in every point within an analysed plane, as shown in Fig.2.15 [99]. Then the data is plotted as a two dimensional matrix. This technique measures the real two dimensional intensity distribution at a particular plane, which is also useful in case of beams with higher orders of transverse electromagnetic modes or non symmetric beams [99, 100]. The main advantage of the pinhole scanners is the combination of good resolution with high damage threshold, enabling measurement of high power lasers. The main drawback is the dependency of accuracy on the diameter of the pinhole. Because only a small part of the energy reaches the sensor, the noise ratio is relatively high in these types of devices [18]. Therefore a high fill factor, which is defined by the ratio of the beam size to the pinhole size, is required for a maximum accuracy. This limits the minimum beam diameter, which can be accurately measured by most of the pin-hole scanners down to 100 µm [101].

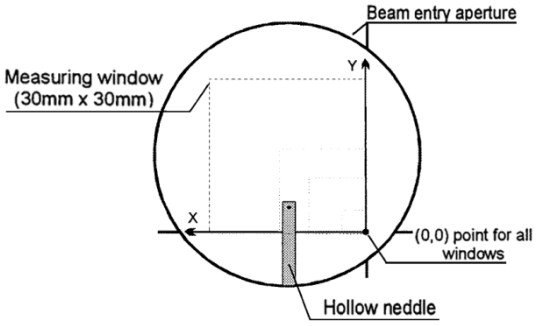

Figure 2.15*: Pinhole scanner – measuring window and hollow needle to acquire the intensity [99].*

2.3.2.2. Definitions of beam diameter

Laser beam is not a physical object that can be touched or simply measured, therefore there are several definitions of beam diameter, among the most commonly used are [18, 92, 102]:

- Full width at half-maximum (FWHM)
- Width at $1/e^2$ intensity

- Diameter containing 86% of total beam energy (D 86)
- Knife-edge width at 10/90
- Second order moment (4σ)

In order to measure the beam diameter with any of the above definitions, the intensity across a plane perpendicular to the propagation direction has to be measured. Then the normalised intensity with respect to a maximum intensity is plotted as a function of x or y position, as shown in Fig.2.16.

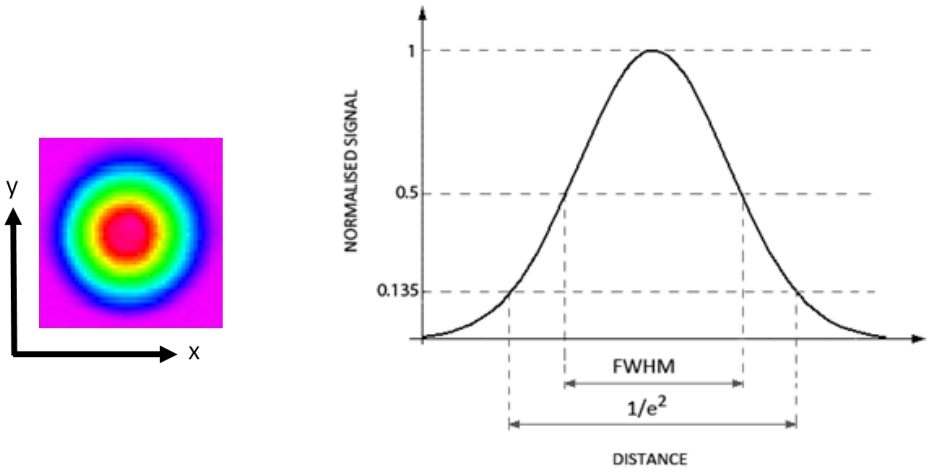

***Figure 2.16**: Beam diameter according to full width at half maximum (FWHM) and 1/e² definition.*

Beam diameter, according to FWHM definition is defined as the width of the intensity distribution profile measured at 50% of the maximum intensity. In contrast $1/e^2$ diameter is equal to the distance between two points on the distribution profile, at which the intensity drops to $1/e^2$ value, as compared to the maximum intensity. In case of a Gaussian distribution this level corresponds to 13.5% of the peak intensity. The fact that the measured beam diameters according to FWHM and $1/e^2$ definitions are only dependent on three points on the intensity distribution profile, which can lead to significant errors in case of non Gaussian beams, is considered to be the main limitation of both methods.

Beam diameter, according to D86 definition, is determined from the area that contains 86% of the total energy. First, the volume of the total energy is calculated by summing the intensity values from each pixel multiplied by the area of a pixel of the detector. Next, the energy is integrated over a circle, which diameter continuously increases from the centroid of the energy distribution in time steps, until 86% of the total power is within this circle, as shown in Fig.2.17 [101]. Then from the number of pixels the beam diameter is calculated with the assumption of circular beam [101]. This definition of beam diameter is useful in many applications, since it reflects a usable power density. In case of a Gaussian distribution the 86% of total energy corresponds to the $1/e^2$ beam diameter. Although the D86 definition takes account of more points than both previous methods it still does not consider the margins of the intensity distribution profile [18].

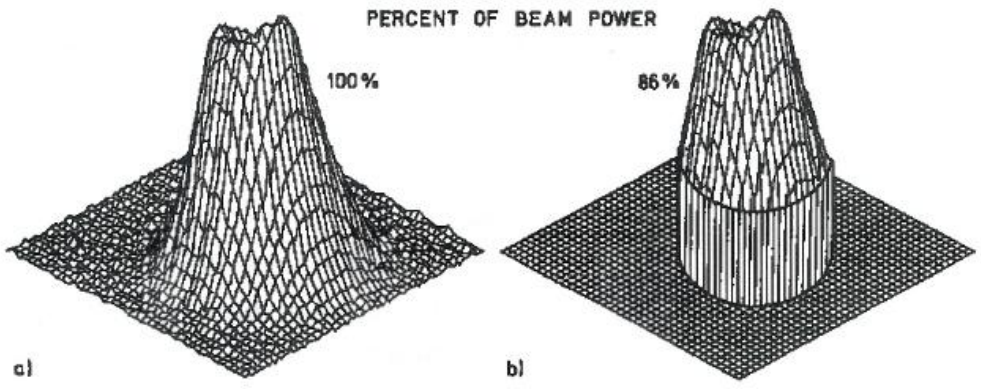

Figure 2.17*: Beam diameter according to D 86 definition [101].*

In knife-edge 10/90 definition the energy or intensity is recorded with respect to the position of the razor when the razor blocks 10% and 90% of the beam. The distance between these two points on the intensity distribution profile corresponds to the 10/90 beam diameter [102].

Second order moment is the official ISO 11146 standard for the measurement of beam quality. In this method the beam diameter is calculated based on the second order moment of the intensity distribution profile I(x,y) for x and y coordinates, given by Equation 2.5 [87, 89, 103].

$$d_\sigma(z) = 4\sqrt{\frac{\sigma_x^2 + \sigma_y^2}{2}} \qquad 2.5$$

Where σ_x^2 and σ_y^2 are calculated according to:

$$\sigma_x^2(z) = \frac{\iint (x - x_0)^2 \cdot I(x,y,z)dxdy}{\iint I(x,y,z)dxdy} \; ; \; \sigma_y^2(z) = \frac{\iint (y - y_0)^2 \cdot I(x,y,z)dxdy}{\iint I(x,y,z)dxdy} \qquad 2.6$$

The value x_0,y_0 are the centres of gravity of the intensity distribution given by:

$$x_0 = \frac{\iint I(x,y,z) \cdot xdxdy}{\iint I(x,y,z)dxdy} \; ; \; y_0 = \frac{\iint I(x,y,z) \cdot ydxdy}{\iint I(x,y,z)dxdy} \qquad 2.7$$

In case of a Gaussian distribution this definition gives the same diameter as $1/e^2$. The second order moment method is the most versatile in terms of the ability of measuring non symmetric beams. However, since the margins of the intensity distributions are also taken in to the calculation this method is sensitive to the noise ratio.

There is no perfect definition of beam diameter and beam quality. All these methods were developed with the assumption of the fundamental mode with a Gaussian intensity distribution and therefore every definition will give different value in case of non Gaussian beams. The key point in accurate characterisation of the beam diameter is the stability of the laser system in terms of output power and focal length during the measurement. The modern laser sources, commonly used for welding or cutting, often have a Gaussian or a top-hat intensity distribution, which combined with the excellent beam stability, enables the accurate measurement.

2.4. Phenomena controlling depth of penetration in laser welding

Interaction of a laser beam with a workpiece can be broadly divided into three regimes, conduction limited, mixed mode and keyhole. In conduction mode the absorbed laser energy is lower than the vaporisation threshold. In this case the surface is heated to a temperature between melting and evaporation and the amount of molten metal is determined by the balance between the energy absorbed and the heat losses. The depth of penetration is limited by the hemispherical isotherms with melting temperature. If however, the power density is sufficient to initiate the vaporisation, a cavity begins to open. If the power density is just over the vaporisation threshold the keyhole is not stable and does not extend beyond the melt front. This regime is considered as the mixed mode. In order to maintain a stable keyhole the recoil pressure from the evaporation needs to significantly exceed the closing force of surface tension. In this regime the depth of penetration is determined by the pressure balance. If the power density is further increased the molten material begins to expel, indicating the drilling regime [1, 104, 105]. The evolution of keyhole is presented in Fig.2.18 [106].

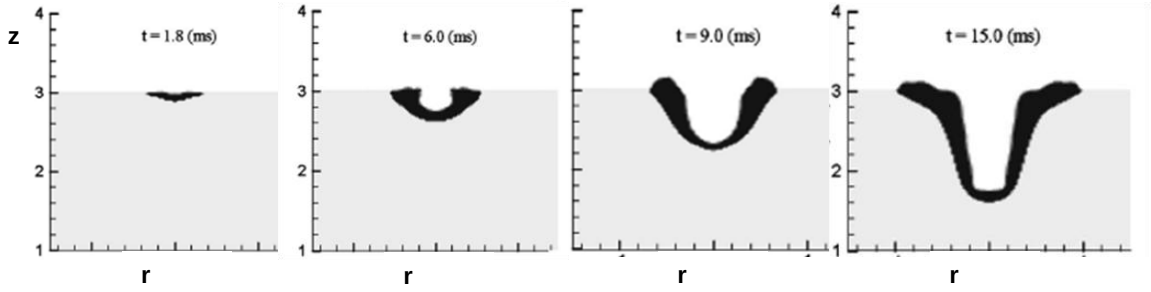

***Figure 2.18**: Keyhole formation process during interaction with laser beam [106].*

Depth of penetration is a key parameter in laser welding, which laser users wish to strictly control. This is, however, rather complicated task, since the depth of penetration is a net result of many forces, which are determined by the balance of

heat [107-110], pressure [111-118], absorption conditions [119-123] as well as the melt flow dynamics [124-129]. The limiting forces of the depth of penetration, according to the literature, are discussed in this section.

A detailed analysis of all forces affecting the depth of penetration in laser welding, according to the literature, is presented in this section. The most important hypothesis of theoretical representations of laser welding, supported by numerous experimental investigations are presented. The main phenomena include: absorption of laser beam, laser-induced vaporisation pressure, hydrodynamic phenomena, plasma/plume absorption and conduction heat transfer. Also some findings from keyhole evolution studies using X-ray imaging and from sub-atmospheric investigations are included.

2.4.1. Absorption

2.4.1.1. Geometrical model of absorption

Absorption coefficient of a material is one of the basic parameters in laser processing. Fresnel law of absorption describes how much energy is absorbed when an electromagnetic wave, such as a laser beam heats a surface. The amount of absorbed light is dependent on the wavelength, polarisation direction and incidence angle. The principle of this approach is shown in Fig.2.19. This model has been successfully applied to laser cutting to calculate the absorption behaviour on the cut front [53, 55, 130, 131]. The lack of plasma in laser cutting, due to the removal effect of the processing gas, justifies the Fresnel law as the main mechanism of absorption. Many researchers also used it to study the keyhole evolution in laser welding [111, 113, 132-137].

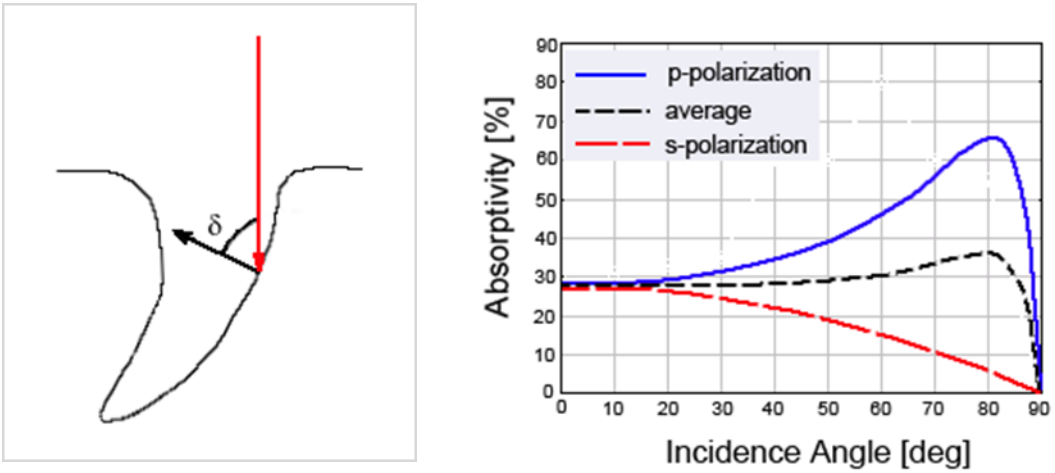

***Figure 2.19**: Dependence of absorption on incidence angle for different polarisations (after [138]).*

Kaplan [132] calculated the keyhole geometry based on the Fresnel model and found that the front wall of the keyhole tended to a specific angle, at which a sufficient amount of energy could be intercepted to balance the heat losses. This determined the wall formation. When the processing speed was increased the keyhole angle and absorption changed accordingly to the new conditions [132]. The amount of laser energy absorbed in a side wall of keyhole increases, but the energy at the bottom of keyhole decreases with increasing travel speed, hence the depth of penetration reduces. This increase of the inclination angle of keyhole with increasing travel speed was confirmed experimentally [139, 140]

Some authors consider that the majority of laser energy is distributed during the primary reflection [141, 142], however, it was also demonstrated that the temperature distribution around the keyhole can be changed drastically by including the multiple reflections into the analysis [143]. The keyhole walls can be considered as shiny surfaces on which the wave guiding by the multiple reflections can occur, as shown in Fig.2.20. The fact that the cavity needs to have a certain depth for the multiple reflections to occur [111, 133, 137] explains the sudden increase of absorption at the beginning of the keyhole mode, observed experimentally [119, 122, 123].

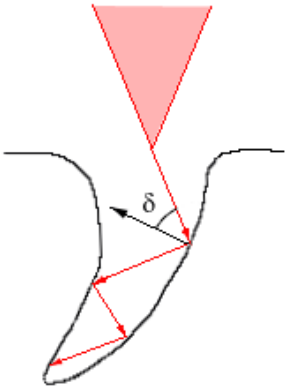

***Figure 2.20**: Multiple reflections inside keyhole.*

Fabbro and Chouf [135] calculated the depth of penetration based on the drilling velocity, which was dependent on the inclination angle of the keyhole. The resultant keyhole geometry evolved according to the multiple reflections. The limit of depth of penetration, in this model, was mainly determined by the geometry. The amount of light that was reflected inside the cavity reduced gradually as the depth reduced, thus at a certain level of depth of penetration no beam reached the bottom of the keyhole.

To improve the multiple reflections model a real geometry of keyhole was necessary, thus there was a great interest in visualising the keyhole using X-ray [111, 116, 144, 145] or by welding transparent materials [113, 117, 146]. A calculation of Fresnel absorption based on the temporal evolution of keyhole, acquired from X-ray, showed an initial increase of absorption with increasing depth of keyhole, followed by a plateau at a certain depth. This plateau was attributed to the increased diameter of the keyhole [111]. The probability of multiple reflections increases with increasing the depth of keyhole and decreases with increasing its width, as demonstrated in Fig.2.21 [122]. Thus keyholes with high ratios of depths to widths are more beneficial in terms of multiple reflections [122, 147]. Furthermore, the total absorption in a cavity is not only determined by its geometry but also by the heat transfer on the walls. The more efficient the heat transfer inside the cavity the higher the absorption efficiency [147].

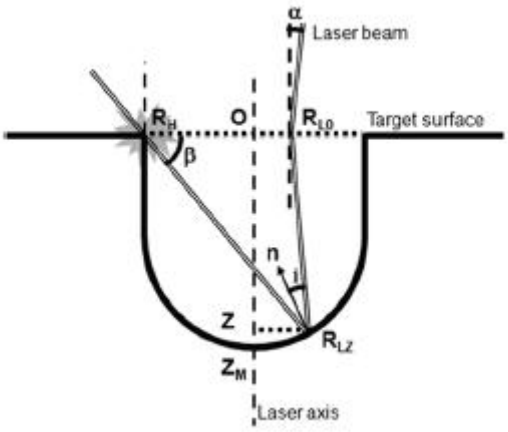

***Figure 2.21**: Dependence of the second reflection on cavity geometry [122].*

One of the important advantages of using the Fresnel law in modelling the laser processing is the possibility of including the beam properties. This geometrical model can be used to study the effect of divergence angle or polarisation on the process [53, 55, 130, 131]. The smaller the divergence angle of a laser the greater the depth of penetration, due to the fact that the first reflection takes place further down in the keyhole [136, 148, 149]. Solana and Negro [115] compared evolutions of keyholes achieved with a Gaussian and a top-hat profile. A greater depth of penetration with a Gaussian beam was observed when only the first reflection was considered. This was attributed to the higher peak intensity of the Gaussian beam. The difference, however, almost disappeared after including the multiple reflections. Further differences diminished after incorporating the plasma absorption, which altered the energy distribution on the keyhole walls by increasing the amount of light absorbed at the upper region of the keyhole [115].

The Fresnel model was also used to explain the experimentally observed differences between laser cutting with CO_2 and solid state lasers [55, 150, 151]. The fibre or disc lasers exhibited better cutting performance than CO_2 laser but only in case of thin plates. As the sheet thickness exceeded approximately 6 mm the same limit of the cutting speed was achieved with both wavelengths, despite a greater focus-ability of the fibre laser. Moreover, the cut quality of CO_2 laser is often is often the quality obtained with the fibre laser [52]. According to the Fresnel law of absorption, 1 μm wavelength (fibre laser) has a higher absorption than 10.6 μm wavelength (CO_2 laser), but only at low incidence angles, as shown in Fig.2.22 [55]. As the angle of

incidence increases over 85.9º, the absorption for 1 µm wavelength becomes lower than for 10.6 µm wavelength. This is due to the difference in Brewster angles between the wavelengths. Brewster angle for a particular wavelength corresponds to the incidence angle at which only s-polarised beam is reflected from the surface, whilst p-polarised beam is totally absorbed by the surface. As shown in Fig.2.22 [55], 1 µm wavelength radiation has its Brewster angle at a lower incidence angle than 10.6 µm wavelength radiation. In the case of cutting of thin sections the cutting edge is almost vertical and only a little absorption takes place on the cutting front with both lasers. Thus the majority of heat is transferred through the surface, which is more beneficial for fibre laser than for CO_2 laser. Because the maximum absorption in the cut front for fibre laser is achieved at lower incidence angles, it is more efficient and therefore the faster cutting speeds can be achieved in thin section cutting, as compared to CO_2 laser. The melt removal improves with increasing absorption in the cut front and thus this explains better performance of fibre laser in thin section cutting. It was demonstrated that when the striation pattern, visible in the cut edges, were inclined at the same angle as the Brewster angle very low roughness was achieved [151]. However, the efficiency of melt removal decreases with increasing sheet thickness, thus the cutting speed has to be decreased in thick section cutting. The greater incidence angle of the cut front at these conditions is more beneficial for a longer wavelength. In this case the cut front is closer to the Brewster angle of CO_2, hence better cut quality is achieved with CO_2 lasers than with fibre or disc lasers in thick sections [21, 53, 55, 151].

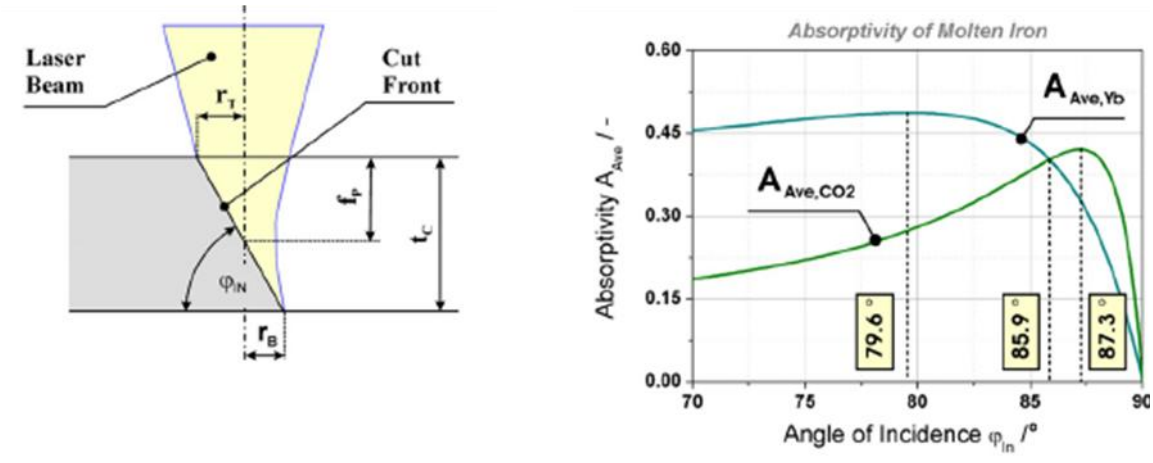

***Figure 2.22**: Absorptivity of molten iron as a function of cut front inclination angle for CO_2 and fibre laser [55].*

There is an additional difference between both lasers. In comparison to CO_2 laser the fibre laser can be more easily guided inside the kerf via the multiple reflections. Thus the energy of subsequent reflections of fibre laser is significantly high. On one hand, this increases the absorbed energy, despite the low Brewster angle. On the other, hand the multiple reflections result in an uneven distribution of the heat inside the cavity, which might lead to the destabilisation of lower parts of the cutting zone, evident as the coarse striations [21, 53]. This was postulated by Pettring [21, 150], as shown in Fig.2.23. Some authors disagree with this and claim that the cut quality is determined by the kerf width, which is attributed with the efficiency of melt removal from the narrow kerf [56-58]. It was shown that this could be improved by using larger beam diameters [56].

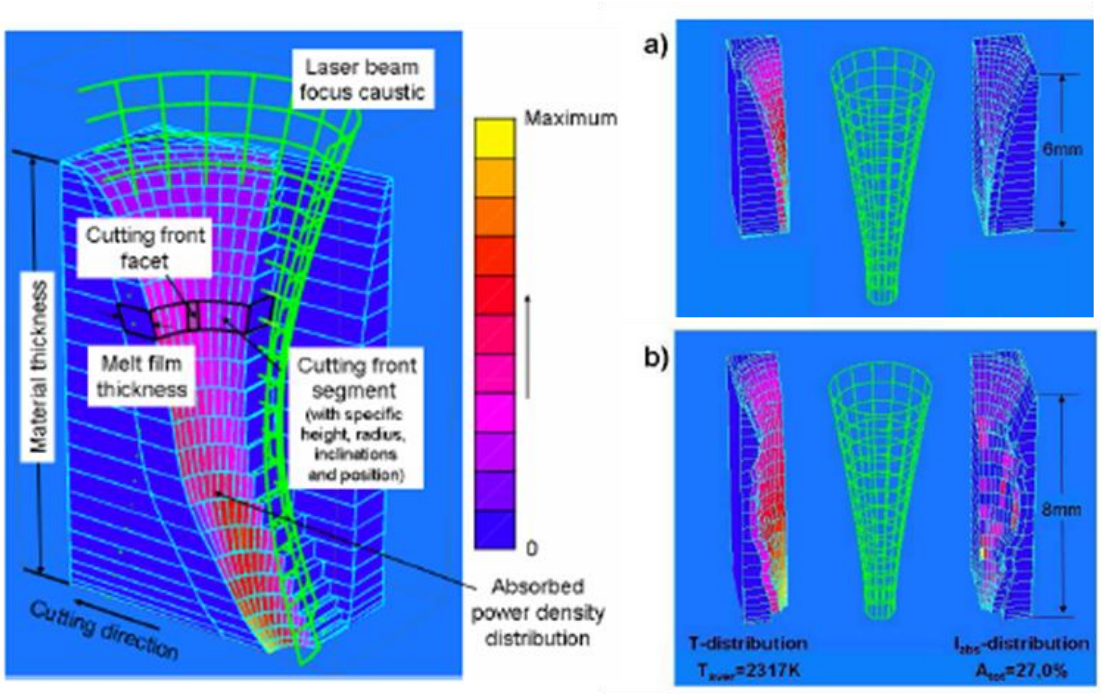

***Figure 2.23**: Energy absorbed on the cut front; **a)** considering only the first absorption; **b)** multiple reflections case [21, 150].*

The effect of polarisation of laser beam was also studied [152-155]. According to the Fresnel law different results should be obtained when beam is polarised in different directions [130, 131, 141, 156]. Different polarisation directions are recommended for different processes. In micro drilling the radially or azimuthally polarised beams

enable an improvement in ablation rate and quality of drilled holes, as compared to the linear polarisation [152, 154]. Nizniev and Nesterov [141] showed that a radially polarised beam was the most effective for laser cutting of thick plates. On the other hand, Zaitsev et al. [155] derived numerically that an elliptically polarised beam would be more efficient for cutting [155]. This was clarified later, the absorption in the cut front is important in cutting, whereas in drilling the wave-guiding inside the channel determines the absorption [154]. According to Weber et al.[138] a cylindrical polarisation (radial or azimuthal) is better for any material processing than the linear polarisation, owing to the absorption being independent of the direction of movement. According to the authors this is particularly beneficial when the beam is adjacent to a cylindrical capillary, such as the keyhole in welding or cutting. In such a case given direction of polarisation is fulfilled over the entire circumference. However, the experimental results demonstrated by the authors did not show clearly the benefits of cylindrical polarisation, as compared to circular polarisation. Although the cutting speed could be increased, however, the effect diminished as the sheet thickness exceeded 8 mm. Furthermore, the reduction of spatter in laser welding, which according to the authors was also due to the change of absorption conditions, as a result of polarization, is questionable. The authors did not include any macrographs to show if the depth of penetration stayed unchanged after polarisation. It is likely that the spatter level would reduce as the result of decreased depth of penetration. It was also shown by Meier at a. [154] that on some materials, such as copper or brass the influence of polarisation was negligible, which was attributed to equal channelling effect for azimuthally and radially polarised beams. In another study the influence of dynamic polarisation on the melt pool stirring was demonstrated, as shown in Fig.2.24 [153]. The low effect of polarisation on the size of the melt pool implies that not only the Fresnel absorption but other effects, such as heat conduction on keyhole walls or melt flow are also important in the energy balance.

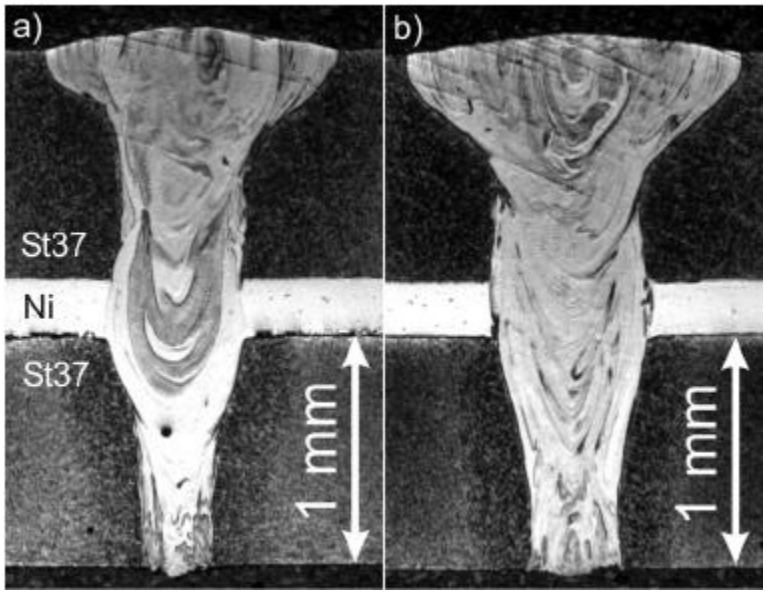

***Figure 2.24**: Effect of dynamic polarisation on melt pool [153].*

2.4.1.2. Experimental measurements of absorption

Experimental measurements have shown that at the beginning of laser interaction the absorption in metals is low. However, the absorption coefficient is proportionally dependent on the temperature of workpiece. Thus the situation improves as soon as the melt pool appears and then further increase of absorption occurs in the keyhole regime, where the laser beam is efficiently absorbed by the internal reflections [62, 157]. An example of absorption evolution in laser processing is shown in Fig.2.25 [28].

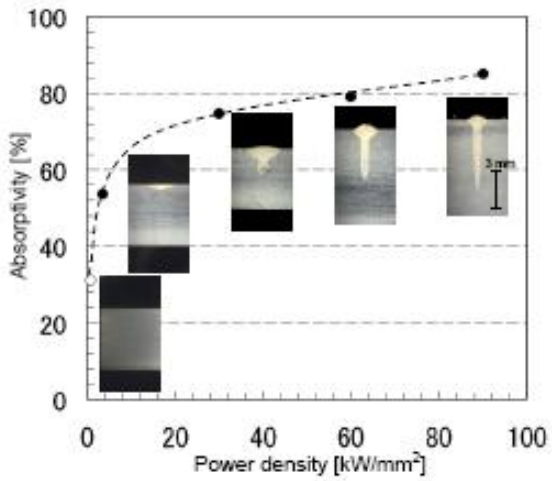

***Figure 2.25**: Absorption and weld profile as a function of power density [28].*

Fuerschbach [119] used a Seebeck envelope calorimeter [158] to measure the heat input absorbed during laser welding. He found that the heat transfer efficiency increased from 0.2 to 0.92 with increasing power density and saturated afterwards. A decrease of absorbed energy with increasing travel speed was found in another study [120]. This was further clarified. The increase of absorbed energy with increasing power density or decreasing travel speed is associated with the depth of the cavity [28, 119-121]. Considering the Fresnel law of reflection the number of internal reflections increases with increasing the keyhole depth [111, 115]. Fabbro [139, 140] showed experimentally that the inclination angle of the keyhole increased with increasing travel speed. Thus the absorption in the front wall of keyhole increases but the probability of multiple reflections decreases with increasing travel speed, which results in the reduction of depth of penetration.

Norris et al. [123] used two integrating spheres with photodiodes in order to capture the reflected beam from workpiece during laser spot welding. The results confirmed that the absorption of laser beam is determined by the welding mode. In conduction regime, most of the beam was reflected from the surface. At the beginning of the irradiation time the reflected rays were parallel to the incident beam. The direction of the reflection became more random once a semi hemispherical weld pool emerged. The transfer efficiency did not exceed 50% in the conduction regime and 75% in the keyhole regime. The transfer efficiency was found to be directly dependent on the keyhole dimensions. Thus the efficiency rose with increasing laser power and pulse duration, as long as it was followed by an increase in depth of keyhole [123]. Katayama et al. [159] reported the efficiency of a fibre laser up to 90% at slow travel speeds and its decrease with increasing travel speed. High speed photography supported by X-ray used in this study revealed that the amount of light entering the keyhole reduced with increasing travel speed, due to the change of the inclination angle of the keyhole. This also resulted in different absorptions between aluminium and steel. At a low power density range, aluminium exhibited a lower absorption than stainless steel, but at high power densities the amount of absorbed heat by aluminium exceeded the one in stainless steel [159]. This means that as soon as the cavity emerges the absorption is mainly determined by its geometry, which supports the theory of internal reflections. Similar was concluded from a comparison of twin spot welding with a single beam welding. The higher transfer efficiency in the single

beam laser welding resulted from a deeper depth of penetration achieved for the same total power [160]. Cremers et al. [161] used an interferometer, as well as a differential transformer to measure absorbed energy from a pulsed laser. The absorbed energy was found to be directly proportional to the depth of penetration, despite melt ejection at high power densities.

Some authors postulate that the absorption inside the keyhole is more complex than the predicted by Fresnel law of absorption. In experiment performed by Schneider et al. [122] the absorption on various material increased with increasing laser power and saturated at approximately 80%. According to the authors the fact that such a high value could be achieved independent of the material, implies that other effects, rather than just internal reflections, must be responsible for absorption. They suggest a possibility of Rayleigh-Taylor instability [162], which enables the multiple reflections on a micro scale by increasing the roughness of the keyhole walls [122]. A similar hypothesis was postulated by Fabbro [140] who reported the absorption ranging from 60% to 70% in a 1 mm thick metal foil. This seems to be very likely, due to the fact that keyhole is surrounded by a layer of molten metal, thus its walls are not smooth as a result of various perturbations. These perturbations increase the area of keyhole walls, which results in the enhancement of absorption inside these small cavities.

Measurement of transfer efficiency during pulsed laser welding, carried out by Fuerschbach and MAcCallum [163] showed, that in contrast to CW laser welding, the values did not exceed 67%. The authors justified this difference between lasers by the energy loss due to the evaporation, which could not be measured in this experiment. The lack of possibility to take account of the energy used for vaporisation or spatter is the main drawback of most calorimetric studies. Another reason for such a difference between both lasers, according to the authors, could be an additional absorption in the laser plasma in the case of CW laser [163]. However, the plasma is apparent in both operating modes, pulsed and continuous. Kim and Kim [164] postulate that the evaporation losses in CW laser welding can also be severe, especially at low travel speeds, which contradicts this theory. In another study, the absorption during pulsed laser processing of titanium varied from 0.32 to 0.8, depending on the welding regime [165]. The transfer efficiency of pulse laser welding is also dependent on the geometry of the cavity. Depending on the pulse parameters the keyhole can collapse and reopen with different frequencies. An X-ray imaging

has revealed that it takes few milliseconds from beginning of irradiation to form the keyhole [111, 116]. Since the absorption during the period of keyhole reopening is low, thus the average absorption of pulse laser welding is lower than CW laser welding [166]. This hypothesis seems to be more likely, but it would mean that the absorption in pulsed laser welding is strongly dependent on the operating parameters, such as the peak energy, duty cycle, overlapping rate. The lower absorption of pulsed laser, as compared to CW laser can be also attributed to the low average power of pulse lasers, which significantly decreases the accuracy of calorimetric measurements. A more accurate equipment would be required to measure the absorption at these low average powers.

The difficulties with welding of copper and its alloys with 1 μm lasers demonstrate the influence of wavelength on absorption. Some experimental results showed an inadequately shallow penetration for the same laser parameters, as compared to steel or aluminium alloys. It was demonstrated that a laser with 500 nm wavelength gave better results than a powerful fibre or disc laser [167, 168]. Therefore, there were few attempts of combining a green laser (frequency doubled IR laser) with a high power 1 μm laser [167-170]. Since the green lasers are only available at significantly lower powers they need to be combined with more powerful infrared lasers. In this solution the green laser just preheats the surface and increases the absorption for the fibre laser, the high power density of which provides the energy for processing. Similar principles can be achieved by adding a high power pulse to the main pulse during pulsed laser welding [171].

2.4.2. Conduction heat transfer

Since the heat balance plays the important role in laser welding, the heat conduction equation is often used to investigate laser fundamentals. The most simple representations of laser welding, such as an analytical solution proposed by Rosenthal [107, 172] uses simplified heat sources. In this particular case the laser beam is represented by a point or a line, as shown in Fig.2.26. This approach allows for calculation of temperature distribution within the workpiece, based on welding speed and applied power. There were further modifications of the Rosenthal equation, which attempted to use more realistic heat sources, which included

combination of a point and a line into one source [173] or using several individual line sources [132] or several point sources distributed at different position within the workpiece [174, 175]. The next step was to use a heat source represented by a Gaussian distribution, which gave a more realistic power distribution on the surface [108-110, 176, 177]. Further improvements included volumetric heat sources, such as double ellipsoid [178, 179] or conical heat source [180, 181], as shown in Fig.2.27.

***Figure 2.26**: Point and line heat source.*

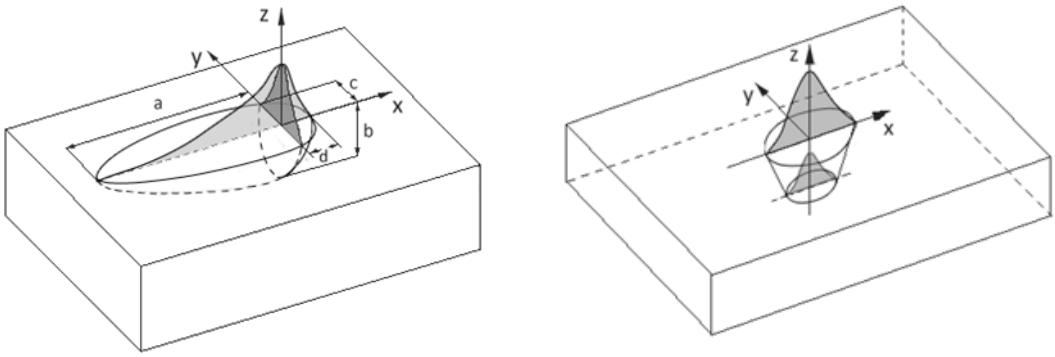

***Figure 2.27**: Volumetric heat sources: **a)** double ellipsoid [178]; **b)** conical heat source.*

The heat conduction equation on its own can be used to predict depth of penetration in conduction limited or shallow penetration laser welding, where the heat is transferred uniformly from the surface and thus the depth of penetration is strongly dependent on the thermal properties of the material [182-184]. But to represent the deep welds from the keyhole laser welding, the experimental data are often required beforehand, output of which is used to determine the characteristic dimensions of the heat source, such as the length of a line source. A similar approach is used in the

case of volumetric heat sources where the characteristic dimensions are tuned to obtain the same weld shape as in the experiments. Therefore these models are often used to study heat effects during welding, such as generation of residual stress [179] rather than to predict forces affecting the depth of penetration in laser welding.

However, the heat conduction model can be extended to include other phenomena. The most common practice is to combine more than one model, such as a heat conduction transfer model with a drilling force [143, 185]. Some more advanced models, which give good representation of real conditions in laser welding, additionally incorporated the fluid flow, multiple reflections and plasma absorption [106, 186].

Heat conduction plays the important role in the energy transfer between a laser beam and a material in laser welding. Shannon [147] showed that the absorption of laser energy inside a keyhole was not only determined by the multiple reflections but also by the efficiency of the heat conduction in the keyhole walls. Thus the more the energy could be thermally radiated inside the keyhole walls the better the utilisation of the energy from every reflection inside the keyhole. Jin et al.[113] studied the evolution of keyhole in Pyrex glass and found that majority of laser energy was absorbed on the front wall of the keyhole and then the heat was conducted into the rear wall.

Conduction heat transfer accounts to a large part of the heat loss during welding. This loss can be significant in conduction welding, as well as in keyhole welding particularly in the initial stage. Fujinaga et at.[116] concluded, based on X-ray observation of keyhole, that initially before the keyhole appeared, the small melt pool was subjected to a strong cooling, due the conduction losses. A numerical analysis of plasma in another study revealed that at low power densities, below the plasma threshold, some part of laser energy was consumed for heating of cold shielding gas [187, 188].

Although some authors conclude that the real temperature profile around the keyhole is not as smooth as the isotherms predicted by the thermal model [117, 189], due to various perturbations of the keyhole, but the temperature distribution must be the driving force for most of these effects. It is known that the thermal properties of the material determine the maximum temperature that is reached for a given conditions.

The majority of phenomena in laser welding, such as vapour pressure and melt pool dynamics are directly dependent on the temperature. Measurements of temperature, using a pyrometer, revealed a strong thermal gradient in various points inside the keyhole. The highest temperature was found at the bottom of keyhole [190]. This gradient is the driving force for other effects, such as fluid flow, which then affects the keyhole behaviour.

2.4.3. Drilling model

Deep penetration from laser or electron beam welding can be represented by a drilling model, in which the evaporation pressure acts on the molten metal. In the model proposed by Anisimov [191] a high power density laser beam caused an intensive evaporation, which further induced a high pressure on the molten metal. This pressure, referred to as recoil pressure, provided a drilling force responsible for deep penetration. In the later drilling model developed by von Allmen [192] the analysis was extended by a melt expulsion, which occurred if the drilling force exceeded the surface tension. This is shown in Fig.2.28 [193]. The recoil pressure acted like a piston and removed a previously molten material. A one dimensional heat flow equation was used to calculate the temperature distribution. A maximum depth of penetration was determined from the balance between the recoil pressure and the surface tension, which was additionally dependent on the amount of molten metal. The depth of keyhole was calculated based on the pulse duration and the drilling velocity, which was proportional to the power density of the laser beam [192]. Since then there were many models published, which incorporated the principle of drilling force from the vapour pressure [185, 194-198].

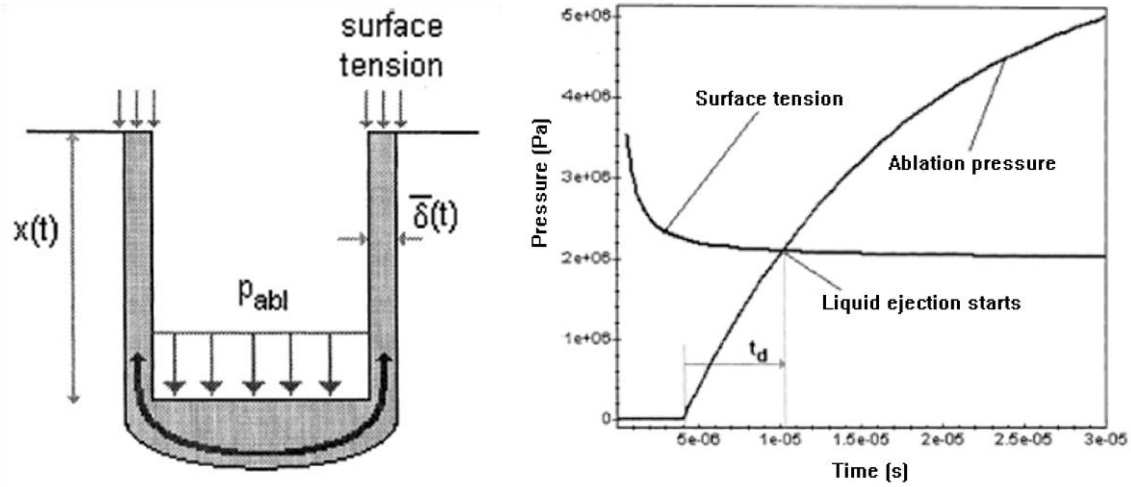

***Figure 2.28**: Drilling model: **a)** forces acting on liquid layer; **b)** balance between surface tension and ablation pressure with duration time [193].*

In the drilling model carried out by Colegrove et al. [199] different welding regimes and the corresponding fractions of depth of penetration due to melting and drilling were identified, as shown in Fig.2.29. The balance between the recoil pressure and the surface tension allowed for an elegant explanation of the effects of heat conduction and vaporisation on the depth of penetration in laser welding.

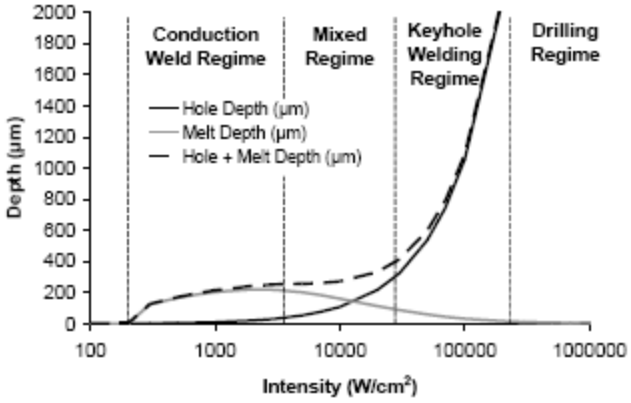

***Figure 2.29**: Four different regimes of laser processing obtained from drilling model [199].*

The main difficulty in the drilling model is to define the ratio of the vaporisation to the melt expulsion. Some works underline the importance of melt flow and estimate that

only a small quantity of material is vaporised and the rest is expelled radially in the liquid state [200-202]. It was demonstrated that the intensive evaporation occurred only in a small region where the temperature was very high [203].Thus the vaporisation pressure induces the drilling force, but a majority of metal is removed by the melt expulsion [201, 202]. In the analysis carried out by Anisimov [204] and Knigth [205] the evaporation rate of alloying elements predicted by a model were higher than those measured experimentally. This according to the authors can be explained by the condensation of vapours, which return back to the melt pool [204, 206]. Thus it seems like the melt expulsion dominates the material removal during the drilling process. However, Solana et al. [193] showed in his model that special conditions were required for liquid ejection to occur. There was a threshold time after which the recoil pressure overcame the surface tension. Thus the welding conditions determine the fraction of liquid ejection in the total material removal [201]. A similar was concluded by Semak and Matsunawa [194]. They demonstrated that the fraction of melt removal by evaporation increased, whilst the fraction due to melt expulsion decreased with increasing the laser intensity, as shown Fig.2.30. This demonstrates the complexity of keyhole laser welding.

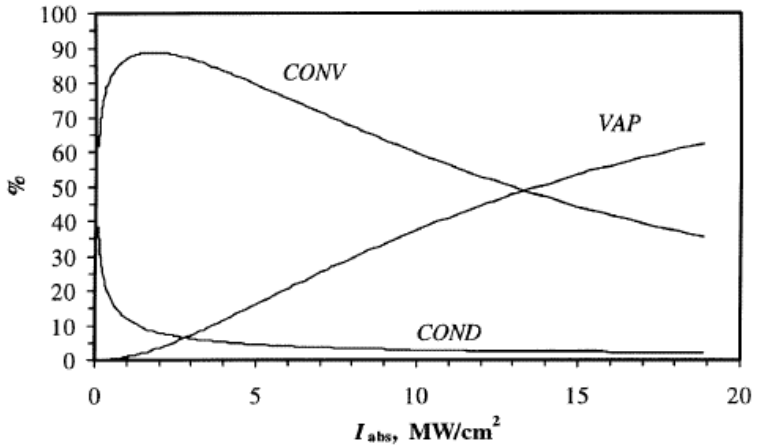

Figure 2.30*: Fractions of absorbed intensity carried away from the interaction zone due to convection (CONV), evaporation (VAP) and conduction (COND) [194].*

The drilling model gives good approximation of the keyhole laser welding, but since it considers the surface tension as the only restoring force for keyhole, it tends to overestimate the depth of penetration, in comparison to the reality [191, 207]. An

example is shown in Fig.2.31 [199]. It is clear that the predicted depths are much greater than the experimental ones.

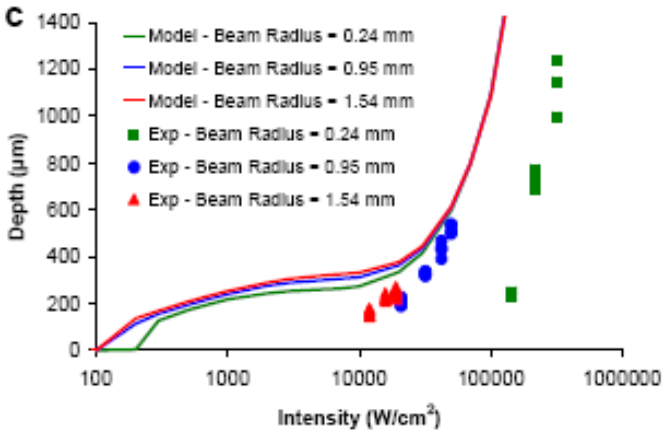

***Figure 2.31**: Comparison of drilling model with experimental results [199].*

Wei [208] for instance showed that the evaporation rate could be overestimated even by 50% if conduction losses were neglected. Alternatively the plasma can be considered as a force, which prevents infinite keyhole depth. Chen et al. [209] demonstrated that, due to neglecting of laser absorption in the plasma, the calculated recoil pressure was much higher than the experimentally measured. Many authors applied a direct attenuation of the laser beam in the plasma [106, 210, 211] or its ability to redistribute the energy distribution by absorbing and reradiating the laser energy [114, 186, 212-214]. A detailed discussion of plasma effect is shown in Section 2.4.4.

The melt dynamics could be another source of energy dissipation, which prevents from infinite deep of penetration in laser welding [106, 194, 200, 215-217].

2.4.3.1. Experimental measurements of vaporisation pressure

There were few successful attempts to measure the recoil pressure experimentally. Zhiryakov et al. [189] carried out a pioneering measurement of the recoil pressure during pulsed laser drilling, using a piezoelectric transducer. They reported a direct dependence of the recoil pressure on the power density of a laser. However, this

dependence did not match with the prediction of a thermal model, which was attributed to the keyhole perturbations. Mizutani and Katayama [218] used an electronic balance method to measure the pressure of laser radiation. The recoil pressure was estimated to be in a range between 3 kPa and 5 kPa. Knorovsky and MacCallum [219] measured the recoil pressure using two different methods, a piezoelectric sensor and sensitive microphones. The measured recoil pressure interacted on a much greater zone than the keyhole diameter.

Vaporisation rate is directly dependent on the temperature and material composition [220]. Schauer et al. [190] used a pyrometer to measure temperatures inside the keyhole during electron beam welding. The temperature was found to be dependent on the chemical composition of the material. The more the volatile elements were in the alloy the lower the temperature at the vapour-liquid surface was recorded. This implies that by increasing the content of volatile elements in the workpiece the vaporisation efficiency increases, allowing for the same vaporisation rate, but at lower temperatures. The analysis of variation in chemical composition during laser welding confirmed that the volatile elements, such as magnesium in aluminium or manganese is steel were dominant in the vapour plume [221-224]. Therefore if the recoil pressure was the main force limiting the depth of penetration in laser welding, it should be dependent on the chemical composition of the welded material.

Not only the volatile elements from the workpice can increase the recoil pressure but also the molecules from shielding gas, as was shown by Zhao et al. [225]. The oxygen from ambient atmosphere, in this study, merged with the carbon from steel into the carbon monoxide, which increased the recoil pressure as a result.

It can be concluded that the recoil pressure is the main driving force responsible for deep penetration laser welds, however, the keyhole stability and therefore resultant depth of penetration must be dependent on many other phenomena, such as melt flow and temperature gradient. Furthermore, the plasma/plume as an unavoidable result of intensive evaporation can additionally complicate interactions within the keyhole.

2.4.4. Absorption of laser by plasma

2.4.4.1. Numerical investigations of plasma effect

Interaction of a high power density laser beam with a workpiece may induce an intensive vaporisation. The vapour cloud suspended over the laser-material interaction point, as a result of this evaporation, can interact with the oncoming laser beam. According to inverse Bremsstrahlung mechanism, the electric field of light can accelerate the free electrons within the vapour, which colliding with atoms and ions, increase their energy, which leads to the absorption [226]. Because an electromagnetic wave with a lower frequency can easier induce oscillations of electrons, the plasma absorption coefficient for CO_2 lasers is much greater than for fibre lasers.

Although the vapour plume in welding is continuously diluted by the shielding gas thus its absorption properties should be significantly low [142] but, some authors still believe that some portion of laser energy in fibre laser welding is absorbed within the vapour [114, 186, 212-214]. Solana et al. [210] developed an analytical model, which included the attenuation of the drilling force by the plasma. They assumed that apart from the attenuation effect of plasma, the laser beam was also scattered by the particles of vaporised metal, based on Rayleigh scattering theory [227]. The results of this analytical model were in good agreement with the experimentally achieved welds.

Some studies assume that a significant portion of absorbed laser energy is transferred to the keyhole walls through the plasma via inverse Bremsstrahlung absorption, which improves the heat transfer [114, 186, 212-214]. The plasma absorbs a part of laser energy and then the heat is conducted into the material. Dowden [228] showed that this type of energy transfer was possible, but only after exceeding a certain threshold energy. In an extensive model developed by Zhou et al. [106] the plasma played a twofold role. On one hand, it initiated keyhole formation at the initial stage and also heated-up the keyhole walls, due to the inverse Bremsstrahlung absorption. On the other hand, it blocked the incident beam at a certain depth of the keyhole. The plasma absorption in this model played a major role in limiting the depth of penetration from increasing infinitely. The validation showed an excellent agreement with the experimental results. The Beer-Lambert law, which

describes the transmission of light as a function of distance when this light propagates through a substance [229] was also used to represent the attenuation of laser energy by the plasma inside the keyhole [211]. According to same analysis a significant part of laser energy can be consumed for heating of cold gas even with power densities below the plasma threshold [187]. However, this effect should be negligible in keyhole laser welding.

Alternatively some authors demonstrated that the plasma attenuation coefficient did not affect the energy balance significantly [132, 230, 231]. A large change of the attenuation coefficient resulted in a less than 10% variation of calculated depth of penetration [132, 231]. This could, however, result from the assumption of a constant attenuation coefficient of the plasma as a function of depth.

2.4.4.2. Experimental investigations of plasma absorption

A weakly ionised state of the vapour plume during processing with 1 µm wavelength radiation was found in most spectroscopic studies [65, 232-235]. An example of the fibre laser plume is shown in Fig.2.32 [236]. This implies that the attenuation properties of such a plume should be negligible [232]. It was shown that despite the intensity of the neutral line spectrum of the main elements of stainless steel i.e. Fe, Cr and Mn increased significantly with increasing laser power, however, the ionised spectra of alloying elements and line spectra of Ar neutral atom were not detected. The calculations of ionisation degrees of Fe and Ar based on Saha's equation [237] regarded the vapour plume as a weakly ionised, which means that the laser absorption would be insignificant [236].

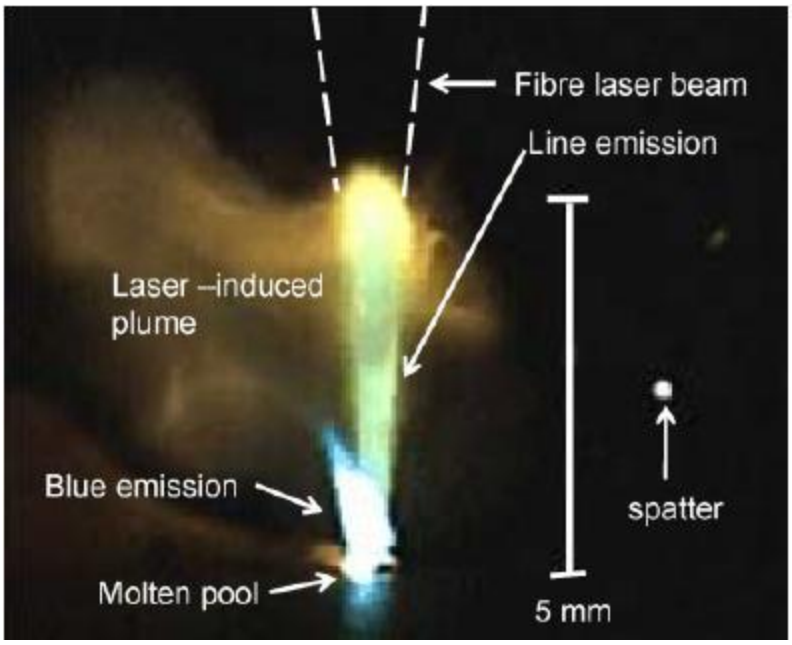

***Figure 2.32**: Plume induced by 10 kW fibre laser radiation in argon environment [236].*

Some authors used a 20 W laser probe in order to measure its attenuation after passing through a vapour plume, generated by a high power fibre laser [28, 63, 238]. In all cases the attenuation of this probe measured near the keyhole exit was approximately 4%. Most of the attenuation was attributed to the Rayleigh scattering. The same measurement carried out at a distance of 15 mm from the surface showed no absorption [63]. The authors justify these low attenuation properties based on the dependence of depth of penetration with the laser power, which unlike in CO_2 laser welding in argon atmosphere, increases linearly even at high powers, rather than saturates if the plasma absorption was significant [63, 64]. However, despite this negligible absorption, a comparison of macrographs revealed an increased depth of penetration by approximately 20% when the plume was suppressed [238]. It is well known that the depth of penetration in partially penetrated welds can fluctuate greatly, due to various instabilities of keyhole, which could be easily mistaken with the plasma absorption effect.

Attenuation of a pulsed Nd:YAG laser in a plasma created by a tungsten-inert gas (TIG) process in argon atmosphere was shown to be negligible [239]. A direct comparison showed that less than 1% of the total power of Nd:YAG laser was absorbed at a distance of 1 cm, whilst passing through the arc plasma. In contrast,

the same test carried out with CO_2 laser resulted in a 40% attenuation [76]. Bibik et al. [240] compared the attenuation properties of the arc plasma in hybrid welding when using CO_2 and He-Ne laser. The measurement of the intensity distribution of the CO_2 laser after passing through the arc plasma revealed a gap in a central part, orientated along the beam axis. This, according to the authors, indicated the absorption of the laser radiation by the arc plasma, caused by a high concentration of charged particles near the axis. An analogous experiment carried out with the Ne-He laser revealed no absorption [240]. This demonstrated the difference between both lasers. However, the plasma absorption can be dependent on many conditions. A measurement of the transmission of Nd:YAG laser through a TIG plasma showed that the attenuation could be as high as 1.3 m^{-1} in the environment of argon and negligible in helium. The effect was additionally dependent on the arc current [241].

Some authors claim that despite the low ionisation potential of the plume during fibre laser processing the laser beam can still be attenuated due to the scattering on the vapour particles [69-75, 242]. There are many speculations regarding the legitimacy of this phenomenon.

It is known that plasma expansion during laser drilling or ablation with ultra-short pulse lasers with extremely high power density (10^{11} W/cm^2) creates a shock wave. It was demonstrated that this high velocity shock waves (30 km/s) reduced the power density of the laser beam inside the drilled holes due to the inverse Bremsstrahlung absorption [243, 244]. In CW laser welding power density is usually not high enough to create shock waves; however, some authors consider the ability of plasma to scatter the laser beam inside the keyhole, as an important factor limiting the depth of penetration [43, 45]. Many authors believe that the scattering of laser beam in the vapour particles, due to the Rayleigh or Mie scattering [227] can reduce the power density at the surface, particularly in the case of high brightness fibre and disc lasers [68-72]. The effect is well known in laser drilling. A minimum diameter of drilled holes is limited by the additional melting by plasma, which if not properly suppressed widens the holes [245, 246].

Olivier et al. [74] showed that the depth of penetration during Nd:YAG laser welding was improved by using a shielding gas with a high atomic mass, which had the ability to blow the plume away from the keyhole entrance. The effect was independent of

the shielding gas, which could suggest that the ionisation potential does not play a significant role. Greses et al. [73] reported the attenuation of Nd:YAG laser beam in the vapour plume as high as 40%. Verhaeghe and Dance [75] carried out an extensive study of welding performance of various laser systems with different beam qualities. They found that when a fibre laser with a good beam quality (2 mm.mrad) was focused using a long focal length focussing lens (500 mm), the plasma absorption became significant. According to them, the high brightness and the long depth of focus provided enough power density to induce a dense plume on a long distance between the workpiece and the optics. The depth of penetration in this case was significantly improved when several cross jets with shielding gas were placed at various positions between the workpiece and the optical head, in addition to the standard shielding nozzle. This effect disappeared after the welding speed exceeded approximately 7.5 m/min. The authors compared this effect to the thermal blooming, which occurs when a CO_2 laser beam passes through the stagnant column of air or a path containing hydrocarbons, causing laser aberration [247, 248]. A similar effect of the significant increase of depth of penetration, when using shielding gas jets during welding with high brightness fibre laser, was reported by Beyer at al. [22].

The controversial effect of plasma is still unexplained. Although most spectroscopic studies revealed a low ionisation potential of the plume during interaction with 1µm laser radiation, however, the scattering effect cannot be excluded. The absorption properties of the plume in the case of fibre laser processing could be underestimated due to the measurement difficulties. In all of the discussed experiments the plume was analysed at a certain distance from the surface, depending on the position of the probe laser. However, the plasma inside the keyhole is certainly much denser, due to the fact that the shielding gas does not reach there, which might lead to a much more significant absorption than assumed. The majority of calculations of the attenuation efficiency were performed with the assumption of a constant density of the plume in the vertical direction, which could lead to an additional error. It is hard to believe that the density of the plasma inside the keyhole is the same as above the surface. It is also known that the ability of shielding gas to deflect the plume from the interaction zone is strongly dependent on the position of the nozzle relative to the keyhole [249]. This high velocity shielding gas can also directly interact with the melt pool. In some conditions it can extend the keyhole, leading to less fluctuations of the rear wall and

as a result resulting in a greater depth of penetration, as compared to the case without shielding gas. [250]. Such an effect could be misinterpreted as the effect of plasma suppression. Alternatively, the oxygen could compensate for the energy absorbed in plasma. In a recent paper Zhao et al. [225] showed that oxygen reacted with the carbon from steel, generating carbon monoxide, which then increased the vapour pressure inside the keyhole. This increase of the recoil pressure increased the width and depth of the keyhole. Thus the depth of penetration might stay unchanged during welding without shielding gas, due to the compensation effect of oxygen for the energy absorbed by the plasma.

2.4.5. Hydrodynamic phenomena

2.4.5.1. Hydrodynamic model

In most welding conditions the keyhole can be represented as a capillary surrounded by a liquid metal, subjected to hydrodynamic phenomena, as demonstrated in Fig.2. 33 [251]. The vapour cavity is the balance between the opening force of vapour pressure and the closing forces of surface tension and hydrostatic pressure of the liquid metal [118, 129, 132, 133, 252-254]. In addition the entire system is subjected to a strong convection caused by the Marangoni flow, buoyancy force, flow around the capillary, as well as frictional effect of vapours [217, 252, 255, 256]. The observed fluid motion around the keyhole is the net result of all these flows.

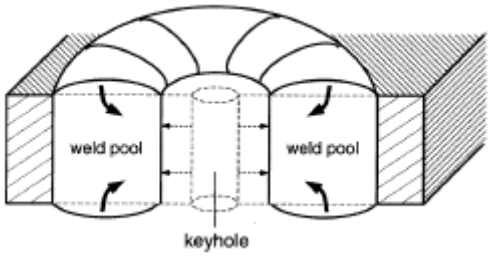

***Figure 2.33**: Representation of hydrodynamic forces acting on keyhole [251].*

The fluid flow has strong effect on the temperature distribution and therefore on the weld shape [47, 106, 186, 195, 215, 257-262]. It was shown in several studies that

intensive evaporation from keyhole can affect the melt pool like a high velocity jet, inducing its stirring [135, 139, 194, 195, 216, 217, 250, 263]. This is illustrated in Fig.2.34 [129]. The shear force of the vapour, which escape from the keyhole and drag the molten metal, is responsible for spatter [28]. Sudnik et al. [125] showed in his model that the rate of different flows changed interchangeably with welding conditions. At slow welding speeds the flows caused by Marangoni convection and vapour friction were dominant, whereas at higher travel speed the flow around the capillary became leading in the net flow. The motions of the melt pool are directly related with the keyhole oscillations [126, 127, 251, 264, 265]. These oscillations, caused by the unstable liquid-gas interface, are responsible for the necking of the keyhole, which are often observed on X-ray [28, 112, 236] and inconsistent depth of penetration, seen in longitudinal macrographs [20, 112, 266].

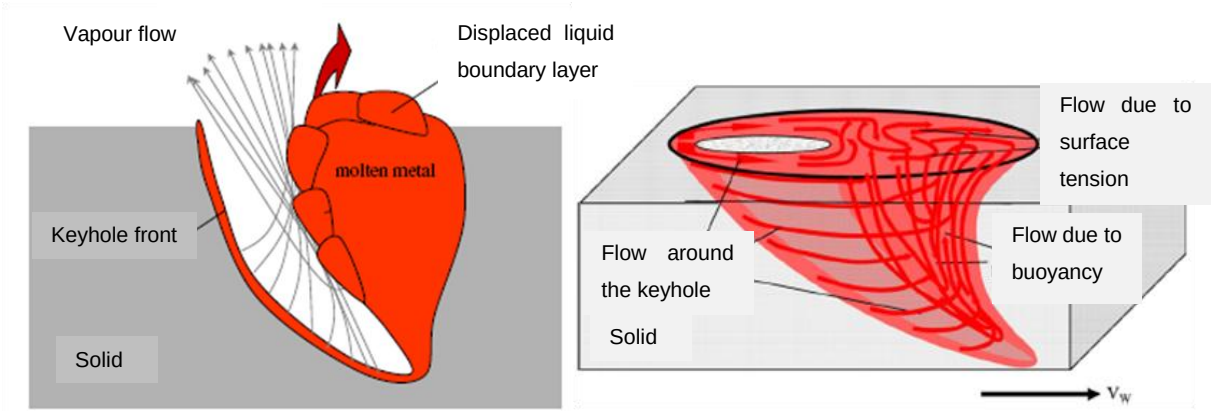

***Figure 2.34**: Vapour friction effect and other components of melt flow around keyhole [129].*

A maximum achievable depth of penetration can be calculated based on the hydrodynamic stability of the liquid-vapour system. The shape of the cavity is determined according to the minimum surface energy. This assumes that for every conditions there is the most optimum shape of the keyhole, in which all forces are minimised. Andrews and Atthey [128] calculated a hydrostatic limit of depth of penetration when material was irradiated by a laser beam. According to this consideration the surface tension and gravity were the main forces balancing the recoil pressure in shallow welds. This was attributed to the large bottom area of the cavity on which the forces were acting. In this range, the depth of penetration was

proportional to the power density, quadratically dependent on the beam diameter. In deep cavities, on the other hand, the gravity was the only restoring force and the depth of penetration was proportional to the ratio of the laser power to the beam diameter [128]. Lee et al. [137] modelled the melt flow at the beginning stage of the keyhole formation. The upward flow of the liquid metal, induced by the recoil pressure, was continuously delivering the liquid metal to the upper part of the keyhole and then this metal exerted a hydrostatic pressure, which together with the surface tension added to the downward flow. Furthermore, the high velocity upward momentum was dissipated by the viscous shear on the keyhole walls, which eventually was unable to remove the liquid metal from the bottom of the keyhole. Thus at a certain depth the downward forces became dominant and the depth of penetration reached its limit [137]. Zhao and DebRoy [230] developed a comprehensive model to predict the transition between conduction and keyhole regime. First, the calculations were carried out for the keyhole regime. If the conditions were sufficient to form a stable keyhole its shape was calculated. But if the cavity did not satisfy the energy balance equations, further calculations were continued with the assumption of conduction regime. The calculated keyhole profiles were in good agreement with the experimental results.

In a model developed by Matsunawa and Semak [254] the energy absorbed at the rear wall of the keyhole decreased with increasing travel speed. This further led to a reduction of recoil pressure. Eventually at a certain travel speed the recoil pressure became lower than the hydrostatic force of the liquid metal and the keyhole totally collapsed [254]. Keyhole remains open as long as the ablation pressure exceeds the surface tension of the keyhole surface [127, 267]. Klemens [268] concludes that the depth of penetration is limited by a pressure gradient along the depth. The keyhole has to acquire a conical shape in order to balance the surface tension. The pressure gradient along with the plasma absorption were the limiting factors of depth of penetration in his analysis [268]. Golubev [252] summarised most of the fluid dynamic phenomena attributed with the laser welding and cutting. The main conclusion of this work is that the keyhole is unstable, due to micro-capillary waves and droplet generation, which cause turbulent submerged streams in the melt pool. This is shown in Fig.2.35 [252]. According to the author, if these instabilities were not present, the depth of keyhole would be entirely determined by the vapour pressure

[252]. Therefore the bigger the diameter of the keyhole the more stable the process, owing to the easier escape of the vapour jets from the keyhole, without dragging the molten metal [124, 269].

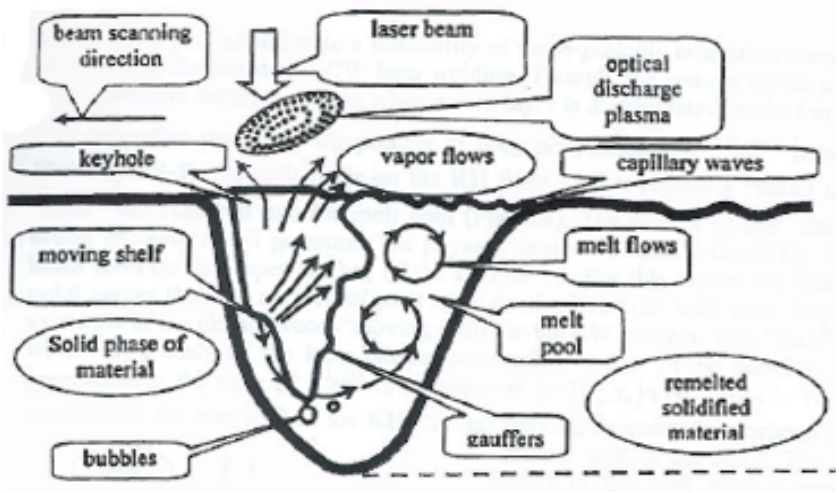

***Figure 2.35**: Hydrodynamic phenomena around keyhole [252].*

2.4.5.2. Experimental observations of melt pool behaviour

The complex fluid flow resulting from many net flows, such as Marangoni flow, buoyancy force, flow around the capillary and frictional effect of vapours was confirmed experimentally by tracking trajectories of tungsten and platinum particles added to the melt pool [242, 270-272]. Experimental measurements of the temperature distribution inside the keyhole revealed the maximum temperatures at the bottom of the keyhole, regardless of the material composition [190]. Therefore the strong melt flow, as a result of this temperature gradient, will force the system to a uniform temperature around the keyhole.

Fabbro et al. [124] showed experimentally that the melt flow was dominant in heat transfer laser welding rather than pure thermal conduction. The comparison of twin spot welding in different configurations revealed that a wider melt pool was achieved in longitudinal configuration, when one beam followed the other, as compared to the transverse configuration, which contradicted the thermal conduction model. This

effect was attributed to the strong hydrodynamic flow expelled from both keyholes [124].

High speed photography has given insight into many phenomena related to the melt pool, keyhole formation and plasma behaviour. The first finding showed strong perturbations of the melt pool [126, 189, 273]. Semak et al. [126] used a laser reflectometer combined with a high speed camera to depict liquid motions during pulsed laser welding. The harmonic oscillations with certain frequencies were attributed to the balancing forces of the recoil pressure against the surface tension and hydrostatic force. Fabbro et al. [250] demonstrated a direct connection between the stability of the liquid-vapour interface and the spatter generation. The escaping vapour column was interacting with the molten metal near the keyhole exit and by dragging it caused the spatter. Different mechanisms of spatter generation occurred in different regimes, depending on the inclination angle of the keyhole and the molten volume, as shown in Fig.2.36 [250]. At low travel speeds and high power densities the vapour column interacted with the melt pool due to the keyhole fluctuations. In contrast, at high travel speeds the increased inclination angle of the keyhole enhanced the interaction between the vapour and the melt pool [250]. This is also shown in Fig.2.37 [112]. Coaxial high speed photography confirmed the change in the inclination angle of the keyhole with increasing travel speed [140].

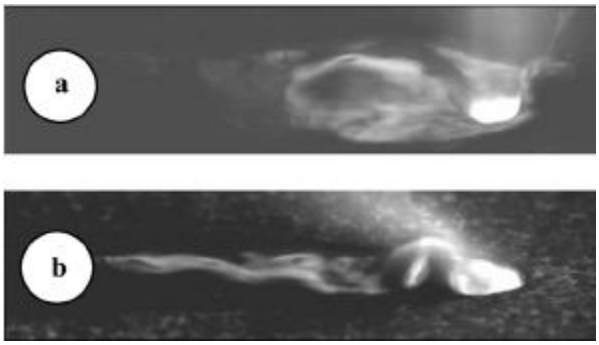

Figure 2.36*: High speed photography of melt pool during laser processing with 3 kW of power at different travel speeds:* ***a)*** *1 m/min;* ***b)*** *5 m/min [250].*

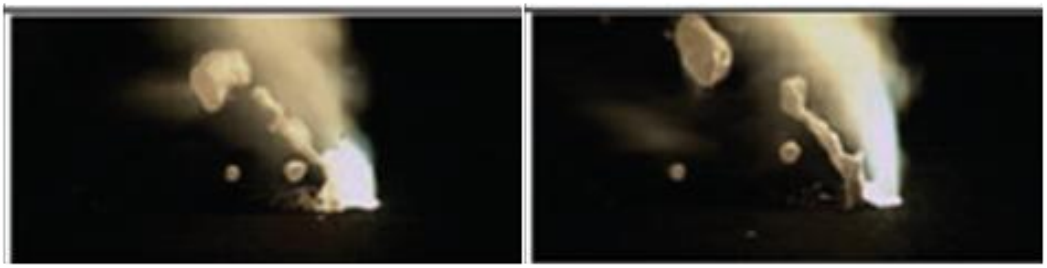

Figure 2.37*: High speed photography of interaction between vapour plume and melt pool at 10 kW of power and 6 m/min travel speed [112].*

The analogy to laser keyhole welding could be found in laser scattering in fluid systems. Interaction of a laser light with a liquid may induce a capillary, similar to the keyhole in laser welding [274-276]. Some observations indicated the crucial role of viscosity of the liquid on the stability of the capillary. A four times deeper capillary was obtained in viscous glycerine than in water [252, 277]. The growth of capillary in water was disturbed by various instabilities, such as formation and collapse of micro-bubbles and waves, which prevented the capillary from a further increase in depth [278]. Mizutani and Katayama [218] used X-ray transmission method to visualize the keyhole during interaction of a laser beam with molten zinc. The stability of the keyhole was determined by its depth and geometry, which were controlled by the distribution of the recoil pressure. Deep and narrow cavities were found to be susceptible for necking due to high surface tension. Furthermore, the authors measured experimentally the recoil pressure for different laser parameters and then used them to estimate numerically the free surfaces of the keyhole. The recoil pressure was balanced by the surface tension and the hydrostatic force. Two different cases from this analysis are illustrated in Fig.2.38. In the first case, a recoil pressure of 6500 Pa resulted in a deep and narrow keyhole with a non-uniform pressure distribution. This type of keyhole exhibited many instabilities resulting in defects, such as porosity. In the second case, a much lower recoil pressure of 1600 Pa resulted in a wide and stable keyhole with the pressure gradually decreasing from the bottom towards the surface [218]. This demonstrates that a high recoil pressure does not guarantee a deep keyhole if the hydrodynamic phenomena will act against it.

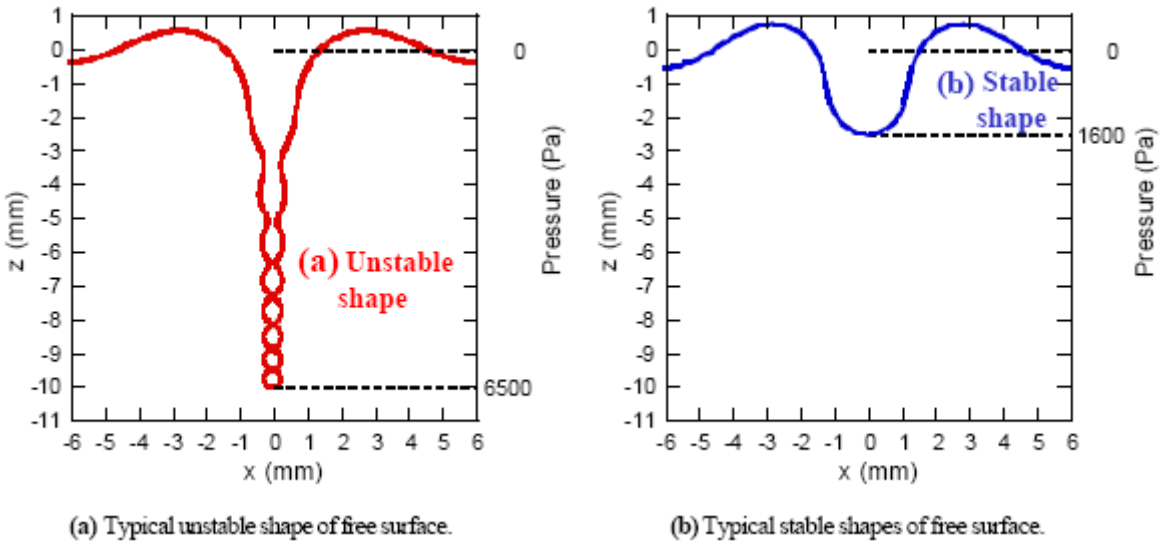

(a) Typical unstable shape of free surface. (b) Typical stable shapes of free surface.

***Figure 2.38**: Representation of keyhole based on observations carried out in liquid zinc [218].*

The relationship between the recoil pressure and the power density of a laser measured by Zhiryakov et al. [189] showed some discrepancies with a thermal model, which according to authors were caused by hydrodynamic perturbations and plasma jet effect. These perturbations were observed on the images of the melt pool [189]. Similar perturbations were suggested to be responsible for different shapes of isotherms between a thermal model and holographic interferometry observations during laser welding of fused silica [117].

It seems that melt flow dynamics can affect strongly the stability of the keyhole and the resulting depth of penetration. However, the effect can be only significant at low travel speeds, where the large amount of molten metal is produced. On the other hand, at faster speeds or short pulse durations in case of pulsed laser welding, only a narrow layer of liquid metal exists, hydrostatic pressure of which is insignificantly lower. Thus, at these conditions the effect should play a minor role on depth of penetration.

2.4.6. Direct studies of keyhole evolution

In order to better understand the forces governing the depth of penetration, it became important to visualise the actual shape of keyhole. The first image of keyhole was obtained by Arata et al. [146] during welding of a transparent material (soda-lime glass). Unfortunately the quality of the image was poor due to the high emissivity of the glass. A similar technique was used on Pyrex glass [113, 114]. The experiment revealed an inclined and rather complex in shape keyhole. The majority of laser energy was absorbed on the front wall of the keyhole by the direct incidence and then the heat was conducted to the rear wall [113]. Olfert and Dudley [117] used a holographic interferometry during laser drilling of fused quartz. This enabled measurement of the thermal field around the keyhole. The evolution of two-dimensional isotherms was compared with a solution of heat transfer equation. The majority of the laser energy in this experiment was transferred to the material by the direct absorption on the keyhole walls. There was a significant difference between the shapes of the isotherms obtained from the modelling and the experiment. The experimental one did not exhibit as uniform distribution as in the numerical solution. This according to the authors, indicate a non-uniform absorption in the keyhole walls, which could be caused by the internal reflections or other fluctuations of the gas-liquid interface. As the authors point out the assumption of the isothermal boundary in the keyhole surface, often made in numerical calculations is incorrect.

The profile of keyhole observed in a glass can be different from that obtained in metals. There is a significant difference in temperatures of vaporisation and melting, as well as in viscosity and conductivity between the materials. Thus many researchers tried to overcome this by using X-ray photography during laser welding of steel [111, 116, 144, 145]. The majority of work was focused on understanding of formation of defects [28, 63, 112, 165, 236, 279, 280]. The transient images of keyhole revealed many instabilities and fluctuations of the liquid-gas interface. The susceptibility of deep and narrow keyholes to necking, due to the surface tension, was demonstrated. This can lead to formation of pores. An example of keyhole image is shown in Fig.2.39 [116].

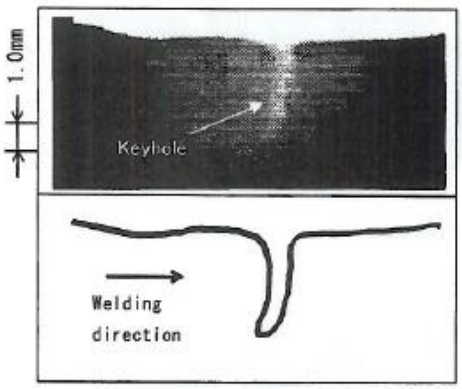

***Figure 2.39**: Typical X-ray image of a keyhole [116].*

Cho et al. [281] obtained the temporal evolution of a keyhole. The keyhole was subjected to periodic fluctuations between closing and reopening cycles. However, the laser power used in this study was not sufficient to observe formation of a deep keyhole. In another work a more powerful laser was used to study the evolution of keyhole [111]. It was shown that for first few milliseconds of the laser emission only melting took place. The keyhole appeared after 3-4 ms and was continuously expanding until the end of pulse duration. The diameter of the keyhole was continuously increasing during the entire pulse duration and eventually approached the size of the laser beam on the surface [111]. In another work a keyhole appeared after less than 1 ms from the beginning of laser irradiation and its depth was continuously increasing until the termination of irradiation [165]. Fujinaga et al. [116] carried out X-ray observations of keyhole during irradiating a workpiece with a modulated Nd:YAG laser. The keyhole appeared after approximately 0.6-0.7 ms and reached a maximum depth of 5 mm after approximately 1.5 ms from the irradiation start. Then the keyhole needed approximately 1 ms to collapse after the laser irradiation terminated. The laser-induced plume, observed on high speed photography, appeared immediately after the laser emission. However, initially the vaporisation pressure was not sufficient to overcome the surface tension. Furthermore, the small melt pool at this stage, was subjected to an intensive cooling due to the heat conduction. Therefore, the keyhole drilling process started with a delay, which was dependent on the operating parameters. In addition, in the same study the effect of high power peaks, superimposed on a squarely modulated beam, revealed an interesting behaviour. If a delay time between this superimposed peak

and the normal pulse (Fig.2.40) was too long, the superimposed peak did not increase the depth of penetration. It was concluded that its energy was used to heat the surface rather than to enhance drilling [116].

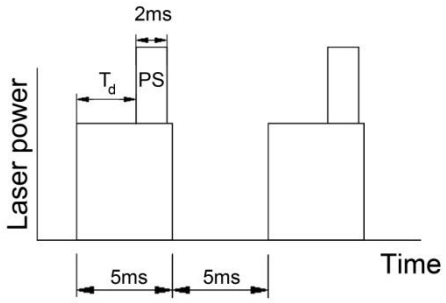

***Figure 2.40**: Superimposed pulse (PS) applied after delay time (T_d) [116].*

These studies provided useful information regarding the balancing forces during the keyhole evolution. The dominant influence of the vapour-induced pressure and heat conduction at the initial stage has been demonstrated. In spot welding with pulsed lasers the keyhole propagates during the entire pulse duration, which underlines the major role of the recoil pressure. On the other hand, the larger melt pool in CW laser welding, as compared to pulsed lasers, results in various fluctuations. However, it is not clear if these fluctuations are responsible for the saturation of depth of penetration. It might be the case that the propagation of depth of penetration terminates immediately after a short period of laser emission and then the energy is further utilised for extending the melt pool. Also the transmissive investigations of keyhole did not give enough information about the plasma absorption.

2.4.7. Effect of ambient pressure

One of the useful ways of investigating the forces limiting depth of penetration in high power laser processing is to carry out the process in vacuum. There are close similarities between the keyholes observed in laser welding and electron beam welding. However, the greater depth of penetration in case of electron beam welding raises a question over the effect of ambient pressure on this difference. The ambient pressure affects both the vaporisation temperature, as well as the density of the

vapour plume. Both effects should influence the depth of penetration in keyhole welding.

There were few attempts of investigating the laser welding under reduced pressures. Arata et al. [282] studied the evolution of keyhole in vacuum using a high speed camera and an X-ray photography. The results showed that the plasma produced by CO_2 laser beam was almost totally suppressed at low pressures, which resulted in an increased depth of penetration. The shape of the keyhole, according to the authors, was resembling that of electron beam welding [282]. An increase of depth of penetration and decrease of keyhole width with reducing pressure was observed in mild steel and stainless steel [283].

Brown and Banas [284] compared CO_2 laser welding with electron beam welding carried out by Meier [285]. Both processes exhibited a similar transition regime when pressure was reduced. The depth of penetration increased with decreasing ambient pressure and reached a plateau at approximately 10^{-2} Torr, as shown in Fig.2.41 [284]. In the case of laser welding the increased depth of penetration by a factor of three was reported at this pressure, as compared to the atmospheric conditions. The lower depth of penetration of the electron beam welding at the atmospheric conditions was attributed to the deceleration of electrons by air molecules.

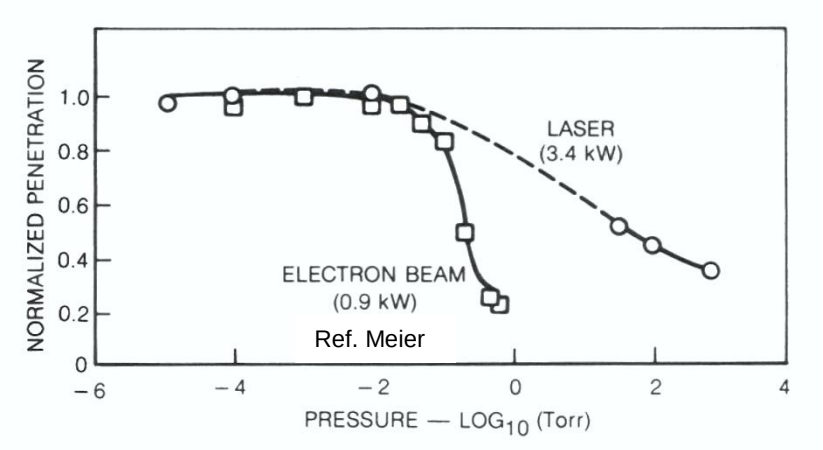

***Figure 2.41**: Effect of ambient pressure on depth of penetration in laser and electron beam welding [284].*

The authors point out that the fact that the plateau for both processes could be reached at the same pressure, implies other effects rather than the plasma suppression only. According to them a maximum depth of penetration that can be achieved at low travel speeds is determined by keyhole stability. Formation of a keyhole at the atmospheric pressure is related to the evaporation of material, which in case of steel requires approximately three times higher temperature than for melting. However, the vaporisation temperature decreases with decreasing ambient pressure and at a pressure of $3\cdot 10^{-2}$ Torr (equal to approximately 4 Pa) the vaporisation temperature is equal to the melting temperature [284]. Thus the vaporisation rate becomes independent of the ambient pressure at this point, and only depends on the vapour pressure inside the keyhole. This argument was used to explain the plateau of depth of penetration at $3\cdot 10^{-2}$ Torr. They further postulate that the fact that the material can be vaporised at a lower temperature as pressure decreases, results in a much lower temperature gradient between the melt pool and the vapour. As a result the melt pool experiences less motion. In addition they claim that the small difference between the temperature of melting and vaporisation leads to a smaller melt volume, which also enhances the keyhole stability. Thus the more stable liquid-vapour boundary enables a more efficient keyhole drilling [284]. A smaller melt pool in vacuum than under the normal pressure was also found in laser cladding. The widths and the depths of deposited layers were smaller in vacuum for the same laser conditions [286]. This can be attributed to the fact that the lower vaporisation temperature at low pressures enhances the vaporisation, leading to less energy being utilised for melting.

Katayama et al. [287] observed a reduced porosity in aluminium and stainless steel when welding with CO_2 and Nd:YAG lasers in vacuum. A more stable keyhole and different flow directions in vacuum conditions, as compared to the atmospheric pressure, was shown in X-ray photography. The fluctuations of keyhole, which usually account for the formation of pores at the atmospheric conditions, were reduced. Totally suppressed porosity in vacuum, despite severe swelling of the keyhole, was attributed to the intensive evaporation rate. Furthermore, unlike at the atmospheric pressure, there was no strong downward flow of the melt at the bottom of the keyhole in vacuum. This combined with the stronger recoil pressure improved

the melt removal from the bottom of the keyhole by improving the upward flow of the liquid [287].

Some researchers attributed the increased depth of penetration at lower pressures to the plasma suppression [288-290]. The dependency of depth of penetration in CO_2 laser welding in vacuum on the ionisation potential and the conductivity of shielding gas was also demonstrated [288]. The previously observed plateau of depth of penetration at low pressures was found to be additionally dependent on the type of shielding gas inside the chamber. For instance, in the atmosphere of helium the plateau was established at a higher level than with argon [288]. There is a close relationship between the ambient pressure and the electron density and temperature of plasma [289]. Thus the plasma at sub-atmospheric conditions has a lower ability to scatter the laser radiation and the multiple reflections inside the keyhole can propagate further into depth [289].

In recent papers an increase of depth of penetration by a factor of three in vacuum, as compared to the atmospheric pressure, was attributed to the plasma suppression [290, 291]. The example macrographs are shown in Fig.2.42 [291]. The increased depth of penetration was only evident at low travel speeds and as the travel speed exceeded 3 m/min the depth in vacuum was similar to that obtained at the atmospheric conditions, as shown in Fig.2.43. High speed images revealed a significant reduction of the vapour plume at a pressure of 100 hPa. A long bright column along the laser beam, rather than the high density plume, was observed at this low pressure, as shown in Fig.2.44 [291]. According to the authors, the high recoil pressure, combined with the lack of friction force of air, at these conditions, accelerated the vaporised particles upwards and enabled the tall column around the laser beam to be formed.

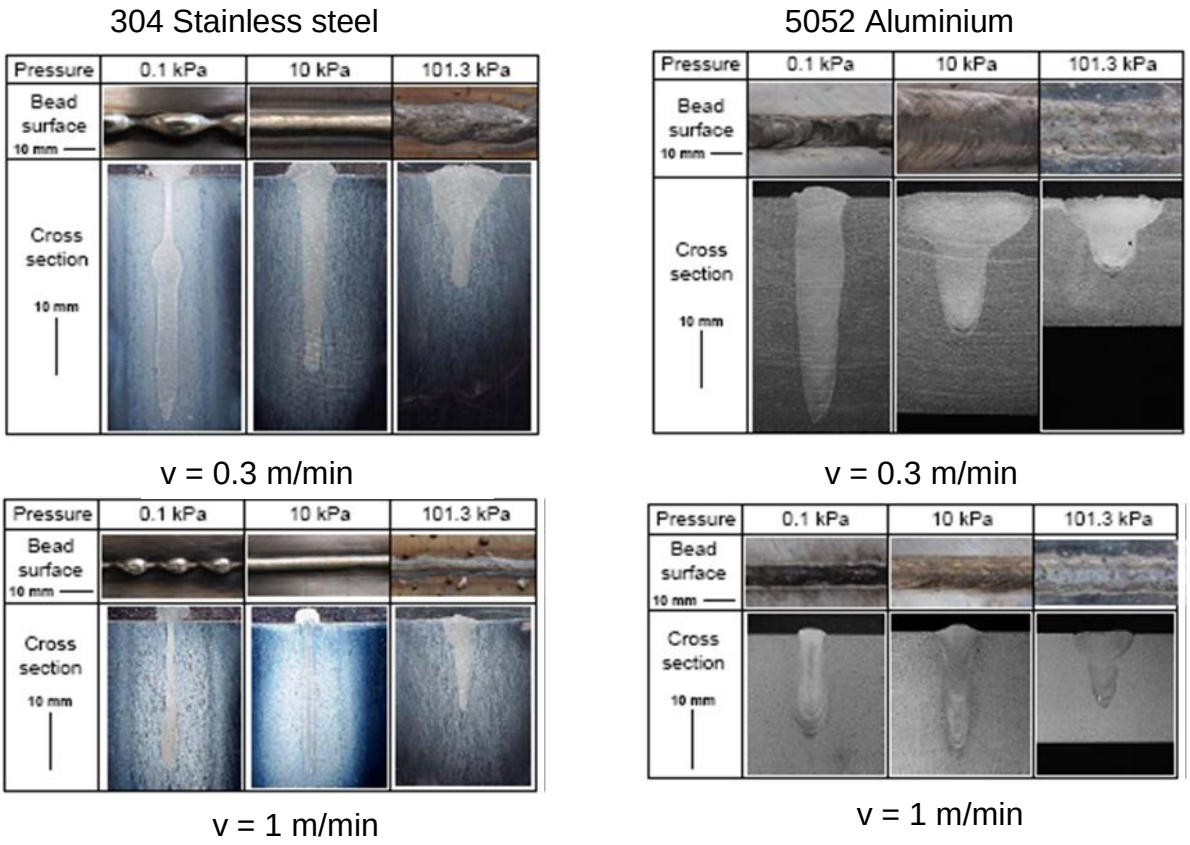

***Figure 2.42**: Effet of ambient pressure on weld bead in stainless steel and aluminium alloy, at travel speeds 0.3 m min^{-1} and 1 m min^{-1} [291].*

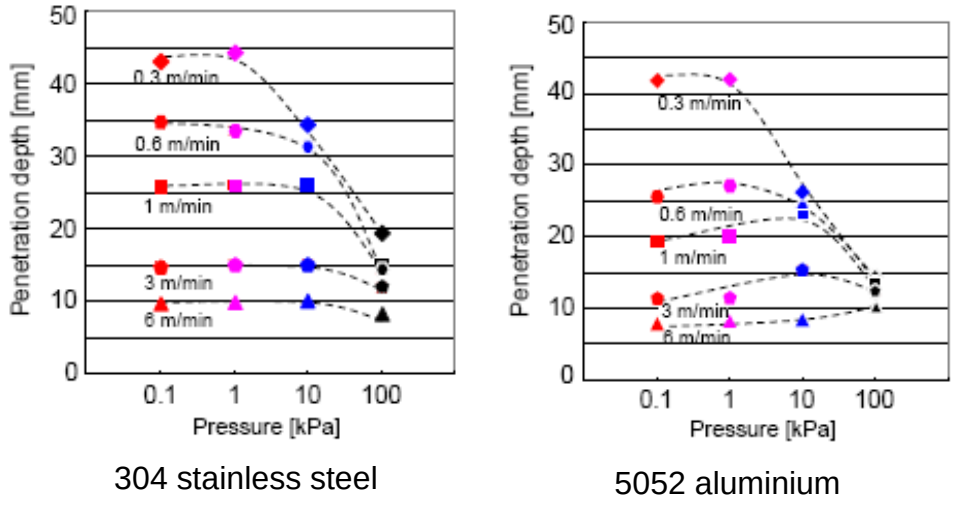

***Figure 2.43**: Increase of depth of penetration with reduction of ambient pressure as a function of travel speed for two different materials [291].*

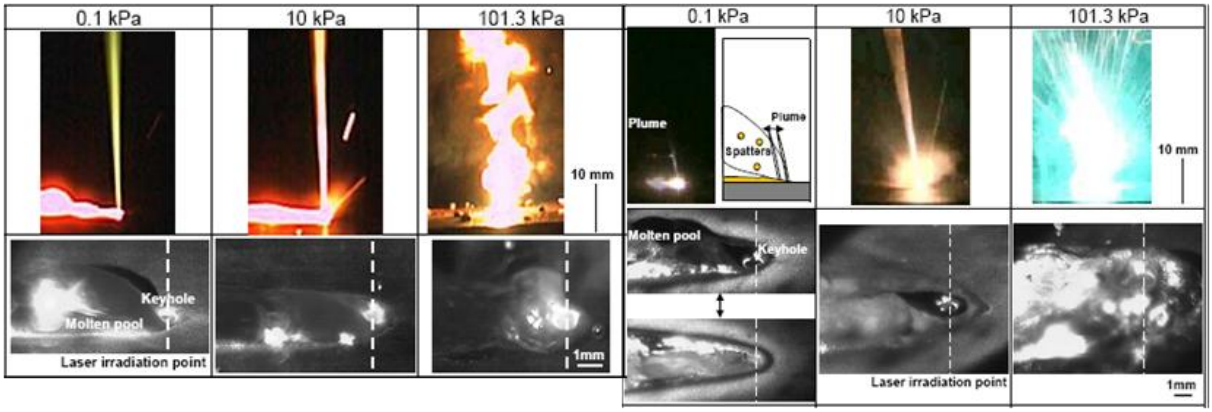

304 Stainless steel 5052 Aluminium

***Figure 2.44**: Effect of ambient pressure on vapour plume and melt pool behaviour at a travel speed 1 m min^{-1} [291].*

Thus it is unclear if the suppression of plasma/plume or the reduced vaporisation temperature is responsible for the increased depth of penetration in vacuum. On one hand, the fact that at a travel speed of 1 m/min the depth of penetration did not increase with a further decrease of pressure from 10 kPa to 0.1 kPa in Fig.2.42, despite almost total suppression of plasma may suggest a secondary effect of plasma. The total plasma suppression is particularly evident in aluminium in Fig.2.44, On the other hand, if the observed increase of depth of penetration in vacuum was due to the lower vaporisation temperature, it is unclear why this effect mitigated at faster travel speeds. It is very likely that the melt pool behaviour is dominant. The smaller amount of molten metal, as the result of lower difference between the vaporisation and melting temperatures, results in the more stable keyhole and greater depth of penetration at low travel speeds. However, at faster travel speeds the melt pool is already very small and its size is not affected by the ambient pressure. Therefore at fast speeds the depth did not increase with decreasing pressure. Alternatively, plasma can be also responsible for the more stable keyhole. The swelling and necking of the upper part of the keyhole at reduced pressure is clearly visible in Fig.2.42, particularly in stainless steel at 0.3 m/min travel speed. Thus it is evident that the plasma/plume helps maintain the upper part of the keyhole open. The lack of this supporting force of plasma can lead to collapsing of keyhole at faster travel speeds. This would also diminish the effect of vacuum on depth of penetration at faster travel speeds. It is probably the net effect of multiple reflections,

vaporisation pressure and plasma/plume that is important. The higher recoil pressure in vacuum is sufficient to maintain keyhole open at low travel speeds even without the plume, but at fast travel speeds the melt pool perturbations, induced by the horizontal acceleration disturb the narrow keyhole. Thus the effect of increased recoil pressure is diminished if the keyhole is not widened by the plume. Furthermore, the increased inclination angle of the keyhole at faster speeds results in more energy being absorbed in the front wall of keyhole, hence the depth of penetration does not increase greatly.

2.5. Alternative parameters in laser welding

Depth of penetration is one of the most critical parameters in laser welding, which users usually need to adjust for the material being welded. For a given beam diameter a range of combinations of laser power and travel speed can be used to achieve a desired depth of penetration [24, 42, 49]. Alternatively for a given combination of power and travel speed, different depths of penetration occur, if different beam diameters are used. Beam diameter is controlled by the laser properties and the optical system and may vary between laser systems [1]. This causes difficulties in both, selecting the optimum laser parameters for a particular application and in transferring parameters between laser systems. A difficult and unclear character of different phenomena affecting the depth of penetration in laser welding has encouraged laser practitioners to use a much simpler approach. Very often parameters are developed individually based on the trial and error method. In most experimental works using CW lasers the depth of penetration is studied based on the system parameters, such as laser output power and travel speed. The system parameter approach makes the process dependent on the particular laser system, due to the unique beam diameter.

Many authors tried to find parameters, which would uniquely define depth of penetration in laser welding and enable an improvement of data transferability between different laser systems. Most of the parameters are summarised in Table 2.1. The first approach included characterisation of the process based on heat input [292, 293]. However, for the same heat input various welds can be achieved if different beam diameters are used. Mannik and Brown [294] collected available laser data and developed a graph showing the energy required per unit of thickness of a workpiece. Swift-Hook and Gick [295] derived normalised parameters that control the depth of penetration in laser and electron beam welding. In another work a model, relating the depth of penetration with the incident power and Peclet number was developed [296]. The Peclet number was calculated based on the welding speed, keyhole radius and thermal diffusivity of the material [296]. All these parameters can be used to roughly estimate general trends in laser welding, such as calculation of the melting efficiency, rather than to predict the depth of penetration. Leong et al [297] developed an equation, which enabled calculation of a threshold irradiance for

melting. However, the predicted values of the threshold irradiance were much lower than those required in real welding conditions. All these approaches are not accurate enough to be applied in real laser welding applications.

***Table 2.1**: Parameters used to characterise laser welding.*

Parameter	Unit	Formula	Reference
Power density	W/m^2	$q_p = 4P_L/\pi d^2$	[298]
Interaction time	s	$\tau_i = d/v$	
Energy density	J/m^2	$E_d = q_p * \tau_i$	
Heat input or line energy	J/m	$HI = P_L/v$	
Peclet number		$Pe = vr_b/2\alpha$	[296]
Energy per unit thickness	J/m^2	$E_{ut} = P_L/vh$	[294]
Normalised speed-weld width		$Y = vw/\alpha$	[295]
Normalised power input		$X = P_L/PD*S$	
Heat function	W/m	$S = \int_0^T k dT$	

Unlike in most experimental works, the power density or heat flux is usually one of the major parameters defining the temperature distribution in modelling [177, 178, 211]. Similarly in pulsed laser processing the fundamental pulse energy, power density and duration time are naturally used to characterise the process [163, 299]. In theory every laser process can be distinguished in terms of applied power density and interaction time, as demonstrated by some authors [298, 300]. An example of a processing map is shown in Fig.2.45 [298].

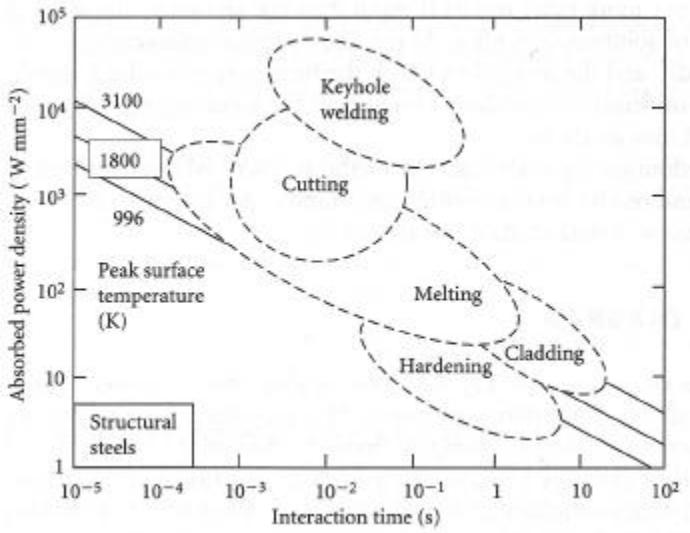

***Figure 2.45**: Laser processing map [298].*

These parameters can be calculated based on the system parameters, as shown in Table 2.1 [298]. This allows them to be applied on different beam diameters, thus on many laser systems. The approach was sporadically used in laser processing. McBride et al. [301] showed that the bending rate was primarily controlled by the line energy and the interaction time. Fabbro and Chouf [135] developed a model, based on keyhole geometry, in which the depth of penetration was dependent on the drilling velocity and the interaction time.

Jebbari [302] et al. assumed that the laser machining process to be a periodical process, determined by the interaction time, which he further used to characterise the width of the thermal affected zone in laser cutting. Although the interaction time did not match the experimental widths of thermal affected zones, this may result from a specific characteristic of cutting. Furthermore, this simple definition of the interaction time might be only adequate in non-keyhole processes, such as conduction welding where the heat is mainly absorbed on the surface and may need some modifications for deep penetration processes. However, the principle of interaction time can be justified from results obtained with elongated beams. It was demonstrated that by using a rectangular spot parallel to the welding direction resulted in an increased depth of penetration for the same welding conditions, as compared to a circular spot or the elongated spot perpendicularly to the welding direction [303]. A similar effect was observed during surface treatment of ceramics. A common difficulty in this

process is susceptibility of ceramics to thermally induced cracks, if the cooling rate is too high. It was shown that the cracking could be significantly reduced by using elongated beams in the travelling direction. This enabled an increase in travel speed, as compared to the standard circular beams [304].

Although the intuitive effect of interaction time and power density is commonly known there is no case reported in literature, where these parameters were used to study the laser welding experimentally. Particularly it is unclear if these parameters are sufficient to characterise laser processing regardless of the beam diameter. Ashby and Easterling [305] developed a processing map for laser hardening process, based on the results of thermal conduction model, supported by the experiment. They showed that the depth of hardened layers could be controlled by the energy density (product of power density and interaction time) and the beam diameter. This implies that the beam diameter may still affect the depth of penetration even if a constant energy density is maintained.

It is commonly known that power density affects the laser welding, however, it is hardly used for characterisation of experimental data. There is a lack of system of parameters, which would specify the laser welding uniquely, based on heat source, similarly as in heat transfer modelling. Power density and interaction time could be potentially used to develop such a system.

2.6. Laser-arc interactions

Laser light can deliver energy of photons to the workpiece directly based on Fresnel absorption [105, 306]. Part of the laser energy can also be transferred to the material through the plasma via inverse Bremsstrahlung absorption [62, 307, 308]. Arc-based welding process, in contrast, transfers the heat via the arc column surrounded by a high temperature plasma. The high temperature results from ohmic resistance and dissociations of atoms and molecules. In other words the electric arc is a discharge of electricity in an ionised gas, which is surrounded by its own magnetic field [309]. Additionally in gas metal arc welding a significant portion of heat is transferred to the workpiece by means of droplets formed during melting of the filler wire [258]. The droplets increase their temperature during passing through the arc column [310]. Theoretically there are many possibilities of different interactions between laser and arc in hybrid welding [309, 311, 312].

Many researchers studied interactions between the arc and the laser when both sources were combined into the hybrid welding. The main symptoms of this interaction were: decreased voltage along with increased current of the arc [15, 313-318], arc contraction visible on high speed photography [15, 77, 314, 316, 319, 320] and increased melting efficiency [314, 321-324]. Another important benefit from these interactions is the ability of maintaining stable arc at high travel speeds, due to the arc rooting effect [15, 309, 313, 325].

For the first time Steen and Eboo [15] reported decreased voltage and increased current of a TIG source, followed by constriction of the arc plasma when a laser was focused in a vicinity of arc, as shown in Fig.2.46(a). The arc column was clearly following the laser irradiation spot on the surface. The stabilisation effect occurred even when the laser beam was focused on the opposite side of the workpiece relatively to the arc, provided that the laser energy was sufficient to heat the surface to approximately 400°C [15]. The laser beam can also stabilise a GMAW process, as shown by Ono et al. [317] in Fig.2.46(b). It was demonstrated that even a low power density laser beam, which would be insufficient to cause any melting could suppress arc wandering [311, 313, 325, 326], particularly on materials with low work function such as titanium [327]. Some researchers attribute this effect to the improved

thermionic emission from the anode spot. The laser radiation increases the temperature of the anode and cathode spot, which enhances the emission of electrons and positive ions and increases the current density as a consequence [313, 328].

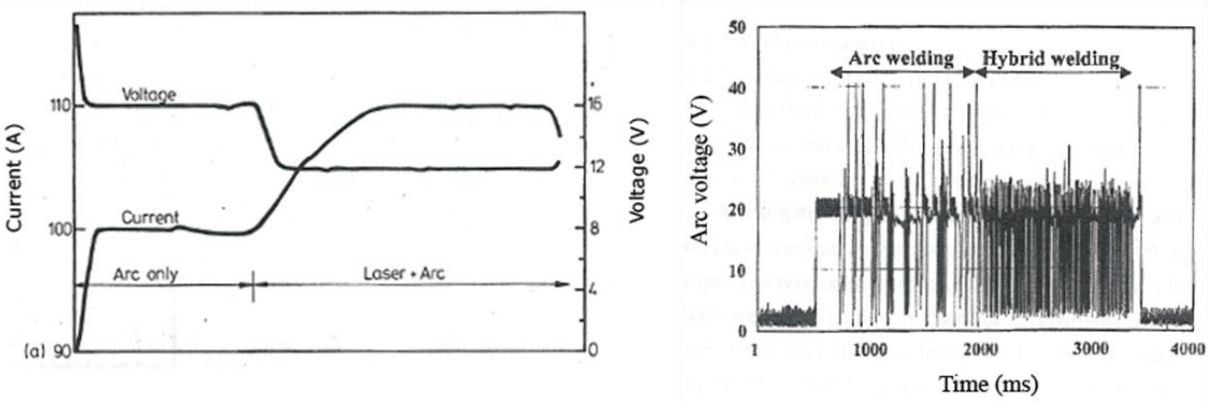

***Figure 2.46**: Stabilisation of arc due to interaction with laser; **a)** decrease of the arc column resistance during TIG/laser hybrid welding [15]; **b)** stabilisation of GMAW by laser [317].*

Other researchers claim the improved thermionic emission as being unlikely to be responsible for the arc contraction effect. As pointed out by Seyffarth and Krivtsum [312] the anode work function is determined by the Fermi energy, which in metals is only slightly dependent on the temperature. Stute et al. [311] estimated that the temperature of aluminium would have to reach approximately 2200°C in order to induce the thermo-emission, but the arc rooting effect works at much lower temperatures. Furthermore, as pointed out by Seyffarth and Krivtsum [312] on one hand in the results presented by Steen and Eboo [15] the arc rooting was observed when both heat sources were placed on the opposite sides of the workpiece, but on the other hand, the reduction of voltage was only detected when they were on the same side. This indicates interaction of the electric arc with the laser-induced plasma [312].

The intensive evaporation caused by the laser radiation increases the amount of electric carriers in the arc plasma, which increases its conductivity [315, 318, 319, 328-332]. This can be seen in Fig.2.47 [77]. Experiments with a plasma arc welding (PAW) confirmed this theory [9]. The arc plasma contracts as its conductivity

increases, in order to minimise the energy losses. This contraction increases the current density [333-336]. It was shown that the conductivity of plasma could be quadrupled by enriching it with vapours of copper [333]. Furthermore, the arc column will tend to join the laser plasma, whose temperature is much higher than surrounding environment, in accordance with the principle of minimum energy [11, 328].

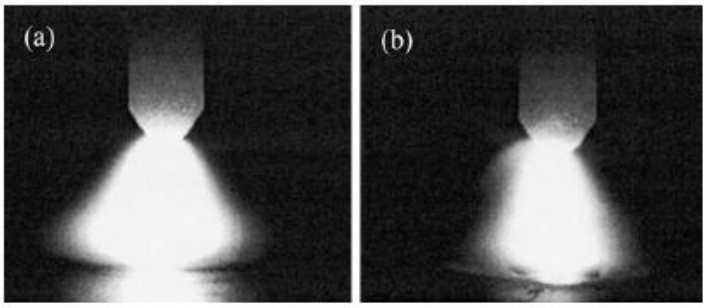

***Figure 2.47**: Contraction of arc of TIG source at 100 A due to interaction with laser; **a)** arc only; **b)** arc and laser source [77].*

The interaction of arc with the laser plasma is likely to stabilise the arc only with high power density lasers, which are able to induce evaporation [311]. However, the arc stabilisation is also possible at low power densities, insufficient for evaporation [311, 317, 329]. Some authors suggest a direct interaction of the arc plasma with the laser radiation to be responsible for the increased conductivity of the arc plasma [11, 311]. Researchers from the Ohio State University showed an electric discharge following the trajectory of 7 W laser beam [337, 338], as demonstrated in Fig.2.48. According to some authors [311, 317, 326, 329] most likely the opto-galvanic effect accounts for the arc stabilisation with low power density lasers. The laser radiation increases the kinetic energy of electrons within the arc plasma, which then increase their excitation states, leading to a higher ionisation. As a result the arc column is discharged from the point of laser irradiation and the arc wandering effect is suppressed. It was demonstrated that even when the laser beam was focused off-axis, the arc followed the laser interaction point, despite the fact this was not the shortest possible path [311, 313, 317].

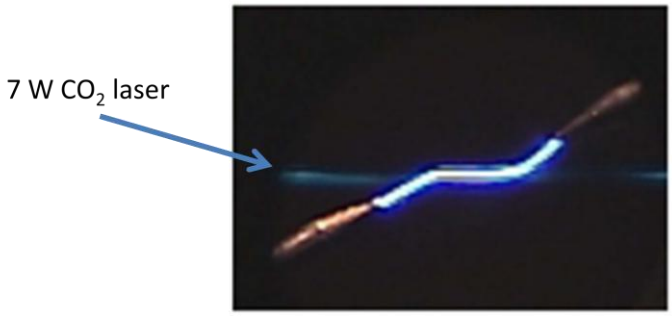

***Figure 2.48**: Deflection of electrical discharge by laser radiation [337, 338].*

Perhaps not only the arc source can benefit from the interaction with laser. It is well known that a high proportion of laser beam can be reflected form the surface, due to the low absorption, if conditions are insufficient to drill a keyhole. The fact that the absorption of metals increases with temperature [330, 339-341] suggests an improved absorption of laser in hybrid welding, due to the preheating effect of the arc source [309, 314, 320, 342]. This is evident during welding of highly reflective materials, such as aluminium, where the coupling of laser is immediately improved after the ignition of arc [9, 313]. This is also advantageous in terms of heat transfer. The thermal diffusivity of a workpiece is diminished by the heat from the arc source allowing less heat of the laser being utilised for conduction losses [314].

The most common observation used for synergic effect between the laser and the arc in hybrid welding is increased melting efficiency. Many authors reported that the volume of molten metal generated by both sources in hybrid process exceeded the sum produced by the laser and the arc separately [314, 323, 324]. A greater depth of penetration in the case of hybrid welding was also found [9, 318, 321, 322, 329, 343]. This is usually attributed to the improved efficiency of the arc source, due to the increased arc density and the higher absorption of laser due to the preheating effect. However, the effect is quite controversial, because often the effect of increased heat input in these studies was ignored. On one hand, Ribic et al. [13] showed numerically that in order to achieve similar welds to those observed experimentally, the radius of the arc had to be reduced, which indicated the arc contraction. On the other hand, the main reason for the wider melt pool in hybrid welding was found to be the increased Marangoni convection, as a result of the increased heat input [13].

The fact that various research groups drew different conclusions indicates that the synergic effect between the laser and the arc is dependent on many factors, such as the leading heat source, gap geometry, as well as a position of the arc source and the separation distance between both sources [203, 320, 331]. The best efficiency is achieved when laser beam is focused between the arc centre and the droplet impact zone [320]. When the two sources are too close to each other the laser disturbs the droplet detachment, causing an unstable metal transfer [203, 331] whilst the droplets impacting into the keyhole exit zone can cause its perturbations [344]. Furthermore, a small distance between two heat sources results in the absorption of the laser beam in the arc plasma in case of CO_2 laser hybrid welding [322]. A very high separation distance on the other hand, ruins any synergy effect and both sources act independently [13, 322].

This implies that welding process does not response in the same way in the entire window of processing parameters. Various cross sections can be achieved, when varying the energy ratio between the laser and the arc in hybrid welding [345] or by changing shielding gas conditions [77]. Ming et al. [77] point out that laser and arc do not interact linearly. This explains so many contradicting results in the literature regarding the synergy in hybrid welding.

Depending on the laser wavelength different effects are responsible for the interactions in hybrid welding. The vaporised metal in CO_2 laser processing can increase its ionisation using energy of laser and arc simultaneously. This gives good conditions for the arc column [67]. The arc benefits from the fact that the ignition resistance in the vicinity of the plasma induced by the laser is relatively low [206, 313, 331, 346, 347]. However, if the density of this combined plasma increases excessively the laser beam becomes absorbed and the process collapses. This was demonstrated by Chen et al. [318], as shown in Fig.2.49. Initially the depth of penetration increased with increasing current of a TIG source, however, at a certain point, the arc plasma became too dense for the laser and the depth of penetration decreased rapidly with further increasing the TIG current [318].

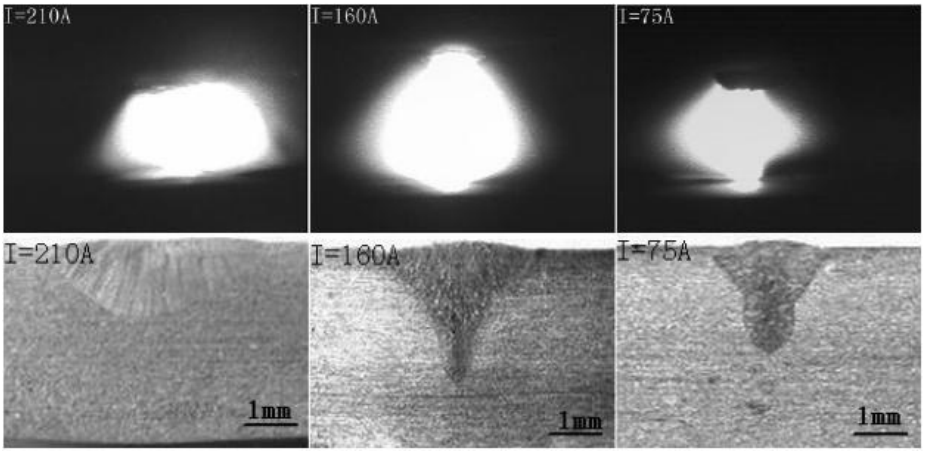

***Figure 2.49**: Effect of voltage of TIG on plasma brightness and weld profile of CO_2 laser TIG welding [318].*

In contrast, in hybrid welding with 1 µm radiation laser, vaporisation of workpiece can also occur but the laser almost does not interact with the plasma. Therefore, only the energy from the arc is utilised for heating and ionisation of this plasma. The mechanisms of arc attraction by the laser beam are also different for both lasers. For example the laser irradiation characteristic for fibre laser, does not attract the arc plasma, as it is in the case of CO_2 laser. Exceptions are materials, such as aluminium where arc tends to the laser interaction point, due to the oxide removal [67]. Gao et al [322] noticed that the increased molten volume in CO_2 laser/GMAW hybrid welding was no longer apparent as the separation distance between both heat sources exceeded 4 mm, despite the preheating effect of the arc source. It seems that the synergy effect can be mainly attributed to the interaction of the arc column with the laser-induced plasma, which is more beneficial in the case of CO_2 laser. In case of solid state lasers the arc preheating effect and oxide removal by laser are likely to be dominant.

Hu and Ouden [319] used a Seebeck calorimeter to compare the transfer efficiency between laser and laser hybrid process. There was no difference between both processes, thus it was concluded that the arc source did not increase the absorption of the laser [319]. However, the laser used in this experiment was not powerful enough to create a deep keyhole, even with the arc source, whereas the only mechanism of synergy in conduction limited welding regime is due to preheating. This experiment implies that the preheating by the arc source does not have any

effect on laser absorption in steel. Kelly et al. [348] claims that the transfer efficiency of CO_2/MIG hybrid process can be even lower than MIG on its own. This was apparent when the metal transfer of the arc source was disturbed by the interactions with the laser plasma. The efficiency of the laser process was additionally dependent on the flow rate of shielding gas, owing to the more stable keyhole when the vapour plasma was suppressed [348].

Some authors, however, claim that the arc plasma interacts with 1 μm laser irradiation. Liu and Hao [239] carried out a spectroscopic study of plasma from a tungsten-inert gas (TIG) during interaction with a pulsed Nd:YAG laser. The electron temperature of the arc plasma decreased, whereas the electron density increased when irradiated by the laser beam. The temperature decrease was attributed to the evaporation and ionisation of the workpiece. According to the authors, some volatile elements with low ionisation potential, such as magnesium in steel can increase their energy when colliding with electrons, inducing the cumulative ionisation. The highly conductive plasma begins to constrict in order to reduce the thermal loss, which causes the voltage reduction and the increase of electron density [77, 239]. Li et al. [346] used a hollow probe spectrometer to measure the radiation from different points of plasma generated by Nd:YAG laser with MIG hybrid welding. The plasma of the hybrid process was more focused than the plasma of the MIG, as shown in Fig.2.50. The laser beam provided ionisation duct for the plasma, therefore the temperature and density of the hybrid plasma increased [346].

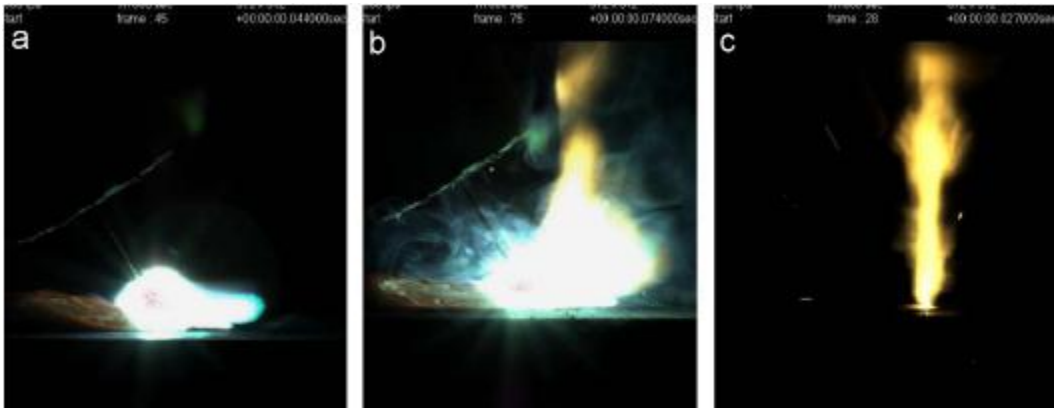

Figure 2.50*: Interaction of Nd:YAG laser on GMAW plasma;* ***a)*** *GMAW;* ***b)*** *hybrid;* ***c)*** *laser [346].*

A similar effect was found in Nd:YAG laser with TIG hybrid welding [349]. A numerical analysis showed a significant concentration of the arc plasma near the laser irradiation point. The local temperature of the plasma increased at this point from 10000 K to 14000 K, due to the laser irradiation. The laser beam modified the temperature, current distribution and the flow pattern of the arc plasma, which increased the heat transfer of the electrons [350]. Hu and Richardson [241] demonstrated that the arc plasma could significantly attenuate a Nd:YAG laser radiation. They found this to be strongly dependent on the arc current and the shielding gas. No laser attenuation was recorded in environment of helium, even after enhancing the plasma with particles of iron, whilst in case of argon the absorption was significant.

The interaction of arc with the laser-induced plume can also have undesired effects on the metal transfer. The high conductivity of the laser plume results in attraction of the arc column during the base current period, as shown in Fig.2.51 [351]. On the one hand, this attraction reduces the spatter generation due to the reduction of the electromagnetic force and the pinching effect of the droplet. On the other hand, the unstable metal transfer can occur, if the time of this interaction between the arc and the plume extends to the beginning of the peak current. A long time of this interaction tends to increase the arc length and decrease the current, resulting in insufficient pulse energy to detach a droplet [351]. This leads to severe spatter [352]. In some cases the interaction of both heat sources in hybrid welding resulted in alteration of metal transfer of GMAW from spray mode to short circuiting transfer [348, 353]. The unstable metal transfer was avoided by using a modulated laser beam [351] or by increasing the arc current [352].

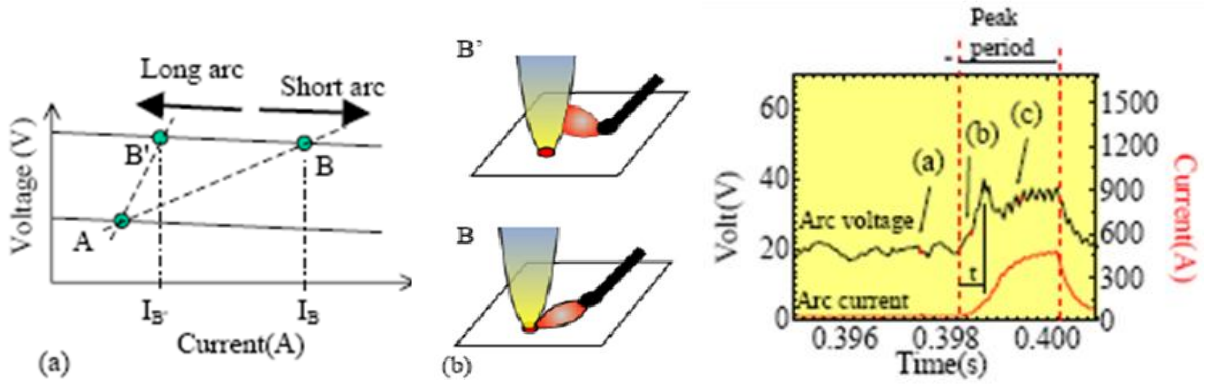

***Figure 2.51**: Destabilisation of metal transfer due to interaction of arc with laser plume;* ***a)** operating points;* ***b)** arc direction;* ***c)** variation of arc current and voltage during transition between peak and base current in hybrid welding [351].*

Not only the plume but also the laser irradiation itself can influence metal transfer of GMAW. Huang and Zhang [354] used a low power diode laser to induce a spray metal transfer. The laser beam was focused at the end of the filler wire inducing an additional detaching force on the droplets. This allowed a spray mode to be achieved at low currents. The effect was attributed to the recoil pressure from the laser beam, which acting on the droplets and enhanced their detachment [354]. This can be also attributed to the extra heat from laser, which enhances melting of the filler wire.

Some researchers investigated interactions between laser and arc by operating both sources in a pulse mode, which enabled synchronisation or modification of waveforms. Liu and Hao [321] synchronised pulses of a laser irradiation with an AC TIG to investigate the plasma behaviour. First of all, the laser plasma significantly intensified after arc ignition. Even when the laser peak occurred during zero passage of the AC TIG, the hybrid plasma was more intensive than the laser plume. This was attributed to the enhanced evaporation from the wider melt pool in the hybrid process. This plasma lowered the power density threshold required to form the keyhole. In another paper [355] an additional high power pulse was superimposed during a pulsed laser TIG hybrid welding. The depth of penetration was only improved when the duration of this superimposed pulse was shorter than 0.4 ms [355]. Unfortunately the authors did not explain this effect but the reason for the decreased depth of penetration with increasing duration of this superimposed pulse could be attributed to the plasma growth. Liu and Hao [356] used a phase matching

technique between laser pulses and AC TIG to observe plasma behaviour in hybrid welding. A greater depth of penetration and a better weld appearance was achieved when the laser pulses were acting during the positive polarity period of the tungsten electrode than during the negative polarity period. This was attributed to the stabilisation ability of the laser. During the positive polarity the workpiece is the cathode spot, which often has low thermionic emission. The laser irradiation stabilises the cathode spot by concentrating the energy of the arc plasma and increasing the current density. In the case of negative polarity the tungsten electrode is the cathode and thus the laser has low effect on the emission of electrons from the tungsten electrode and the arc does not interact with the laser. Therefore the stronger arc contraction was observed during the positive polarity period. Moreover, the authors suggest that during the positive polarity ions are accelerated by the cathode drop to impact on the surface. The mass of the positive ions and the cathode drop voltage are higher than the mass of the negative ions and the anode drop voltage. Therefore, if the cathode spot can be stabilised by laser, a greater depth of penetration is achieved with the positive polarity [356]. In DC TIG welding with positive polarity this effect is deteriorated by insufficient temperature of the cathode spot (workpiece) [2, 357]. In another study the arc rooting was observed with both polarities but it required a much higher power density from a laser in the case of DC positive polarity [323].

The improved depth of penetration in hybrid welding may suggest synergies between both heat sources. However, the effect of electromagnetic force of the arc column, acting on the melt pool should not be neglected. This additional downward force can change the direction of melt flow and the bead shape [258, 316]. Additionally, in GMAW the electromagnetic force accelerates the droplets, which transfer this high momentum to the melt pool, causing its depression [78, 214, 330, 358-361]. This was shown on X-ray imaging by Uchiumi et al. [203] as presented in Fig.2.52. The electromagnetic force is quadratically proportional to the current therefore, thus in the extreme conditions it can induce a surface depression [362]. In hybrid laser welding high currents are usually used in order to meet the demand of high productivity.

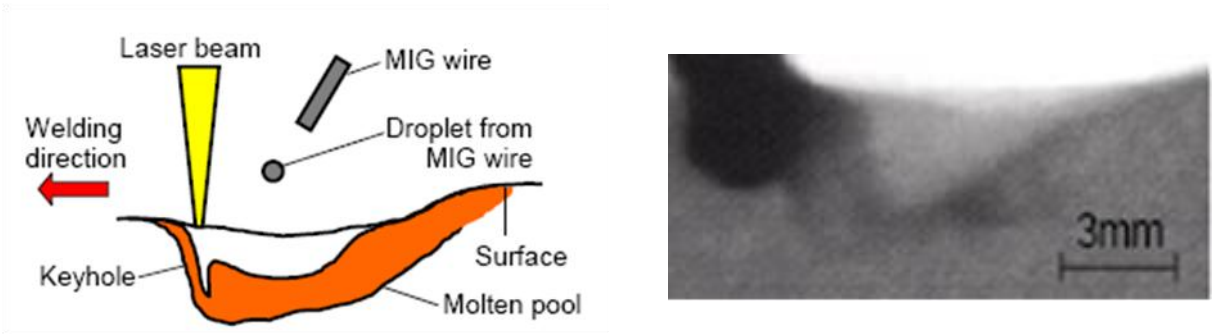

***Figure 2.52**: Depression of melt pool caused by arc pressure at 240 A [203].*

The electromagnetic force was found to be an important mixing force in the melt pool. It increased the backfilling speed of the liquid metal during the keyhole collapsing stage and enabled the molten metal from the top surface to reach the bottom of the keyhole [363, 364]. This strong electromagnetic force and resulting arc pressure along with droplet impingement can extend the keyhole [214]. Katayama's group [203] reported a desired effect of this additional opening force from the arc on suppression of porosity. It was observed experimentally that hybrid welding is less susceptible to porosity than the autogenous laser welding [4, 6, 316, 365, 366]. The higher the arc current the more heat can be driven into the weld root, leading to a more uniform weld shape and chemical composition [345]. This effect is also dependent on the separation distance between laser and arc. At large distances the droplets from the filler metal are impinging at a point, where only a small amount of molten metal exists and the downward force does not have enough time to mix the melt pool, due to the fast solidification rate [367].

On the other hand the reduction of porosity in hybrid welding can also result from the additional heat input from arc. This would reduce the solidification rate and provide more time for any gas to dissolve from the liquid metal. It was shown that the porosity in zinc coated sheets during CO_2 laser welding of could be suppressed by adding another laser beam [368], which proves that the larger melt pool rather than the electromagnetic force is dominant in the porosity suppression.

The most beneficial effect of the synergy between the laser and the arc in hybrid welding is the stabilisation of the arc, which enables the processing speed to be increased. The biggest topic of controversy in hybrid welding is the increased melting

rate, as compared to the sum of melting rates of both processes separately. Although many researchers suggested various synergies responsible for the greater melting volume the effect of additional heat input cannot be omitted. Very often the differences in the heat input between the comparing processes were disregarded. In such cases an autogenous laser welding was often compared against a hybrid process having a much greater overall heat input and then the increased melting efficiency was concluded. There was no attempt to compare laser and hybrid process with the same overall heat inputs. In other cases laser welding or hybrid process were investigated near the transition region between conduction and keyhole regimes or otherwise reflective aluminium at low power density was investigated. In such cases any small variation of welding conditions can have a significant effect on depth of penetration and melting rate.

2.7. Fit-up tolerance

The main drawback of laser welding is poor fit-up tolerance, which corresponds to a significant sensitivity of the process to the variation of gap between joined components. The small character of the laser beam as a heat source is not particularly advantageous when welding thick sections. It is ineffective to maintain the narrow tolerances required for laser welding, due to the high cost of pre-welding preparation. Furthermore, the narrow and deep fusion zone promotes high cooling rates, which can have undesired effects on microstructure. The low amount of molten metal combined with the fast solidification does not give much opportunity for the filler metal to be spread uniformly through the depth. This can also lead to severe issues with solidification cracking [369, 370].

The high interest in twin spot laser welding, as a promising solution for widening the melt pool, indicates the issues of laser welding [269, 368, 371-374]. In this case a laser beam is often split into two beams or rarely two different lasers are used. The twin spot laser welding offers better fit-up tolerance than the single beam laser welding, but the ability of adding the filler wire is still limited. Another disadvantage of this technique is shallower penetration, as compared to the single beam welding with the same overall energy. Thus the welding speed has to be decreased in order to achieve the required depth of penetration [27]. The benefits of twin spot welding seem to be deteriorated by the lower productivity. Similarly the trade-off between the gap bridging ability and the productivity has to be made with all kind of beam manipulation methods, such as beam spinning or oscillating [375-377].

Alternatively, the hybrid welding, as a result of incorporating the deep penetration and high productivity of lasers with the gap bridging ability of arc, can improve the fit-up tolerance. The productivity and gap bridging ability of hybrid welding was found to be much better, as compare to the laser welding with filler wire [330, 378-382]. In some cases gaps up to 2 mm could be accommodated with hybrid process [383-385]. The influence of gap on the weld shape is shown in Fig.2.53 [386]. Another way of increasing the fit-up tolerance and productivity beyond this limit is to use multi-wire systems, such as laser tandem arc hybrid welding [382, 387].

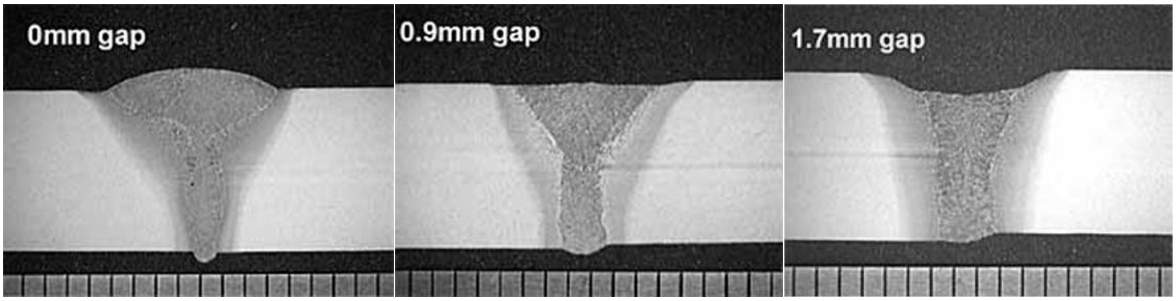

***Figure 2.53**: Effect of size of the gap between joined components in hybrid laser/GMAW butt welding; 4 kW laser power, 4 kW MAG power, 1 m min^{-1} travel speed [386].*

The bead shape and gap bridging ability are dependent on many factors, such as the ratio of the laser power to the arc power [345, 384, 388], bevel configuration [6, 309, 343, 389] and shielding gas conditions [390-394]. Since the filler wire mainly provides the metal to bridge the gap, it is desired to increase the melting rate by increasing the wire feed speed. The higher the power of the arc source, relative to the laser, the more uniform the weld bead across the thickness can be achieved [345]. Shielding gas also affects the bead shape, by altering the surface tension of the liquid metal [391, 395-399], as shown in Fig.2.54(a) [400]. The surface tension plays two contradicting effects on the fit-up tolerance. A low surface tension at the top bead increases the spread-ability of the molten metal, as shown in Fig.2.54(b) [401]. In contrast, a high surface tension is desired in the root face in order to support the molten metal against gravity [383, 402]. Large gaps in general are difficult to accommodate without undercut and excessive penetration, due to gravity [142].

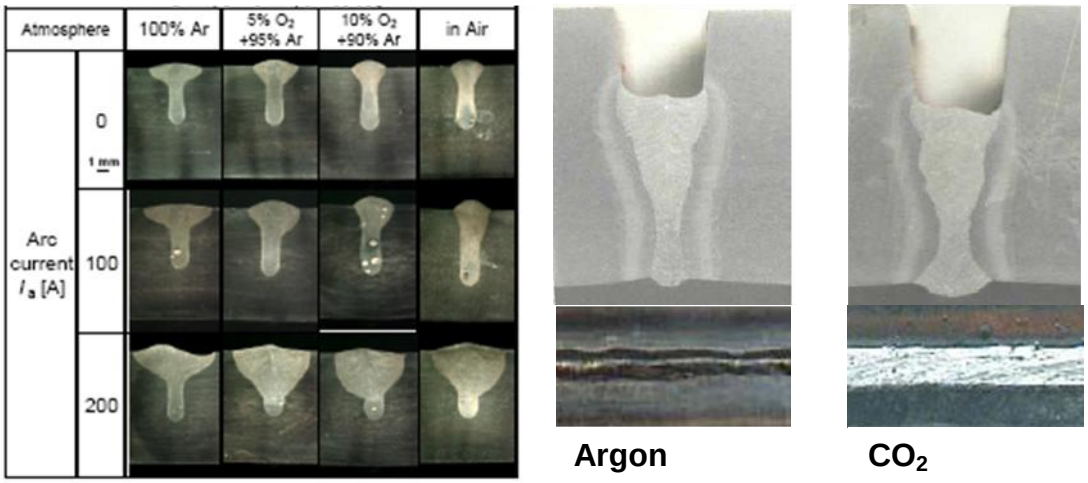

a) Bead-on-plate in 304 stainless steel b) Butt joint

Figure 2.54*: Influence of various parameters on weld profile;* ***a)*** *effect of shielding gas and arc current at constant laser power of 3.3 kW and travel speed of 10 mm/sec [400];* ***b)*** *effect of shielding gas at the root face on surface tension and weld width at a constant travel speed of 0.6 m/min [401].*

A choice of leading source and separation distance between the heat sources also influence the bead shape in hybrid welding [6, 353, 384]. In the laser leading configuration the wine cap shape of the cross section with a wider top bead and a narrower root is common. In the arc leading configuration, on the other hand, the laser interacts with the surface, which was already molten by the arc, leading to a greater depth of penetration [353, 384]. For larger gaps the arc leading configuration is recommended. Although lasers are dedicated for deep and narrow weld profiles, often V or Y shaped grooves are used in order to avoid solidification cracks. Wider bevels allow more room for the filler metal to flow downwards, which results in a lower gradient of chemical composition between the top bead and the root face [383].

Type of filler wire also has an effect on the deposition rate and thus on the fit-up tolerance. The metal cored wires provide higher melting rates for the same arc power, as compared to the solid state wires [403]. The melting efficiency of GMAW strongly depends on arc parameters, such as voltage, current, electrode diameter, electrode extension and polarity. There is a trade-off between the melting of workpiece and electrode. The melting efficiency of the electrode increases with increasing current, extension distance and decreasing voltage and wire diameter. In contrast, the melting efficiency of the workpiece increases with increasing current,

voltage and wire diameter and decreasing electrode extension. Higher melting rates can be also achieved with the negative polarity, as compared to the positive polarity [310, 404]. In pulse GMA welding the amount of molten metal increases with increasing peak time and frequency of pulsing [405].

In addition the fit-up tolerance is determined by arc stability. The spatter in particular can significantly reduce the amount of molten metal available to form the joint. Type of shielding gas has a major effect on the arc stability and droplet transfer [391, 393, 406]. For instance a small amount of oxygen in argon improves the droplet transfer drastically [406]. Moreover, in order to maximise the melting efficiency in hybrid welding the composition of filler wire should be tailored for the special need of the process [407].

Distortion induced by residual stress, due heat effects of welding, can also result in problems with assembly and fit-up. Thus control of residual stress and distortion is an important aspect in welding and joining technology. A large longitudinal residual stress is caused by a compressive plastic flow that occurs in front of the weld pool during the welding thermal cycle [408]. The compressive plastic flow is not balanced by the tensile plastic flow on cooling, leading to a large tensile residual stress developing across the weld zone. This tensile zone is then balanced by a compressive stress in the surrounding parent material. Distortion is proportional to the area of the tensile peak [409-411]. Distortion is severe in case of thin components in particular, where the compressive stress field can easily exceed the critical buckling load, resulting in buckling distortion, the removal of which is expensive and time consuming. A lot of work was carried out on understanding the residual stress and distortion in the past [410, 412, 413]. The most popular methods of minimising welding distortion are post weld rectification, design optimisation and in process manufacturing methods. In addition to these there are some techniques to mitigate distortion during welding, referred to as stress engineering [411, 414-419].

The easiest and most practical method of reducing residual stress is to use low energy input welding processes, such as laser welding. It was shown that the laser welding can produce low distortion joints, as compared to the traditional arc-based welding methods [420]. However, due to the flexibility of the laser welding the same depth of penetration can be achieved with many different combinations of

parameters, hence resulting in different properties of the joint. It was demonstrated that unlike in MIG welding, the heat input in laser welding is ambiguous and various welds can be achieved with the same heat input, if different beam diameters are used [421]. Thus not every laser weld will result in low residual stress and distortion. Furthermore, in hybrid laser welding the extra heat from the arc in some cases can exceed the heat from the laser beam. Therefore, at certain conditions the benefit of low heat input of lasers might be diminished by a high heat input from the arc in hybrid welding, particularly at very high wire feed speeds. Thus from the above a trade-off between the fit-up tolerance and distortion would be expected.

2.8. Summary and research objectives

The extensive literature review of phenomena involved in deep penetration laser welding have not given a clear answer regarding the major force limiting the depth of penetration. The keyhole evolution studies revealed a balance between the heat distribution, pressure and absorption conditions driven by the multiple reflections of the laser light inside the cavity. Various investigations under sub-atmospheric conditions and using X-ray, as well as numerical modelling demonstrated the complex character of keyhole in deep penetration laser welding. The geometry of keyhole results as a net consequence of the energy balance. Only a particular shape of keyhole can satisfy the equilibrium between the recoil pressure and the surface tension. Also the keyhole shape is affected by the multiple reflections and fluid flow, which can change the balancing forces. In addition, in hybrid laser welding there are significant interactions between both heat sources, which increase the complexity of physical phenomena.

There are many contradicting hypothesis, such as the absorption of laser beam in vapour or dominating effect of the melt flow. Very often the experimental conditions significantly differ from each other, making the results difficult to compare. In contrast, different assumptions and simplifications made in numerical investigations, significantly affect the achieved results. It seems like most of the measurement techniques have limited capabilities to study all these effects separately, which is required to draw unbiased conclusions, whereas the accuracy of numerical models is limited by our knowledge of the process.

This work undertakes an attempt to understand the hybrid laser welding from the perspective of basic laser material interaction parameters. Although it was shown that the achieved weld profile in laser and hybrid laser welding results as a net effect of many complicated phenomena, but it is believed that these effects are determined by the principal conditions of the heat source in the workpiece, such as the absorbed power density and interaction time. These fundamental parameters characterise the response of the material to the imposed laser energy, which together with material properties determine other conditions including: evaporation rate, pressure, melting rate, fluid flow etc.

The main objectives of this thesis can be formulated:

- To understand how the fundamental laser material interaction parameters affect the depth of penetration in laser welding;
- To identify parameters that uniquely control depth of penetration in laser welding;
- To find parameters which would allow a given depth of penetration to be achieved independent of the beam diameter;
- To develop an empirical model which would enable achievement of a particular hybrid laser weld on different laser systems;
- To evaluate benefits of fibre laser technology in pipeline industry;
- To optimise hybrid laser welding in order to maximise the fit-up tolerance.

Chapter 3. Experimental set-up and sample preparation

A general set-up and the main equipment used for the purpose of this thesis is presented in this chapter. This includes the laser system, power sources used for hybrid laser welding, as well as equipment to characterise the laser and the arc sources. The chemical compositions of the materials and procedure of sample preparation are also shown. More specific descriptions and parameters used are specified in methodology sections in each corresponding chapter.

3.1. Laser system

In all experiments presented in this thesis an IPG YLR-8000 CW multimode fibre laser with a maximum power of 8 kW and a beam parameter product (BPP) of 16 mm.mrad was used. The laser beam was delivered through an optical fibre of 300 µm diameter and collimated with a 125 mm focal length lens. To achieve different beam diameters a set of focussing lenses with focal lengths of 150 mm, 200 mm, 250 mm and 300 mm were used. This enabled variation of the beam diameter, whilst maintaining the same intensity distribution. For some experiments additional focusing lenses with focal lengths of 500 mm and 680 mm were used, providing additional beam diameters. The set of focusing lenses gave the beam diameters at the focal points as given in Table 3.1. At the end of this project the delivery fibre was replaced, thus the beam diameters and other properties changed slightly, as shown in Table 3.2.

In the majority of experiments the welding was carried out at the focal point, i.e. with the laser beam focused on the surface, unless otherwise stated. In the case of using out of focus position the focal point was focused either above or below the surface, referred to as positive and negative defocusing. In every case the beam diameters and the appropriate focusing distances were measured precisely by a beam profiler.

***Table 3.1**: Beam properties of different optical set-ups used in this thesis*

Diameter of delivery fibre (µm)	**Collimation lens** (mm)	**Focusing lens** (mm)	**Beam diameter*** (mm)	**Rayleigh length** (mm)	**Divergence angle** (mrad)
300	125	150	0.38	2.1	181.4
		200	0.5	3.3	149.6
		250	0.63	5.6	112.9
		300	0.78	8	96.4
		500	1.24	22	55.7
		680	1.67	40	41.9

*According to the second order moment definition

***Table 3.2**: Correction of beam propagation properties after delivery fibre replacement*

Diameter of delivery fibre (µm)	**Collimation lens** (mm)	**Focusing lens** (mm)	**Beam Diameter*** (mm)	**Rayleigh length** (mm)	**Divergence angle** (mrad)
300	125	150	0.37	2.25	161.1
		200	0.48	3.9	121.8
		250	0.6	6.2	98
		300	0.75	9.3	80.2

Depending on the material, different propagation angles of laser beam were used. The laser beam propagating perpendicularly to the workpiece was used for all bead-on-plate welds made in low carbon steel. To protect the optical head from back reflection in case of aluminium alloy and stainless steel, an inclination angle of 5° from the weld centreline was applied. This is shown schematically in Fig.3.1.

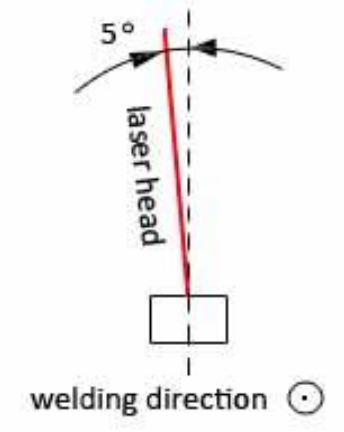

***Figure 3.1**: Inclination angle of the optical head relative to the vertical axis used for laser welding of aluminium and stainless steel.*

3.2. Motion system and clamping arrangement

The translation of the workpiece relative to the laser beam was achieved by a six-axis Fanuc M700i B45 robot integrated with a single axis translation stage. The experimental set-up is shown in Fig.3.2. The motion system was also integrated with a Lincoln Electric wire feeder and power source, which were used for hybrid laser welding. All autogenous laser, as well as hybrid laser samples were clamped along the entire length and no backing bar was used. The clamping system is presented in Fig.3.3.

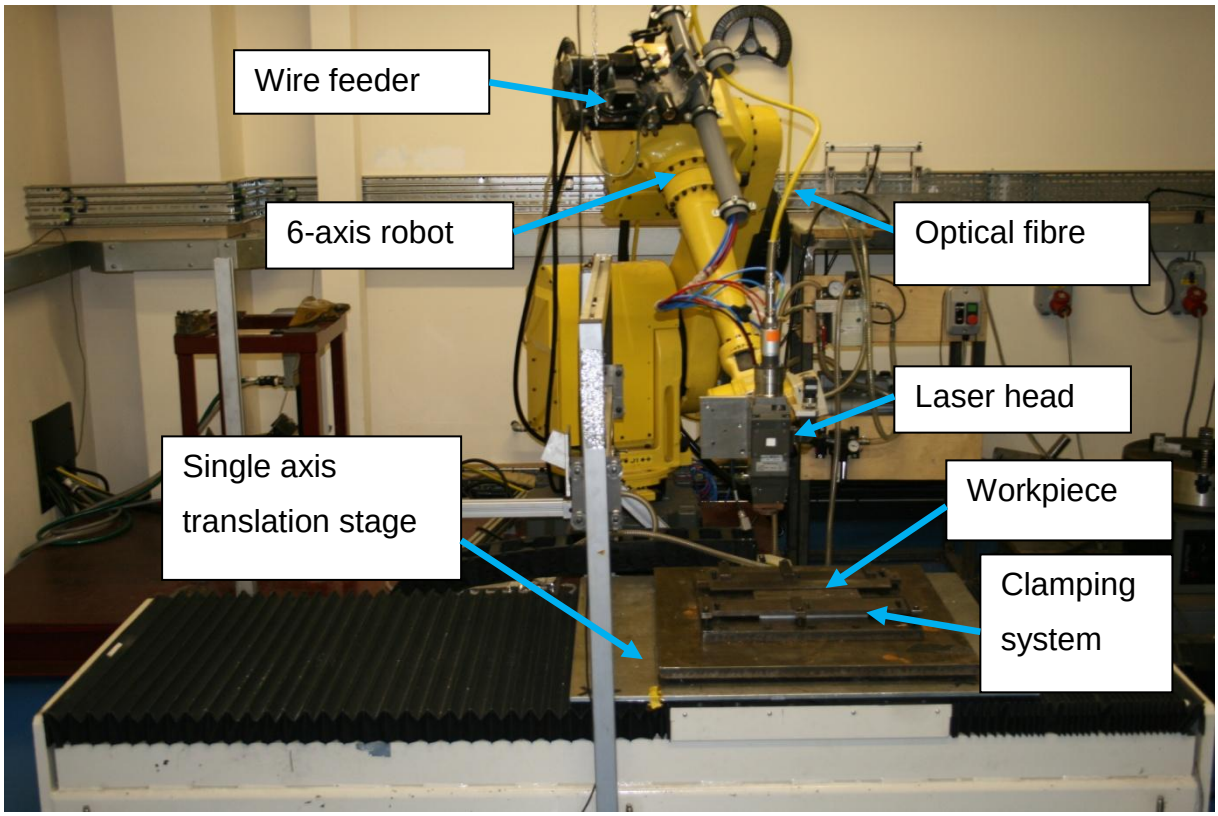

***Figure 3.2**: Experimental set-up.*

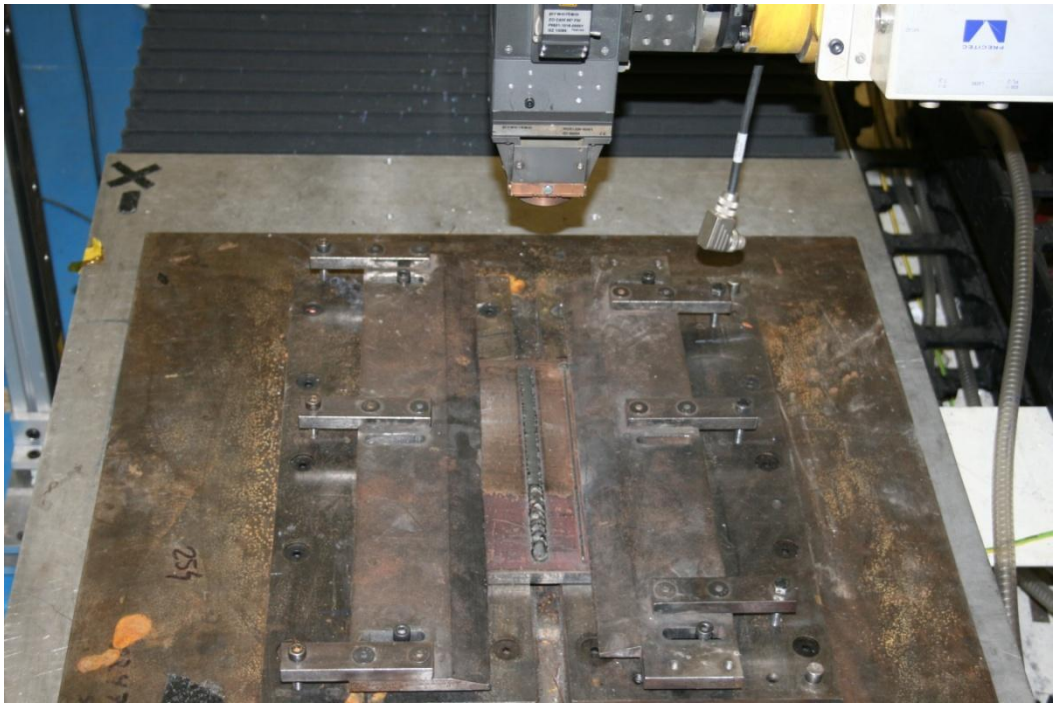

***Figure 3.3**: Clamping system*

3.3. Equipment for characterisation of laser

Properties of the laser beam such as beam diameter, focus position, divergence angle were measured by means of a Primes GmbH focus monitor, shown in Fig.3.4. The device works based on the principle of rotating pin-hole. The second order moment method [87-89] was used for the beam diameter evaluation. To exclude the effect of focus shift the measurement of beam diameter was carried out with a minimum laser power up to 2 kW. All the beams exhibited a top-hat intensity distribution at the focal points. An example of the intensity distribution profile and its cross section is shown in Fig.3.5.

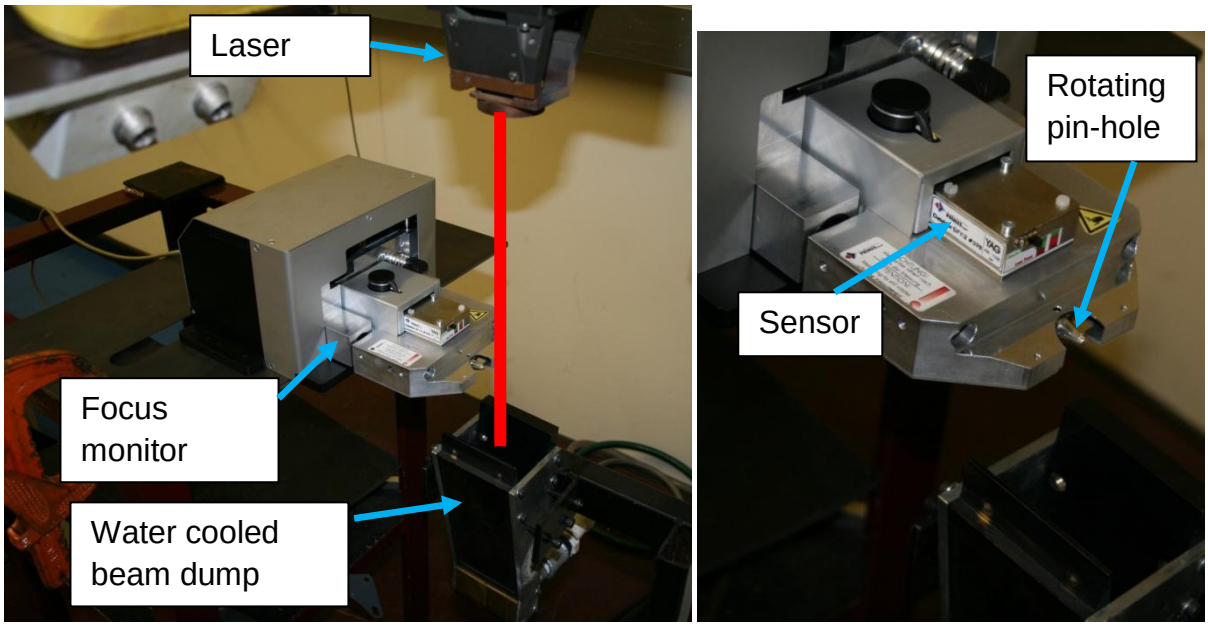

***Figure 3.4**: Experimental set-up for beam diameter and focus shift measurement.*

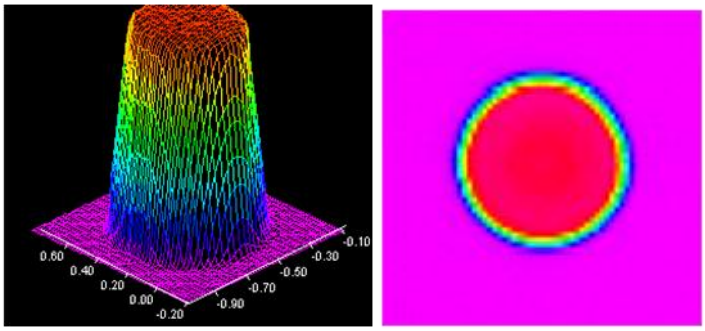

***Figure 3.5**: Example of intensity distribution and beam profile of the fibre laser.*

The output laser power was measured prior to every experiment, using an Ophir calorimetric power meter shown in Fig.3.6. The readings from the power meter were used to calibrate the laser source in order to achieve a desired power on the workpiece.

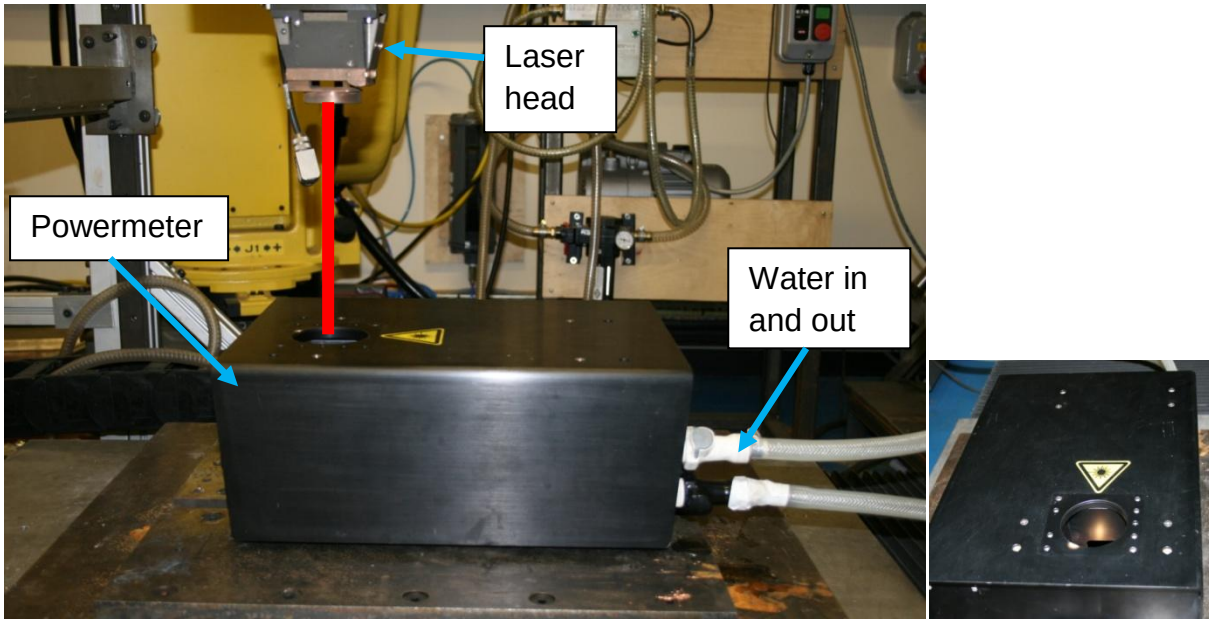

***Figure 3.6**: Experimental set-up for power measurement*

To measure the temporal behaviour of the laser a photodiode was also used. The device contains a silicon detector suitable for signals in the range of wavelength from 350 to 1100 nm and with the peak sensitivity at 970 nm. It was powered with 12 V current and gave an output signal up to 10 V depending on the intensity of scattered light. The output signal from the photodiode was recorded on a Yokogawa oscilloscope with a sampling rate of 200 Hz. To provide the maximum accuracy the laser beam was irradiated into a ceramic water cooled beam dump, whose surface was not affected by the laser beam during the emission time. The experimental set-up is shown in Fig.3.7.

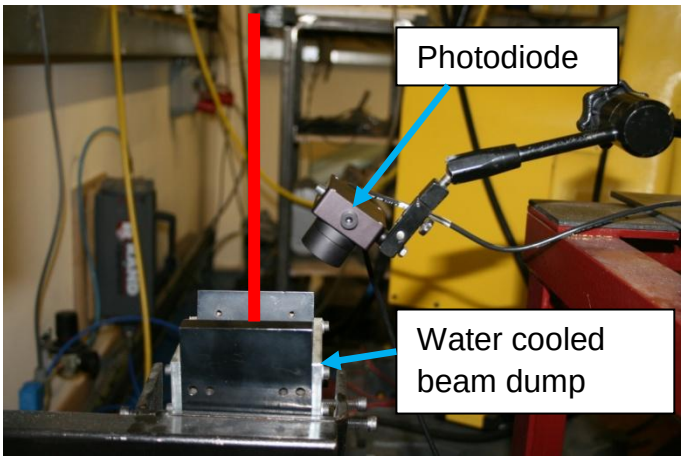

***Figure 3.7**: Experimental set-up for temporal behaviour measurement.*

3.4. Equipment for characterisation of arc sources

The energy inputs, as well as the waveforms of the arc sources were recorded by means of a Yokogawa DL 750 oscilloscope shown in Fig.3.8. The sampling rate used for the voltage and current accusation was 5 kHz. The beginning and end parts of the waveforms were ignored for calculations of the heat input. Depending on the conditions two definitions of power were used [422]:

- Average arc power in case of DC TIG process

$$P_{AV} = I_{AV} V_{AV} \qquad 3.1$$

- Instantaneous arc power in case of pulse MIG and tandem MIG welding

$$P_{AI} = \sum_{i=1}^{n} \frac{I_i V_i}{n} \qquad 3.2$$

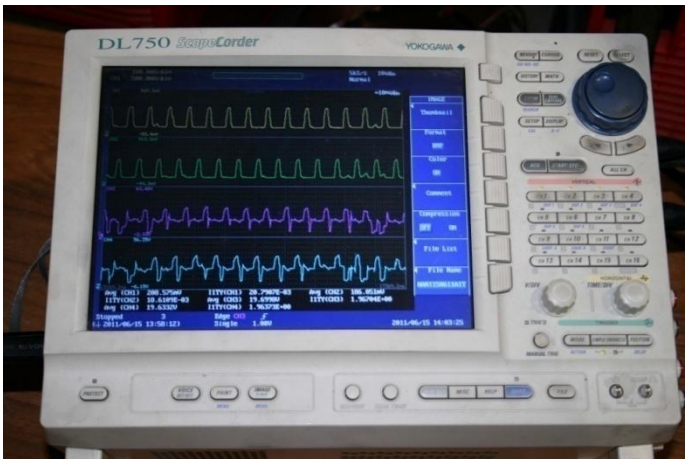

***Figure 3.8**: Oscilloscope used for arc characterisation.*

3.5. Additional equipment:

- High speed camera Phantom VR 0608 with a tele-macro lens and a fibre delivered green diode light for the illumination,
- Vickers Micro-hardness Zwick Intendec ZHV 1

3.6. Material composition

All autogenous bead-on-plate laser welds were carried out in 250 mm long and 12 mm thick S355 low carbon steel, 304 stainless steel and 7075 aluminium alloy. The width of the samples varied between the experiments. For some conditions the 12 mm thickness was insufficient, in which case 20 mm thick plates were used. The chemical compositions of the materials are given in Tables 3.3 to 3.5.

***Table 3.3**: Chemical composition of S355 low carbon steel.*

Element	C	Mn	Si	P	S
%wt	<0.23	<1.6	<0.5	<0.05	<0.05

***Table 3.4**: Chemical composition of 304 stainless steel.*

Element	Cr	Ni	Mn	C	Si	P	S
%wt	18-20	8-10.5	<2	<0.08	<1	<0.045	<0.03

***Table 3.5**: Chemical composition of 7075 series aluminium alloy.*

Element	Zn	Cu	Cr	Mg	Fe	Mn	Si	Ti
%wt	6.8-8	1.6-2.6	0.18-0.35	2.6-3.4	<0.4	<0.2	0.35	0.2

3.7. Filler wire

Supra-MIG (Lincoln Electric) filler wire with a diameter of 1 mm was used in all laser/MIG hybrid and laser/tandem MIG hybrid experiments. The chemical composition of the filler wire is given in Table 3.6.

***Table 3.6**: Chemical composition of filler wire Supra MIG from Lincoln Electric.*

Element	C	Si	Mn	P	S	Cr	Ni	Mo	Cu
%wt	0.09	0.67	1.06	0.004	0.01	2.37	0.06	0.93	0.2

3.8. Shielding gas

3.8.1. Autogenous laser welding

Pure shield argon delivered by means of a side jet nozzle was used as a shielding gas in all autogenous laser experiments, as shown in Fig.3.9. The flow rate was varied from 10 – 15 l/min depending on experiments.

***Figure 3.9**: Shielding gas nozzle used in autogenous laser welding*

3.8.2. Hybrid laser welding

Argon heavy shield mixture from BOC gases was used in all hybrid welds. This mixture contains 20% of CO_2, 2% of O_2 and argon balance. The shielding gas was delivered through the arc torch and no additional shielding nozzles were used in hybrid welding experiments. The flow rate was set to be 20 l/min.

3.9. Power sources and experimental set-ups for hybrid laser welding

The following arc power sources were used in hybrid laser trials:

- TIG (Tungsten Inert Gas) – for residual stress investigation
- MIG (Metal Inert Gas) – for all single wire hybrid laser welds
- Two synchronised MIG sources – for all tandem arc hybrid laser welds

3.9.1. Hybrid laser/TIG hybrid welding

A Migatronic BDH 550 power source was used in laser/TIG hybrid welding. The experimental set-up and power unit are shown in Fig.3.10. The laser beam was propagating perpendicularly to the workpiece, whilst the TIG torch was set to be 30° in push position. In all cases the laser leading configuration was used.

***Figure 3.10**: Experimental set-up and arc power source used in hybrid laser/TIG welding.*

The tungsten inert gas (TIG) source was operated in DC electrode negative polarity. To avoid an excessive heating of the electrode during the hybrid welding the electrode with a diameter of 3.2 mm was used. The opening angle of the tungsten electrode was 60 degrees.

3.9.2. Hybrid laser/MIG

A Lincoln Power Wave 455M/STT MIG/MAG arc source was used in laser/MIG hybrid welding, as shown in Fig.3.11. The power source was mainly operated in pulsed synergic mode (Rapid Arc) with the positive polarity in the torch. This power source allowed wire feed speeds up to 20 m/min for 1 mm wire diameter. To enable the laser beam to reach the proximity of the filler on the workpiece, a triangular gap was machined in the shroud. The separation distance between the laser spot and the filler wire was between 2 and 3 mm. The contact-tip-to-workpiece-distance CTWD of 17 mm was used for most experiments, unless otherwise stated.

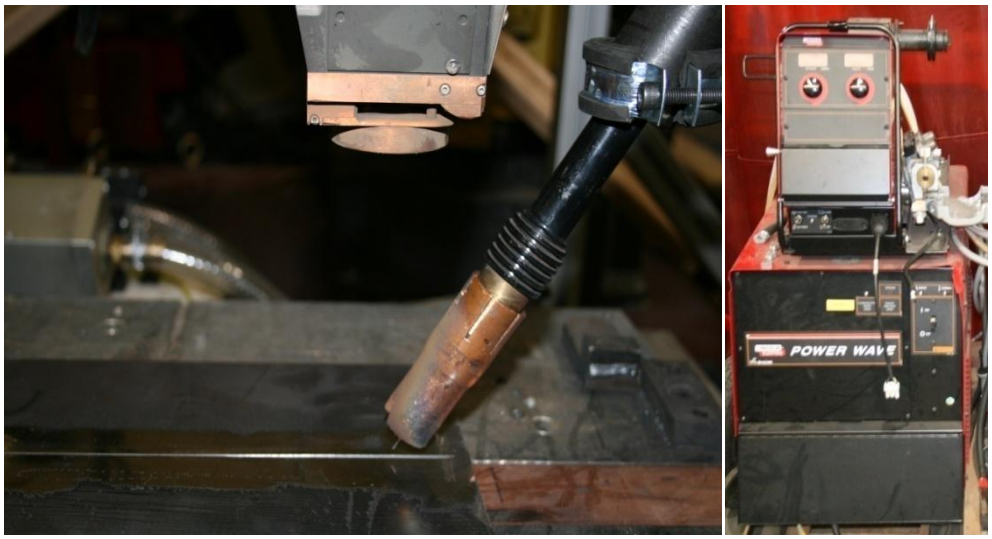

***Figure 3.11**: Experimental set-up and arc power source used in hybrid laser/MIG welding.*

As shown schematically in Fig.3.11 the laser head was perpendicular to the workpiece and the arc torch was set with 30° inclination. Depending on requirements either the laser leading configuration or the arc leading configuration was used. As shown in Fig.3.12 the arc torch was pushing in the laser leading configuration, whereas in the arc leading configuration the arc torch was pulling.

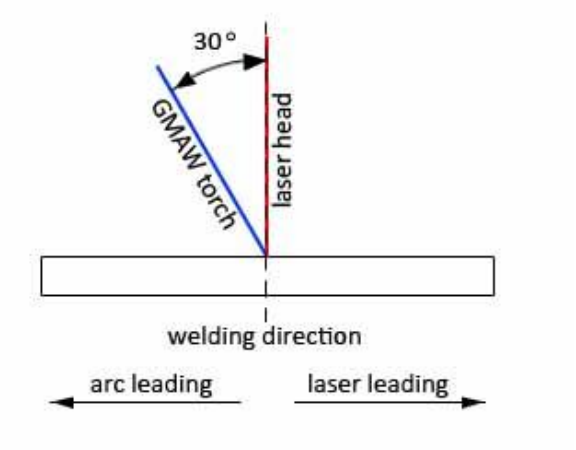

***Figure 3.12**: Configuration of MIG torch relatively to the laser head in arc leading and laser leading configurations.*

3.9.3. Hybrid laser/tandem MIG

Two synchronised Fronius Trans Puls Synergic 5000 power sources were used in laser/tandem MIG hybrid welding. The experimental set-up and power units are

presented in Fig.3.13. The power sources were operated in pulsed modes, synchronised and shifted in phase by 180°. This prevented electromagnetic interactions between the filler wires. An example of the waveform is shown in Fig.3.14. These power sources enabled wire speeds up to 30 m/min per wire for 1 mm wire diameter. The shroud was also machined out to accommodate the laser beam in the proximity of both filler wires on the workpiece. The separation distance between the wires and the laser spot was 2 – 3 mm. Depending on conditions the tandem torch was used either in a longitudinal configuration with one wire following other or in a transverse configuration. Both configurations are shown in Fig.3.15. The distance between the wires was fixed by the torch design; however, it was additionally dependent on the CTWD and in most cases was approximately 5 mm. The CTWD of 14 mm was used in tandem hybrid welding.

***Figure 3.13**: Experimental set-up and arc power sources used in hybrid laser/tandem MIG welding.*

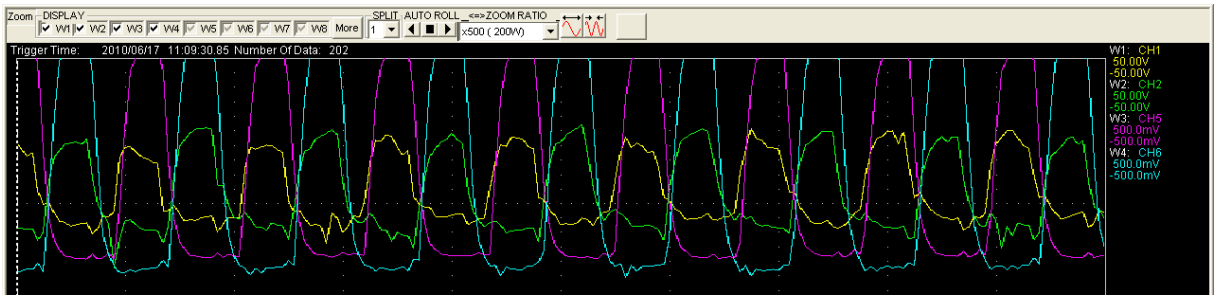

***Figure 3.14**: Waveform characteristics of tandem MIG (purple curve – current 1, yellow curve – voltage 1, blue curve – current 2, green curve voltage 2).*

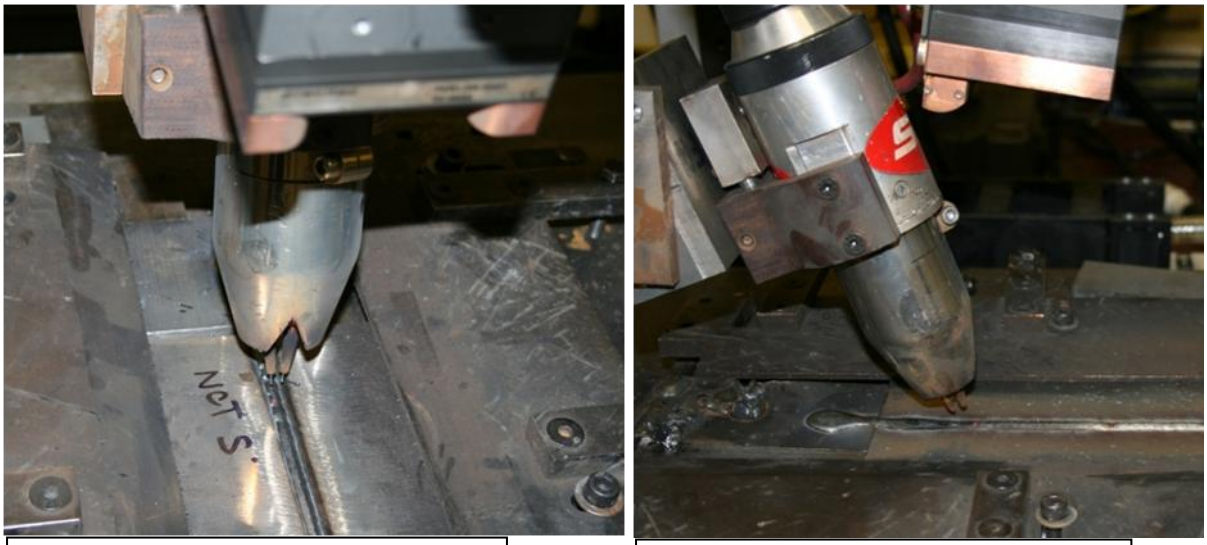

Transverse configuration of wires

Longitudinal configuration of wires

***Figure 3.15**: Tandem torch in transverse and longitudinal arrangements of filler wires.*

Considering the large dimension of the tandem torch, both the laser head and the tandem torch were tilted to achieve an appropriate distance between the laser spot and the wires. Depending on whether the laser leading or the arc leading configuration was used, different positions of the arc torch and the laser head were apparent, as presented in Fig.3.16.

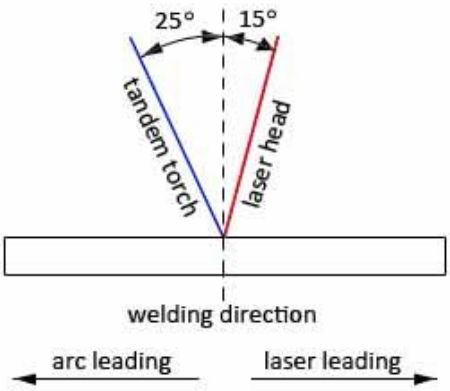

***Figure 3.16**: Configuration of tandem MIG torch relatively to the laser head in arc leading and laser leading configurations*

3.10. Preparation of samples

3.10.1. Before welding

All plates for bead-on-plate tests were subjected to grinding to remove the oxide layer and then linished with a fine grade abrasive disk to make the surface flat, but without unnecessary polishing. The samples were cleaned with acetone prior to welding to remove any residuals of grease.

3.10.2. Macrograph preparation

All welds were sectioned approximately at half length and mounted in special moulds using an epoxy resin, in order to fit them into an automatic polisher. The samples were mechanically ground in three steps using different grades of grinding paper as follows: 120, 240 and 1200. Next the polishing using 5 µm diamond paste was performed. Additionally some autogenouns laser welds, which exhibited small fusion zones were polished with a 1 µm silica suspension in water in the final step. To reveal the microstructure and distinguish various zones within the welds, the samples were etched with 2% or 5% Nital solution, prior to microscopic examination. The macrographs were analysed in terms of dimensions of fusion zone and bead quality. The depth of penetration and the melting area were measured using a Carl Zeiss Axio Vision 4.6 image analysis software.

Chapter 4. Stability study of fibre laser

According to the literature shown in Section 2.2 the new generation of solid state lasers, such as fibre laser offer many benefits for welding applications, as compared to Nd:YAG and CO_2 lasers. The usefulness of fibre lasers in hybrid welding applications is investigated in this chapter. In particular, the stability of the output power and the focus shift and its effect on welding conditions are scrutinised.

4.1. Experimental set-up

All details of the equipment used for this study can be found in Chapter 3. To investigate the stability of the fibre laser, power measurement using an Ophir calorimetric power meter was carried out. Furthermore, the properties of the beam and their variation with the emission time were analysed using a Primes Focus Monitor and a photodiode. Some additional experiments were carried out at Nottingham University using a 2000 YLR IPG fibre laser with a maximum power of 2 kW. The optical set-ups used with this laser will be described in the methodology in Section 4.3.1.

4.2. Power measurement

4.2.1. Methodology

The power measurements at several power levels ranging from 1 kW to 8 kW using the power meter were carried out. In each case the emission time of the laser was set to 3 minutes. Then the response signal was plotted as a function of emission time and analysed in terms of fluctuations. In addition the average power was compared with the applied power indicated by the control system of the laser.

The data obtained from the power meter give quantitative information about the amount of optical energy from the laser. However, considering the slow response

time of this particular device, additional measurements of the temporal variation of the laser were performed by means of a photodiode.

4.2.2. Results

The measurement obtained from the power meter is shown in Fig.4.1. It can be seen that the power meter needed from 30 to 80 seconds in order to reach equilibrium, depending on the power level. There are no major fluctuations of the power during the emission time, apparent in this figure, after the plateau is reached. The actual measured output power, in general was very close to the power indicated by the control system of the laser. This is also confirmed in Fig.4.2, where the average power measured after approximately 60 seconds from the emission beginning is shown. Even at the maximum power the difference between the applied and the measured values does not exceed 3%, as shown in Fig.4.3.

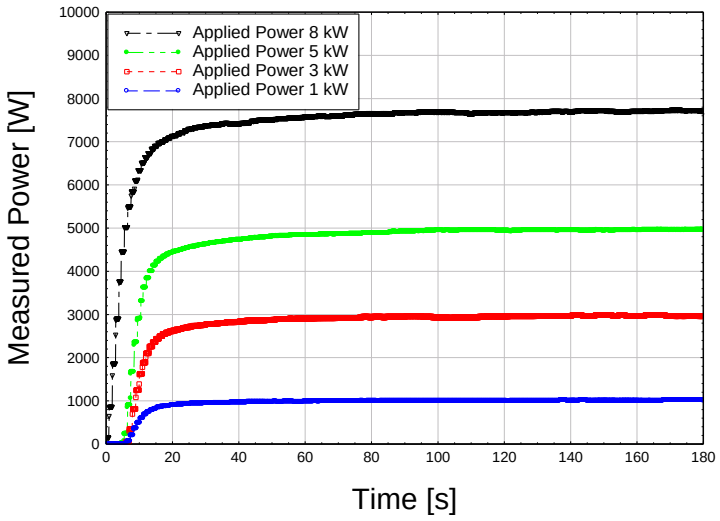

***Figure 4.1**: Laser output power as a function of time for different power settings.*

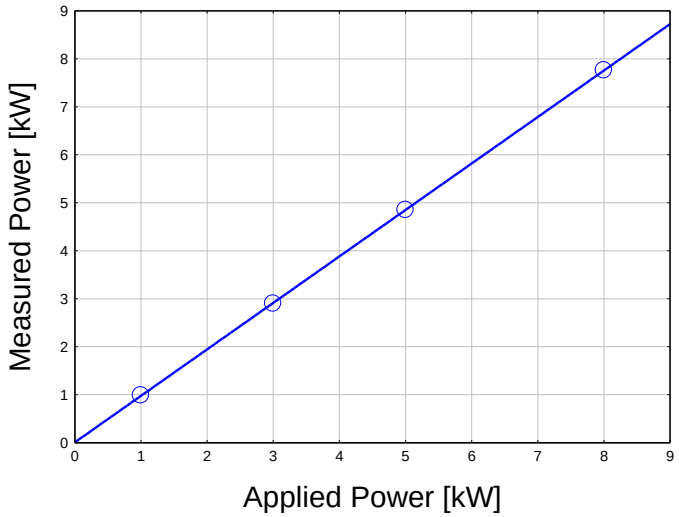

***Figure 4.2**: Measured average power as a function of applied power.*

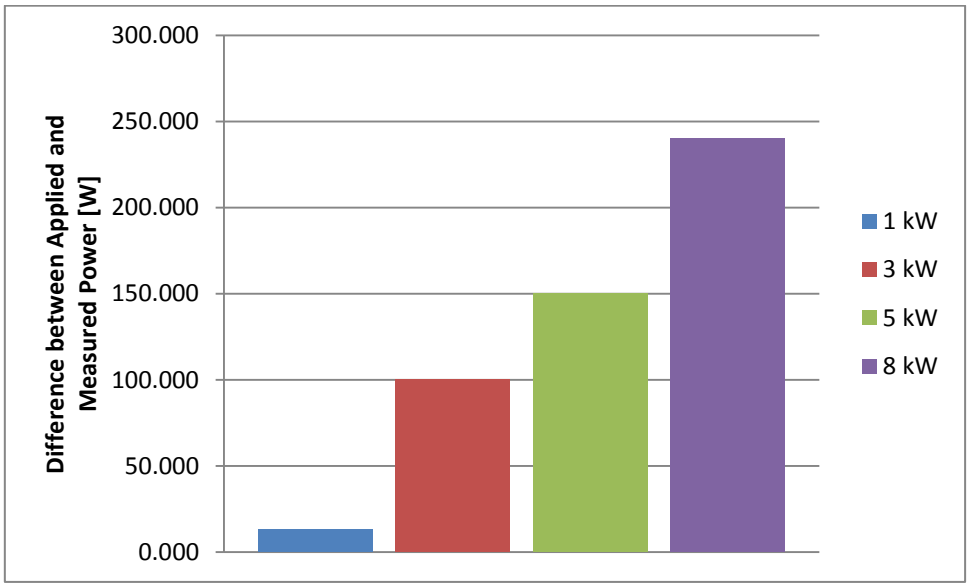

***Figure 4.3**: Difference between applied power on laser controlling system and measured power.*

The response signal from the photodiode, recording the scattered light from the beam dump, is shown in Fig.4.4. At first the immediate response of this device, in comparison to the power meter, can be depicted. Also the temporal stability of the fibre laser from the beginning to the termination of the emission is evident for all range of powers.

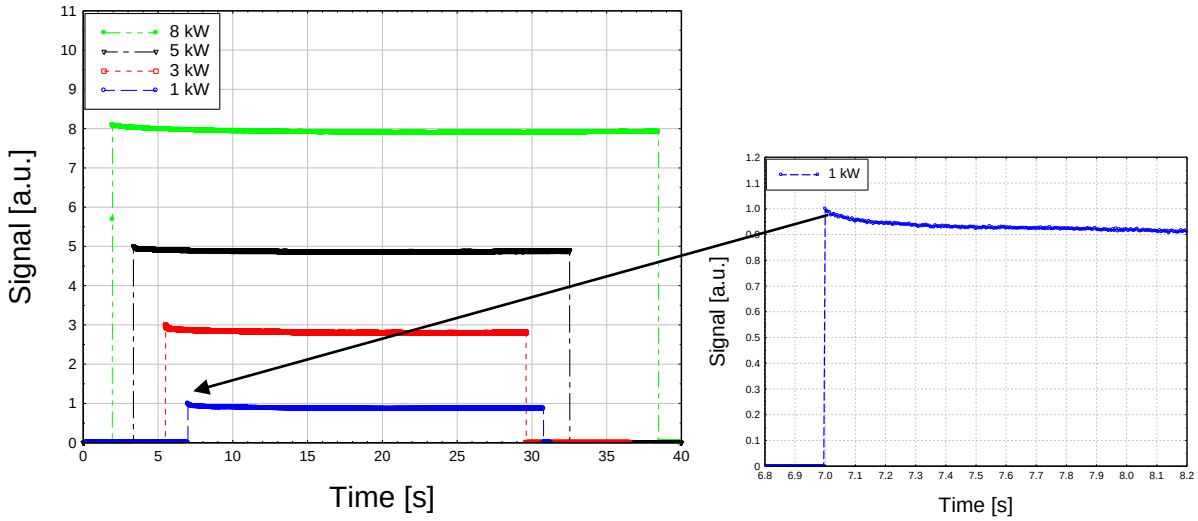

***Figure 4.4**: Signal recorded by photodiode as a function of emission time for different laser powers.*

4.3. Focus shift

4.3.1. Methodology

First a drift of the focal point, using the beam profiler, was investigated. A position of the focal point was measured continuously during a 10 minutes period of laser emission. To provide an optimum balance between the time of the measurement and the accuracy, the beam was scanned at 16 different planes along the propagation direction for each measurement. The time of full measurement was approximately 3 minutes. Then the measurements were performed at various power levels. Most of the experiments were carried out on the Cranfield University laser described in Chapter 3. To check the effect of optical magnification several focusing lenses with focal lengths ranging from 150 mm to 680 mm were used. This optical arrangement resulted in beam diameters ranging from 0.38 mm to 1.67 mm. At certain stage of this PhD some optical components inside the processing head were found to give an unacceptable performance, hence the optical head was subjected to cleaning. It turned out that the collimation lens was contaminated with water. Before the repair we took the opportunity to measure the focus shift. These experiments are referred to as dirty optics trials. Additional experiments were carried out at Nottingham University on a 2000 YLR IPG fibre laser. In this case the laser beam was collimated with a 125

mm focal length lens and focused with a 200 mm focal length lens. To measure the effect of diameter of the optical fibre on the focus shift, two different optical fibres having diameters of 0.2 mm and 0.6 mm were used with the same focusing and collimating units. These optical arrangements provided beam diameters of 0.31mm and 0.95 mm.

To investigate the effect of focus shift on the weld shape and the depth of penetration, long bead-on-plate welds were made. In the first case a laser power of 5 kW and a travel speed of 1 m/min were applied. The second weld was made with 8 kW of power and 2 m/min travel speed. This combination of parameters provided continuous welding times of 3 and 2 minutes respectively. In both cases a 250 mm focal length focusing lens, providing a beam diameter of 0.63 mm, was used. At the time when this experiment was carried out, a maximum focus shift for this optic was approximately 3 mm. The welds were made on 1200x250x12 mm S355 low carbon steel. The samples were appropriately clamped along the entire length. In order to exclude the effect of distortion on the focus shift, each of the long welds was performed on a special path, with the beam being reversed back and forth on the same plate with an off-set, as shown in Fig.4.15 and Fig.4.16. This allowed for relatively long welding times on a relatively short workpiece. Then the metallographic cross sections from different parts of the same weld were prepared, as indicated in Fig.4.15 and Fig.4.16 and compared in terms of depth of penetration and bead shape.

To evaluate the fluctuations of depth of penetration, commonly seen in partially penetrated welds, an additional bead-on-plate weld on 150x50x12 mm S355 low carbon steel was performed. The weld was subjected to a longitudinal cross section and two transverse cross sections in positions where the depth of penetration exhibited a maximum and minimum. This particularly short workpiece was selected to exclude the effect of focus shift and to investigate only the fluctuations of depth of penetration due to the instabilities of keyhole.

4.3.2. Results

Position of the focal point as a function of emission time for a focusing lens with a 250 mm focal length is shown Fig.4.5. It can be seen that the shift of the focal point

increases with the laser power and the emission time and saturates after approximately 7 minutes. After this time the focus shift stabilises itself and does not increase further. Note that the focal point shifted towards the optical head, which corresponds to a reduction of focal length of a focusing lens. From the results presented here it can be deducted that the effect of laser power on the focus shift is more significant than the effect of emission time. This is also shown in Fig.4.6. For a given optical set up the focus shift is proportional to the laser power. The effect of focus shift on the beam diameter at a given plane is demonstrated in Fig.4.7. This graph was achieved by a sudden change of laser power during the emission time. It is apparent that the beam diameter increases slowly without any sudden variations after increasing the power. This slow change of the beam diameter indicates a continuous build-up of the thermal gradient in the optical components.

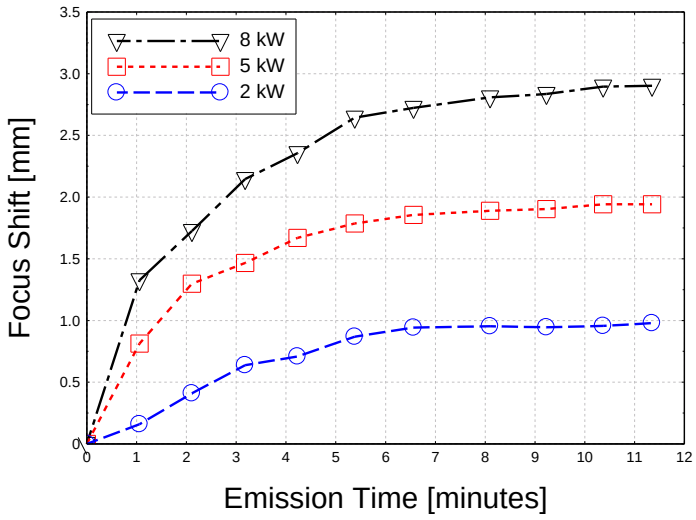

***Figure 4.5**: Focus shift with F 250 mm focussing lens as a function of emission time of the laser for different levels of power and.*

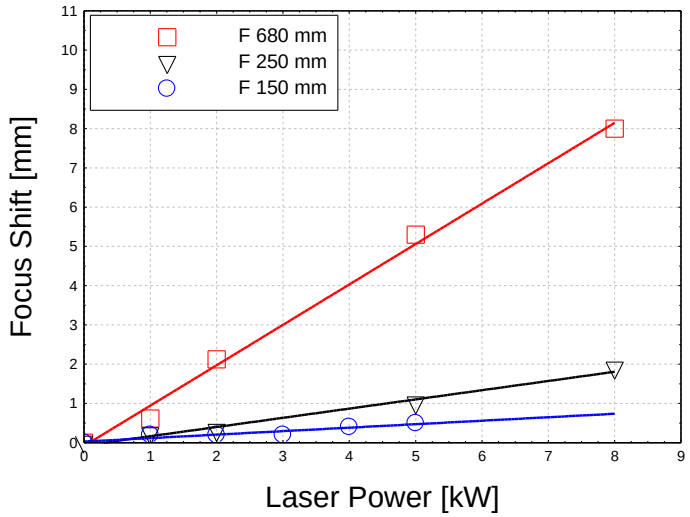

***Figure 4.6**: Focus shift as a function of laser power for different focussing lenses after 2 minutes of emission time.*

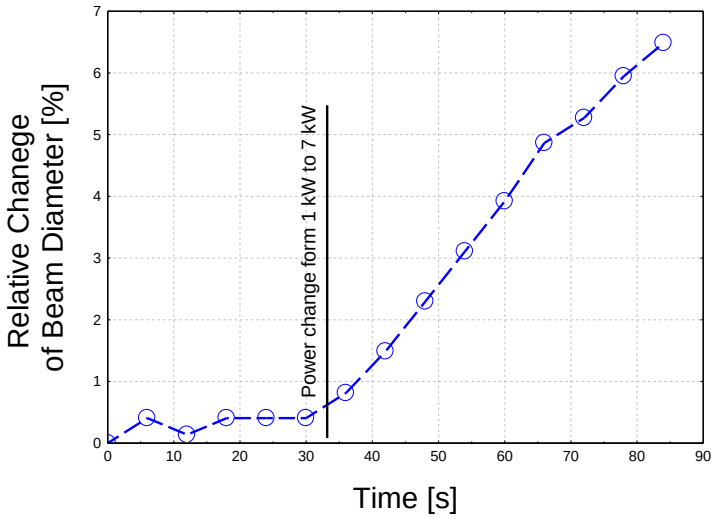

***Figure 4.7**: Relative change of beam diameter at a given plane due to sudden change of laser power from 1 kW to 7 kW for a focusing lens F 250 mm.*

Influence of the optical set-up on the focus shift is shown in Fig.4.6. The focus shift is strongly dependent on the optical magnification. The fact that different focusing lenses were used to achieve different beam diameters, whilst the collimating unit remained unchanged, resulted in a variation in optical magnification. The optical magnification corresponds to the ratio of the focal length of a focusing lens to the focal length of a collimation lens. In Fig.4.8 the focus shift measured after 10 minutes

of emission time is plotted as a function of optical magnification. There is a linear dependence. Therefore a focusing lens with a focal length of 680 mm exhibits 16 mm of focus shift. However, the optical depth of focus also increases with the optical magnification. It can be seen in Fig.4.9 that the ratio of the Rayleigh length to the focus shift in all cases is greater than two. This means that Rayleigh length (half of depth of focus) of all the optical set-ups used in this theses was greater than the focus shift.

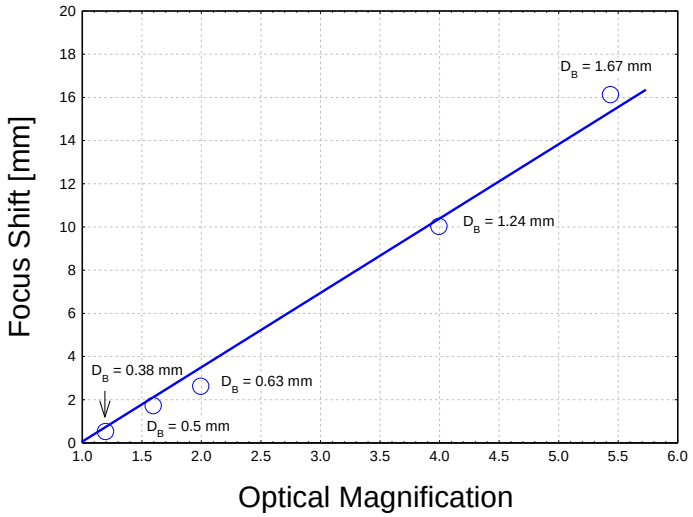

***Figure 4.8**: Focus shift as a function of optical magnification at a power of 7 kW for focusing lenses F 200 – 680 mm and 4 kW of power for a focusing lens F150 mm measured after the emission time of 10 minutes.*

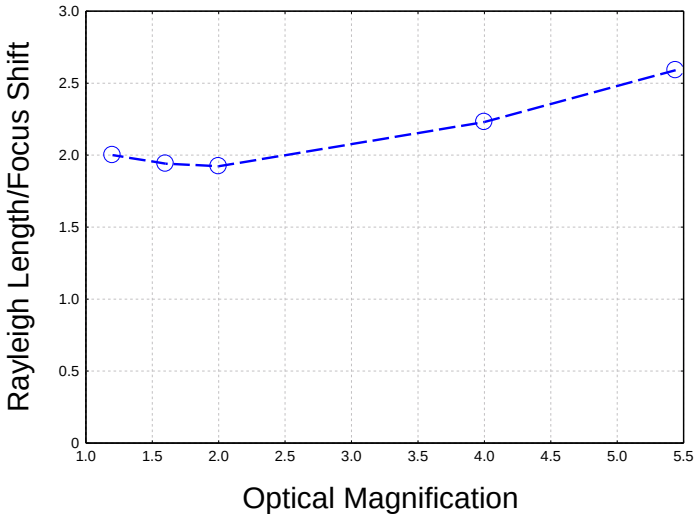

***Figure 4.9**: Ratio of Rayleigh length to focus shift as a function of optical magnification; focus shift measured after the emission time of 10 minutes with 7 kW of power.*

Another way of changing the beam diameter without affecting the optical magnification is by using different optical fibres. As shown in Fig.4.10 by changing a diameter of an optical fibre from 0.2 mm to 0.6 mm the beam diameter increased from 0.31 mm to 0.95 mm, whilst the focus shift increased only by 30%. Comparing this with Fig.4.8 shows that such a solution increases the focus shift in a much less extent than by changing the optical magnification. To get the same increase of beam diameter from 0.31 mm to 0.95 mm an optical magnification would have to increase from 1.6 to 4.8, which would lead to an increase of focus shift by a factor of 7, according to Fig.4.8.

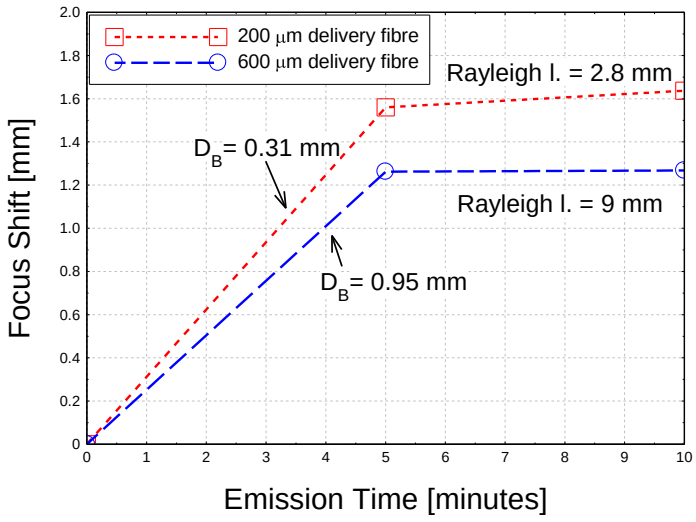

***Figure 4.10**: Focus shift as a function of emission time for different diameters of optical fibres and a constant magnification 1.6, measured at 2 kW of laser power (Nottingham laser).*

All the results presented so far were obtained with a clean optic. Comparison of a clean optic with a contaminated one is shown in Fig.4.11. The contaminated optic exhibits twice as large focus shift as the clean one for the same laser parameters. In Fig.4.12 the effect of such a focus shift on the beam diameter, at the original focal plane, is shown. The beam diameter changed by more than 32% when contaminated optic was used in comparison to an 8% diameter variation in the case of clean optic. This large increase of beam diameter corresponds to a 43% reduction in power density on the surface, which can change conditions of the laser welding significantly.

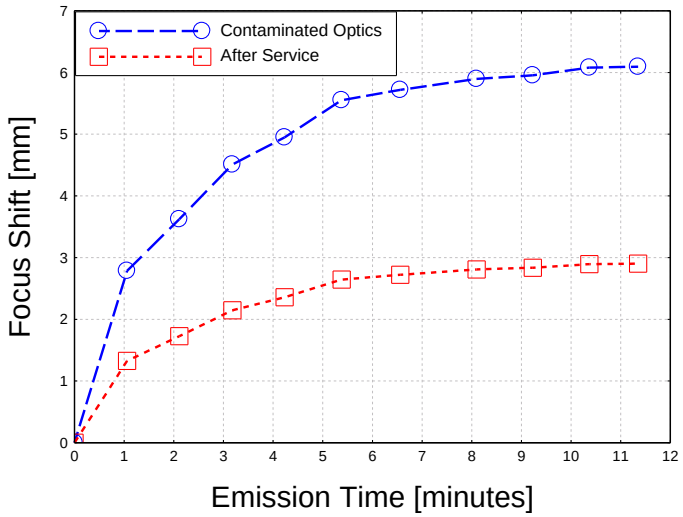

***Figure 4.11**: Effect of contamination of optics on focus shift with focusing lens F 250 mm and power of 8 kW.*

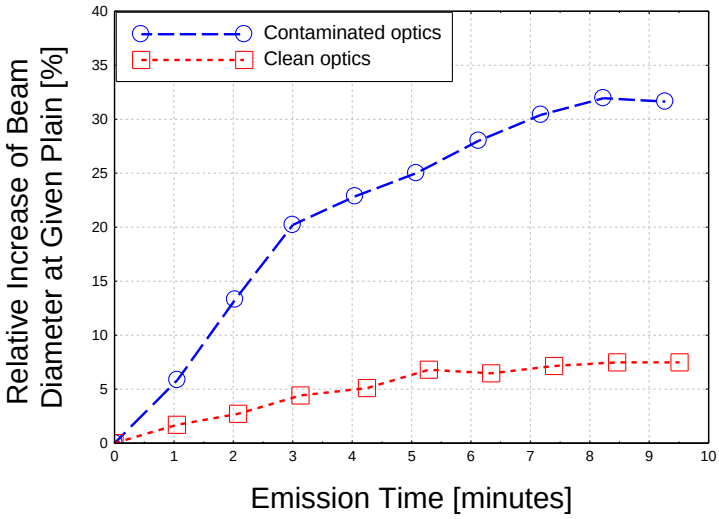

***Figure 4.12**: Effect of focus shift on relative change of beam diameter in case of contaminated and clean optics.*

Measurement of the beam properties on a regular basis can be useful in monitoring conditions of the optical components. The evolution of a maximum focus shift over time for a focusing lens with a 250 mm focal length is shown in Fig.4.13. A distinct increase of focus shift in a period from April 2008 to July 2008 is evident. As it turned out later, this was caused by contamination of a collimation lens. After the

replacement of a collimation lens and cleaning of other optical components the focus shift returned to the standard level.

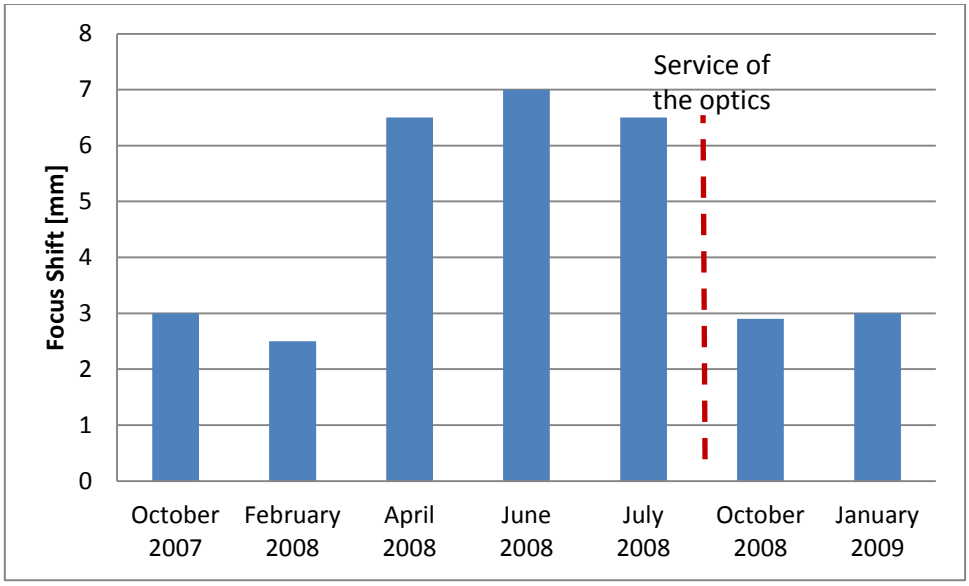

***Figure 4.13**: Evolution of focus shift over time with focusing lens F 250 mm and 8 kW of power.*

To investigate the effect of focus shift on the depth of penetration and the weld shape, long welds at two different conditions were carried out, as indicated in the methodology Section 4.3.1. The welding paths with numbers corresponding to the macrographs are shown in Fig.4.14 and Fig.4.15. The macrographs shown in Fig.4.14 indicate that the cross section with number 3 is slightly outstanding from others. However, despite this deviation, the total variation of depth of penetration does not exceed 0.5 mm. A similar variation of depth of penetration can be seen in Fig.4.15 for a greater laser power. Both figures do not reveal any systematic change of depth of penetration which would indicate the effect of focus shift.

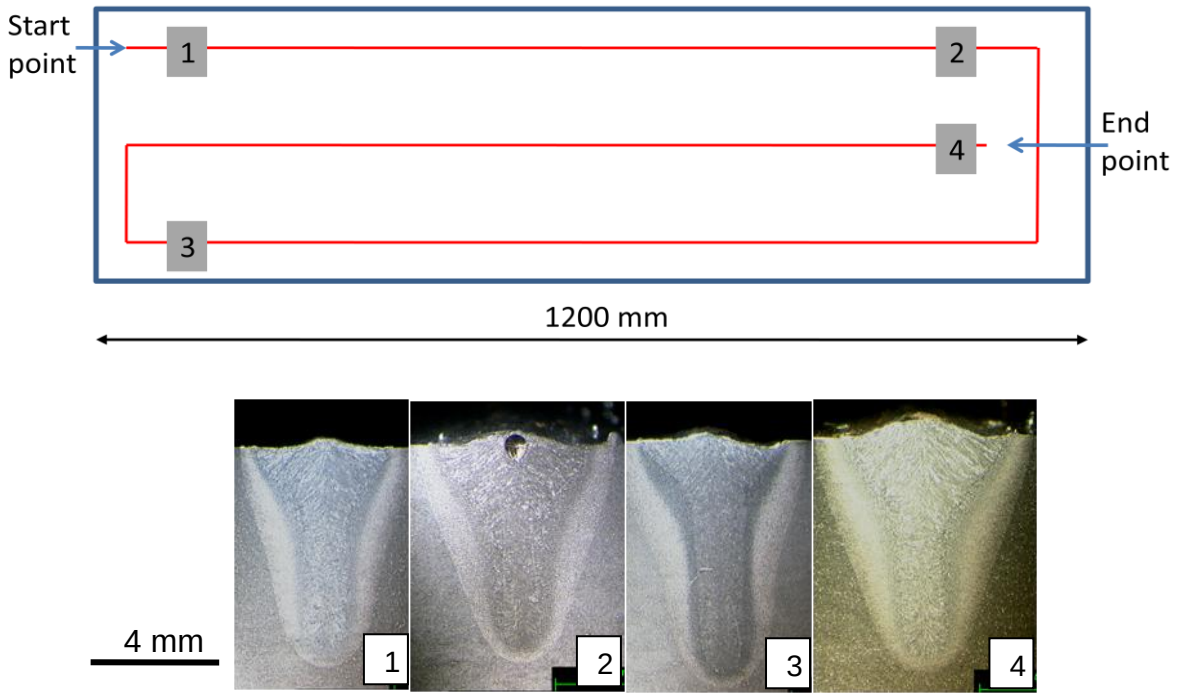

***Figure 4.14**: Welding path and macrographs form different sections of long weld achieved at 1 m min^{-1} travel speed and 5 kW of power (welding times: 1 - 3 sec; 2 – 65 sec; 3 – 137 sec; 4 – 209 sec).*

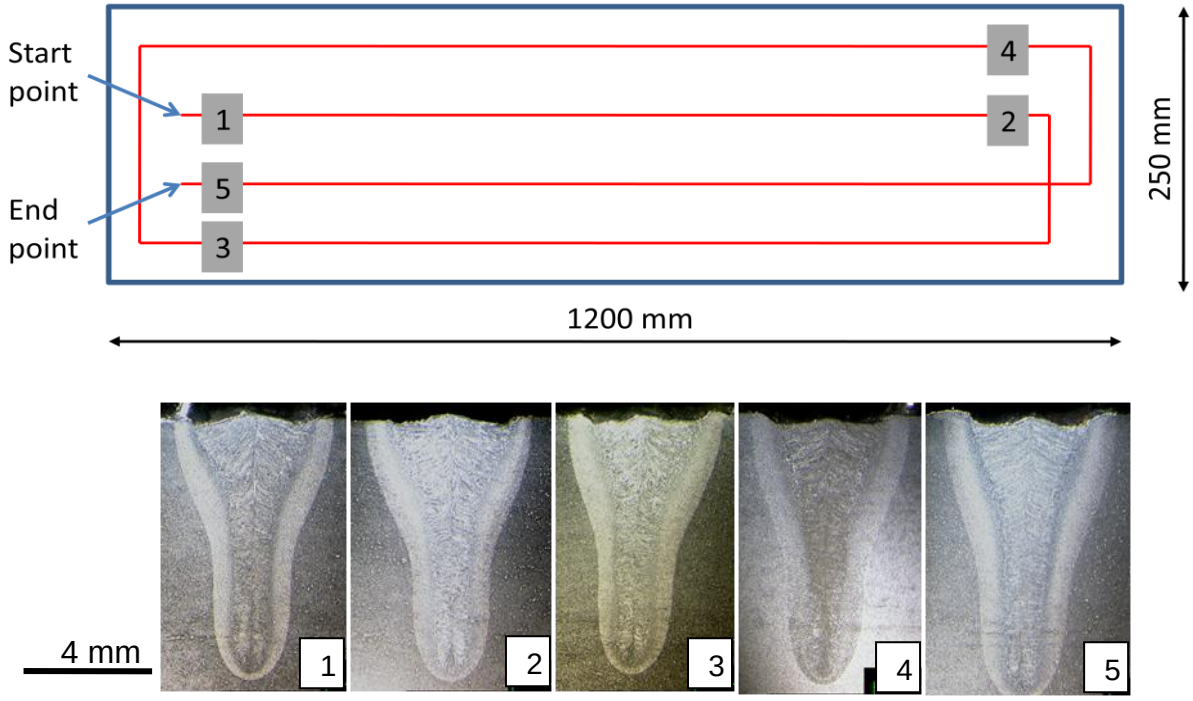

***Figure 4.15**: Welding path and macrographs form different sections of long weld achieved at 2 m min^{-1} travel speed and 8 kW of power (welding times: 1 - 2 sec; 2 – 31 sec; 3 – 66 sec; 4 – 103 sec; 5 – 140 sec).*

To distinguish the effect of focus shift from the fluctuations of keyhole the variation of depth of penetration in partially penetrated welds was examined. The longitudinal macrograph is presented in Fig.4.16. The red arrows indicate points with a maximum and a minimum depth of penetration. The corresponding transverse cross sections indicate significant variations in depth of penetration and shape between the points. The macrograph denoted as **A** taken from the point with a maximum depth of penetration exhibits much narrower bead profile in the upper part, than the same weld at the point **B**. It was found that despite the insignificant focus shift the fluctuation of depth of penetration induced by the keyhole instabilities could exceed 1 mm (approximately 10% of total depth of penetration).

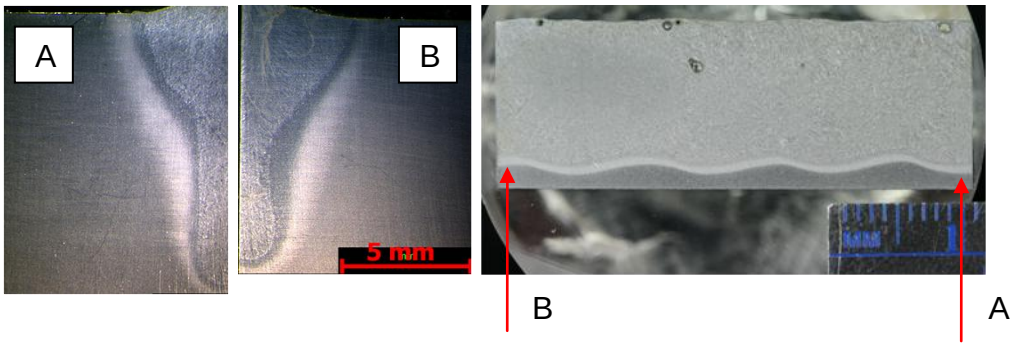

***Figure 4.16**: Effect of keyhole fluctuations on bead shape in partially penetrated weld for 1 m min^{-1} travel speed of and 8 kW power.*

4.4. Discussion

4.4.1. Laser power

Numerous experiments carried out with a power meter and a photodiode in Section 4.2 indicate high stability of the fibre laser. This was shown in Fig.4.1 to Fig.4.3 (pages 110-111). The average measured power was very close to the applied power, indicated by the control system of the laser. The small difference apparent at the maximum power could be caused by the absorption of laser beam in the optical components, on its way from the optical cavity to the workpiece. In addition the

measurements of reflected light using a photodiode (Fig.4.4 page 112) did not reveal any temporal variation of power or initial peaks.

4.4.2. Focus shift

The beam diameter along with the power is considered to be the most important property of lasers. The measurements carried out with a beam profiler indicate the focus shift. It can be concluded from Fig.4.5 and Fig.4.6 (pages 114-115) that the focus shift is dependent on the emission time, power level and the optical magnification. The saturation of the focus shift after approximately 7 minutes (Fig.4.5) implies, that after this time an equilibrium between the absorbed energy and the efficiency of cooling of the optics is reached. A similar equilibrium of focus shift after few minutes of emission time was reported in the literature [423]. The results presented in Fig.4.7 (page 115) indicate that the thermal load in the optical components propagates slowly. Thus the beam diameter increases continuously without any sudden change after increasing laser power, until the plateau is established.

The propagation of focus shift with increasing laser power, similar to that from Fig.4.6 (page 115) can cause several problems in real applications. This may lead to difficulties in specifying the effective focal point, particularly when optical heads with large optical magnifications are used. A strong dependence of focus shift with the optical magnification, which was demonstrated in Fig.4.6 and Fig.4.8 (pages 115-116) underlines the importance of appropriate selection of the optical components for a particular application. In general it is undesirable to use larger optical magnifications than two. Even though the half of depth of focus (Rayleigh length) is usually larger than the focus shift (Fig.4.9 page 116) this may no longer be the case when the optic gets contaminated.

A good way of increasing the beam diameter without affecting the focus shift significantly is by using larger optical fibres. This allows for an increase of beam diameter and depth of focus, whilst maintaining the optical magnification. It was shown in Fig.4.10 (page 117) that in such a case the focus shift increased insignificantly, as compared the case when altering the optical magnification. In Table 4.1 the combinations of different optical components and the corresponding beam

diameters with the optical magnifications used in this experiment are shown. Note that these are the real values measured by means of a beam profiler. The optical magnification below 2 is evident in both cases. In Table 4.2 various alternative ways of achieving a few, commonly used in laser welding, beam diameters and their approximate properties are shown. In this case all values are hypothetical and were achieved according to simple geometrical calculations, based on data from Table 4.1. In theory every beam diameter can be achieved by using many different combinations of the optical components. However, in reality there are many practical limitations. As shown in Table 4.2 a beam diameter of 0.3 mm can be achieved with an optical fibre having a diameter of 0.1 mm, using a long focal length focusing lens (case 1). On one hand, this gives a large processing distance between the optics and the workpiece and also a large optical depth of focus, but on the other hand, the large magnification might lead to a severe focus shift. Alternatively, the same beam diameter can be achieved using a processing fibre with a diameter of 0.3 mm (case 2). This solution leads to almost no focus shift due to the optical magnification of 1, but the relatively short focal length of this focusing lens (150 mm) makes it difficult to work with such an optical set-up, especially to protect it against spatter. Thus the best set-up for a beam diameter of 0.3 mm is to use an optical fibre with a diameter of 0.2 mm combined with a 150 mm focal length collimation lens and a 250 mm focal length focusing lens (case 3). A long focal length of a collimation lens allows for a reduction of beam diameter at the focus, but on the other hand, the diameter of the beam on the optics increases. Therefore the longer collimation lenses require optics with larger apertures. Similarly there are many options to achieve 0.6 mm beam diameter. As shown in Table 4.2 (case 6) using a small diameter optical fibre of 0.1 mm will require optics with a high optical magnification, resulting in a significant focus shift. At the same time an optical fibre with 0.6 mm diameter (case 7) will provide the best performance in terms of a low focus shift, but a relatively short focal length of the focusing lens will not provide enough working distance, required in most welding applications. Thus the best solution for 0.6 mm beam diameter is to use an optical fibre with 0.3 mm diameter, combined with a collimation lens and a focusing lens with focal lengths of 150 mm and 300 mm respectively. This will give the acceptable magnification of two and the optical depth of focus, whilst providing a long working distance between the optics and the workpiece. If the collimation unit with a focal length of 150 mm is not acceptable due to the large diameter of the optics (case 5),

shorter collimation and focusing lenses need to be used, as shown in case 4. The magnification and other properties will stay the same but the working distance will be shorter.

Summarising Table 4.2 the best solution for any beam diameter is to use an optical fibre with a diameter slightly lower than the required beam diameter on the workpiece, as shown in cases 2,4,5 and 8. This gives the best trade-off between the optical depth of focus, focus shift and working distance. However, if a short working distance between the optics and the workpiece is not a problem, than the optical fibre with a larger diameter will lead to a minimum magnification and therefore minimum focus shift, as shown in cases 3 and 7.

***Table 4.1**: Influence of diameter of processing fibre on achieved beam diameter (d) and half of depth of focus (Rayleigh length) with a constant optical set-up.*

D_{fibre} (mm)	$F_{collimation\ lens}$ (mm)	$F_{focusing\ lens}$ (mm)	Θ (mrad)	d (mm)	Rayleigh l. (mm)	Optical magnification
0.2	125	200	107	0.31	2.8	1.6
0.6	125	200	105	0.95	9	1.6

***Table 4.2**: Recommended optical set-ups for the following beam diameters: 0.3 mm, 0.6 mm and 1 mm, with assumption of θ=170 mrad divergence angle of out-coming beam from fibre.*

Case	D_{fibre} (mm)	$F_{collimation\ lens}$ (mm)	$D_{on\ lens}$ (mm)	$F_{focusing\ lens}$ (mm)	d (mm)	Rayleigh l. (mm)	Optical magnification
1	0.1	100	17	300	~0.3	5.4	3
2	0.2	150	26	250	~0.3	3.3	1.66
3	0.3	150	26	150	0.3	1.8	1
4	0.3	125	22	250	0.6	7.2	2
5	0.3	150	26	300	0.6	7.2	2
6	0.2	125	22	400	0.6	12	3.2
7	0.6	150	26	150	0.6	3.6	1
8	0.6	150	26	250	1	10	1.66

The lack of cleanness of the optics can have a detrimental effect on the focus shift. It was shown in Fig.4.11 (page 118) that the maximum value of focus shift was doubled in the case of contaminated optics, as compared to its normal state. It was shown further in Fig.4.12 (page 118) that such a change of focus position by 6 mm resulted in an increase of beam diameter on the surface of workpiece by 30%, which is equivalent to a decrease of power density by approximately 40%. Therefore, it is good practice to monitor properties of a laser on a regular basis. An example was shown in Fig.4.13 (page 119). This can help in detecting some abnormal behaviour of the laser system.

4.4.3. Effect of focus shift on depth of penetration

The experimental work carried out in Section 4.3 indicates that the effect of focus shift on depth of penetration is negligible. The variation of depth of penetration in Fig.4.14 and Fig.4.15 (page 120) did not exceed 0.5 mm. Although initially the macrograph number 3 in Fig.4.14 could suggest the focus shift effect, but there was no evidence of a systematic change of depth of penetration with the welding time, which would indicate the effect of focus shift. This variation of depth of penetration is likely to be caused by the instabilities of keyhole. It was shown in Fig.4.16 (page 121) that the fluctuations of keyhole can influence the weld shape and the depth of penetration. As the keyhole is translated in the welding direction it experiences continuous alteration in shape, which leads to a non-uniform depth of penetration. At these particular conditions the variations of depth of penetration exceeding 1 mm were found. It can be also deducted from Fig.4.16 that these fluctuations can affect the shape of the weld. This implies that the natural fluctuations of the keyhole can be mistaken with the focus shift effect. Also the effect of preheating due to the long welding time of the same workpiece cannot be excluded. Although the welds in Fig.4.14 and Fig.4.15 were carried out on special paths to exclude the effect of distortion, but some differences could also result from the effect of heat build-up. However, the fact that the depth of penetration changed randomly in Fig.4.14 and Fig.4.15, rather than increasing systematically indicates the influence of keyhole fluctuations.

Although it was shown in Section 4.3 that the effect of focus shift on the depth of penetration in laser welding is negligible, but according to the literature [42], severe focus shift may change the welding conditions during the processing when using contaminated optics or incorrectly selected optical set-up. The reason that in this experimental work no effect of focus shift on welding conditions was found is due to the large depth of focus. It was shown in Fig.4.9 (page 116) that for all the optical set-ups the Rayleigh length (half depth of focus) exceeded the focus shift. This underlines the benefits of using optical set-ups with low optical magnifications. However, the situation can change dramatically when any optical components get contaminated or damaged. The problem can also become more significant with much more powerful laser sources than these used in this study.

Chapter 5. Laser material interaction parameters (LMIP) in laser welding

This chapter includes investigation of basic laser material interaction parameters in laser welding to find, which parameters control the depth of penetration and the weld width in keyhole laser welding. The effect of beam diameter for different combinations of parameters, including constant power and travel speed or constant power density and interaction time is studied. The experimental depth of focus is compared with the optical definition described by the Rayleigh length. In the final part in Section 5.8 the influence of divergence angle of a laser beam on the depth of penetration is studied.

5.1. Basic laser material interaction parameters

Every heat process can be characterised uniquely by basic parameters, which relate to the fundamental interactions between the heat source and the workpiece. However, in reality these basic parameters are incorporated into the system parameters of a particular machine, which are directly controlled by the user. The effect of system parameters on the material in laser processing is demonstrated in Fig.5.1. There are many complex factors and their interactions between the system parameters set on a given welding system and the response in the workpiece. Therefore it is desired to find basic parameters which control the laser welding in order to understand it.

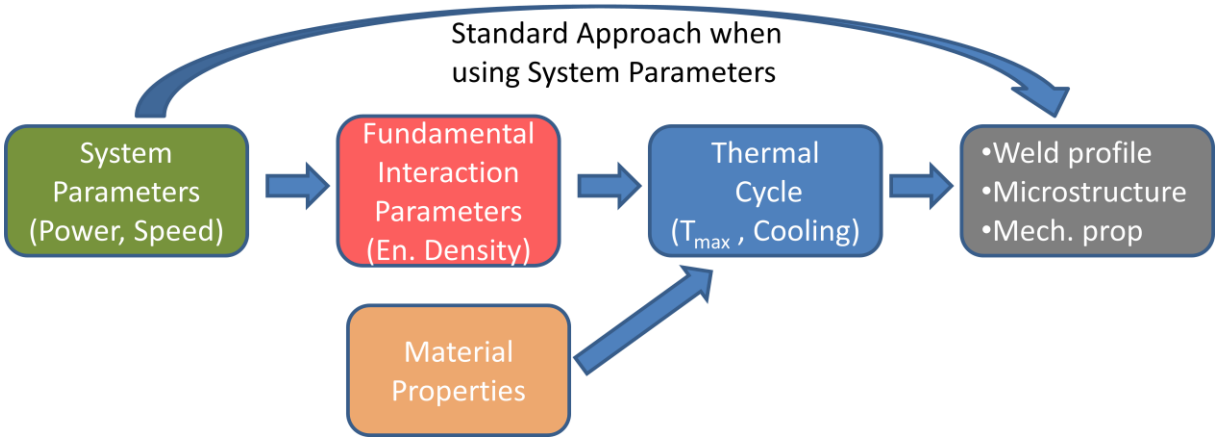

***Figure 5.1**: Effect of parameters on interaction with material.*

On the processing maps (Fig.5.2), various laser processes can be distinguished according to the power density and the interaction time, the product of which is the energy density. This figure, however, ignores the effect of size of the heat source on the surface.

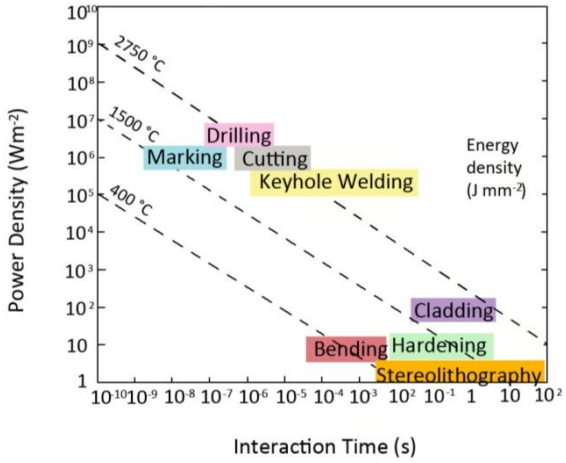

***Figure 5.2**: Processing map based on power density and interaction time; after [298, 300].*

Interaction of a laser beam with a workpiece is determined by the power density, time of irradiation and the size and shape of the heat source. For a laser beam with a top-hat energy distribution, the average power density q_P is defined as the ratio of the laser power P_L to the area of laser spot on the surface A_S, which is given by Equation 5.1.

$$q_P = \frac{P_L}{A_S} \ [Wm^{-2}] \qquad 5.1$$

Interaction time defines the time, in which a particular point is exposed to the laser beam, whilst the beam is moving with a constant speed, as indicated in Fig.5.3. This is similar to the pulse duration from pulsed laser welding. Considering a point in the weld centre line, the interaction time τ_i in case of a circular beam with a diameter **d**, which travels with a welding speed **v** is given by Equation 5.2. This definition defines the maximum interaction time in the weld centreline. In reality the interaction time may vary across the weld centre line, due to the reduction of beam length as we move from the weld centreline, unless a square or a rectangular beam is used or in case of spot welding with a stationary beam.

$$\tau_i = \frac{d}{v} \ [s] \qquad 5.2$$

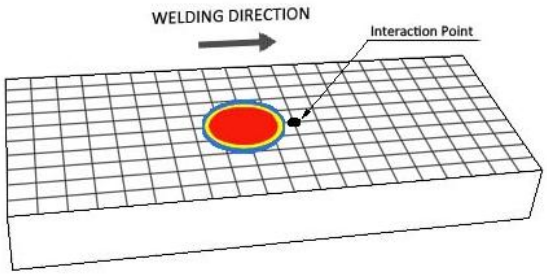

***Figure 5.3**: Interaction of laser beam with workpiece.*

To uniquely characterise the laser processing a third parameter is necessary. This is due to the fact that the same energy density (product of power density and interaction time) applied on different beam sizes on the surface will result in different energies delivered to the workpiece. If the laser welding is considered as a periodic process, whose period is the interaction time, the energy delivered to the laser spot, denoted as the specific point energy E_{SP} is proportional to the product of power density q_p, interaction time τ_i and the area of laser spot on the surface A_S, which also corresponds to the product of absorbed laser power P_L and interaction time τ_i and is given by Equation 5.3.

$$E_{SP} = q_P \cdot \tau_i \cdot A_S = P_L \cdot \tau_i = \frac{P_L \cdot d}{v} \ [J] \qquad 5.3$$

This simple definition of the specific point energy assumes a constant interaction time across the weld centreline in the transverse direction to welding and a uniform intensity distribution, which is only fulfilled in case of square or rectangular top-hat beams. However, this assumption is relevant for relatively small beam diameters on the surface, which are commonly used in laser welding.

5.2. Experimental procedure

The experimental set-up and specifications of the laser are shown in Chapter 3. In this case beam diameters ranging from 0.38 mm to 0.78 mm were used. Different beam diameters were achieved by using different focusing lenses. All welds were performed at the focal point on the surface, unless otherwise stated. The welds were sectioned, polished and examined under an optical microscope in order to measure the depth of penetration. Parameters were chosen to ensure only the keyhole regime to exclude the effect of changing absorption, which occurs near the conduction regime. Most of the welds were made in 12 mm thick S355 low carbon steel. Some additional trials were carried out in additional materials: 7075 aluminium and 304 stainless steel, both with 12 mm thickness.

5.3. Interaction parameters at constant beam diameter

5.3.1. Methodology

The effect of power density and interaction time on the depth of penetration was studied. The power density was varied by changing the laser power in a range from 2 kW to 8 kW, whilst the interaction time was varied by changing the travel speed from 0.3 m/min to 15 m/min, according to Equations 5.1 and 5.2. In all cases a constant beam diameter of 0.63 mm was used.

5.3.2. Results

The effect of laser power and travel speed on the depth of penetration at a constant beam diameter of 0.63 mm is shown in Fig.5.4. Whilst the effect of power density and interaction time on the depth of penetration at a constant beam diameter is shown in Fig.5.5. The data in Fig.5.5 represent the same results as in Fig.5.4 but recalculated with respect to the power density and the interaction time, according to Equations 5.1 and 5.2.

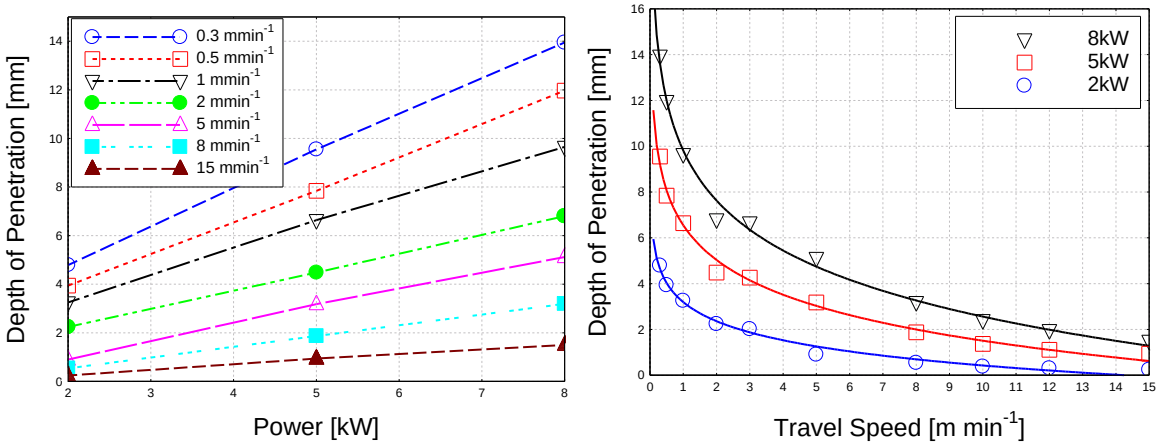

***Figure 5.4**: Depth of penetration as a function of: **a)** laser power for different travel speeds; **b)** travel speed for three levels of power; constant beam diameter of 0.63 mm in both cases.*

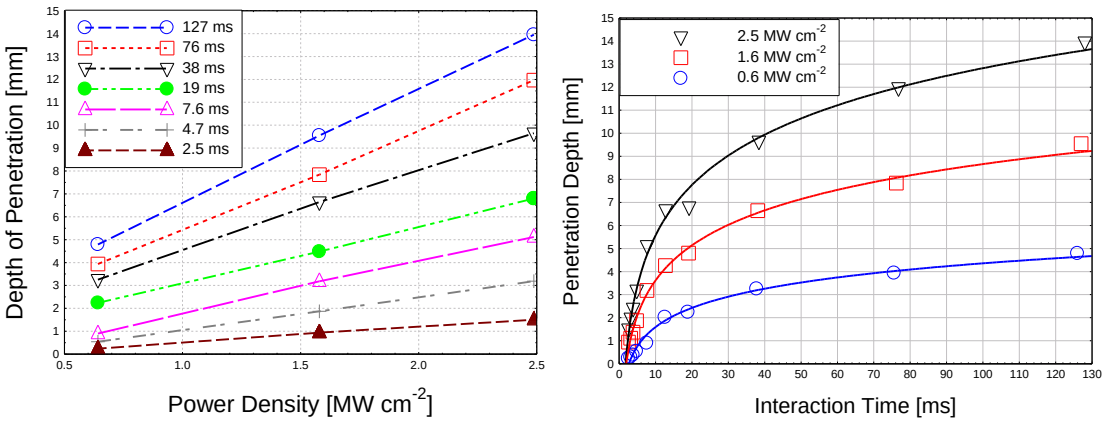

***Figure 5.5**: Depth of penetration as a function of: **a)** power density for different interaction times; **b)** interaction time for three levels of power density; constant beam diameter of 0.63 mm in both cases.*

A linear dependence of power density on the depth of penetration, where the slope is dependent on interaction time, can be observed in Fig.5.5(a). In contrast there is a logarithmic dependence on the interaction time which is shown in Fig.5.5(b), suggesting different effects in different operating regimes. Initially the slope of the curve is very high; indicating that the interaction time has a strong effect on the depth of penetration. When the interaction time is large, its effect is smaller with penetration being primarily dependent on the power density.

5.4. Effect of specific point energy

5.4.1. Methodology

Since the previous experiment was carried out at a constant beam diameter it was necessary to investigate if constant power density and interaction time provide the same depth of penetration, independent of the beam diameter. In this case the power density and the interaction time were kept constant, whilst the specific point energy was varied by changing the beam diameter. This was achieved by adjusting the laser power and the travel speed to a given beam diameter, according to Equations 5.1 and 5.2. Considering the power limit of the laser used here, a medium power density of 1.6 MW/cm^2 was selected. This enabled us to investigate this power density on four beam diameters in a range from 0.38 mm to 0.78 mm.

Furthermore, the effect was investigated at different levels of power density and a constant interaction time. The power densities were used as follows: 1.6 MW/cm^2, 1 MW/cm^2 and 0.5 MW/cm^2. To ensure the keyhole regime a long interaction time of 38 ms was used.

5.4.2. Results

The effect of beam diameter on depth of penetration at a power density of 1.6 MW/cm^2 and different interaction times is shown in Fig.5.6. The depth of penetration increases with increasing beam diameter, which is the opposite to that observed when changing the beam diameter at a constant power and travel speed [22, 63]. In

addition there is a dependence of interaction time on the rate of increase of depth of penetration. The longer the interaction time the higher the rate of increase of depth of penetration.

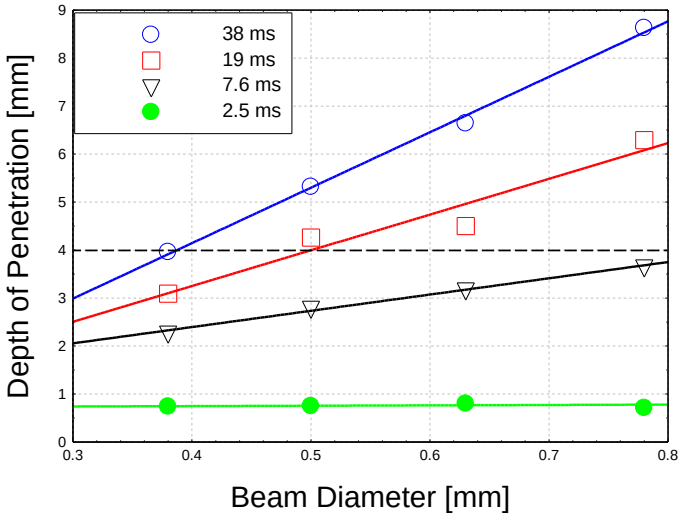

***Figure 5.6**: Effect of beam diameter and interaction time on depth of penetration at 1.6 MW cm^{-2} power density.*

The effect of beam diameter on the depth of penetration at a constant interaction time of 38 ms and three levels of power density is presented in Fig.5.7. In all cases the depth of penetration increases steadily with increasing beam diameter.

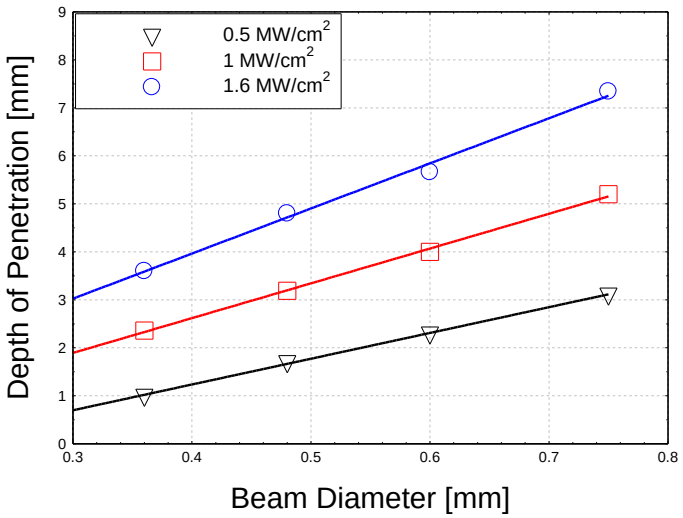

***Figure 5.7**: Effect of beam diameter and power density on depth of penetration at 38 ms interaction time.*

5.5. Parameters controlling depth of penetration

A constant power density and interaction time do not provide a constant depth of penetration when varying the beam diameter, due to the change in specific point energy. However, a closer analysis of Fig.5.6 reveals that some points in this graph have similar depths of penetration, as indicated by a horizontal dashed line, despite the significant difference in the interaction times. It was found that all the points with the similar depths of penetration also had similar specific point energies. Since the power density in Fig.5.6 was also constant, an additional test was carried out. The effect of interaction time on the depth of penetration at constant power density and specific point energy was investigated.

5.5.1. Methodology

In this experiment the power density and the specific point energy were maintained constant whilst the beam diameter was varied. This means that the laser power and the travel speed were adjusted with respect to the beam diameter, according to Equations 5.1 and 5.3. The tests were carried out at two levels of power density of 1.6 MW/cm^2 and 2.6 MW/cm^2 respectively and three levels of specific point energy of 34 J, 60 J and 95 J.

5.5.2. Results

Macrographs for 1.6 MW/cm^2 power density are shown in Fig.5.8. They reveal that the depths of penetration are the same within the experimental error. In Fig.5.9 macrographs for 60 J specific point energy and 2.6 MW/cm^2 power density also show equal depths of penetration. Note the large variation of power and travel speed in the example shown in Fig.5.8. The widths of the welds are determined by the interaction time. The same trend is shown for other values of specific point energy in Fig.5.10 and Fig.5.11.

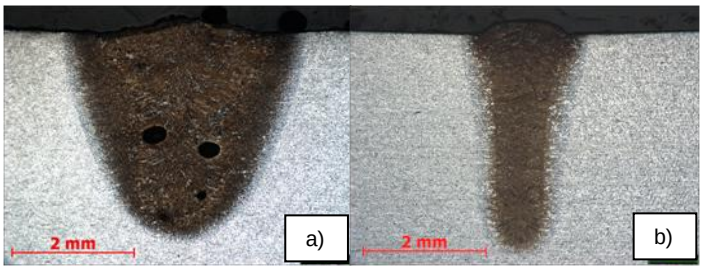

***Figure 5.8**: Macrographs at constant power density of 1.6 MWcm^{-2} and specific point energy of 60 J: **a)** interaction time of 38 ms (P_L = 1.8 kW, v = 0.68 m min^{-1}, d = 0.38 mm); **b)** interaction time of 8 ms (P_L = 7.6 kW, v = 5.9 m min^{-1}, d = 0.78 mm).*

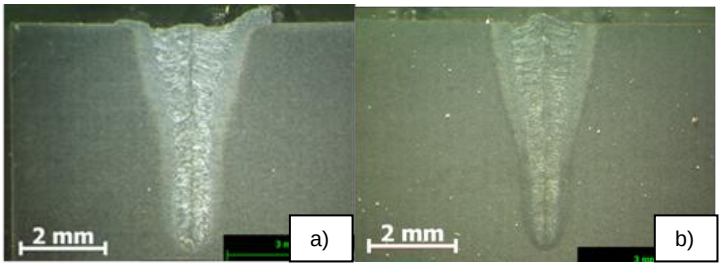

***Figure 5.9**: Macrographs at constant power density of 2.6 MWcm^{-2} and specific point energy of 60 J: **a)** interaction time of 12 ms (P_L = 5 kW, v = 2.5 m min^{-1}, d = 0.5 mm); **b)** interaction time of 7.6 ms (P_L = 8 kW, v = 5 m min^{-1}, d = 0.63 mm).*

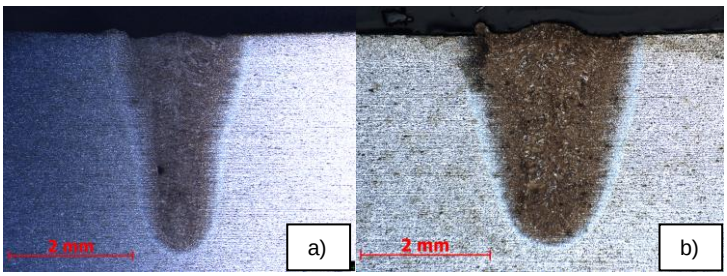

***Figure 5.10**: Macrographs at constant power density of 1.6 MWcm^{-2} and specific point energy of 34 J: **a)** interaction time of 11 ms (P_L = 3.14 kW, v = 2.75 m min^{-1}, d = 0.5 mm); **b)** interaction time of 19 ms (P_L = 1.82 kW, v = 1.2 m min^{-1}, d = 0.38 mm).*

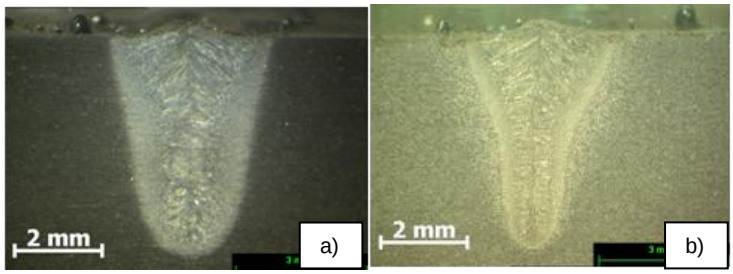

***Figure 5.11**: Macrographs at constant power density of 1.6 MWcm^{-2} and specific point energy of 95 J: **a)** interaction time of 30 ms (P_L = 3.14 kW, v = 1 m min^{-1}, d = 0.5 mm); **b)** interaction time of 19 ms (P_L = 5 kW, v = 2 m min^{-1}, d = 0.63 mm).*

5.6. Comparison of different materials

The rate of increase of depth of penetration with the beam diameter in Fig.5.6 is strongly dependent on the interaction time. To investigate the effect of heat conduction on this behaviour, additional experiments on different materials, having different thermal properties, were carried out.

5.6.1. Methodology

The same experiment as in Section 5.4 was replicated in 304 stainless steel and 7075 aluminium alloy. The laser power and travel speed were adjusted to the beam diameter to maintain the power density and the interaction time constant, whilst the beam diameter was varied, according to Equations 5.1 and 5.2. All tests were carried out at a constant power density of 1.6 MW cm^{-2}. The results were compared with those achieved in low carbon steel.

Additionally, calculations of the recoil pressure acting on the top surfaces of the materials, based on their surface temperatures, were carried out. All the relevant equations, as well as the material properties and laser parameters are presented in Appendix I (Table I.1 and Table I.2). The surface temperatures were approximated by the analytical solution of heat equation proposed by Ashby [305], shown in Appendix II. In all cases constant laser parameters were maintained to enable for the investigation of the effect of material thermal properties on the depth of penetration. The pressure acting on the top surface, due to evaporation, was calculated based on few commonly available hypotheses, given by different authors.

5.6.2. Results

The effect of beam diameter on the depth of penetration in stainless steel, at a constant power density of 1.6 MW cm^{-2} and different interaction times, is shown in Fig.5.12. The main behaviour is similar to that observed in low carbon steel shown in Fig.5.6. The depth of penetration also increases with increasing beam diameter. The same trend is apparent in aluminium, as shown in Fig.5.13. Macrographs shown in Fig.5.14 reveal significant differences in depths of penetration and melting rates

between the materials. For the same welding conditions, aluminium alloy exhibits the greatest depth of penetration and melting rate among the materials. The narrowest weld profile is achieved in stainless steel. In contrast, when the same intensity of 1.6 MW cm^{-2} is applied, but using a smaller beam diameter of 0.38 mm, aluminium sample exhibits the lowest depth of penetration among the alloys, as shown in Fig.5.15. Note that the welds in stainless steel and aluminium in Fig.5.14 and Fig.5.15 are tilted due to a 5º inclination angle of the laser beam, as shown in Chapter 3, but this was taken into account during the measurement of depth of penetration.

The slopes in Fig.5.6, Fig.5.12 and Fig.5.13 exhibit different values for the same interaction times. For all conditions the highest slope is apparent in aluminium, whilst the lowest in low carbon steel.

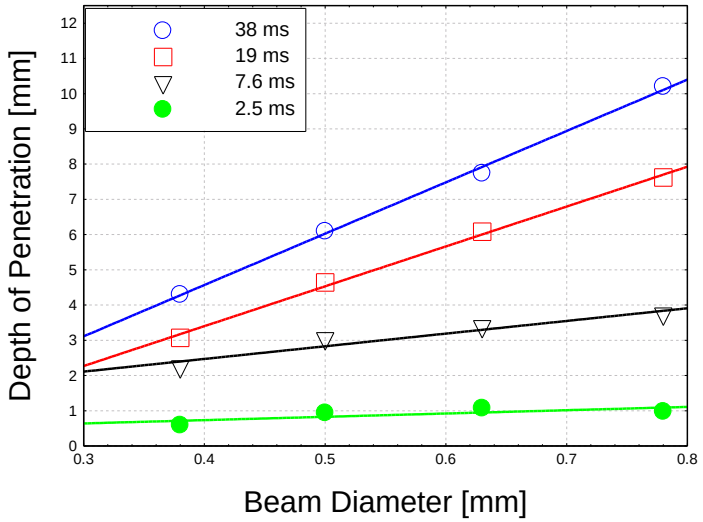

***Figure 5.12**: Effect of beam diameter and interaction time on depth of penetration in 304 stainless steel at 1.6 MW cm^{-2} power density.*

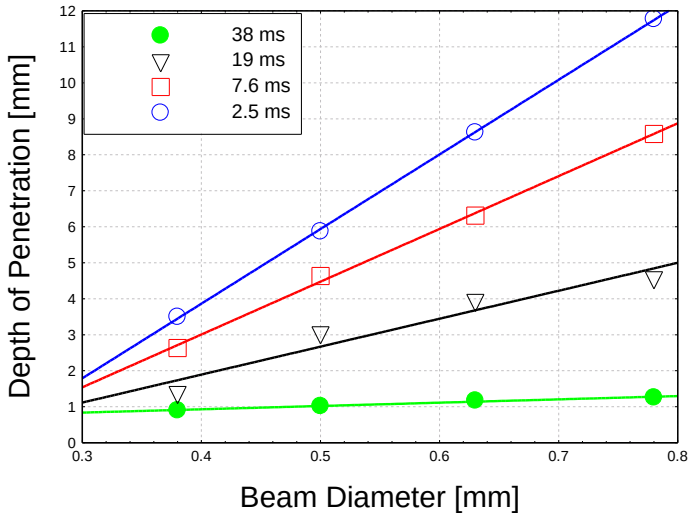

***Figure 5.13**: Effect of beam diameter and interaction time on depth of penetration in 7075 aluminium at 1.6 MW cm^{-2} power density.*

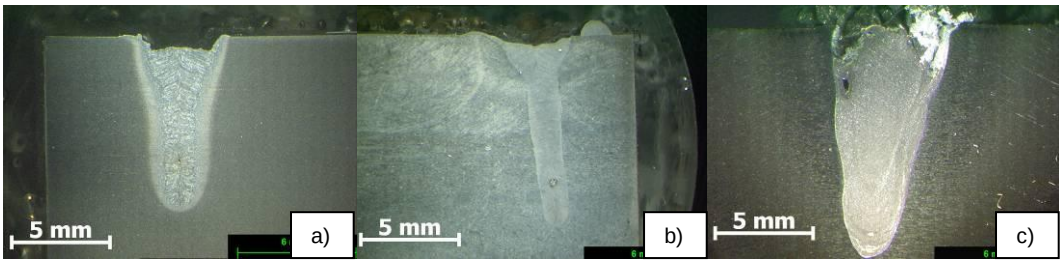

***Figure 5.14**: Macrographs for constant power density of 1.6MW, interaction time of 38 ms and beam diameter of 0.78 mm for three different materials: **a)** S355 mild steel; **b)** 304 stainless steel; **c)** 7075 aluminium.*

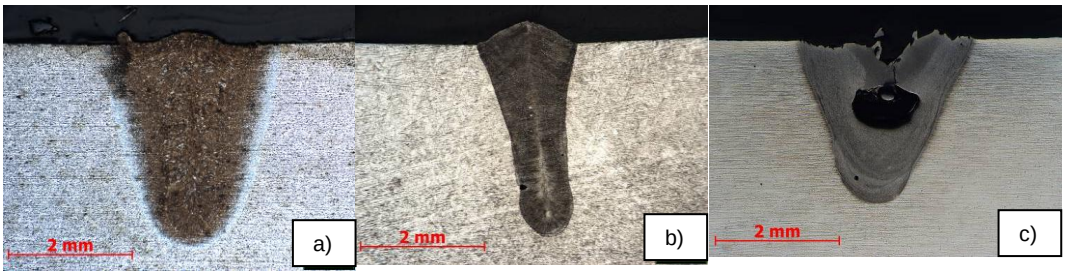

***Figure 5.15**: Macrographs for constant power density of 1.6MW, interaction time of 19 ms and beam diameter of 0.38 mm for three different materials: **a)** S355 mild steel; **b)** 304 stainless steel; **c)** 7075 aluminium.*

The comparison of surface temperatures and recoil pressures between the materials, according to various hypotheses, is shown in Fig.5.16. The highest temperature is reached in stainless steel and the lowest in aluminium. The calculated recoil pressures vary significantly depending on the applied hypothesis. In general, the highest recoil pressure acts on the surface of stainless steel, whilst aluminium experiences the lowest pressure, among all shown materials.

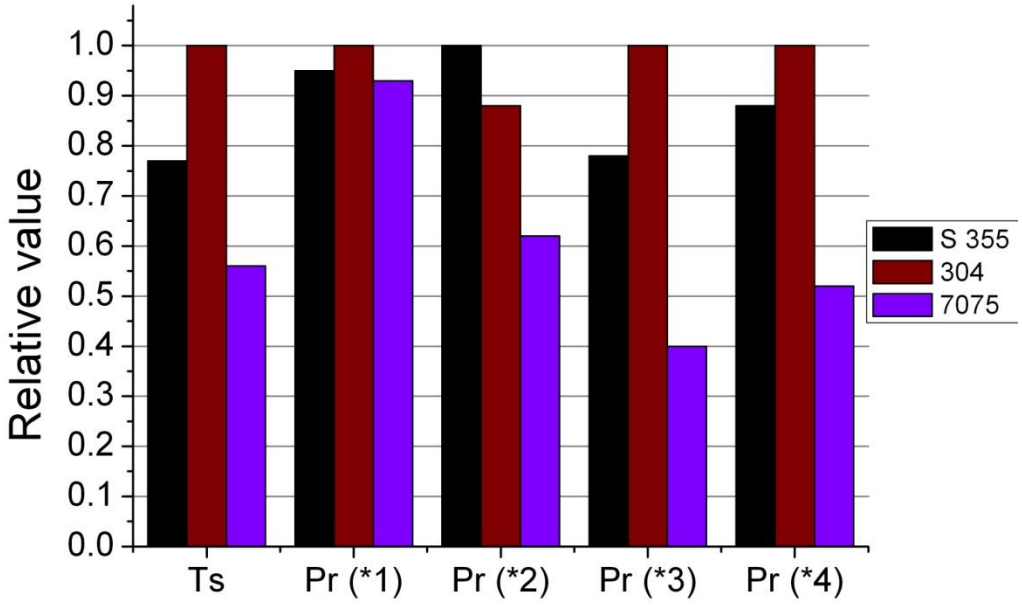

Figure 5.16: *Comparison of temperature (Ts) and pressure acting on surface of different materials: S 355 low carbon steel, 304 stainless steel and 7075 aluminium alloy at constant welding conditions (see Appendix I); calculations according to various analytical equations: p_r (*1) – von Allmen [307], p_r (*2) – Semak and Matsunawa [194], p_r (*3) – Anisimov [424], p_r (*4) – Chen [209]*

5.7. Depth of focus

A large depth of focus is observed in many CW laser welding situations. This observed depth of focus is usually much greater than might be expected by considering the variation of power density with beam diameter. Therefore, in order to investigate this effect in terms of laser material interaction parameters, the

experiment with a defocused beam is carried out. This experimental depth of focus is compared with the optical one. The Rayleigh length is commonly used as a definition of depth of focus and is equal to the distance between the focal point and a point at which the beam diameter increases by the root square of two. This will be analysed in terms of power density.

5.7.1. Methodology

To measure the experimental depth of focus a focusing lens with a 250 mm focal length was used. All welds were made at a constant laser power of 5 kW and three travel speeds: 0.75 m/min, 2 m/min and 5 m/min. The laser beam was defocused up to 10 mm in negative and positive direction for all three travel speeds. This distance resulted in a variation of beam diameter from 0.63 mm at the focal point to 1.25 mm at the maximum out of focus plane. The positive and negative directions of defocusing correspond to the focal point placed above and below the surface respectively.

According to the measured beam profile of our system the Rayleigh length of this optical set up was ± 5.6 mm. One Rayleigh length corresponds to the drop of power density by a factor of two. The effect of power density on the depth of penetration was examined by changing the power density by a factor of two. Two different cases were compared. In the first case, the power density was changed by varying the laser power at a constant beam diameter of 0.63 mm and travel speed of 2 m/min. The power was changed from 1 kW to 8 kW with 1 kW intervals. In the second case, the power density was varied by defocusing the beam at a constant power of 5 kW and travel speed of 2 m/min.

5.7.2. Results

The experimental depth of focus of this optical set-up (F250 mm focusing lens) is shown in Fig.5.17. The Rayleigh length measured by a beam profiler for this optics was ±5.6 mm. It can be seen in Fig.5.17 that if the beam is defocused by approximately one Rayleigh length, in case of a travel speed of 2 m/min, the depth of penetration decreases by 10%, as compared to the focal point. This depth of focus is

indicated by the dashed lines in Fig.5.17. In laser macro-welding applications a practical depth of focus is often defined by a maximum acceptable variation of depth of penetration. If we assume this 10% reduction of the depth of penetration, as being the experimental depth of focus, the other values for other travel speed from Fig.5.17 will be the following: ±8 mm and ±4 mm, as shown in Table 5.1.

The polynomials in Fig.5.17 are predicted values based on the variation of power density and specific point energy with the beam diameter, which will be highlighted in the discussion in Section 5.9.2

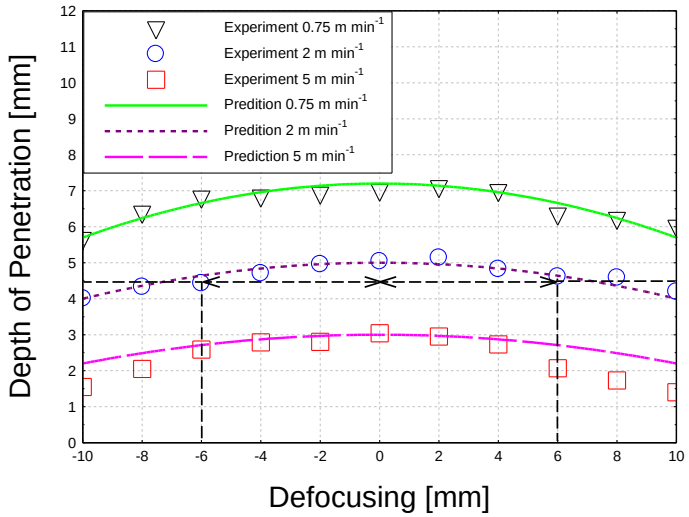

***Figure 5.17**: Comparison of experimental depth of focus with that predicted theoretically from variation of power density and specific point energy (see Fig.5.29 page 156); for F 250 mm focusing lens.*

***Table 5.1**: Comparison of experimental depth of focus (Exp DOF) with Rayleigh length (Rayleigh DOF) as well as calculated according to power density (q_P DOF).*

Travel Speed (m/min)	Rayleigh length DOF (mm)	Experimental DOF (mm)	Power density DOF (mm)
0.75	±5.6	±8	±2
2	±5.6	±6	±2
5	±5.6	±4	±2

The experimental depth of focus for 2 m/min travel speed from Fig.5.17 is plotted in Fig.5.18 as a function of power density. In the case of defocusing the power density was changed by varying the beam diameter at a constant laser power of 5 kW. Also in the same figure the depth of penetration as a function of power density, but changed by varying the laser power at a constant beam diameter of 0.63 mm is compared. It can be seen that the reduction of power density by a factor of two (one Rayleigh length), in case of defocused beam, results in a decrease of depth of penetration by only 10%. In contrast, the same change of power density at a constant beam diameter results in a decrease of depth of penetration by a factor of two. Thus in order to achieve the 10% reduction of depth of penetration in this case, the power density can only decrease by 0.2 MW/cm^2. For this optical set-up this would correspond to the change of focus position by ±2 mm. Thus the effect of power density on depth of penetration is strongly dependent on other parameters i.e. either the beam diameter or laser power is kept constant when changing the power density.

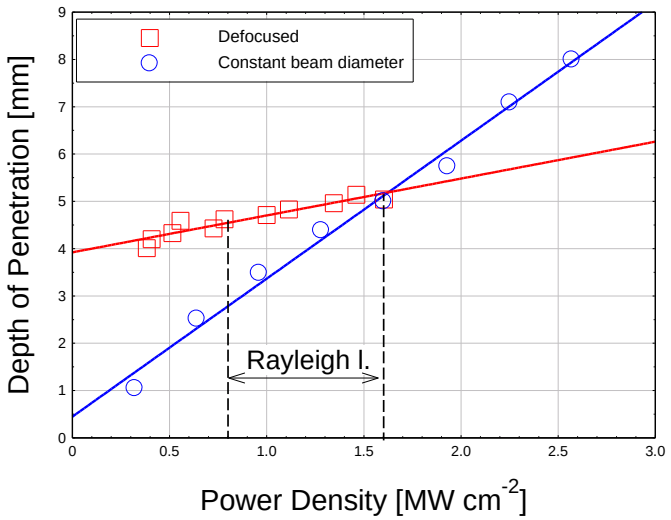

***Figure 5.18**: Effect of reduction of power density on depth of penetration in case of defocused beam (5 kW, 2 m min^{-1}) and at constant beam diameter of 0.63 mm (variation of power); for F250 focusing lens.*

All results from the evaluation of depth of focus are compared in Table 5.1. It can be seen that the depth of focus varies with the travel speed. Only at 2 m/min travel speed the depth of focus matched the Rayleigh length. In addition in all the

presented cases the experimental depth of focus was much greater than the depth of focus expected from the variation of power density only.

5.8. Effect of divergence angle

In all experiments presented in this chapter different beam diameters were achieved by applying a range of focusing lenses. This solution has some advantages, such as maintaining a constant intensity distribution. However, the modifications of the optical set-up resulted in changing of the Rayleigh length and the divergence angle along with the beam diameter. To investigate the effect of divergence angle on the depth of penetration and the weld shape, different optical set-ups, providing the same beam diameter on the surface were used.

5.8.1. Methodology

The first experiment included a comparison of welding performance of two focusing lenses with a significant difference in the divergence angles. This was achieved by comparing the experimental depth of focus between a focusing lens with a focal length of 150 mm and a focusing lens with a focal length of 300 mm. According to the beam profiler the Rayleigh lengths of these set-ups were ±2 mm and ±8 mm respectively. A series of welds at a constant power of 5 kW and travel speed of 2 m/min was carried out with both lenses. The laser beam was defocused up to 10 mm in the positive and negative directions. This distance resulted in a variation of beam diameter from 0.38 mm at the focal point to approximately 1.9 mm at the maximum out of focus plane for the short focal length lens (F150 mm). The same defocusing distance, in the case of long focal length lens (F300 mm), resulted in a change of beam diameter from 0.78 mm to 1.25 mm. Positive and negative directions of defocusing correspond to the focal point placed above and below the surface.

To investigate the effect of power density on the depth of penetration and to compare the Rayleigh length with the experimental depth of focus, an analogous experiment

as in Fig.5.17 was performed. In the first case, the power density was changed by defocusing the laser beam at a constant power of 5 kW and travel speed of 2 m/min. In the second case, the power density was changed by varying the laser power from 1 kW to 8 kW with constant beam diameters. Both focusing lenses were investigated in this way.

In the second experiment, two lenses with different focal length were used for bead-on-plate welding, in such a way to achieve the same beam diameter on the surface. This was realised by using a focusing lens with a longer focal length in the focal point and compared with a lens having a shorter focal length appropriately defocused. Two cases were considered as shown in Table 5.2. In the first case, lenses with focal lengths of F200 mm and F150 mm were compared. The first lens (F200) was used in the focal point, whilst the lens F150 mm was defocused by 2 mm in the positive and then in the negative direction. The beam diameters achieved with both focusing lenses were 0.5 mm. This enabled comparison of welding conditions with different divergence angles for the same beam diameter. In the second case, lenses with focal lengths of F300 mm and F150 mm were compared. The first lens (F300) was used in the focal point, whilst the lens F150 mm this time was defocused by 4 mm in both directions, to achieve 0.78 mm beam diameter. Then the depths of penetration and the shapes of the welds were compared.

5.8.2. Results

The experimental depths of focus of both focusing lenses are compared in Fig.5.19. It can be seen that initially in the proximity of the focal points, the lens with a shorter focal length (F150) exhibits a greater depth of penetration. However, at a certain point of defocusing the depth of penetration of the lens with a longer focal length (F300) exceeds the other one. The lens with a longer focal length exhibits more stable depth of penetration in the entire range of defocusing.

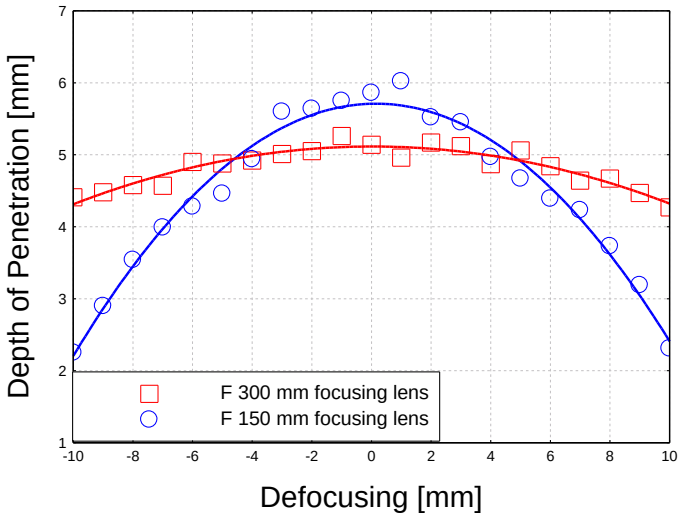

***Figure 5.19**: Comparison of experimental depths of focus achieved with different focusing lenses, F150 and F300.*

In Fig.5.20 the depth of penetration as a function of power density of two different focusing lenses is compared. In both cases the variation of power density by changing the laser power at constant beam diameters results in a more rapid change of depth of penetration than when varying the power density by defocusing. It can be seen that the depth of penetration of the lens with a longer focal length (F300 mm) reduces steadily in the whole range of defocusing. In contrast, the lens with a shorter focal length (F150 mm) exhibits a steady reduction of depth of penetration only at the initial stage of defocusing and then the depth rapidly drops after a certain point. Note that for the same defocusing distance of 10 mm from the focal point, the lens F300 mm was defocused by only one Rayleigh range, whilst the lens F150 mm was defocused by 5 Rayleigh ranges.

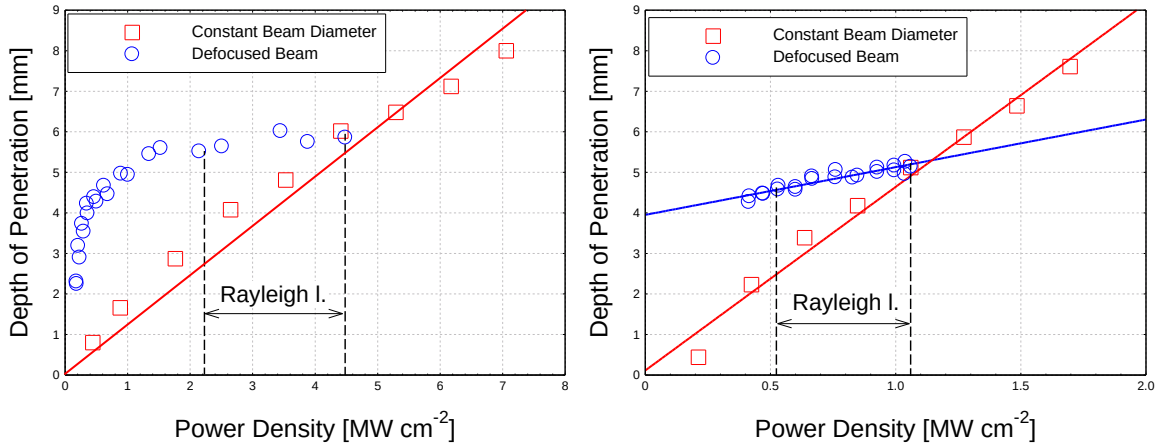

***Figure 5.20**: Effect of reduction of power density on depth of penetration in case of defocused beam (5 kW, 2 m min^{-1}) and at constant beam diameter (variation of power);* ***a)** F150 focusing lens; **b)** F300 focusing lens.*

A direct comparison of welding performance with different focusing lenses does not show any difference in weld shape, as long as the same beam diameter is used on the surface. All data from this experiment are listed in Table 5.2. In the first case, the F150 mm focusing lens was compared with the F200 mm focusing lens to achieve a beam diameter of 0.5 mm. It can be seen that the depths of penetration achieved with these lenses are the same. A similar conclusion is obtained from the comparison of the F150 mm focusing lens against the F300 mm focusing lens for a beam diameter of 0.78 mm. The depths of penetration are the same within the experimental error, despite the difference in divergence angles. Macrographs of the related welds for positive and negative defocusing are presented in Fig.5.21 and Fig.5.22. It can be seen that the welds have the same depths of penetration and shapes, irrespective of the optical set-up. There is some difference in the top beads between the macrographs, it seems like the welds achieved with the negative defocusing exhibit less undercut than the corresponding welds achieved with the focal point on the surface or with the positive defocusing, but beside this there is no evidence of the effect of divergence angle on the achieved welds.

The intensity distributions of two focusing lenses are compared in Fig.5.23. It is shown that the top-hat intensity distribution of the F150 mm focusing lens disappeared after being defocused by ±2 mm from the focal point.

***Table 5.2**: Optical set-ups used for investigation of divergence angle on depth of penetration.*

Fig.	F lens (mm)	Rayleigh length (mm)	Div. Angle (°)	Defocusing (mm)	Beam Diameter (mm)	Depth of Penetration (mm)
21(a)	150	2	-10.5	-2	0.5	5.6
21(b)	200	3.3	-8.4	0	0.5	5.8
21(c)	150	2	+10.5	+2	0.5	5.5
22(a)	150	2	-10.5	-4	0.78	5.2
22(b)	300	8	-5.5	0	0.78	5.1
22(c)	150	2	+10.5	+4	0.78	4.9

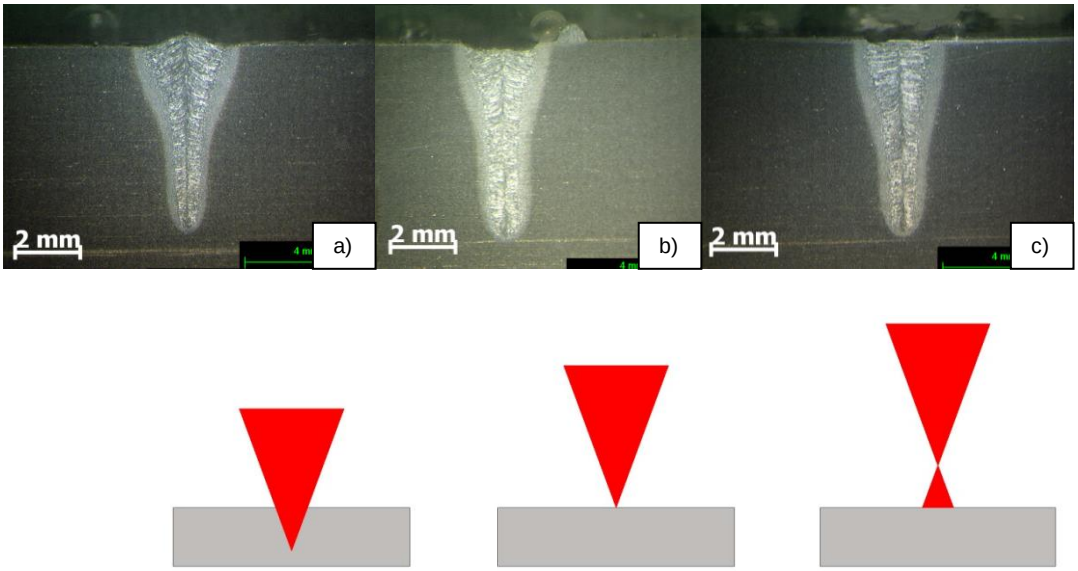

***Figure 5.21**: Macrographs for 5 kW of power, 2 m min^{-1} travel speed and beam diameter of 0.5 mm made with different focusing lenses: **a)** F150 defocused by 2 mm below the surface; **b)** F200 focused on the surface; **c)** F150 lens defocused by 2 mm above the surface.*

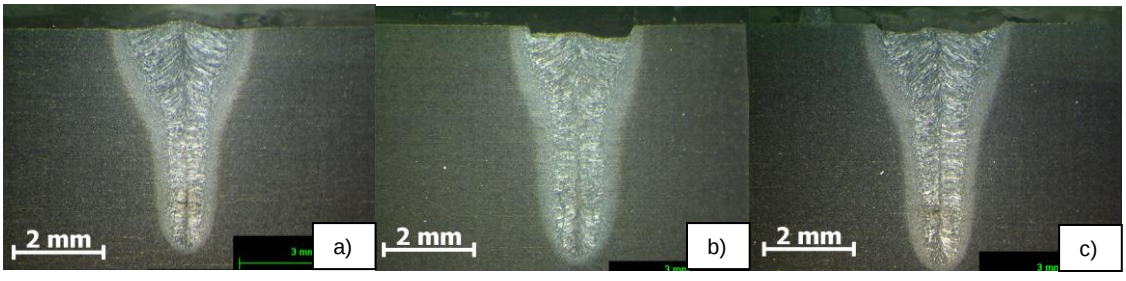

***Figure 5.22**: Macrographs for 5 kW of power, 2 m min^{-1} travel speed and beam diameter of 0.78 mm with different focusing lenses: **a)** F150 defocused by 4 mm below the surface; **b)** F300 focused on the surface; **c)** F150 defocused by 4 mm above the surface.*

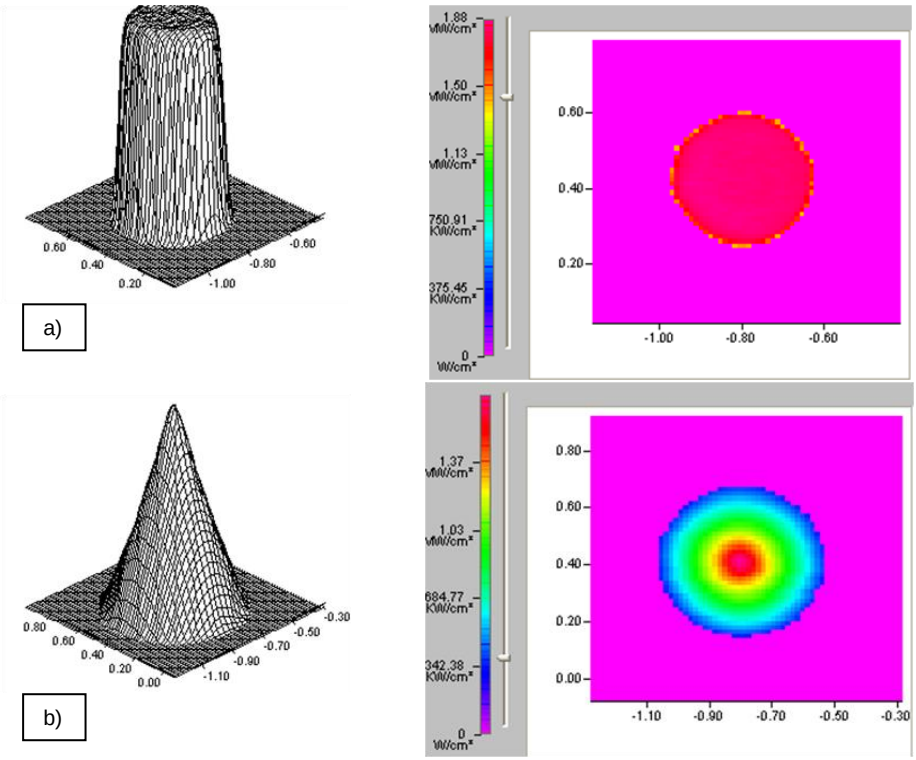

***Figure 5.23**: Intensity distribution profiles and their transverse cross sections of F150 focusing lens: **a)** in focal point; **b)** 2 mm out of focus.*

5.9. Discussion

5.9.1. Depth of penetration

In Fig.5.5 (page 131) the effect of power density and interaction time on the depth of penetration was shown, as the analogy to power and travel speed from Fig.5.4. The interaction time had more effect on depth of penetration at shorter interaction times than at longer interaction times. This implies that for a given power density there is a minimum interaction time that will produce a keyhole, corresponding to the threshold energy density (product of power density and interaction time). This is the energy density needed to bring matter to the boiling point and to increase the vaporisation rate to a level sufficient to generate a keyhole. Thus a certain part of the energy density is first utilised to initiate the keyhole and only the remaining part, if there are no further losses, is available for the increase of depth of penetration. Therefore, the

resultant depth of penetration is determined by the amount of energy density that is applied in relation to the threshold value.

At short interaction times the process conditions are more likely to be nearer the threshold energy density. Thus at this range, any small variation of parameters can have a significant effect on depth of penetration, demonstrated as the rapid change of depth of penetration with interaction time in Fig.5.5(b). At long interaction times, in contrast, the keyhole is relatively stable due to the high energy density, thus any further increase of the interaction time has only a small effect on depth of keyhole.

It was shown in Fig.5.6 (page 133) that constant power density and interaction time do not provide a constant depth of penetration, as the beam diameter is changed. This is due to the effect of specific point energy. This trend is exactly opposite to the behaviour observed, when varying the beam diameter at a constant power and travel speed. The specific point energy clarifies this phenomenon. When the beam diameter is increased at a given power density and interaction time, the energy delivered to the laser spot also increases, as indicated by Equation 5.3. This increase of the specific point energy results in the increase of depth of penetration observed in Fig.5.6 in Section 5.4.

All the interaction parameters are dependent on the beam diameter. This means that there is only one beam diameter which can give a particular combination of power density, interaction time and specific point energy. However, it was demonstrated on macrographs in Fig.5.8 to Fig.5.11 (page 135) that the power density and the specific point energy control the depth of penetration. In Fig.5.24 all data from Fig.5.6 (page 133) are plotted as a function of specific point energy. It can be seen that at a constant power density the depth of penetration is indeed proportional to the specific point energy and is independent of the interaction time down to a minimum level. The weld width, on the other hand, is controlled by the interaction time and thermal properties of material and is independent of the beam diameter. In all macrographs in Fig.5.8 to Fig.5.11 (page 135) short interaction times resulted in narrower weld beads, irrespective of the beam diameter.

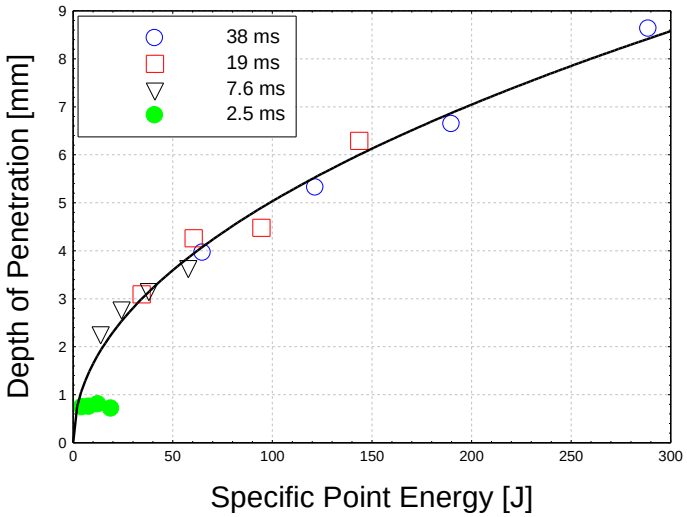

***Figure 5.24**: Effect of specific point energy on depth of penetration in S355 mild steel at 1.6 MW cm^{-2} power density, (data from Fig.5.6 on page 133, presented as a function of specific point energy).*

The simultaneous change of power density and specific point energy with the beam diameter could explain the plateau of depth of penetration when beam diameter is reduced below a certain value, as reported in separate studies [43, 425]. A similar behaviour was observed in this study, as shown in Fig.5.25 (note inverse beam diameter). The decrease of beam diameter at a constant power and travel speed significantly increases the depth of penetration, but only at a certain range of beam diameters. As the beam diameter decreases below a few hundred microns the rate of increase of depth of penetration drops. This indicates that it is not always beneficial to decrease the beam diameter beyond a certain limit. According to the literature various effects can be attributed to this plateau. The most common among these is the high divergence angle, resulting from using optics with short focal lengths, which are usually required to obtain these small beam diameters [24, 42, 45, 48, 49]. Other hypotheses include severe plasma absorption due to the high power density [42, 43] or high surface tension around the keyhole [20, 42]. Alternatively, the laser material interaction parameters can explain this phenomenon. Because the depth of penetration depends on both the power density and the specific point energy, the reduction of specific point energy dominates over the increase of power density at very small beam diameters. Hence, the depth of penetration does not

increase with further reduction of beam diameter, despite the extremely high power density.

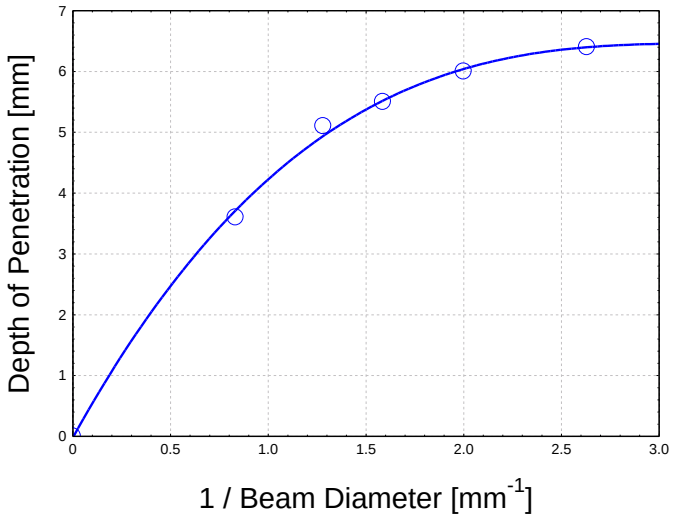

***Figure 5.25**: Depth of penetration as a function of inverse beam diameter at 5 kW of power and 2 m min^{-1} travel speed.*

The effect of interaction time on the depth of penetration cannot be neglected totally. Although in most conditions the depth of penetration is mainly dependent on the power density and the specific point energy, the results in Fig.5.24 show that there are some exceptions. Namely all welds obtained with 2.5 ms interaction time have significantly lower depths of penetration; despite the specific point energy being comparable. This was also reflected in Fig.5.6 (page 133) where the rate of increase of depth of penetration with the specific point energy at 2.5 ms interaction time was close to zero. This indicates that the increase of specific point energy does not always contribute to the depth of penetration. The phenomenon is also attributed to the threshold energy density needed for keyhole. At a given power density the specific point energy cannot be efficiently utilised if the process is carried out below the threshold interaction time.

The same experiments carried out in stainless steel and aluminium (Fig.5.12 and Fig.5.13 pages 137-138) revealed similar trends as in mild steel (Fig.5.6 page 133). The depth of penetration also increased with increasing beam diameter, as a result of increasing specific point energy; and this increase was strongly dependent on the interaction time. However, there was a significant difference between the materials at

2.5 ms interaction time. Unlike in mild steel, the depth of penetration in stainless steel and aluminium still increased with increasing beam diameter even at this low interaction time in Fig.5.12 and Fig.5.13. These two graphs plotted as a function of specific point energy are shown in Fig.5.26 and Fig.5.27. It is evident, particularly in aluminium, that the specific point energy affects the depth of penetration even at this low interaction time of 2.5 ms. This indicates that the way the specific point energy is utilised for the increase of depth of penetration is additionally dependent on the material properties.

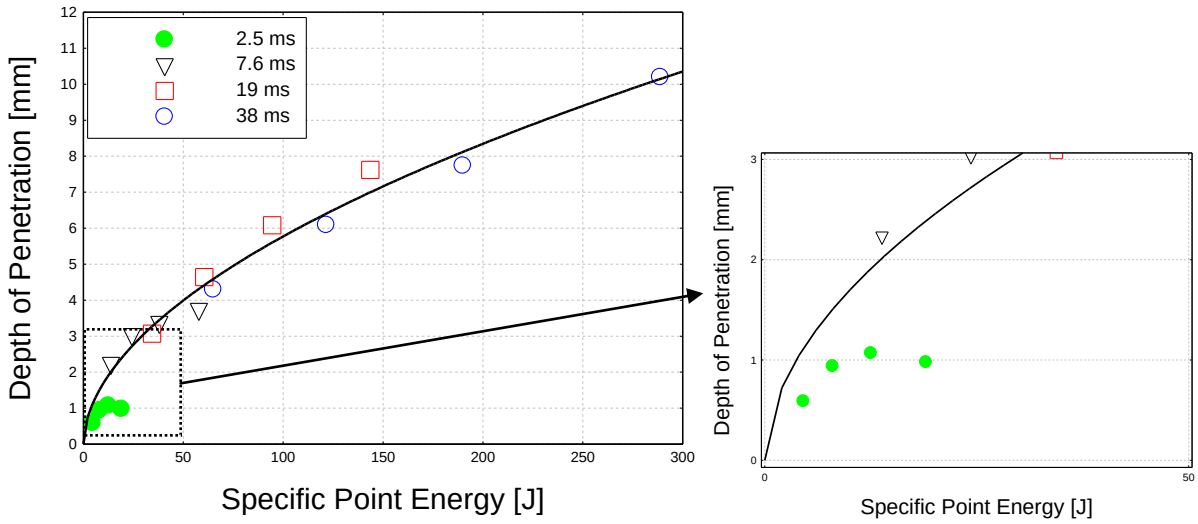

***Figure 5.26**: Effect of specific point energy on depth of penetration in 304 stainless steel at 1.6 MW cm^{-2} power density, (data from Fig.5.12 on page 137, presented as a function of specific point energy).*

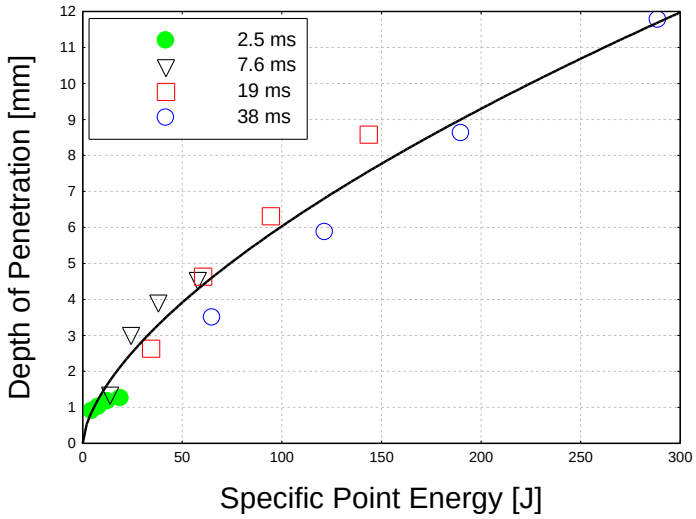

***Figure 5.27**: Effect of specific point energy on depth of penetration in 7075 aluminium at 1.6 MW cm^{-2} power density, (data from Fig.5.13 on page 138, presented as a function of specific point energy).*

The macrographs from Fig.5.14 (page 138) confirmed that for the same conditions the greatest depth of penetration among the alloys was achieved in aluminium. However, in Fig.5.15 (page 138) the trend was reversed and aluminium exhibited the shallowest depth. The same power density of 1.6 MW/cm^2, but achieved with smaller beam diameters than previously, led to a lower specific point energy range. The high thermal conductivity of aluminium became dominant at this low range of specific point energy. Aluminium alloy can dissipate much greater portion of heat by conduction, thus the threshold energy density required for the keyhole formation in aluminium is higher than in steel. This resulted in the lower depth of penetration at low energy levels in aluminium, as compared to both steels. Alternatively, at higher energy levels, where the threshold energy density for keyhole was exceeded, the depth of penetration achieved in aluminium was greater than in both steels. This indicates that above the threshold energy density for keyhole the conduction losses have secondary effects.

Surface temperatures and recoil pressures for different materials were compared in Fig.5.16 (page 139). The highest surface temperature in stainless steel resulted from a relatively low thermal conductivity. A higher surface temperature in stainless steel for approximately the same energy required for vaporisation, as compared to low carbon steel will lead to a greater recoil pressure. Since the recoil pressure is the main driving force for depth of penetration in keyhole regime, this will result in a deeper penetration in stainless steel, as compared to low carbon steel. Furthermore, the higher the temperature of the liquid metal the lower its viscosity, and thus the efficiency of melt removal from the bottom of keyhole increases. Also the low thermal conductivity of stainless steel results in a lower volume of liquid metal around the keyhole. Thus the steeper curves in Fig.5.12 (page 137) for stainless steel than for mild steel in Fig.5.6 (page 133) can be explained by a higher temperature and a better efficiency of drilling and melt removal. On the other hand, the deepest penetration at high energy density levels in the case of aluminium can be explained by its low viscosity. The thermal properties of materials are compared in Table I.1 in Appendix I. A several times lower viscosity of aluminium, as compared to both steels, enables more efficient melt removal from the bottom of the keyhole. The lower viscosity makes metal more liquid, which improves heat transfer from the heat source via convection. Therefore, for the same laser conditions greater depth of penetration

was achieved in aluminium, despite the much lower surface temperature and lower recoil pressure (Fig.5.16 page 139). This explains the higher slopes of the curves in Fig.5.13 (page 138) for aluminium than for both steels in Fig.5.6 (page 133) and Fig.5.12 (page 137).

5.9.2. Depth of focus

There is a large depth of focus observed experimentally in many welding situations, which is much greater than expected from the consideration of power density. It was shown in Fig.5.17 (page 141) that during defocusing by one Rayleigh length the depth of penetration reduced by approximately 10%, whereas the same reduction of power density at a constant beam diameter led to the reduction of depth of penetration by 50% (Fig.5.18 page 142). According to the data from Table 5.1 in Section 5.7 the depth of focus (10% variation of depth of penetration) for this optical set-up, which would result from the decrease of power density only was approximately ±2 mm. In addition the dependency of the experimental depth of focus on the travel speed indicates the influence of interaction time.

The situation is clarified when the remaining laser material interaction parameters are taken into account. According to the Equations 5.1 - 5.3 all interaction parameters change simultaneously with the beam diameter, as shown in Fig.5.28. This means that when a laser beam is defocused at a constant power and travel speed two competing effects occur, on one hand the power density decreases, but on the other hand the specific point energy increases. It was shown in Section 5.5 that the depth of penetration is controlled by these two parameters, thus the increase of specific point energy compensates for the drop of power density during defocusing. Thus the depth of penetration reduces less rapidly during defocusing than it would result from the reduction of power density only, as was shown in Fig.5.18 (page 142).

The variation of interaction parameters with the beam diameter shown in Fig.5.28 corresponds to the focus study case for 2 m/min travel speed from Fig.5.17 (page 141). It can be seen that an increase of beam diameter from 0.63 mm to 1.25 mm, due to defocusing by a distance of 10 mm from the focal point, results in a decrease of power density from 1.6 MW/cm^2 to 0.4 MW/cm^2 and an increase of specific point

energy from 94 J to 187 J. The consequences of such variations of the interaction parameters can be evaluated.

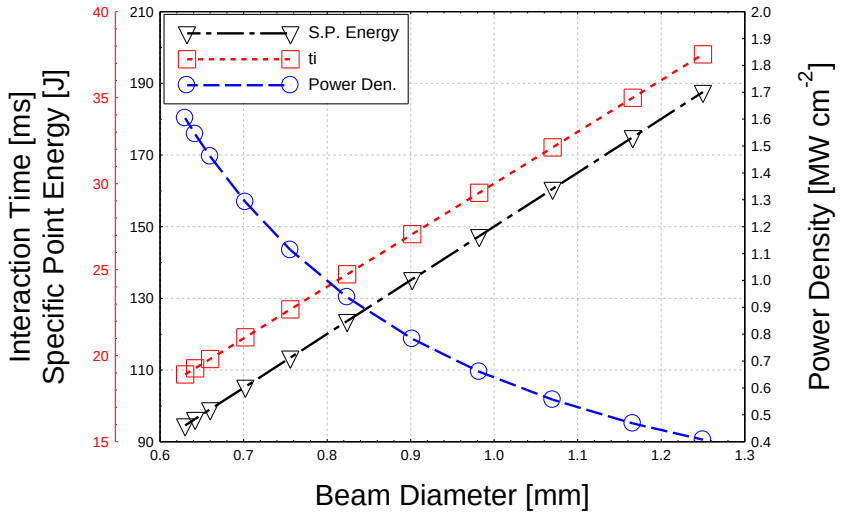

***Figure 5.28**: Simultaneous variation of interaction parameters with beam diameter at 2 m min^{-1} travel speed of and 5 kW power.*

To prove the compensating effect of specific point energy on the depth of focus an additional experiment was carried out. As shown in Fig.5.28 when the laser beam with this particular optical set-up (F250 mm focusing lens) was defocused by 10 mm, the power density decreased from 1.6 MW/cm^2 to 0.4 MW/cm^2, as compared to the focal point. To match these two levels of power density, two combinations of laser power and beam diameter were used. To achieve a power density of 1.6 MW/cm^2 a laser power of 5 kW and a beam diameter 0.63 mm were used, whilst to achieve a power density of 0.4 MW/cm^2 a laser power of 2 kW and a beam diameter of 0.78 mm were used. In both cases a range of travel speeds from 0.3 m/min to 15 m/min was used and bead-on-plate welds were carried out. The achieved depths of penetration were plotted as a function of specific point energy, for two levels of power density, as shown in Fig.5.29. This figure can be used to investigate the effect of specific point energy and power density on the depth of penetration from the previous focus study at 5 kW of power and 2 m/min travel speed. It can be seen in Fig.5.29 that a decrease of power density from 1.6 MW/cm^2 to 0.4 MW/cm^2 due to defocusing will result in a decrease of depth of penetration from point 1 to point 2, whereas an

increase of specific point energy from 94 J to 187 J will increase the depth of penetration from point 2 to point 3. Thus as a net result the depth of penetration will only decrease from point 1 to point 3, due to the compensating effect of specific point energy for the drop of power density. This explains the large depth of focus observed experimentally in Fig.5.17 (page 141).

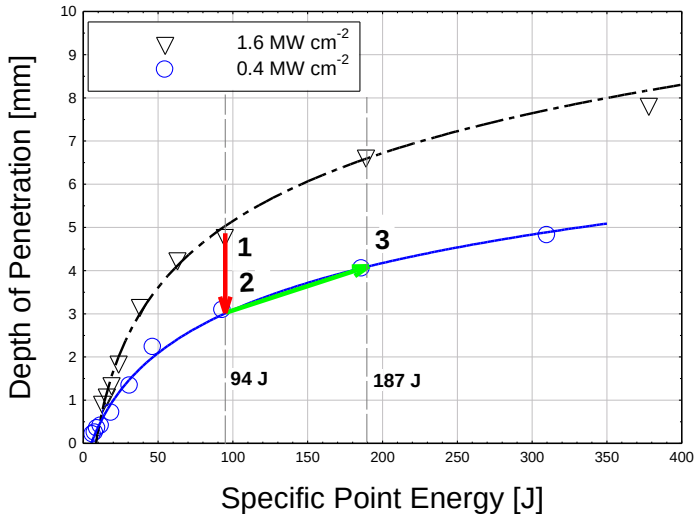

***Figure 5.29**: Effect of specific point energy on depth of penetration at two levels of power density: 1.6 MW cm^{-2} (P_L = 5 kW, d = 0.63 mm) and 0.4 MW cm^{-2} (P_L = 2 kW, d = 0.78 mm).*

Note that Fig.5.29 was obtained by varying the travel speed. Macrographs in Fig.5.30 show that the same weld depth, as in the defocused case, can be obtained by any combination of system parameters, as long as the power density and the specific point energy are the same. This is quite striking because it shows that during defocusing or any other case when the beam diameter is changed the behaviours occurring are not a lot more complex than during changing the laser power or the travel speed with respect to the power density and specific point energy.

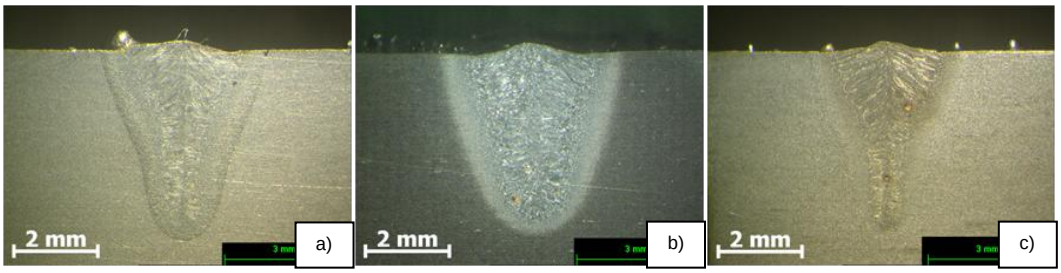

***Figure 5.30**: Macrographs for constant power density of 0.4 MW/cm^2 and specific point energy of 187 J; **a)** v =2 m min^{-1}, P_L = 5 kW, 10 mm positive defocusing, d =1.25; **b)** v = 0.5 m/min, P_L = 2 kW, focused on the surface, d = 0.78 mm; **c)** v =2 m min^{-1}, P_L = 5 kW, 10 mm negative defocusing, d =1.25 mm.*

The experimental curves from Fig.5.29 can be represented by Equation 5.4. This equation can be used to predict the depth of focus for other levels of specific point energy at these two power densities.

$$PD = a - b \cdot \ln(E_{SP} + c) \qquad 5.4$$

Where a, b, c are constant dependent on power density. For a power density of 1.6 MW/cm^2: a = -5.54, b = -2.31, c = 2.69; and for a power density of 0.4 MW/cm^2: a = -6.7, b = -1.98, c = 24.8.

The difference in the response of depth of penetration to the applied power density from Fig.5.18 (page 142) can be clarified using Equation 5.4 and Fig.5.29. Both cases are shown in Fig.5.31. When the power density is decreased by reducing laser power at a constant beam diameter, not only the power density reduces but also the specific point energy decreases at the same time. This causes the rapid drop of depth of penetration in Fig.5.31. It can be seen that this case, as the analogy to Fig.5.18 (page 142), does not match the experimentally observed depth of focus. On the other hand, when the power density is reduced by defocusing at a constant laser power, an increase of specific point energy compensates for a reduction of power density. It can be seen in Fig.5.31 when the compensating effect of specific point energy is taken into account, based on the logic from Fig.5.29, the predicted curve matches the experimental results in Fig.5.31 very well. Note that both curves in this figure are fitted parabolas based on predicted depths of penetration in three points

(focal point, 10 mm negative and 10 mm positive defocusing) calculated from Equation 5.4.

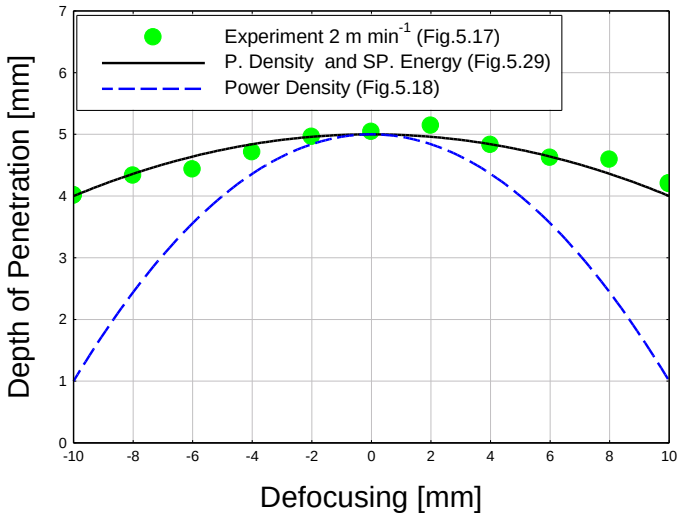

***Figure 5.31**: Comparison of predicted depth of focus based on variation of interaction parameters with beam diameter and experimental focus study at 2 m min^{-1} travel speed and 5 kW power for F250 focusing lens.*

In the same way Equation 5.4 was used to determine the predicted curves in Fig.5.17 (page 141). These curves in this figure were achieved also by fitting parabolas, based on predicted depths of penetration in three points (focal point, 10 mm negative and 10 mm positive defocusing) calculated from Equation 5.4. A good agreement for all travel speeds confirms that the large depth of focus occurs due to the simultaneous increase of specific point energy and decrease of power density when the beam diameter increases. Thus the dependency of depth of focus with the travel speed is related to the rate of increase of specific point energy with the interaction time, which is greater at longer interaction times. As a matter of fact there was a small discrepancy at 5 m/min travel speed in Fig.5.17 (page 141). This is attributed to the change of welding regime from keyhole to conduction at the maximum out of focus position in the experiment. The specific point energy in this case over-predicted the depth of penetration.

5.9.3. Effect of divergence

The experimental results imply that the divergence angle of a laser beam does not affect the achieved depth of penetration, as long as the beam diameter on the material surface is constant. The results were presented in Fig.5.21 and Fig.5.22 as well as in Table 5.2 (page 147). It is quite striking that the same depths of penetration, within the experimental error, were achieved in Fig.5.21 and Fig.5.22, despite the large difference in the divergence angles between the positive and negative directions of defocusing. Note that the divergence angle changes from positive to negative with changing the defocusing direction. The only difference visible on the macrographs is less undercut with a converging beam (negative defocusing). These results are in contrast to the work shown by Weberpals [49]. However, in their experiment much smaller beam diameters were used, which in some cases resulted in a Rayleigh length below 1 mm. Such a low depth of focus could affect the real beam diameter achieved on the surface. Also the effect of divergence might be more profound with these small beam diameters, due to the extremely small size of the keyhole.

The fact that the same depth of penetration was achieved with such different conditions, namely focused and defocused beams with different intensity distribution profiles (Fig.5.23 page 148) led to the same depths of penetration, justifies the simple definitions of power density and interaction time used in this thesis. Although the average power density according to Equation 5.1 from Section 5.1 in principle is fulfilled only for beams with a top-hat intensity distribution, the results from Fig.5.21 and Fig.5.22 (page 147) showed that even with non-top hat beams the same depths of penetration were achieved.

The divergence angle affects the beam diameter and therefore the laser material interaction parameters on the surface. This was demonstrated in Fig.5.19 (page 145). For the same defocusing distance, the beam with a larger divergence (Fig.5.19a) experienced a more rapid increase of beam diameter followed by a decrease of power density. Thus at a certain level of defocusing the power density reduced below a critical level, leading to a rapid drop of depth of penetration. This happened despite the continuous increase of specific point energy with defocusing. At this point the compensation ability of specific point energy was reduced due to the low energy density and the depth of penetration could not be further maintained. It seems that

the divergence angle does not affect the depth of penetration directly, but it determines the tolerance of achieved beam diameter and therefore the interaction parameters achieved in practice. This is shown in Fig.5.32. For the same defocusing distance of 10 mm the beam diameter with the F150 lens was increased four times, as compared to a 60% increase of beam diameter in the case of F300 lens. This demonstrates that the same defocusing distance used on different optical set-ups will have different effects. High divergence results in a more rapid increase of beam diameter for a particular defocusing distance, therefore the point at which the energy density reduces below the keyhole threshold can be reached sooner. This leads to a more rapid reduction of depth of penetration when beams with very high divergence angles are used.

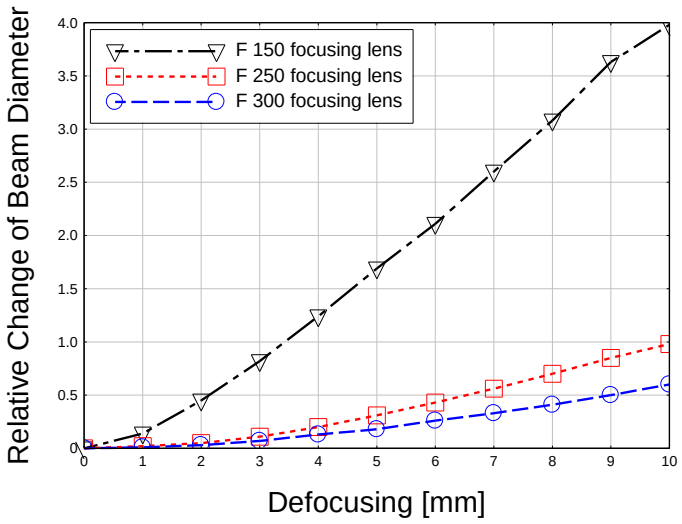

***Figure 5.32**: Effect of optical set-up on a relative change of beam diameter for a constant defocusing distance.*

Chapter 6. Parameter selection in laser welding using the power factor

In the previous chapter the parameters controlling depth of penetration in laser welding were identified. However, these parameters cannot be used as an application model, because there is a unique combination of the laser material interaction parameters for any beam diameter. Frequently in laser applications the beam diameter is a parameter which is fixed for a given laser system. Thus it would be useful to have a system of parameters, which could be applied on various beam diameters and therefore different laser systems. This chapter investigates if it is possible to find a phenomenological model of parameters, which would specify depth and width of the fusion zone in laser welding, independent of the beam diameter. This would allow a potential user to select a suitable weld for a particular application, in terms of depth of penetration and weld width, and then the concept would tell which system parameters should be used in order to achieve this weld. These parameters could be transferred to the system parameters and applied on different laser systems with different beam diameters.

6.1. Experimental procedure

The experimental set-up and specifications of the laser are given in Chapter 3. The laser beam was focused using a set of focusing lenses with focal lengths ranging from 150 mm to 300 mm. The set of focusing lenses resulted in beam diameters at the focal points ranging from 0.38 mm to 0.78 mm. Some experiments were carried out with a new delivery fibre, which resulted in slightly different beam diameters for the same optical set-up, as described in Chapter 3. All welds were sectioned, polished and examined under an optical microscope in order to measure depth of penetration. The welding procedure included a set of bead-on-plate, as well as butt welds in 12 mm thick S355 low carbon steel. Some additional bead-on-plate welds in 20 mm thick steel were made.

6.2. Effect of system parameters on weld bead

First the effect of system parameters on the weld bead is investigated. The same depth of penetration in laser welding can be achieved with many combinations of parameters. For example if we consider the laser power and the travel speed, there are many possible combinations of these two parameters, which will give the same depths of penetration. However, apart from the similar depths of penetration, these welds may exhibit different properties. The parameters used to achieve a particular weld will be further reflected in the properties of the joint, such as the mechanical properties, weld width, bead quality, size of the heat affected zone and microstructure. Consequently it is important to specify in advance which type of weld will suit the specific application and then try to achieve the appropriate weld.

6.2.1. Methodology

To investigate the effect of system parameters on the shape of laser welds, a set of bead-on-plate welds with different powers in a range from 2 kW to 8 kW and travel speeds from 0.3 m/min to 15 m/min were made. Two focussing lenses with focal lengths of 150 mm and 300 mm were used to achieve beam diameters of 0.38 mm and 0.78 mm. The widths of the fusion zones and general quality of the welds were examined.

In the second set of experiments the effect of beam diameter on the weld width was investigated. The data from the previous experiment were used to achieve welds with the same depths of penetration, using two beam diameters of 0.38 mm and 0.78 mm and different travel speeds of 0.5 m/min, 2 m/min and 3 m/min. The welds were produced in a butt-joint configuration with zero-gap between the plates. To ensure the zero gap condition the adjacent edges were machined before welding. The laser power was appropriately adjusted to achieve a depth of penetration of 6 mm. Then the macrographs corresponding to the same travel speeds were compared.

6.2.2. Results

The experimental results show that the weld profile changes with the processing parameters. The macrographs from Fig.6.1 and Fig.6.2 show that the weld width decreases with increasing travel speed at a constant beam diameter. The weld width decreased, despite the fact that the laser power was appropriately increased with the travel speed to maintain the same depth of penetration. It can be seen that the quality varies significantly across the parameters. A large heat affected zone and severe porosity are apparent at a slow speed of 0.3 m/min for both beam diameters. Very high travel speeds, on the other hand, combined with a small beam diameter lead to severe undercut, as shown in Fig.6.2(c). Thus the parameters used for welding have further consequences on the properties of the joint.

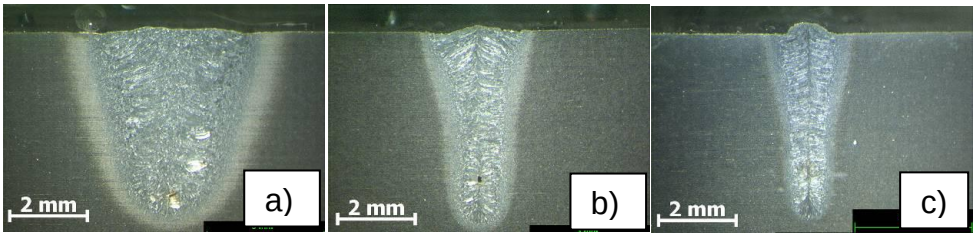

***Figure 6.1**: Macrographs of bead-on-plate welds for 0.78 mm beam diameter, combinations of parameters required for 5 mm depth of penetration **a)** P_L = 2 kW, v = 0.3 m min^{-1}; **b)** P_L = 5 kW, v = 2 m min^{-1}; **c)** P_L = 8 kW, v = 5 m min^{-1}.*

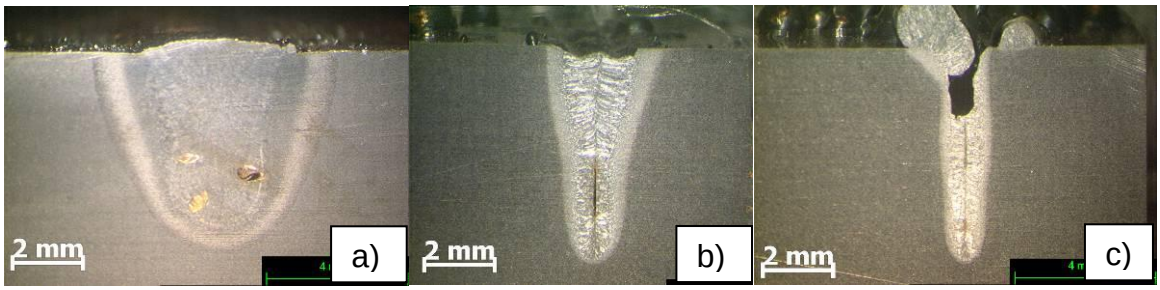

***Figure 6.2**: Macrographs of bead-on-plate welds for 0.38 mm beam diameter, combinations of parameters required for 6 mm depth of penetration **a)** P_L = 2 kW, v = 0.3 m min^{-1}; **b)** P_L = 5 kW, v = 2 m min^{-1}; **c)** P_L = 8 kW, v = 5 m min^{-1}.*

The effect of beam diameter on the weld width at different travel speeds is shown in Fig.6.3. In all cases the laser power was appropriately adjusted to the beam diameter and travel speed as described in the methodology (Section 6.2.1). It can be seen that for these conditions the width of the welds is almost independent of the beam diameter. The only difference is that the more laser power was required to achieve the same depth of penetration, as the beam diameter increased at a given travel speed.

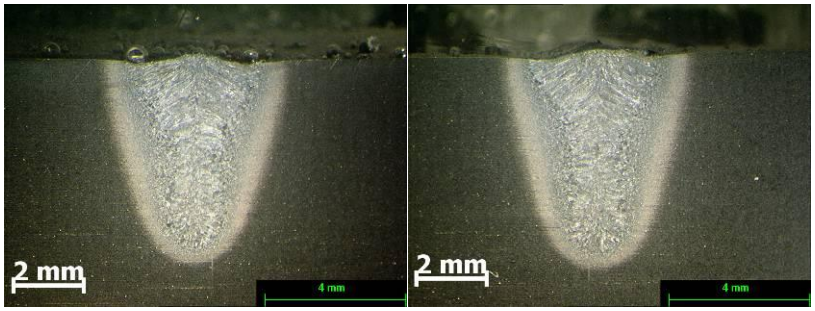

d = 0.37 mm; P_L = 3 kW, v = 0.5 m min^{-1} d = 0.75 mm; P_L = 3.5 kW, v = 0.5 m min^{-1}

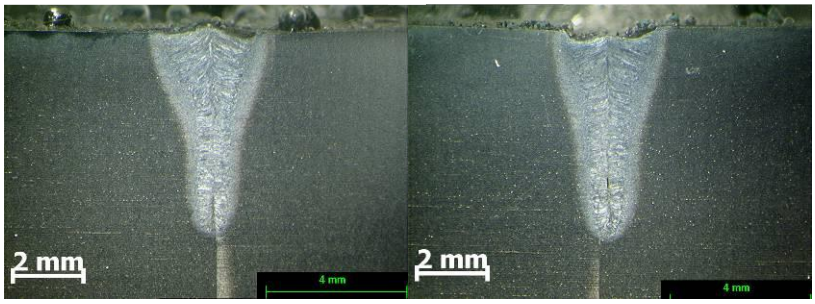

d = 0.37 mm; P_L = 5 kW, v = 2 m min^{-1} d= 0.75 mm; P_L = 6 kW, v = 2 m min^{-1}

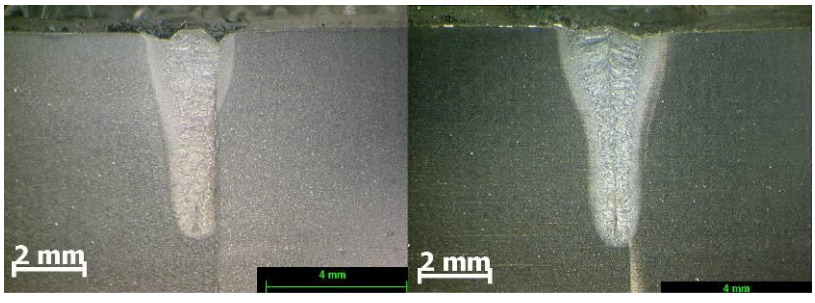

d = 0.37 mm; P_L = 6 kW, v = 3 m min^{-1} d = 0.75 mm; P_L = 7.5 kW, v = 3 m min^{-1}

***Figure 6.3**: Effect of beam diameter on bead width at different travel speeds.*

The analogous comparison at faster travel speeds of 5 m/min, 8 m/min and 10 m/min is shown in Fig.6.4. The depths of penetration achieved in this experiment are lower

than in previous cases, due to the power limit of the laser. It can be seen that the effect of beam diameter on the weld width is more profound at this fast travel speeds. All welds achieved with a beam diameter of 0.78 mm are significantly wider than the corresponding welds achieved with a beam diameter of 0.38 mm, for the same travel speed and comparable depths of penetration.

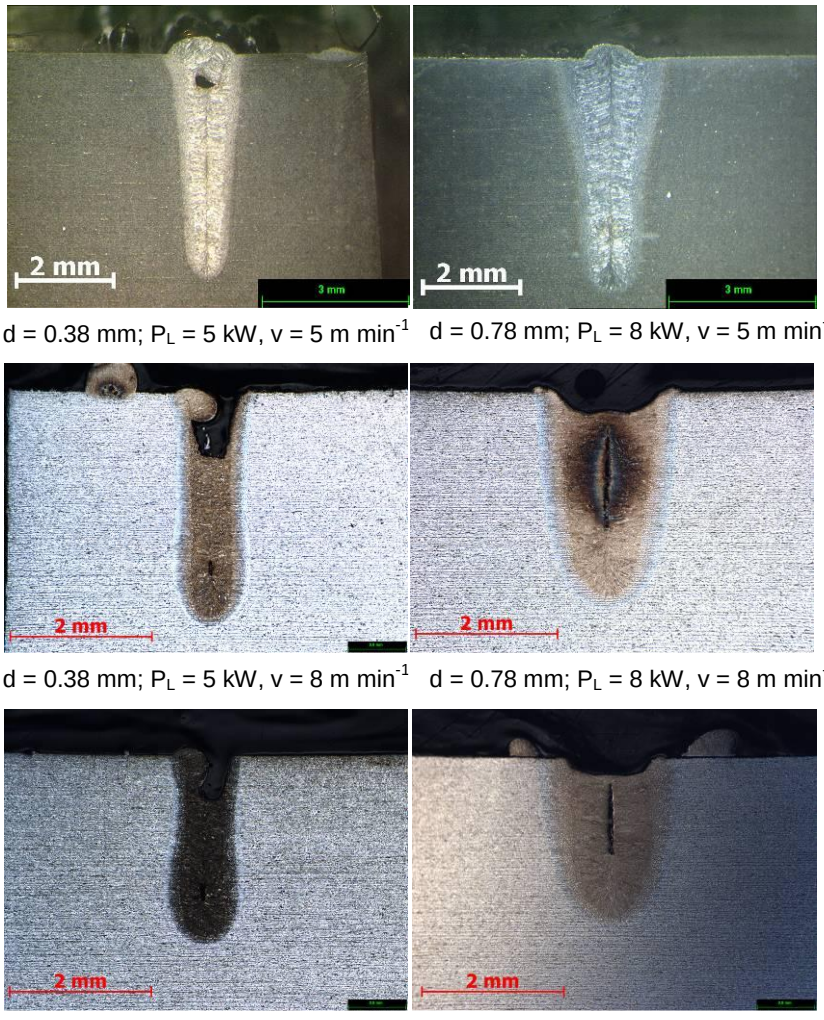

d = 0.38 mm; P_L = 5 kW, v = 5 m min^{-1} d = 0.78 mm; P_L = 8 kW, v = 5 m min^{-1}

d = 0.38 mm; P_L = 5 kW, v = 8 m min^{-1} d = 0.78 mm; P_L = 8 kW, v = 8 m min^{-1}

d = 0.38 mm; P_L = 5 kW, v = 10 m min^{-1} d = 0.78 mm; P_L = 8 kW, v = 10 m min^{-1}

***Figure 6.4**: Effect of beam diameter on weld profile at fast travel speeds.*

It was shown that various welds can be achieved when varying the processing parameters. The parameter selection procedure is even more complicated due to the effect of beam diameter on the depth of penetration. The depth of penetration as a function of travel speed for two beam diameters is shown in Fig.6.5. It is

demonstrated that a depth of penetration of 5 mm can be achieved either with a travel speed slightly below 2 m/min when a beam diameter of 0.38 mm is used or with a travel speed of 3.5 m/min when applying a beam diameter of 0.78 mm. Both combinations require the same laser power of 5 kW. There are multitudes of combinations of parameters for other beam diameters. This extends the number of parameters, which have to be considered when setting up the laser welding process.

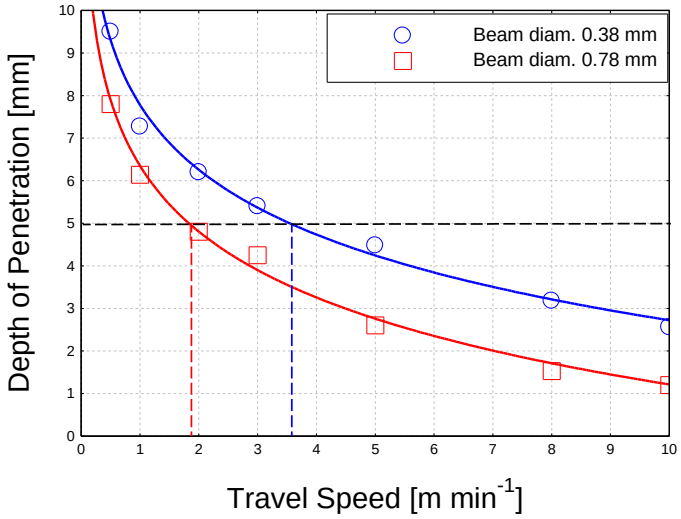

***Figure 6.5**: Effect of beam diameter on parameters selection at a constant power of 5 kW.*

6.3. Effect of power factor and interaction time on depth of penetration

It was shown that the system parameters do not specify uniquely the laser welding process, unless the beam diameter is specified. Furthermore, the laser material interaction parameters from Chapter 5: the power density, interaction time and specific point energy all change simultaneously with the beam diameter. The power density was determined as the ratio of the laser output power $\mathbf{P_L}$ to the area of laser spot on the surface, which for a circular beam with a diameter **d** is given by

$$q_P = \frac{4P_L}{\pi d^2} \ [Wm^{-2}] \qquad 6.1$$

The interaction time was defined as the ratio of the beam diameter to the travel speed, as given by

$$\tau_i = \frac{d}{v} \ [s] \qquad 6.2$$

Finally the specific point energy was determined as the product of power density, interaction time and the area of laser spot on the surface, given by

$$E_{SP} = q_P \cdot \tau_i \cdot A_S = P_L \cdot \tau_i = \frac{P_L \cdot d}{v} \ [J] \qquad 6.3$$

It can be seen that all laser material interaction parameters are dependent on the beam diameter, therefore for any beam diameter there is only one combination of them, which cannot be replicated with other beam diameters. Thus both cases, the system parameters approach, as well as the interaction parameters, require the beam diameter to be adjusted in order to replicate a particular weld on different laser systems. Since very often the beam diameter of a given laser system is fixed, a new approach is investigated in this section.

6.3.1. Power factor definition

It was shown in Section 5.4 (Fig.5.6) that constant power density and interaction time do not provide constant depth of penetration when the beam diameter is varied. The depth of penetration increases with increasing beam diameter due to the increase of specific point energy. Considering these two parameters and their relationship with the beam diameter: the power density (inverse square of the beam diameter) and the specific point energy (linearly dependent on the beam diameter) it is likely that the depth of penetration should be proportional to the ratio of the laser power to the beam diameter. Furthermore, it is anticipated from Fig.5.6 in Section 5.4 that for a given interaction time the depth of penetration in the keyhole regime is proportional to the product of power density and beam diameter, which is consistent with results reported by Beyer [426] and Fuershbach [163]. Thus the power factor $\mathbf{P_F}$ defined by

the product of power density $\mathbf{q_P}$ and beam diameter **d**, which also corresponds to the ratio of the laser power **P** to the beam diameter **d** and is given by Equation 6.4 can be used to characterise the depth of penetration in laser welding.

$$P_F = q_P \cdot d \ = \frac{P}{d} [W \cdot m^{-1}] \qquad 6.4$$

The power factor is not a fundamental laser interaction parameter, but it can be considered as a simplified power density, which in contrast to the power density does not consider the cross sectional area of the beam but only its one dimensional width. The power factor along with the interaction time is used in this section as a parameter selection model.

6.3.2. Methodology

The effect of beam diameter on the depth of penetration, at a constant power factor and interaction time was investigated. A constant power factor of 11 MW/m and various interaction times were used. The concept was tested on four beam diameters as follows, 0.38 mm, 0.5 mm, 0.63 mm and 0.78 mm. The beam diameters were achieved by applying four focusing lenses with different focal lengths as described in the experimental set-up (Chapter 3). To maintain constant power factor and interaction time the laser power and the travel speed were continuously adjusted to the beam diameter, according to Equations 6.4 and 6.2.

6.3.3. Results

The effect of beam diameter on the depth of penetration at a constant power factor and interaction time is shown in Fig.6.6. A constant depth of penetration for this wide range of beam diameters at any given interaction time is demonstrated. The maximum difference in the depth of penetration between the beam diameters is only approximately 1 mm, which corresponds to 10% of total depth of penetration. Unfortunately the power limit of the laser system used here did not allow this power factor to be tested on larger beam diameters.

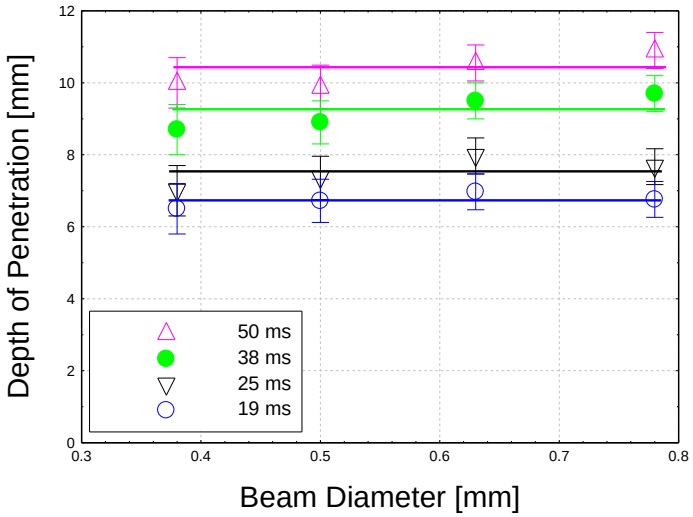

***Figure 6.6**: Effect of beam diameter on depth of penetration at different interaction times and a constant power factor of 11 MW m^{-1}.*

6.4. Depth of penetration – application model

A potential application model has to rely on system of parameters, which precisely control the dimensions of a weld, regardless of the laser system. It was shown in the previous paragraph (Section 6.3.3) that the power factor and interaction time allow a particular depth of penetration to be achieved with any beam diameter in the investigated range. To extend this concept it is necessary to investigate this on a wider range of conditions.

6.4.1. Methodology

In the following experiment various parameters were used to achieve the same depth of penetration. The laser power was varied from 1 kW to 8 kW and the travel speed was varied from 0.3 m/min to 10 m/min. Four different beam diameters were used in the range from 0.38 mm to 0.78 mm. A range of travel speeds and laser powers was used for every beam diameter. Then the welds with the same depths of penetration were selected and the parameters used to achieve these welds were converted into

the power factor and interaction time. The following depths of penetration were considered: 4 mm, 6 mm and 8 mm.

6.4.2. Results

The data from parametric study on four different beam diameters, as described in the methodology (Section 6.4.1), are shown in Fig.6.7. First, it can be seen that all data for all beam diameters follow the same trend. Second, there is a strong relationship between the interaction time and the power factor required for a given depth of penetration. The shorter the interaction time the greater the power factor that needs to be applied in order to achieve a particular depth of penetration. A high power factor corresponds to a small beam diameter or a high laser power, which in both cases may be limited by the laser system. Such a graph can be created for any depth of penetration and used as an application tool.

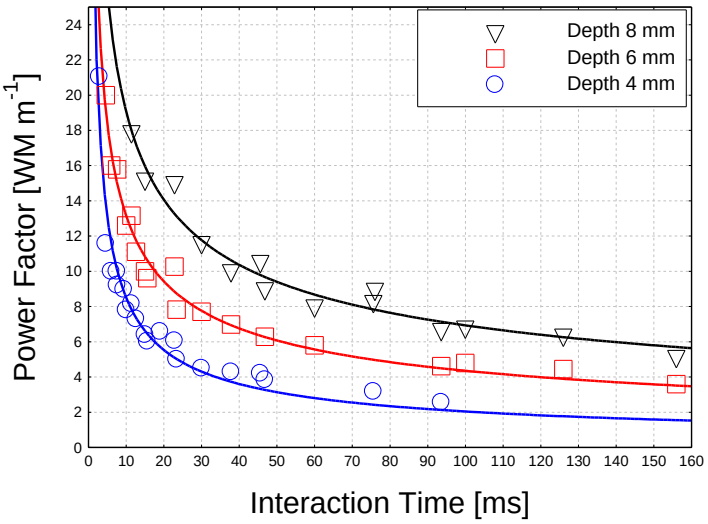

***Figure 6.7**: Required power factor for depths of penetration of 8 mm, 6 mm and 4 mm as a function of interaction time (range of beam diameters 0.38 mm to 0.78 mm).*

The data presented in Fig.6.7 were used to derive an empirical equation of power factor $\mathbf{P_F}$ required to achieve a particular depth of penetration **PD** (mm) at a given interaction time $\boldsymbol{\tau_i}$ (ms)**,** as given by

$$P_F = (4.25PD + 17) \cdot \tau_i^{(0.045PD - 0.782)} \ [MW \cdot m^{-1}] \qquad 6.5$$

Solving iteratively Equation 6.5 for depth of penetration gives:

$$PD = (6.5 \cdot 10^{-3} P_F^2 - 0.29P_F + 8.31) \ln\left[(2.3 \cdot 10^{-3} P_F^2 + 4.67 \cdot 10^{-2} P_F + 0.26) \ln(\tau_i)\right] [mm] \qquad 6.6$$

Note that these equations were validated only up to a maximum laser power of 8 kW.

6.5. Sensitivity analysis

The key point of the power factor model is the ability to achieve any depth of penetration, irrespective of the beam diameter. Then depending on the interaction time and required depth of penetration a suitable power factor can be selected from Fig.6.7 or Equation 6.5. However, the fact that the power factor is just a simplified parameter, which incorporates the beam diameter and the laser power, it is necessary to attribute the limits of the model. The sensitivity analysis of the power factor model was carried out. The effect of beam diameter at constant power factor and interaction time was previously examined (Fig.6.6). Nevertheless this was carried out on a rather narrow range of interaction times. In this experiment only two beam diameters are investigated using a much wider range of interaction times, which resulted in a range of depths of penetration from 12 mm to approximately 1 mm.

6.5.1. Methodology

To investigate the sensitivity of depth of penetration on the beam diameter when using a constant power factor and interaction time, some data from previous parametric study from Section 5.3 were used. The welds corresponding to the same power factor, amongst all welds achieved with various beam diameters, travel speeds and laser powers, were compared. This provided the sufficient variation of interaction time in a range from 100 ms to 2 ms. In all cases a constant power factor of 10 MW/m and two beam diameters: 0.5 mm and 0.78 mm were used. To obtain this power factor on the selected beam diameters laser powers of 5 kW and 8 kW were used respectively.

6.5.2. Results

A comparison of depth of penetration as a function of interaction time at two different beam diameters of 0.5 mm and 0.78 mm and a constant power factor of 10 MW/m is shown in Fig.6.8. In general the effect of beam diameter seems to be small in the entire range of interaction times. In a range of interaction times from 10 ms to 100 ms the difference in depth of penetration between the beam diameters does not exceed 10% of the maximum depth. In contrast, below 10 ms interaction time this difference approximates 25% of the maximum depth. It is interesting to notice that in a range of interaction times above 15 ms the higher depths of penetration are achieved with a larger beam diameter (0.78 mm). Whilst as the interaction time decreases below 15 ms there is a turnover of the trend and higher depths of penetration are achieved with a smaller beam diameter (0.5 mm). A similar behaviour was observed for other values of the power factor.

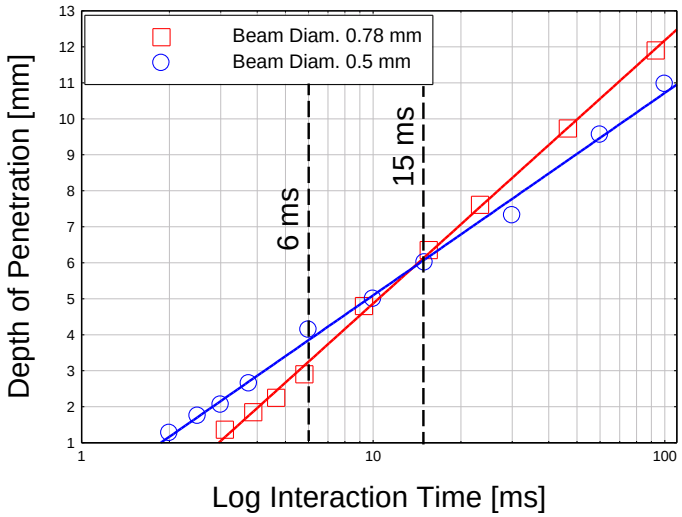

***Figure 6.8**: Depth of penetration as a function of interaction time at 10 MW m^{-1} power factor, for two beam diameters of 0.5 mm and 0.78 mm.*

Macrographs of the corresponding welds are shown in Fig.6.9. The same depth of penetration and weld shape in a medium range of interaction times is evident, as shown for 10 ms and 15 ms. The depth of penetration is slightly different between the beam diameters at long interaction times, as shown for 100 ms in Fig.6.9. Note that this long interaction time, for a beam diameter of 0.5 mm corresponds to a travel speed of 0.3 m/min. The difference between both beam diameters is even greater as the interaction time decreases below 10 ms. In this range of parameters, a deeper penetration is achieved with a smaller beam diameter, in case of a constant power factor and interaction time. In contrast, the melting area, measured from the macrographs, seems not be affected by the beam diameter in the entire range of interaction times, when a constant power factor and interaction time is used, as shown in Fig.6.10.

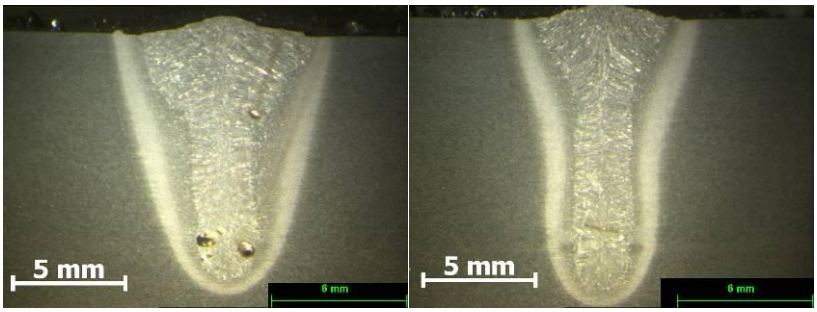

d = 0.5 mm; Ti = 100 ms d = 0.78 mm; Ti = 100 ms

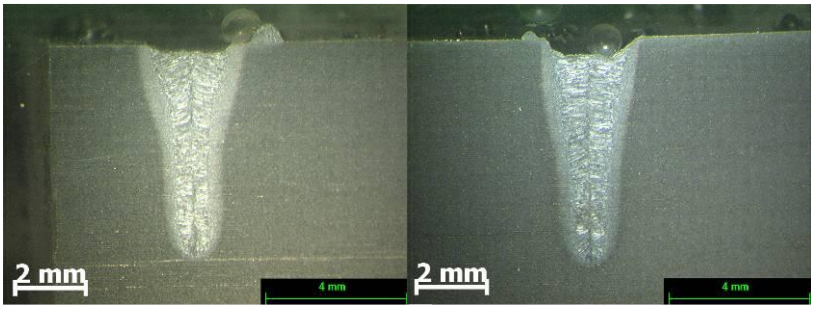

d = 0.5 mm; Ti = 15 ms d = 0.78 mm; Ti = 15 ms

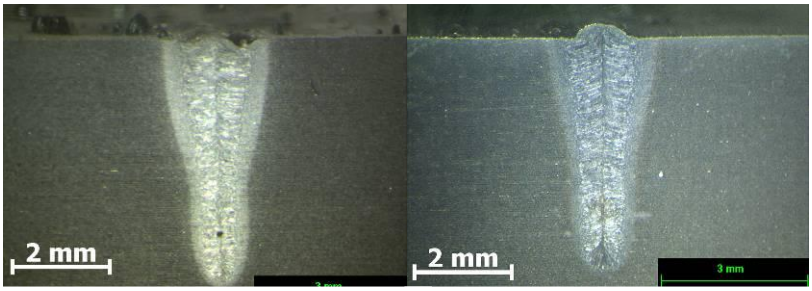

d = 0.5 mm; Ti = 10 ms d = 0.78 mm; Ti = 10 ms

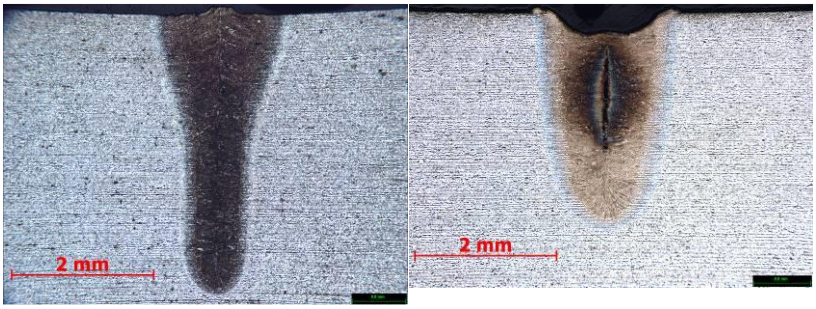

d = 0.5 mm; Ti = 6 ms d = 0.78 mm; Ti = 6 ms

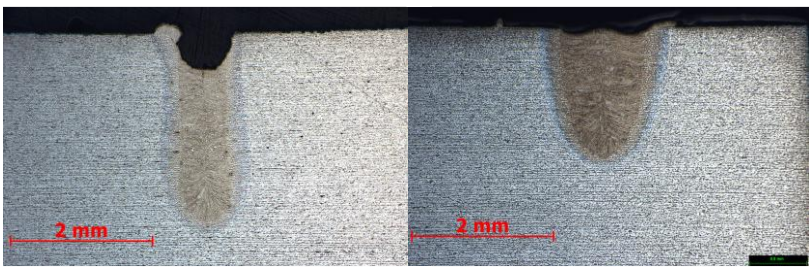

d = 0.5 mm; Ti = 3.8 ms d = 0.78 mm; Ti = 3.8 ms

***Figure 6.9**: Macrographs achieved at a constant power density of 10 MW m^{-1} and various interaction times with two beam diameters of 0.5 mm and 0.78 mm.*

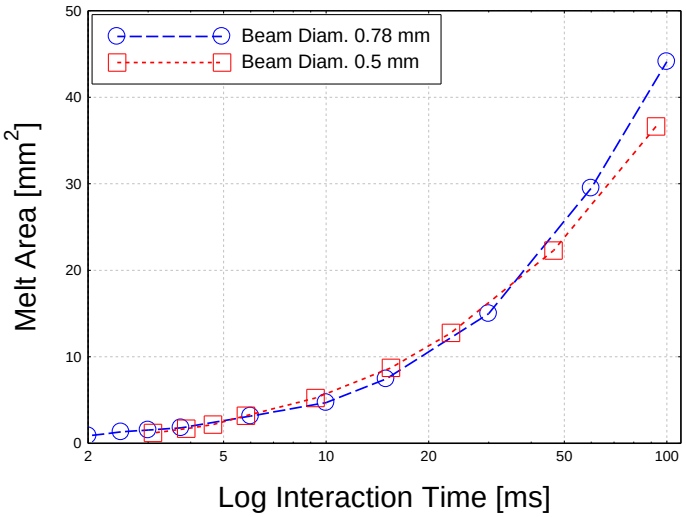

***Figure 6.10**: Melt area as a function of interaction time at 10 MW m^{-1} power factor for two beam diameters of 0.5 mm and 0.78 mm.*

6.6. Discussion

6.6.1. Effect of system parameters on weld profile

Selecting the right parameters and the suitable laser system for a particular laser welding process can be complicated task, due to the variety of parameters that have to be considered. This is even more complicated when using system parameters, such as travel speed and output power. Randomly changed power or travel speed, in order to achieve a desire depth of penetration, leads to unpredictable properties. This was demonstrated in Fig.6.1 (page 163). The weld width, which is important in the case of fit-up tolerance, residual stresses and distortions, in some range of parameters is strongly dependent on the travel speed, whereas in other range is more dependent on the beam diameter. The beam diameter stars affecting the weld width in low carbon steel only as the travel speed exceeds 3 m/min (Fig.6.4 page 165). This effect is dependent on the thermal properties of the material. The travel speed at which the beam diameter starts affecting the weld width decreases with decreasing thermal diffusivity of the workpiece. In addition, different depths of penetration can be achieved at a constant power and travel speed if various beam diameters are used. Thus the beam diameter additionally complicates the parameters

selection issue. This was demonstrated in Fig.6.5. The travel speed or power has to be adjusted appropriately to the beam diameter to achieve a required depth of penetration.

6.6.2. Power factor - application model

All the issues of parameters selection, discussed above, require a new approach. The most sensible solution would need to determine dimensions of a weld in a given material, independent of the beam diameter. The new parameters have to be more flexible than the fundamental laser material interaction parameters from Chapter 5.

Under certain conditions the depth of penetration is proportional to the interaction time and the power factor, and it is almost independent of the beam diameter. The independent character of depth of penetration of the beam diameter at a constant power factor and interaction time was shown in Fig.6.6 and Fig.6.7 (pages 169-170). This means that the same conditions can be achieved on different laser systems with different beam diameters. Furthermore, the effect of travel speed and beam diameter on the weld width can be incorporated in to one parameter, the interaction time. According to Equation 6.2 the interaction time can be altered by changing either the travel speed or beam diameter. Based on this a parameter selection model for the laser keyhole welding process can be formulated, a schematic of which is shown in Fig.6.11.

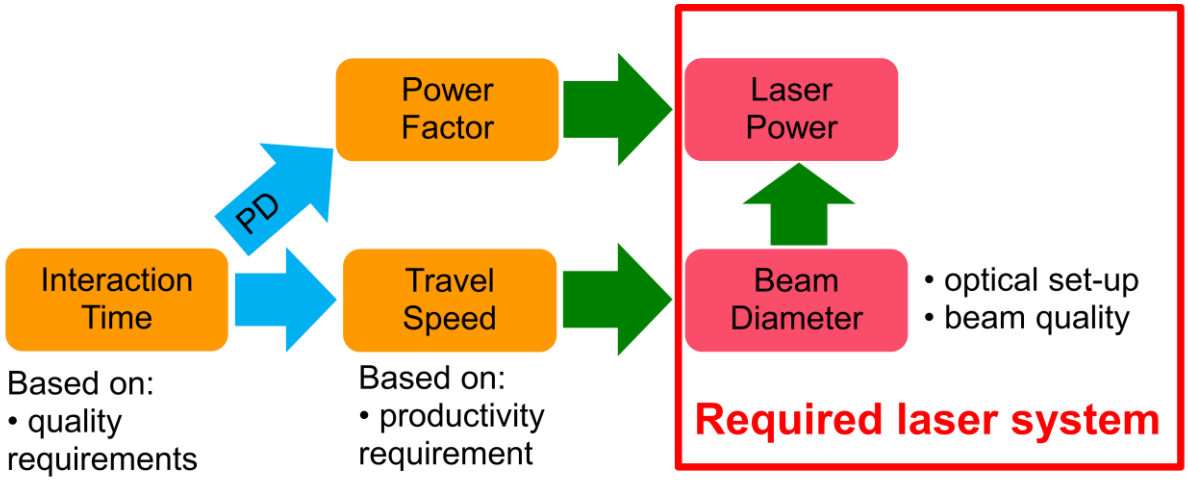

***Figure 6.11**: Parameter selection chart.*

According to the model, first the interaction time is selected based on various criteria. The weld quality in the following discussion refers to the lack of undercut and keyhole-induced porosity, which are mainly dependent on the laser parameters. The effect of interaction time on the weld shape was shown in Fig.6.9 (page 174). The appropriate interaction time is very important since it determines the shape and the properties of a joint. The interaction time is selected according to the quality or the weld profile requirement. Then the travel speed should be selected based on the required productivity. Next, based on the selected combination of interaction time and travel speed, the model will suggest the beam diameter. Note that there is only one beam diameter for every particular combination of these two parameters. If the beam diameter that the model suggests is unrealistic, then other interaction time or travel speed has to be selected. The next step after selecting the interaction time, travel speed and beam diameter is selection of power factor needed to accommodate a particular thickness, from Fig.6.7 or Equation 6.2 (page 170). Finally, the appropriate laser power needed for this power factor and previously chosen beam diameter is selected by the model. It was shown Fig.6.7 that the lower the interaction time the higher the power factor has to be applied for a given depth of penetration. Thus if the suggested laser power is unrealistic a longer interaction time has to be used.

Alternatively, if the beam diameter is fixed then the interaction time determines the travel speed, whilst the power factor will be dependent on the depth of penetration that needs to be achieved. A shorter interaction time leads to a higher productivity, but it requires a higher power factor for a given depth of penetration and also the quality might get compromised. Note that for most applications an excessive power factor would be desire to provide enough energy in the root face of the weld. Therefore to accommodate a thickness of 5 mm it is safer to select parameters for 6 mm of depth of penetration.

Unlike in the standard parametric approach where a particular weld results from the limitations of the laser system, in the power factor model the user decides which type of weld is desired for a particular application and then tries to achieve it. In the parametric approach a particular depth of penetration is usually achieved using a maximum possible travel speed for the available laser power and beam diameter. In the power factor model the appropriate combination of power factor and interaction time can be transferred into the system parameters and achieved on various laser

systems with various beam diameters. This is useful in selecting a laser system. As shown in Fig.6.11 the model suggests the beam diameter and the output power required for the process. By knowing the beam diameter and the optical system it is possible to estimate the beam quality of the laser needed to provide this beam diameter.

6.6.3. Limitation of the power factor

The power factor model has some limitations. It was shown in Fig.6.8 and confirmed on macrographs in Fig.6.9 (page 174) that there were discrepancies in depth of penetration between different beam diameters, despite a constant power factor and interaction time. As far as at very long interaction times this difference did not exceed 10% of the maximum depth of penetration, which is of the order of the experimental error. However, at short interaction times the difference was more significant, reaching up to 25%. This means that the power factor model becomes slightly dependent on the beam diameter as the interaction time decreases below 10 ms. Such an interaction time, with 0.5 mm beam diameter corresponds to a travel speed of 3 m/min. A comparison of Fig.6.5 (page 166) with Fig.6.8 (page 173) demonstrates that the power factor is still by far less sensitive to the variation of beam diameter than the laser power and travel speed.

As mentioned previously the power factor is not one of the laser material interaction parameters. The depth of penetration in laser welding is controlled by the power density (Equation 6.1) and the specific point energy (Equations 6.3). The power density is dependent on the beam diameter as $1/d^2$, whilst the specific point energy is linearly proportional with the beam diameter. Thus as a net result the depth of penetration is linearly proportional to the beam diameter. This explains why the power factor model works. The power factor enables a constant depth of penetration to be maintained when the beam diameter is changed by using a trade-off between the power density and the specific point energy. However, in some conditions, at short interaction times in particular, this trade-off led to up to 25% difference in depth of penetration.

Increasing the beam diameter, at a constant power factor and interaction time, induces a reduction of power density and an increase of specific point energy. As

shown in Table 6.1 for an interaction time of 15 ms and a power factor of 10 MW/m an increase of beam diameter from 0.5 mm to 0.78 mm results in a reduction of power density from 2.55 MW/cm^2 to 1.7 MW/cm^2 and at the same time an increase of specific point energy from 75 J to 125 J. As long as at medium range of interaction times the trade-off between the power density and the specific point energy provides a constant depth of penetration and weld profile, as was shown in Fig.6.9 (page 174), but at some conditions the difference becomes more significant.

***Table 6.1**: Variation of fundamental laser interaction parameters with beam diameter at 10 MW/m power factor of and three different interaction times of 100 ms, 15 ms and 6 ms*

τ_i (ms)	100		15		6	
d (mm)	0.5	0.78	0.5	0.78	0.5	0.78
q_P (MWcm^{-2})	2.55	1.7	2.55	1.7	2.55	1.7
E_{SP} (J)	500	750	75	125	30	46
PD (mm)	11	12.2	6.1	6.3	4.1	2.9

τ_i – interaction time, d – beam diameter, q_p – power density, E_{SP} – specific point energy, PD – depth of penetration.

The two extreme cases from Fig.6.8 and Fig.6.9 (pages 173-174) are shown in Fig.6.12. As mentioned previously the power factor works based on the trade-off between the power density and the specific point energy, when beam diameter varies at a constant power factor and interaction time. This trade-off has its optimum operating range, where the increase of specific point energy almost equally compensates for the drop of power density. In this case the optimum conditions were in a range of interaction times between 10 ms and 50 ms, as shown in Fig.6.12. At this range the achieved welds are the same, in terms of depth of penetration and weld shape. As the interaction time increased beyond 50 ms, for these particular conditions, the higher specific point energy in the case of larger beam diameter provided slightly deeper welds, as compared to the higher power density in the case of smaller beam diameter. This is shown in Fig.6.12 for 100 ms interaction time. Note that the difference in depth of penetration is below 10%, which corresponds to the order of the experimental error. At this long interaction time (0.3 m/min speed for 0.5 mm beam diameter) there is a significant fluctuation of depth of penetration and weld

width caused by the keyhole instabilities, due to the large melt pool. It was shown in Fig.4.16 in Chapter 4 (page 121) in a longitudinal cross section that these fluctuations can be responsible for significant variations of weld depth and width, in case of partially penetrated welds.

The problem becomes more significant as the interaction time decreases below a certain critical level, as shown in Fig.6.12 for 6 ms interaction time. In this range of conditions the difference in depth of penetration reached up to 25%. Looking at macrographs in Fig.6.12 it can be seen that, unlike at long interaction times, in this case the higher power density was more beneficial than the higher specific point energy (Table 6.1). The weld achieved with the smaller beam diameter was still in the keyhole regime, whilst the weld with the larger beam diameter was near the transition between keyhole and conduction regime. At this low energy density conditions (product of power density and interaction time) the specific point energy was not fully utilised for depth of penetration, due to low drilling force. Therefore as the conditions are close to the threshold energy density for the keyhole regime, the higher the power density the longer the process is in the keyhole regime. At this low energy density the trade-off between power density and specific point energy failed to maintain deep penetration. Thus although a larger beam diameter provides more specific point energy for the same power factor and interaction time, but if there is not enough energy density this additional specific point energy is utilised for melting rather than for drilling.

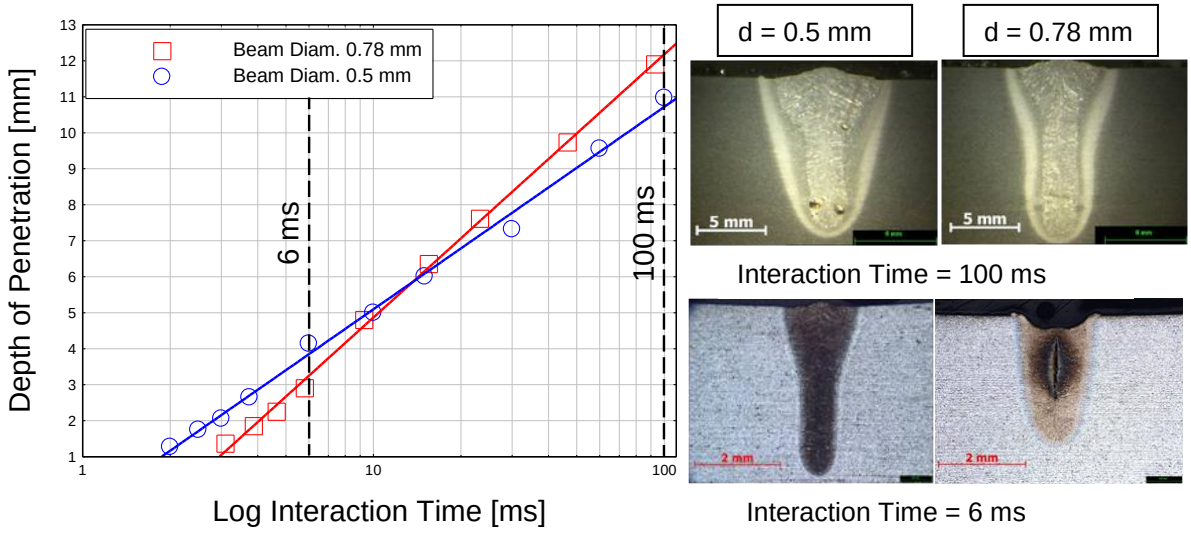

***Figure 6.12**: Effect of beam diameter at constant power factor of 10 MW/m for two beam diameters 0.5 mm and 0.78 mm at two extreme cases of interaction time: 6 ms and 100 ms*

This was also confirmed in Fig.6.10 (page 175), where the same melting rate was achieved regardless of the beam diameter for the entire range of interaction times studied in this chapter, when a constant power factor and interaction time was used. Thus the trade-off between the power density and the specific point energy, as a result of constant power factor and interaction time on different beam diameters, provides the same amount of energy for melting. However, the drilling force determines the ratio between the depth of penetration and the melting rate. Thus if the process is far beyond the threshold energy density, the drilling is efficient and both power density and specific point energy affect the depth almost equally. At this range the power factor provides the same depth of penetration with different beam diameters on the surface.

In contrast, if the process is near the threshold energy density for keyhole regime, high specific point energy will provide a similar melting rate as compared to high power density, but a higher power density will lead to deeper welds. Therefore, it is believed that the difference in depth of penetration at short interaction times in Fig.6.12 is attributed to the shallow character of welds and would diminish at higher levels of power factor, which unfortunately could not be tested on the current laser system, due to the power limit. It can be concluded that the power factor model is limited to the keyhole regime, which is the primary regime used in hybrid laser welding.

6.8 Example on using the power factor model

The power factor model can be useful in determining the parameters needed for a particular application. In this example a butt-weld in 5 mm thick plate is required, according to the requirements presented in Table 6.2. The main impact is put on the quality of the joint rather than on the productivity. The trade-off between the weld width, undercut and porosity is controlled by the interaction time. In general a higher interaction time leads to a better quality, however, an excessive interaction time may lead to a large heat affected zone and distortion. In this case an interaction time of 30 ms is suggested. This should provide enough time to spread the molten metal and

form a uniform bead, whist avoiding the excessive heat dissipation inside the plates, thus minimising distortion.

***Table 6.2**: Requirements assumed in the analysed example.*

Main requirements	Plate thickness	Additional requirements
• Premium quality • No undercut • Low distortion • Desired bead shape	5 mm	• Low investment costs (low output power of laser source) • Filler metal (hybrid welding)

The next step is the selection of the power factor, according to the required depth of penetration. Although in this particular case the plate thickness is only 5 mm but it is recommended to apply a slightly excessive power factor to ensure a uniform root face; therefore, the power factor for 6 mm depth of penetration will be used. According to data from Fig.6.7 (page 170) to achieve 6 mm depth of penetration, at 30 ms interaction time, a power factor of 8 MW/m needs to be used. The system parameters that provide this combination of power factor and interaction time are shown in Fig.6.13. The bigger the beam diameter the more the laser power needs to be applied, but on the other hand, bigger beam diameters enable an improvement in productivity.

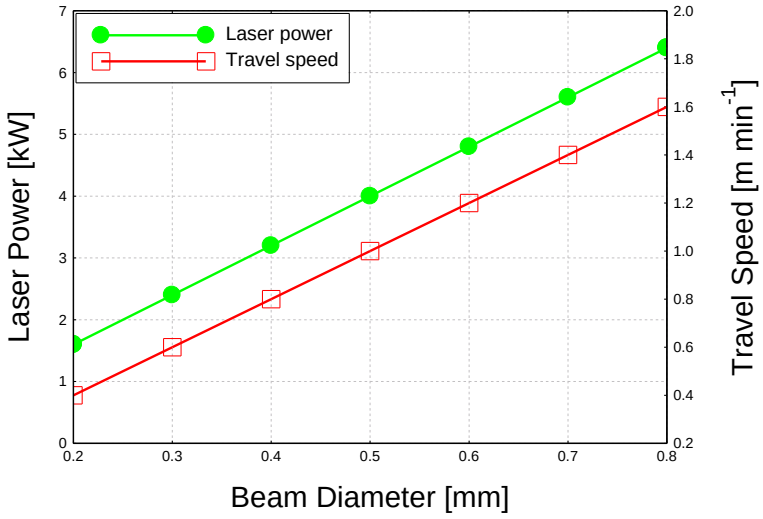

***Figure 6.13**: Dependence of laser power and travel speed required for 30 ms interaction time and 8 MW/m power factor with beam diameter.*

Since low investment cost of the laser system is one of the main requirements in the example analysed here, the following combination of parameters is selected:

- 3 kW of power,
- 0.4 mm beam diameter
- 0.8 m/min travel speed

Additionally in hybrid laser/MIG welding the MIG conditions will determine the shape of the top bead. This will be dependent on the bevel shape and the gap between joined components. In this case we assume no gap between the plates and no bevel. In Fig.6.14 the effect of deposition rate of MIG process on the shape of the hybrid weld is shown. It can be seen that for the initially selected travel speed of 0.8 m/min, a reinforcement of 8 mm^2 requires an approximately 3 kg/h deposition rate. Note that for a wire diameter of 1 mm this deposition rate corresponds to 8 m/min wire feed speed, which is achievable with a standard MIG power source. However, if a wider bead was required or the MIG power source could not provide this deposition, the travel speed would have to be decreased and the parameters reselected. In thick section welding, with bevels in particular, the overall travel speed of hybrid welding will be limited by the deposition rate of the filler metal. In this particular example the parameters do not have to be corrected according to the limits of the arc source.

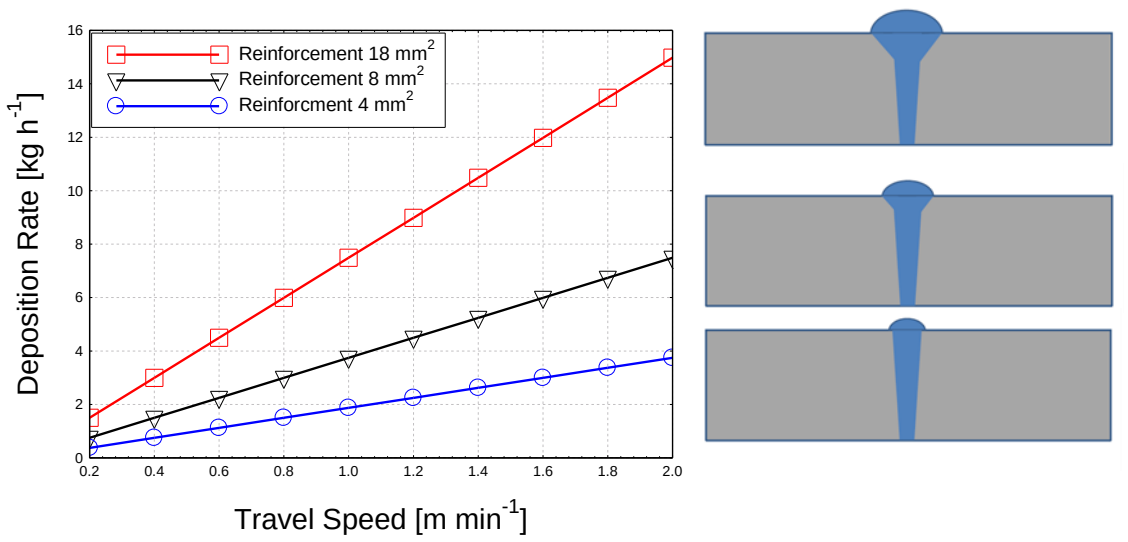

***Figure 6.14**: Effect of deposition rate of MIG source on weld shape.*

Selecting a suitable laser system for a particular job is another important issue in laser processing. In most cases the user wants to buy as cheap laser as possible. There are two main factors affecting the price of the laser system. The first is the output power and the second is its focus-ability, which is determined by the optical set-up and beam quality. There is a fundamental question in laser macro-welding: is it better to use a laser with a higher output power or is it more beneficial to reduce the beam diameter? The common logic resulted from the consideration of power density only, have driven laser manufacturers towards improving the focus-ability of lasers. Since the power density is proportional to the output power and beam diameter, according to P_L/d^2 (Equation 6.1), it might imply that the reduction of beam diameter has more effect on the process than the increase of laser power. However, the results from Chapter 5 suggest that not only the power density controls the depth of penetration but also the specific point energy (Equation 6.3). Thus with decreasing beam diameter the power density increases and the specific point energy decreases simultaneously, whereas with increasing laser power both power density and specific point energy increase. This shows that in most cases it is more beneficial to increase the laser power than to decrease the beam diameter.

The power factor model can be useful in finding the trade-off between laser power and beam diameter, with respect to a particular application. Such a trade-off for 6 mm of depth of penetration, calculated based on the power factor and interaction time (Equation 6.5) is shown in Fig.6.15.

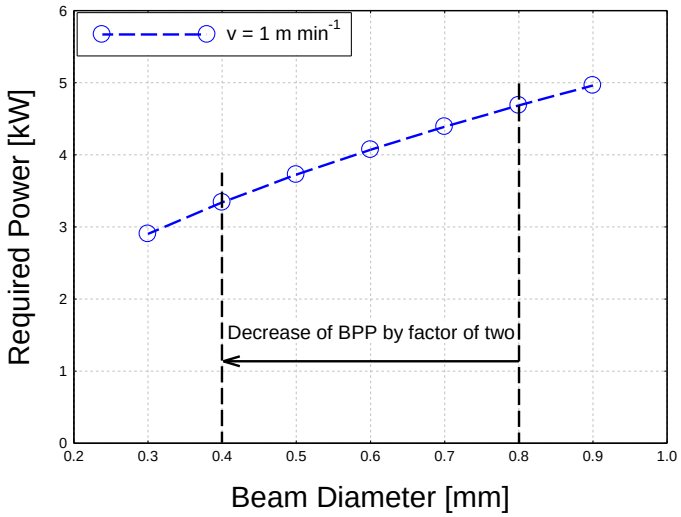

***Figure 6.15**: Trade-off between beam diameter and laser power required for 6 mm depth of penetration.*

It can be seen that an increase of beam diameter from 0.4 mm to 0.8 mm can be compensated by an increase of laser power by approximately 40%. Although a reduction of beam diameter is often seen as more advantageous than an increase of laser power, however, the beam diameter is limited by the beam quality of the laser source and the optical set-up. In some cases it might be more difficult to reduce the beam diameter than to increase the laser power. The power factor model enables the user to estimate the benefits of either.

Chapter 7. Joining efficiency and residual stresses in laser and hybrid laser welding

The quality of autogenous laser welds is often insufficient, thus there is a considerable interest in hybrid laser processes. Laser welding can produce efficient welds with a high aspect ratio, due to the high energy density of the laser source. However, in order to obtain a high quality weld, which is less sensitive to the fit-up tolerance, the narrow welds produced by the laser welding are not always desired, particularly in case of thick sections. On the other hand, hybrid process, where the laser is combined with a conventional arc-based welding process, offers better weld quality than autogenous laser welding. However, in order to fully utilised benefits of hybrid laser welding, in comparison to arc-based welding processes, the effect of additional heat input from the arc on the residual stress has to be assessed.

The interactions between laser and arc were widely studied previously. This was reviewed in Section 2.6. However, in none of these studies was laser welding compared with hybrid welding for the same overall heat input. In this chapter laser welding with 7 kW power is evaluated against the hybrid welding with the same overall power. Furthermore, the combination of laser and autogenous TIG source enables a more direct study of the heat effects on the residual strains without the influence of filler metal.

Residual stress and distortion of autogenous laser welding and laser hybrid welding are investigated in this chapter. It was shown in Chapter 5 that the fundamental parameters in laser welding that control depth of penetration and width of the fusion zone are the power density, specific point energy and interaction time. However, in some cases it is difficult to measure the size of the heat source on the surface, in particular in arc welding where it may vary with the applied current, voltage, stick-out distance, surface conditions, shielding gas and etc. Thus in this chapter the heat input per unit length, as the ratio of the applied power to the travel speed, is used to characterise the hybrid process. Additionally a new parameter referred to as joining efficiency, which combines the heat input with depth of penetration is used. This parameter is defined as the ratio of the depth of penetration to the heat input. The

relationship between joining efficiency and residual stress is investigated. In further part the autogenous laser welding process is compared against the hybrid laser/TIG welding. The trade-off between fit-up tolerance and distortion is analysed.

7.1. Experimental set-up

7.1.1. Welding

The experimental set-up and specifications of the laser system, as well as the Tungsten Inert Gas (TIG) source used in hybrid laser welding can be found in Chapter 3. A range of beam diameters from 0.38 mm to 0.78 mm achieved by using a set of lenses with focal lengths ranging from 150 mm to 300 mm was used. A set of bead-on-plate welds in 250x50x12 mm^3 S355 low carbon steel, 304 stainless steel and 7075 aluminium alloy was made. All tests, including the hybrid trials, were carried out without any filler wire. Every weld was made on a separate plate. To ensure a stable welding process over the full length of the workpiece, start and stop plates were used, as shown in Fig.7.1. The specimens were clamped along the whole length and no backing bar was used. All welds were sectioned, polished and examined under an optical microscope in order to measure depth of penetration.

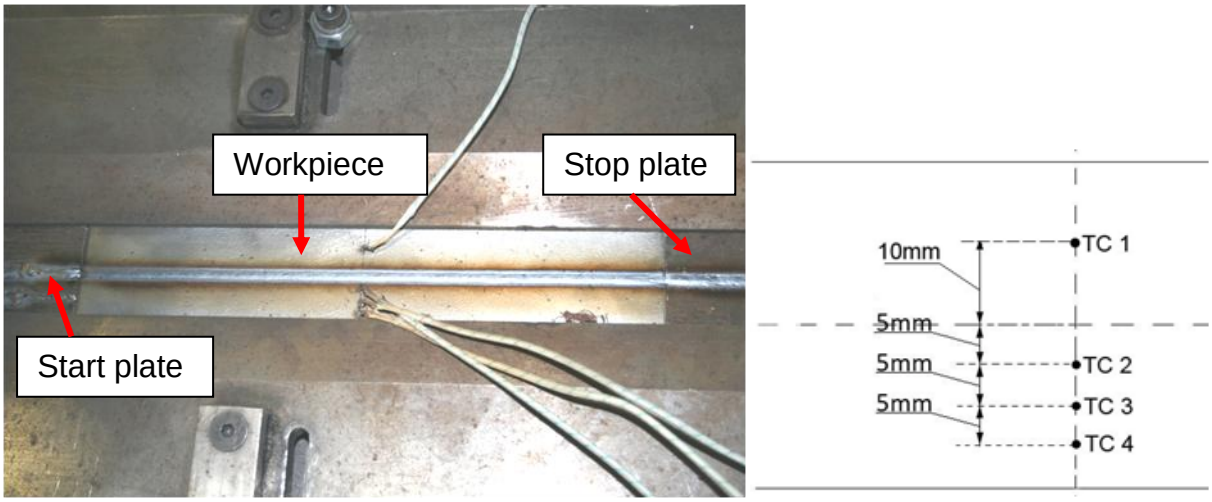

***Figure 7.1**: Experimental set-up and distribution of thermocouples.*

A tungsten inert gas (TIG) operated in DC electrode negative was used as a secondary heat source in the hybrid laser welding. The hybrid process was operated in the laser leading configuration with the TIG torch being inclined at 30° push direction. The heat inputs of the laser process, as well as of the TIG process were calculated as the ratio of the applied power to the travel speed, without taking account of transfer efficiency. The applied power of the TIG process was calculated from the average voltage and current, which were measured using an oscilloscope, more details of which can be found in Section 3.9. In some cases the temperature distribution was recorded with K-type thermocouples. The thermocouples were attached at 5 mm, 10 mm and 15 mm from the weld centreline, as shown in Fig.7.1. Micro-hardness across in the weld centreline at 2 mm below the surface was measured, according to the Vickers method with a load of 500g and a dwell time of 15 sec. More detailed description of the welding parameters will be shown in the methodology of each subsection.

7.1.2. Residual strain measurement

Neutron diffraction measurement was carried out at the ENGIN-X strain scanner at the spallation neutron source at ISIS, RAL, Oxford, UK. The details of ENGIN-X could be found elsewhere [427, 428]. A schematic of the detection unit is shown in Fig.7.2. On this equipment multiple diffraction peaks are analysed simultaneously, which allows the texture of a material to be considered. In the present experiment a time of flight (TOF) range of 20-40 ms was used which resulted into an inter-planar spacing of 1.1 to 2.1 Å. The (110), (200) and (211) families of crystallographic planes were analysed. An incoming beam dimension of 2 mm × 2 mm was used for the longitudinal and normal strains measurement which allowed for the measurement of variations in strains at an appropriate length scale. A 2 mm collimator was used for all the measurements, which resulted in a cuboid gauge volume of 2×2×2 mm^3. For the transverse strain measurement the gauge volume of 2x2x10 mm^3 was used. Refinement of the diffraction spectrum was performed using the General Structure Analysis System (GSAS) programme which gave an average lattice parameter (*a*) of the irradiated volume [429].

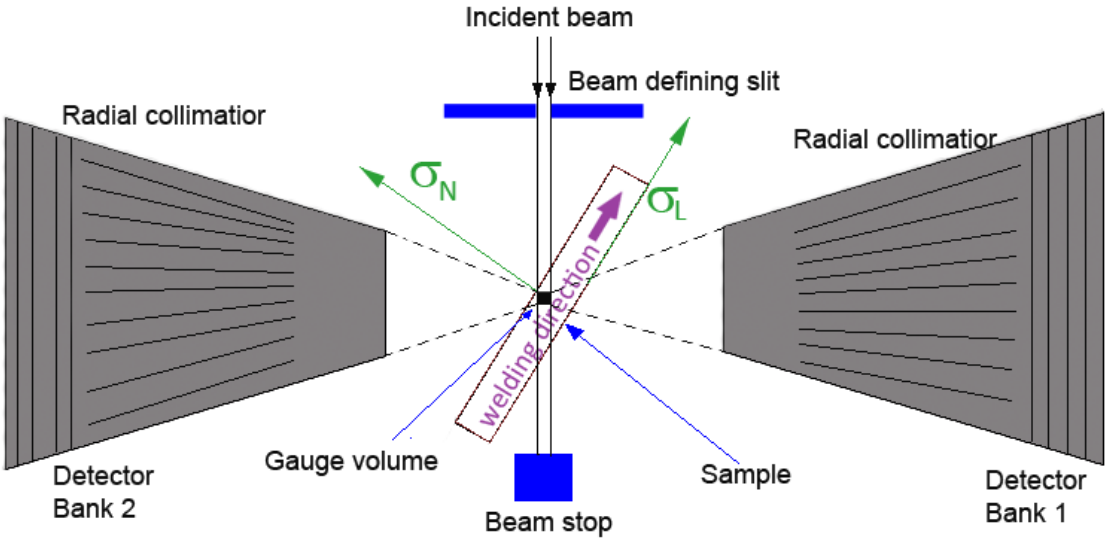

***Figure 7.2**: Relationship between sample position relatively to the detectors and principal direction of strains on ENGIN-X neutron diffraction facility.*

The parent metal was used as a reference stress free sample. The strains in longitudinal ε_L, normal ε_N, and transverse ε_T directions were calculated from the lattice parameters a_L, a_N and a_T with respect to the reference stress-free sample a_0, according to:

$$\varepsilon_{L,N,T} = \frac{a_{L,N,T} - a_0}{a_0} \qquad 7.1$$

To minimise the time needed for set-up, the specimens were mounted in coupons, as shown in Fig.7.3(a). The residual strains were measured in the middle of the weld length. The gauge volume was focused 2 mm under the top surface and the samples were approximately translated to acquire strains across the weld centre line, as shown in Fig.7.4. Additional measurements at different depths from the surface were performed on two selected samples. The direction at which the residual strains are analysed in the neutron diffraction technique depends on the position of the sample with respect to the detectors. According to Fig.7.2 two directions of diffraction can be measured simultaneously on the Engin-X source. Therefore the residual strains in two principal directions, longitudinal and normal were measured in majority of samples.

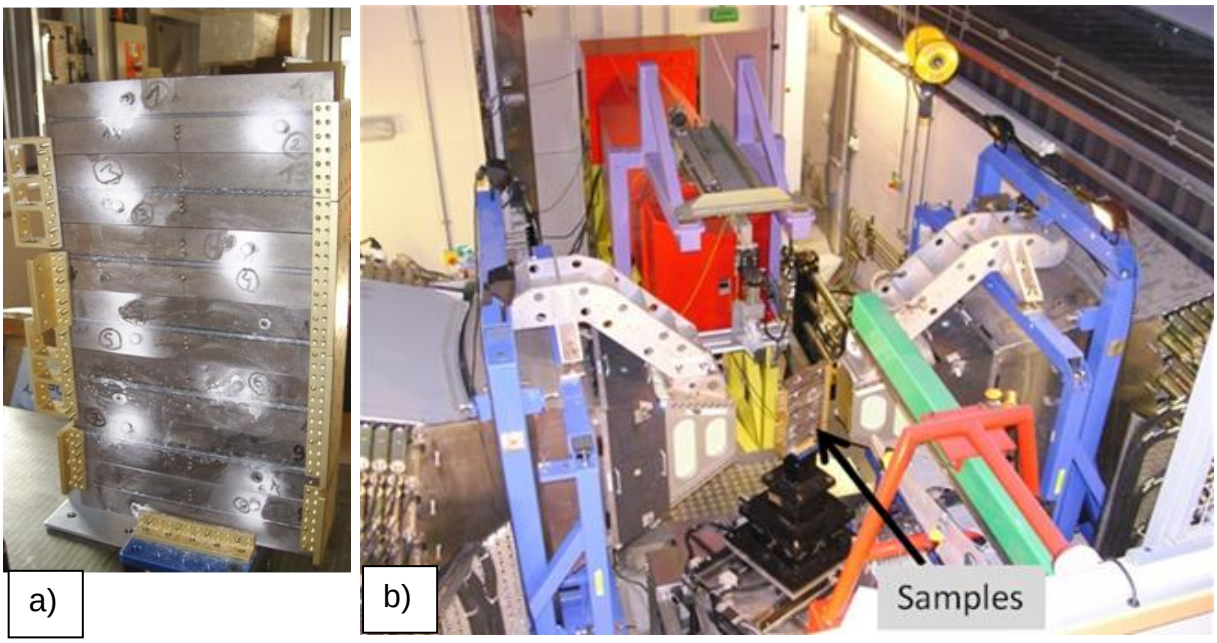

***Figure 7.3**: Experimental set-up used for residual strain analysis; **a)** arrangement of samples into coupons; **b)** view of samples mounted on the translation stage between the detectors.*

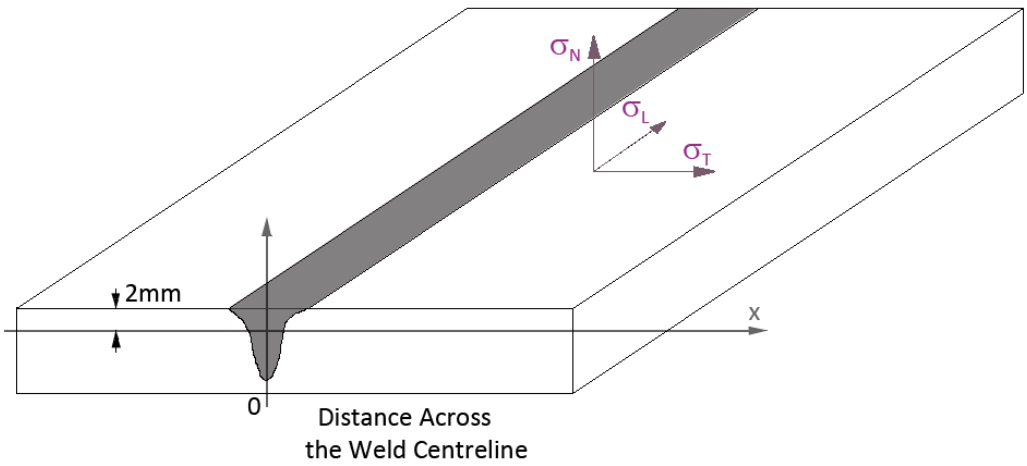

***Figure 7.4**: Position of the gauge volume during measurement and direction of three principal strains (longitudinal, normal and transverse) in sample.*

7.2. Efficiency parameters

7.2.1. Joining efficiency

The same depth of penetration in laser welding can be achieved with different combinations of parameters, which correspond to different values of heat input per unit length. Furthermore, for the same heat input per unit length (ratio of the laser power to the travel speed) different depths of penetration can be achieved, particularly in laser welding where different beam diameters can be applied. Thus although the heat input is insufficient to specify the dimensions of the fusion zone, it is widely used to characterise various welding processes.

In order to characterise a welding process in terms of energy utilised for making the joint, we use the term joining efficiency. The joining efficiency defines how much energy per unit length of a particular process is utilised per unit of depth of penetration. Thus the joining efficiency is equal to the ratio of the depth of penetration (**PD**) to the heat input per unit length (**HI**), which in terms of welding parameters corresponds to the ratio of depth of penetration (**PD**) and welding speed (**v**) to the output power ($\mathbf{P_L}$) and is given by Equation 7.2.

$$JE = \frac{PD}{HI} \quad \frac{[m]}{[J\ m^{-1}]} = \frac{PD}{P_L / v}[m^2 J^{-1}] \qquad 7.2$$

Consequently a high joining efficiency for a given depth of penetration corresponds to a low heat input. In practice it should also mean low residual stress and distortion. The conditions at which a maximum joining efficiency is reached ensure the weld with the highest aspect ratio of depth to width and with a relatively low heat input. The joining efficiency can be calculated for every welding process, thus it can be used to compare different processes and to find the most efficient way of joining a particular component. In this study the joining efficiency is used to compare laser welding with hybrid laser welding.

7.2.2. Melting efficiency

In some processes, such as cladding or conduction welding, in which the melting rate rather than the depth of penetration is more important, the joining efficiency may lead to ambiguous results. In these cases the melting efficiency can be used to evaluate the utilisation of energy used for the process. The melting efficiency is equal to the ratio of the melting area of a weld cross section (**MA**) to the heat input per unit length (**HI**), which in terms of welding parameters corresponds to the ratio of melting area (**MA**) and welding speed (**v**) to the output power (**P**) and is given by Equation 7.3.

$$ME = \frac{MA}{HI} \quad \frac{[m^2]}{[J\ m^{-1}]} = \frac{MA}{P_L / v}[m^3 J^{-1}] \qquad 7.3$$

7.3. Effect of joining efficiency and melting efficiency in laser welding

A particular component with a given thickness can be accommodated with various welding methods and parameters, leading to different joining efficiency values. In this section the joining efficiency of various welds achieved with different combinations of parameters and with different beam diameters is investigated.

7.3.1. Methodology

The joining and melting efficiencies were calculated based on the welding parameters and depths of penetration or melting areas obtained from the macrographs, according to Equation 7.2 and 7.3. First, the effect of interaction time on the joining efficiency at constant beam diameter of 0.63 mm and power density was studied. This was carried out on a set of bead-on-plate welds in low carbon steel. The interaction time was varied by changing the travel speed from 0.3 m/min to 15 m/min. Three different power densities were used: 0.64 MW/cm^2, 1.6 MW/cm^2 and 2.6 MW/cm^2 corresponding to the following laser powers: 2 kW, 5 kW and 8 kW.

Then the effect of beam diameter at a constant power density of 1.7 MW/cm^2 achieved with two beam diameters of 0.38 mm and 0.78 mm was investigated. To achieve this power density with these beam diameters, the following laser powers were applied: 2 kW and 8 kW. The interaction time was varied by changing the travel speed from 0.3 m/min to 15 m/min.

Next, a similar experiment with a constant power factor of 10 MW/m and two beam diameters of 0.5 mm and 0.78 mm was analysed. To achieve the required power factor with these beam diameters, laser powers of 5 kW and 8 kW were applied respectively.

Finally, the effect of material properties was evaluated. Three different materials, S355 low carbon steel, 304 stainless steel and 7075 aluminium were compared at constant welding conditions. The joining and melting efficiencies were calculated for each of the materials, according to Equation 7.2 and Equation 7.3. The parameters included a constant power density of 2.6 MW/cm^2 (corresponding to 8 kW of power) and beam diameter of 0.63 mm. The interaction time was changed by varying the travel speed.

7.3.2. Results

A typical plot of joining efficiency as a function of interaction time is shown in Fig.7.5. It can be seen that the joining efficiency initially increases with increasing interaction time and then after reaching a maximum tends to decrease again. A similar trend can be observed for the aspect ratio, calculated from macrographs as the ratio of the depth of penetration to the weld width. It can be seen that the aspect ratio of the welds and the joining efficiency of the process are in close relationship, as they exhibit maximum values at the same interaction time. This will be discussed in Section 7.8.1

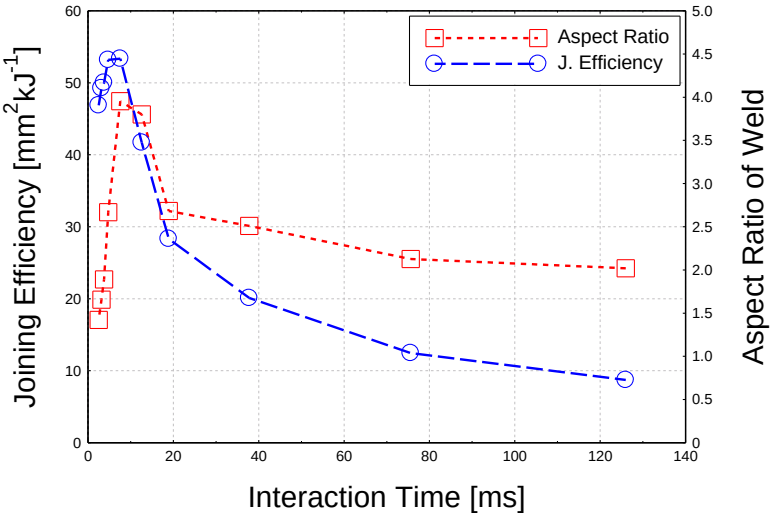

***Figure 7.5**: Joining efficiency and aspect ratio of a weld as a function of interaction time at 1.6 MW cm^{-2} power density of and 0.63 mm beam diameter.*

As shown in Fig.7.6 at a constant beam diameter the joining efficiency is almost independent of the power density. The joining efficiency of both processes with power densities of 1.6 MW/cm^2 and 2.6 MW/cm^2 exhibit their maximum at the same interaction time of 7 ms. In contrast, the joining efficiency of the process with 0.64 MW/cm^{-2} power density is significantly lower at short interaction times and then after the interaction time exceeds 12 ms the same efficiency is exhibited for all three power densities.

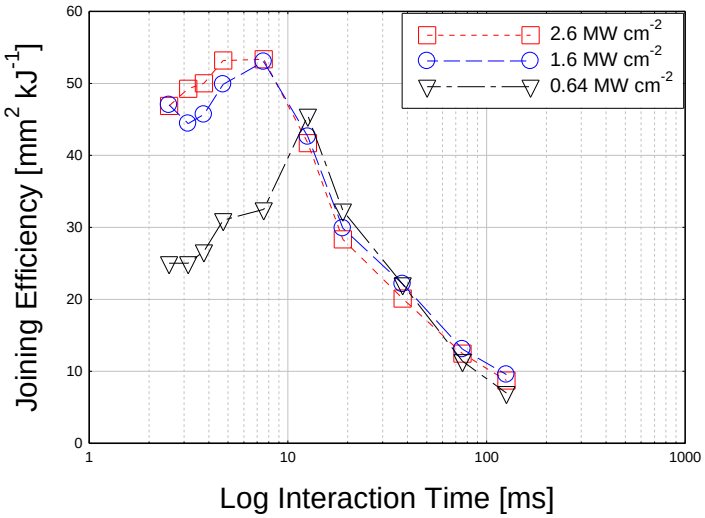

***Figure 7.6**: Joining efficiency as a function of interaction time for three power densities 2.6 MW cm^{-2} (8 kW), 1.6 MW cm^{-2} (5 kW), 0.64 MW cm^{-2} (2 kW) and a constant beam diameter of 0.63 mm.*

The effect of beam diameter on the joining efficiency at a constant power density is shown in Fig.7.7. The process with a smaller beam diameter exhibits a higher joining efficiency only at short interaction times and then after the interaction time exceeds approximately 10 ms both curves for both beam diameters show the same joining efficiencies. A similar behaviour occurs when two different beam diameters are used at a constant power factor, as shown in Fig.7.8. The process with a smaller beam diameter shows a higher joining efficient only at short interaction times.

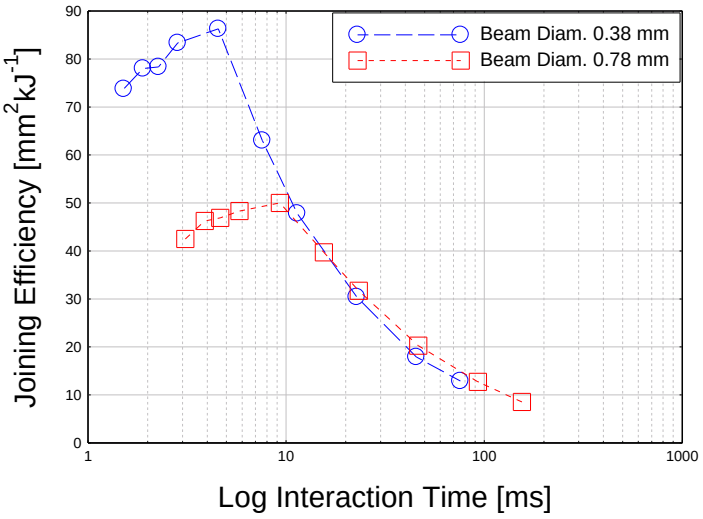

***Figure 7.7**: Joining efficiency as a function of interaction time for two beam diameters of 0.38 mm and 0.78 mm and a constant power density of 1.7 MW cm^{-2}.*

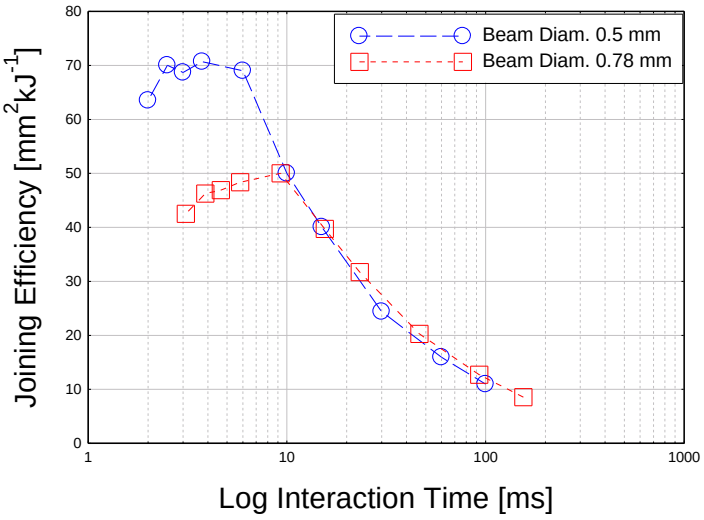

***Figure 7.8**: Joining efficiency as a function of interaction time for two beam diameters of 0.5 mm and 0.78 mm and a constant power factor of 10 MW m^{-1}.*

Fig.7.9 shows that the optimum interaction time, at which the joining efficiency reached the maximum value, is approximately the same for all materials. However, there is a significant difference in the magnitude of joining efficiency between the materials. The greatest joining efficiency is exhibited in the case of aluminium, followed by stainless steel and then low carbon steel, in almost entire range of interaction times. Unlike the joining efficiency, the melting efficiency does not exhibit any maximum; instead a stable value over the entire range of interaction times can be seen in Fig.7.10. The aluminium alloy outclassed both steels in terms of melting efficiency. Macrographs of the corresponding welds for 7.6 ms interaction time (5 m/min) are shown in Fig.7.11. It is confirmed that the aluminium alloy exhibits the largest fusion zone.

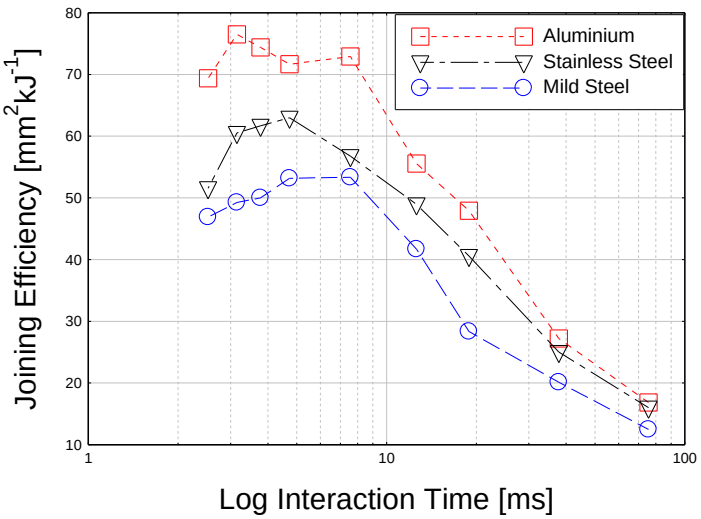

***Figure 7.9**: Joining efficiency as a function of interaction time at constant power density of 2.6 MW cm^{-2} and beam diameter of 0.63 mm for different materials.*

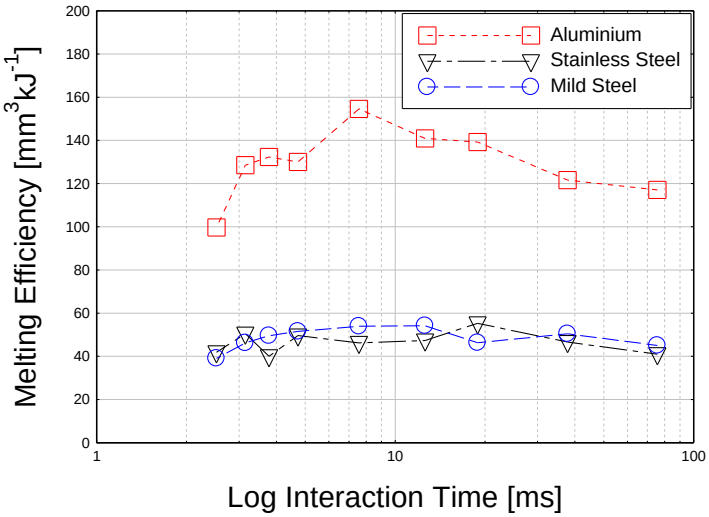

***Figure 7.10**: Melting efficiency as a function of interaction time at constant power density of 2.6 MW cm^{-2} and beam diameter of 0.63 mm for different materials.*

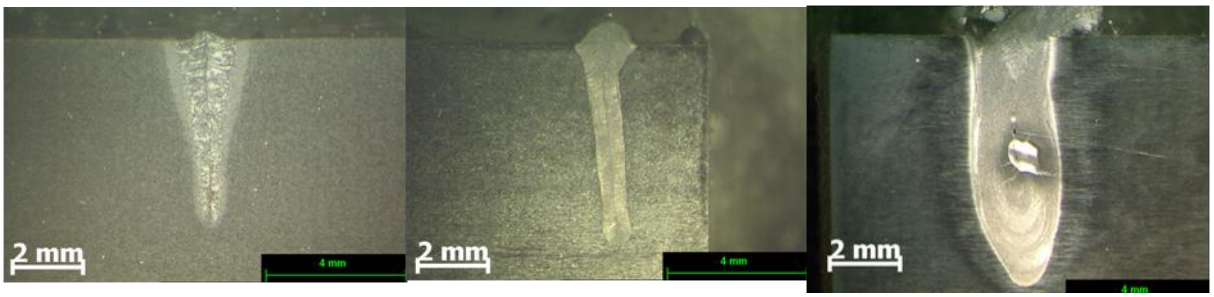

***Figure 7.11**: Macrographs of laser welds with constant power density of 2.6 MW cm^{-2}, interaction time of 12.6 ms and beam diameter of 0.63 mm for different materials: **a)** S355 low carbon steel, **b)** 304 stainless steel, **c)** 7075 aluminium.*

7.4. Comparison of laser welding with hybrid laser welding

The aim of this section is to compare the joining efficiency and the residual strains of autogenous laser welding and hybrid laser/TIG welding, for the same applied heat input. The hybrid laser welding is often found to be more reliable process, in terms of fit-up tolerance and general quality than the laser welding. However, the additional heat input may lead to issues with residual stress and distortion. In order to investigate the relationship between weld quality, heat input and residual strain generation, a series of laser and hybrid welds were produced. Different sets of welding parameters were used to produce bead-on-plate welds with different aspect

ratios and bead characteristics. Since it is difficult to specify the diameter of the arc on the surface, which is required to calculate the power density and other interaction parameters, therefore the heat input is used in this study. By doing so two welding processes can be compared directly, as long as the beam diameter on the surface is kept constant.

7.4.1. Methodology

A number of samples were analysed with varying heat input and manufactured using laser and laser/TIG hybrid process. The welding conditions can be broadly divided into three groups: laser welding with 4 kW power, laser welding with 7 kW power and hybrid laser/TIG welding with 7 kW overall power, which included 4 kW from laser and 3 kW from TIG. The latter combination of conditions allowed a direct comparison of laser and hybrid laser welding for the same heat inputs. In all cases a constant beam diameter of 0.63 mm was used. Travel speed was varied between 1-8 m/min for each of the processes. The material was S355 low carbon steel. All tests, including the hybrid trials were carried out without any filler wire.

In the further tests the residual strains of all three processes (laser welding with 4 kW and 7 kW power and hybrid welding with 7 kW overall power) were investigated, at the conditions required for the same depth of penetration of 6 mm. The parameters of every process were separately adjusted to achieve this particular depth of penetration. A travel speed of 1 m/min was used for the laser welding with 4 kW of power and the hybrid laser/TIG with 7 kW of overall power, whilst in the case of laser welding with 7 kW of power the same depth could be achieved with 3 m/min travel speed.

Since the objective of this work was to correlate the residual strain generation for different kind of welding processes with a range of heat inputs, rather than the quantitative calculation of residual stress, thus the residual strains only in one direction were analysed. In welding the residual stresses and therefore strains are the most significant in the longitudinal direction, which is the same as the welding direction. Thus the longitudinal strain measurement was carried out and compared for different welding processes, as it would give a proportional indication of the

longitudinal stress state. The gauge volume of 2x2x2 mm^3 was focused 2 mm below the surface of the specimens.

The Vickers hardness measurement at 2 mm under the top surface with a load of 500 g and a dwell time of 15 s was carried out on the specimens.

7.4.2. Results

7.4.2.1. Residual strains

The investigated processes were analysed in terms of joining efficiency and longitudinal residual strain generation. The results of joining efficiency are presented in Fig.7.12. Note that in this case the joining efficiency is plotted as a function of travel speed, due to difficulties with evaluation of the diameter of the arc source, which is required for the calculation of interaction time and other interaction parameters of the hybrid process. The laser welding with 4 kW power and the hybrid welding with 7 kW overall power (4 kW laser and 3 kW TIG) show a maximum joining efficiency at the same travel speed of approximately 4 m/min. The laser welding with 7 kW power shows a maximum joining efficiency at approximately 6 m/min. It can be also seen in Fig.7.12 that the joining efficiency of the hybrid process is up to three times lower, in comparison with both laser processes.

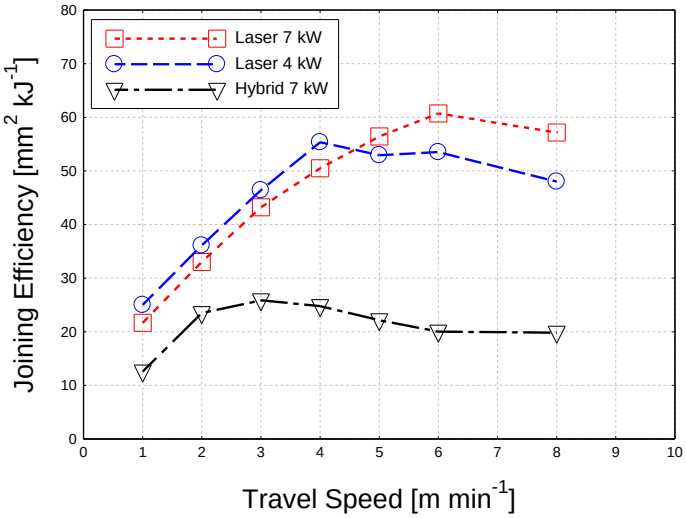

***Figure 7.12**: Joining efficiency as a function of travel speed: laser welding with 7 kW of power, laser welding with 4 kW of power and hybrid laser/TIG with 7 kW of overall power (4 kW laser and 3 kW TIG).*

However, the hybrid process exhibits the best bead quality corresponding to the lowest sensitivity to fit-up, despite the fact that no filler wire was used. Macrographs of corresponding welds are shown in Fig.7.13. It can be seen that although the hybrid process had much higher heat input than 4 kW autogenous laser process, the depths of penetration obtained for the same travel speed are similar. At all travel speeds the greatest depths of penetration were achieved in case of 7 kW laser process. In Fig.7.14 the cross sectional areas of the fusion zones, measured from macrographs, are compared. A larger fusion zone of 7 kW laser welds, as compared to the corresponding 7 kW hybrid welds is evident.

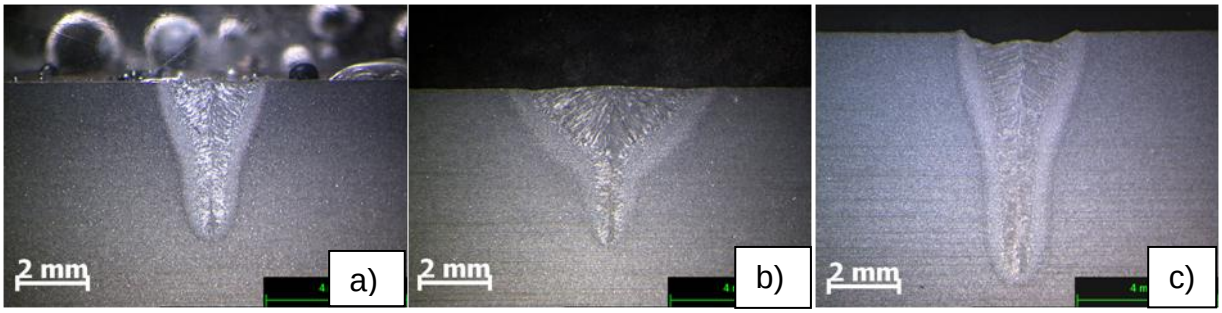

***Figure 7.13**: Macrographs at a constant travel speed of 2 m min^{-1};*
***a)** laser 4 kW (120 J mm^{-1}); **b)** hybrid 7 kW (210 J mm^{-1}); **c)** laser 7 kW (210 J mm^{-1})*

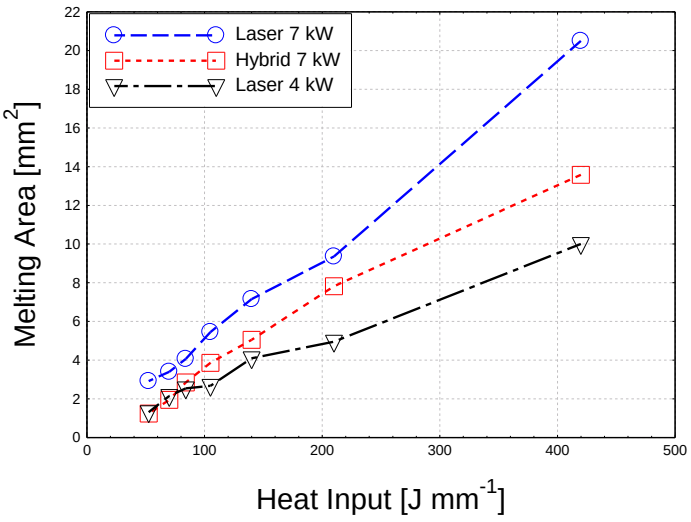

***Figure 7.14**: Cross sectional area of fusion zone measured from macrographs as a function of heat input for three welding processes.*

In Fig.7.15 the longitudinal strains, measured 2 mm below the top surface of 7 kW autogenous laser welds as a function of the distance from the weld centre line and the travel speed are plotted. The travel speed seems only to affect the width of the longitudinal tensile strain curve, with it reducing as the travel speed increases. In contrast, the peak magnitude of the tensile strain remains almost constant. This can be also seen in Fig.7.16 where the area under the longitudinal tensile strain curve for all three processes is plotted against the travel speed. There are two important aspects to notice in this figure. First, the area of the tensile strain reduces with increasing travel speed (decreasing heat input). Second, the tensile strain of 7 kW autogenous laser welding and 7 kW hybrid welding are similar, whereas in the case of 4 kW autogenous laser welding the area of the tensile peak is significantly lower.

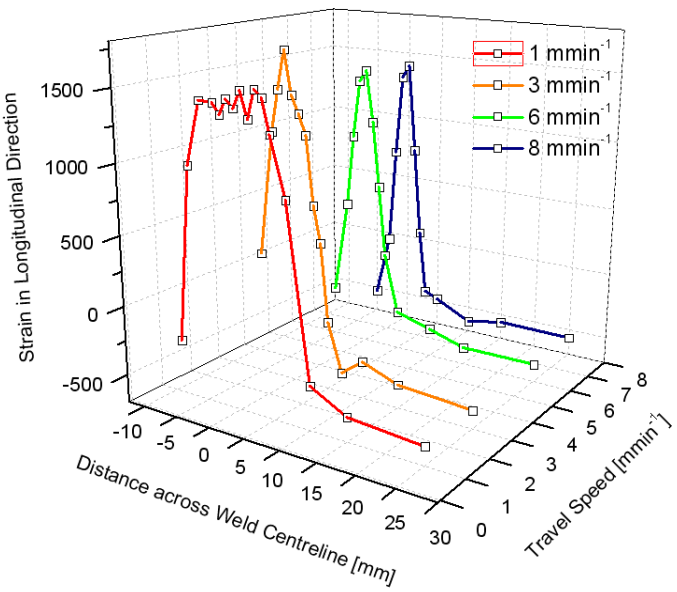

***Figure 7.15**: Longitudinal strain profile as a function of position across the weld centre and travel speed, produced with 7 kW of laser power*

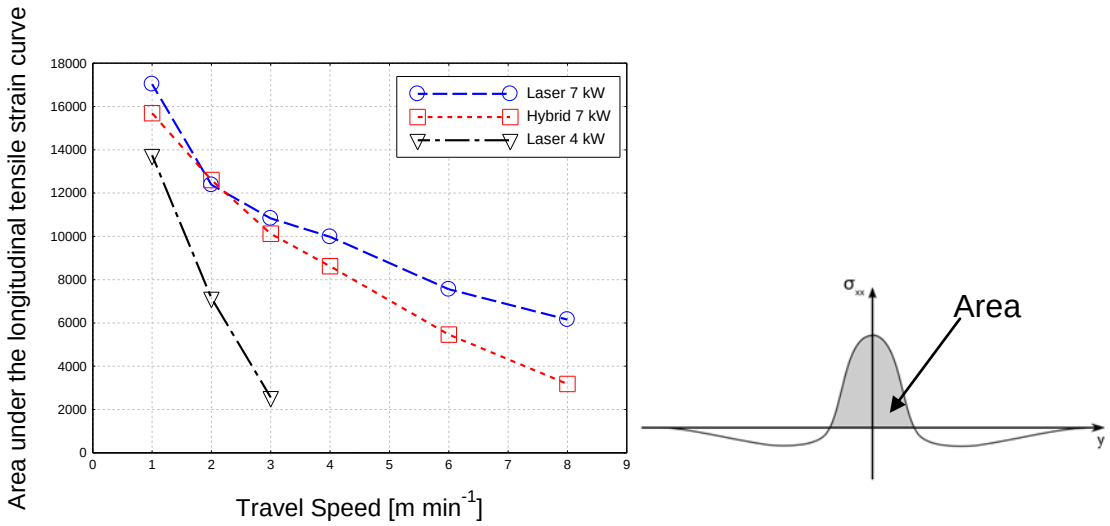

***Figure 7.16**: Area under the longitudinal tensile strain curve as a function of travel speed for: laser welding with 4 kW of power, laser welding with 7 kW of power and hybrid welding with 7 kW of total power*

The reduction of heat input and residual strain with increasing travel speed occurs irrespectively of the depth of penetration. Therefore, the results in the next part are presented in a way to enable a direct comparison of different welding processes for the same depth of penetration. In this test the travel speed of different processes (laser welding with 4 kW and 7 kW of power and hybrid welding with 7 kW of overall power) was varied to obtain the same depth of penetration of 6 mm, as described in the methodology in Section 7.4.1. The macrographs are presented in Fig.7.17. It is worth noticing that the weld obtained with 7 kW laser power (Fig.7.17c) is narrower that the weld obtained with 4 kW laser power (Fig.7.17a). The applied heat inputs per unit length in the laser welding with 4 kW power, hybrid welding with 7 kW power and laser welding with 7 kW power were: 240 J/mm, 420 J/mm and 140 J/mm respectively. In Fig.7.18 the longitudinal strains of the corresponding specimens are plotted. The largest longitudinal tensile strain profile is exhibited in the case of hybrid weld, whereas the smallest longitudinal strain profile is shown by 7 kW laser weld.

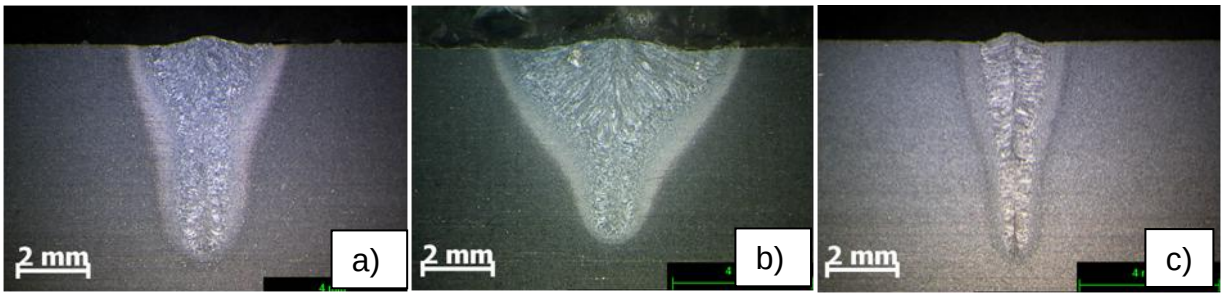

***Figure 7.17**: Macrographs for combination of parameters required for 6 mm depth of penetration: **a)** laser welding 4 kW, 1m min^{-1} (240 J mm^{-1}); **b)** hybrid welding 7 kW, 1 m min^{-1} (420 J mm^{-1}); **c)** laser welding 7 kW, 3 m min^{-1} (140 J mm^{-1})*

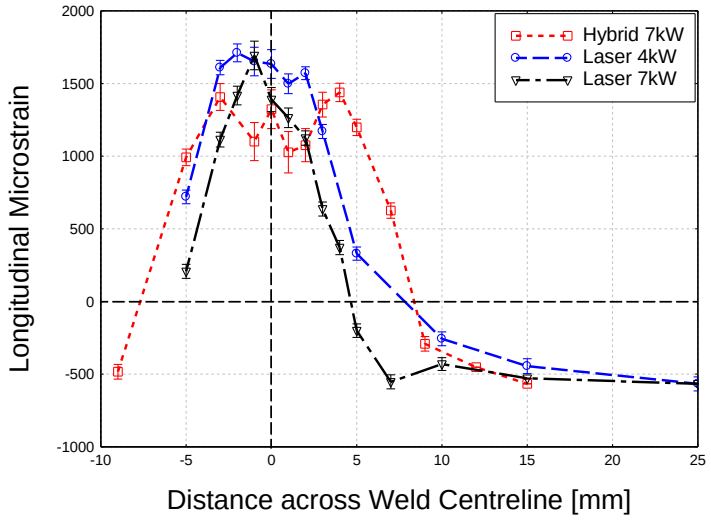

***Figure 7.18**: Comparison of longitudinal strains between three processes for combination of parameters required for 6 mm depth of penetration.*

The applied heat input per unit length as a function of depth of penetration is shown in Fig.7.19 (the dashed line indicates a depth of penetration of 6 mm). It is demonstrated that, in the entire range of investigated parameters, the hybrid welding required more heat input to achieve a particular depth of penetration, as compared to both autogenous laser processes. If both autogenous laser processes (4 kW and 7 kW laser welding) are compared, 7 kW laser welding required less heat input for a given depth of penetration. The laser welding with 7 kW of power exhibits the greatest joining efficient at all conditions in Fig.7.19. The exception is at shallow

depths of penetration where the energy requirement for the laser welding with 4 kW of power approaches the one needed for the laser welding with 7 kW power.

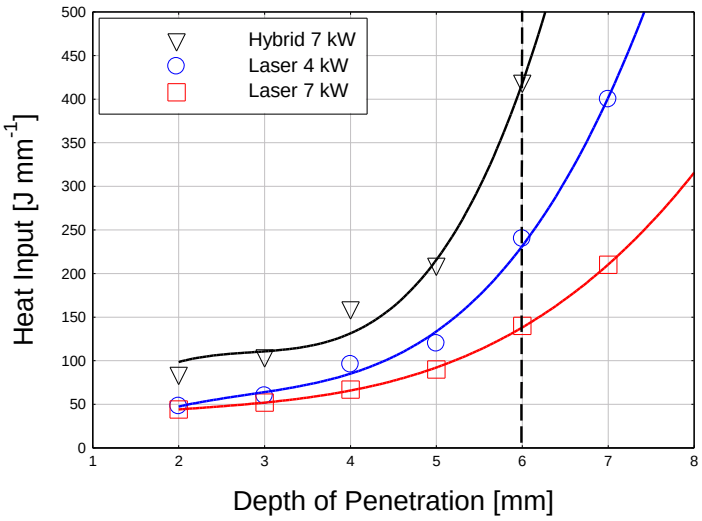

***Figure 7.19**: Comparison of heat input as a function of depth of penetration between laser welding with 4 kW of power, laser welding with 7 kW of power and hybrid welding with 7 kW of overall power*

7.4.2.2. Thermal profiles and hardness

Hardness distribution at 2 mm below the top surface was measured on some of the welds. In Fig.7.20 the hardness profiles of three investigated processes, the laser welding with 7 kW and 4 kW power and the hybrid welding with 7 kW of total power are compared. The values of heat inputs are given in brackets. It can be seen that at 2 m/min travel speed the magnitude of the hardness is similar for all the processes and the only noticeable difference is in the width of the hardness profiles. The widest hard zone is exhibited by the hybrid weld with 7 kW power, followed by 7 kW laser weld and then 4 kW laser weld. A similar behaviour is apparent at a higher welding speed, as shown in Fig.7.21 for 8 m/min travel speed. Here also the maximum value of the hardness is similar for all processes. Considering the very low heat inputs at this high speed it is difficult to distinguish the very fine difference in width between the hardness profiles.

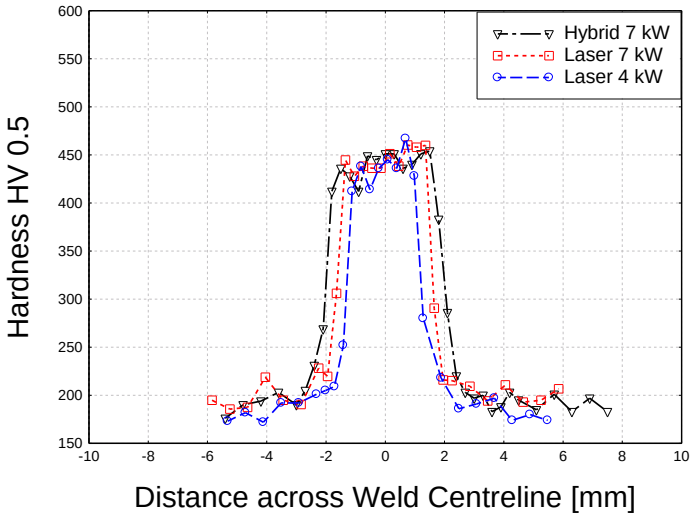

***Figure 7.20**: Micro-hardness profiles of welds achieved with different processes 4 kW laser welding (120 J mm^{-1}), 7 kW hybrid welding (210 J mm^{-1}) and 7 kW laser welding (210 J mm^{-1}); for a constant travel speed of 2 m min^{-1}.*

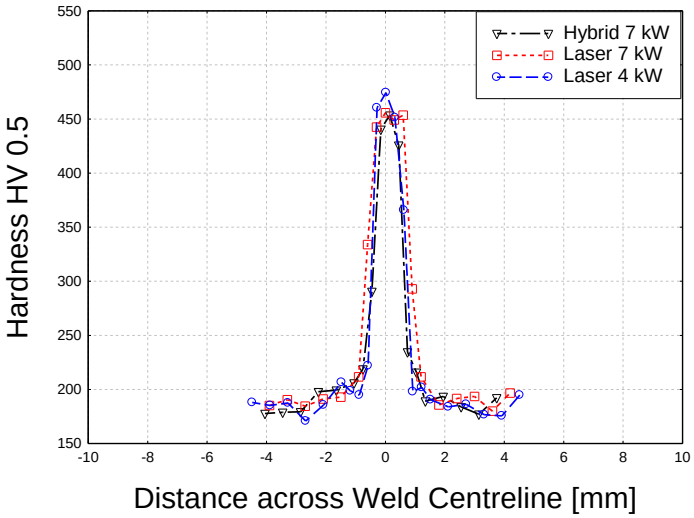

***Figure 7.21**: Micro-hardness profiles of welds achieved with different processes: 4 kW laser welding (30 J mm^{-1}), 7 kW hybrid welding (52 J mm^{-1}) and 7 kW laser welding (52 J mm^{-1}); for a constant travel speed of 8 m min^{-1}.*

In Fig.7.22 the thermal cycles measured at a distance of 5 mm from the weld centrelines of the corresponding samples from Fig.7.20 and Fig.7.21 are shown. The thermal cycles are directly proportional to the heat input. At both travel speeds the maximum temperatures recorded for the hybrid welding and the laser welding with 7 kW powers are the same, whilst the laser welding with 4 kW power exhibits much

lower peak temperature. It is important to mention that the arc column of TIG provides a much wider distributed heat, as compared to the laser beam.

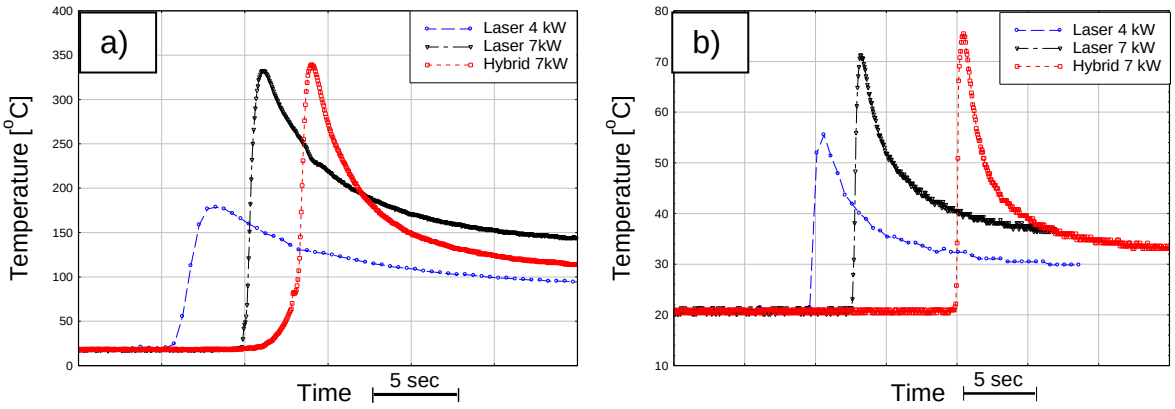

***Figure 7.22**: Thermal cycles of 4 kW laser welding and 7 kW hybrid welding for travel speeds of: **a)** 2 m min^{-1}; **b)** 8 m min^{-1} (measured 5 mm from weld centerline).*

In Fig.7.23 the hardness profiles of three processes at the conditions required for 6 mm of the depth of penetration, are compared. This figure corresponds to the macrographs from Fig.7.17. As expected from previous results, the peak values are the same, whereas the widths of the hardness profiles are directly proportional to the heat input. The highest heat input used in the hybrid weld with 7 kW of power (420 J/mm) is responsible for the broadest hard zone amongst the processes, whilst the lowest heat input of 7 kW laser weld (140 J/mm) is reflected by the narrowest hard zone.

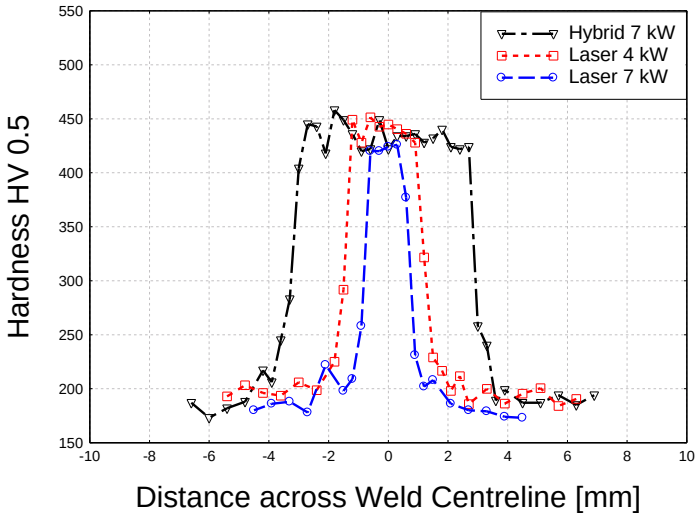

***Figure 7.23**: Micro-hardness profiles of welds achieved with three processes, 4 kW laser welding at 1m min^{-1} (240 J mm^{-1}), 7 kW hybrid welding at 1 m min^{-1} (420 J mm^{-1}) and 7 kW laser welding at 3 m min^{-1} (140 J mm^{-1}), with combination of parameters required for 6 mm of depth of penetration.*

7.5. Comparison of different materials

In the next experiment the residual strains in two different materials, S355 low carbon steel and 304 stainless steel are compared for the same welding conditions.

7.5.1. Methodology

Two bead-on-plate laser welds with a power of 4 kW and travel speeds of 1 m/min and 2 m/min were subjected to the residual strain measurement on neutron diffraction. Only one principal direction of strains, the longitudinal direction was measured. The gauge volume of 2x2x2 mm^3 was focused at 2 mm below the top surface.

7.5.2. Results

The longitudinal residual strains in two materials are compared in Fig.7.24. The global behaviours are very similar for both materials. At 1 m/min travel speed a

higher magnitude of tensile peak is exhibited in low carbon steel, but at 2 m/min travel speed (Fig7.24(b)) the trend is reversed and a higher tensile peak in stainless steel is shown. The area under the tensile peaks from Fig.7.24 is shown in Fig. 7.25. At a low travel speed of 1 m/min both materials demonstrate a similar distribution of the longitudinal residual strain. In contrast, at a faster speed the area under the longitudinal tensile strain in stainless steel is higher.

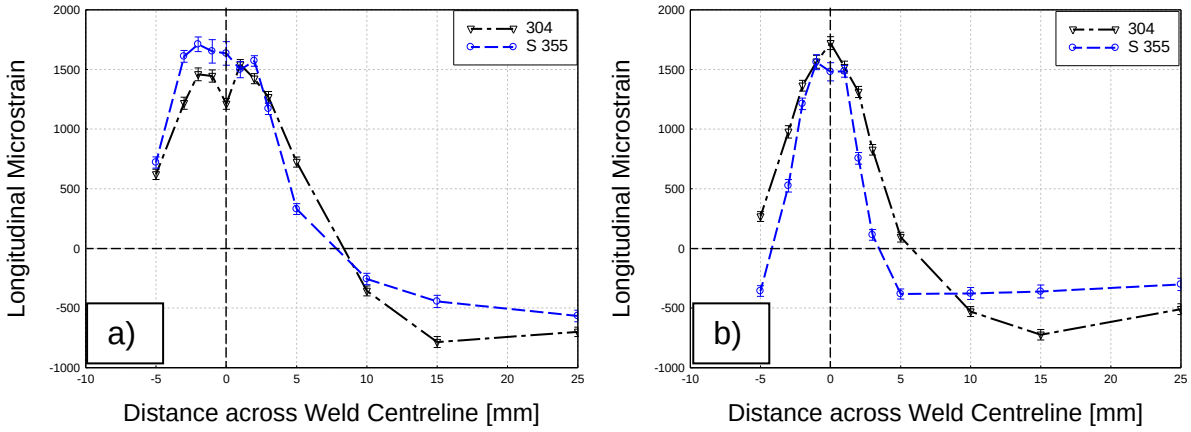

***Figure 7.24**: Comparison of longitudinal residual strains between S 355 low carbon steel and 304 stainless steel; **a)** laser welding with 4 kW and 1 m min^{-1}, b) laser welding with 4 kW and 2 m min^{-1}*

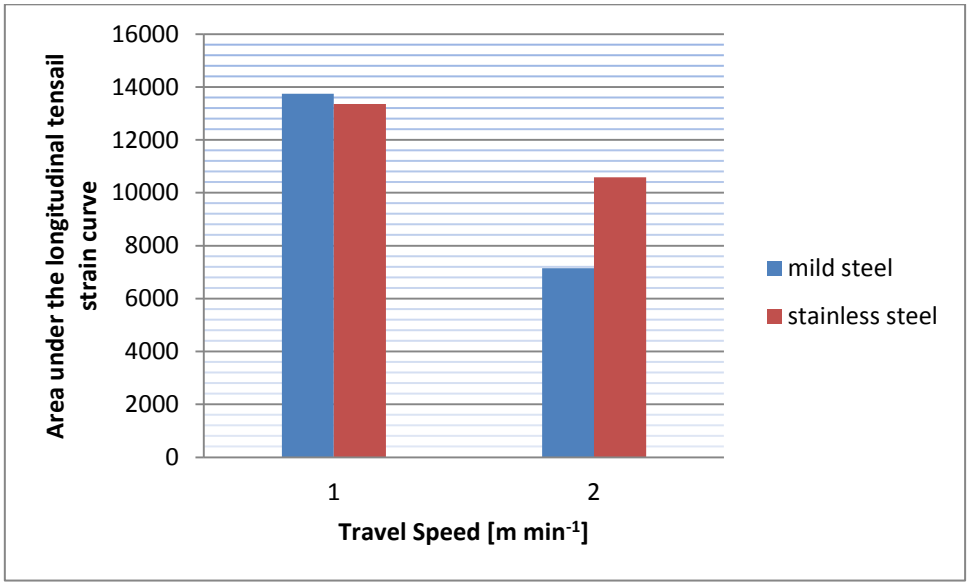

***Figure 7.25**: Area under the longitudinal tensile strain in two materials, S355 carbon steel and 304 stainless steel as a function of travel speed and a constant power of 4 kW.*

7.6. Validation tests

7.6.1. Gauge volume

In previous experiments the residual strains were measured at 2 mm below the top surface. However, the partially penetrated character of the welds achieved with various combinations of parameters, the depths of penetration of which varied from 10 mm to less than 3 mm, could lead to significant errors. Particularly in case of shallow welds a certain part of the gauge volume could reach much below the weld zone. To evaluate the minimum depth of penetration that could be accurately measured with the current set-up, the measurements of longitudinal strains on different depths across the thickness were carried out.

7.6.1.1. Methodology

To evaluate the effect of depth of penetration on the residual strain measurement, two laser welds with different depths of penetration of 10 mm and 4 mm were investigated. The welds were achieved with 7 kW of power, 0.63 mm beam diameter and travel speeds of 1 m/min and 6 m/min respectively. Longitudinal residual strains across the weld centreline at different depth of 2 mm, 6 mm and 10 mm from the surface were measured. Additional measurements across the depth were carried out.

7.6.1.2. Results

In Fig.7.26 the longitudinal residual strains measured at different depths of a sample with a deep penetration (10 mm) are shown. The magnitudes of the tensile peaks at all depths are the same, whereas the widths of the peaks reduce towards the bottom of the workpoece. In contrast, a shallow weld (4 mm) shown in Fig.7.27 exhibits a clear tensile peak only at a depth of 2 mm below the top surface. Related macrographs are shown in Fig.7.28. Note that in this perspective the gauge volume is asymmetric with 2 mm height and $2\sqrt{2}$ mm width. It seems like the width of the tensile strains reflects the shape of the fusion zone, as demonstrated in Fig.7.28(a). In the case of shallow weld a valid measurement could only be acquired at a depth of 2 mm below the surface. In Fig.7.29 the size and positions of the gauge volume at the

measured depths are visualised. It is evident that at a distance of 10 mm below the surface only a part of the gauge volume reached the fusion zone of this weld. Despite this still a clear tensile peak is exhibited at this depth. In contrast, the macrograph shown in Fig.7.29(b) reveals that apart from 2 mm below the surface all other measurements were carried out far below the fusion zone.

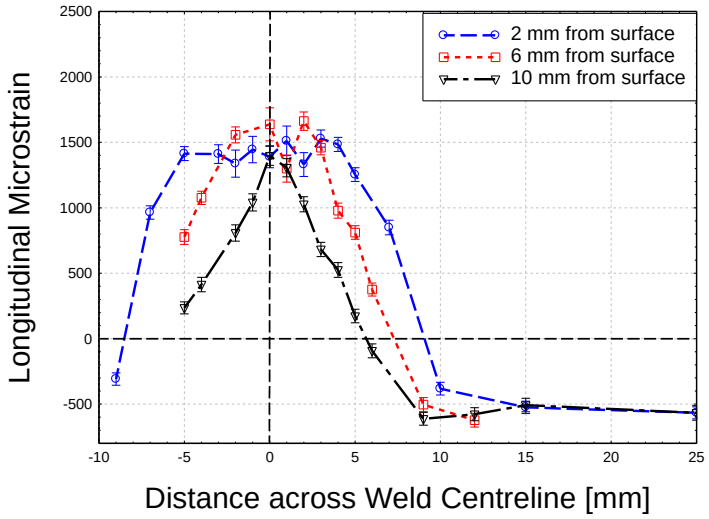

***Figure 7.26**: Longitudinal strain across weld centreline at different depths for laser welding with 7 kW and 1 m min^{-1}.*

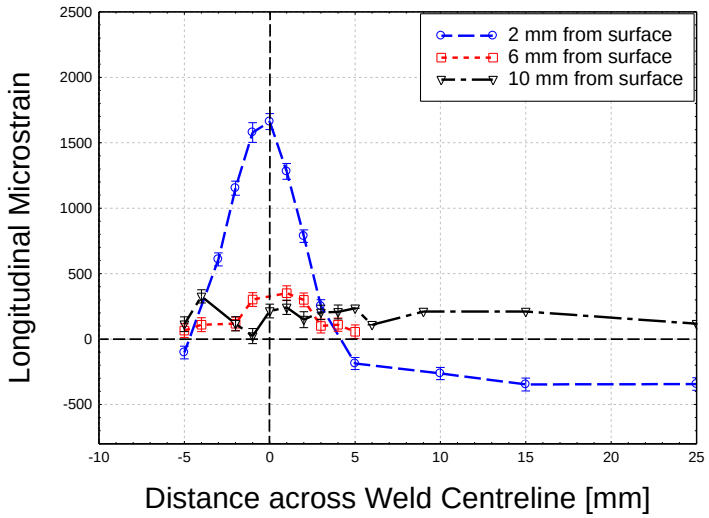

***Figure 7.27**: Longitudinal strain across the weld centreline at different depths, for laser welding with 7 kW and 6 m min^{-1}.*

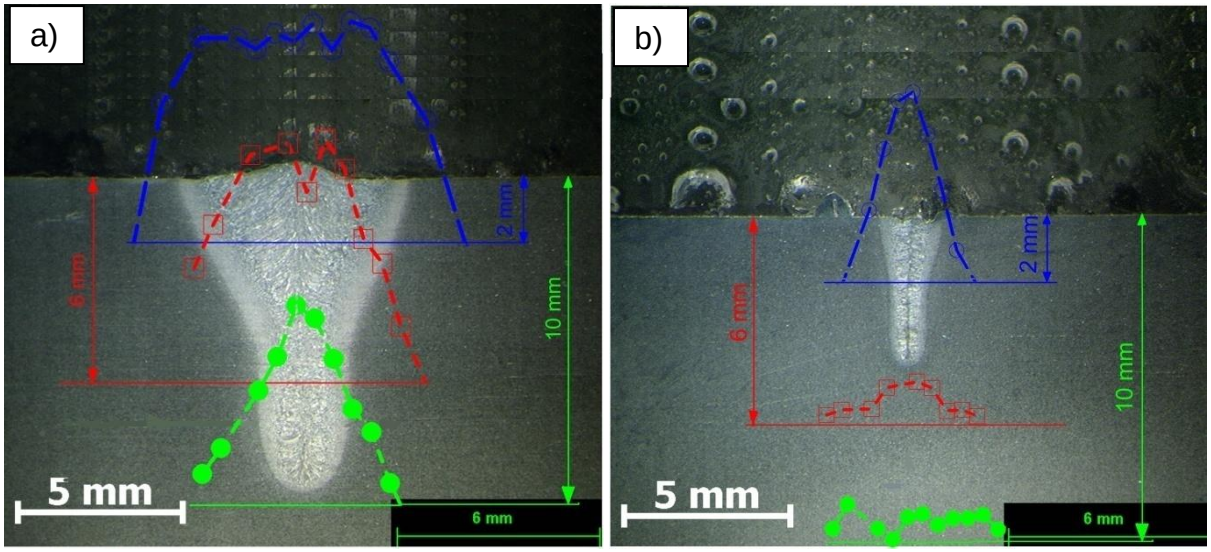

***Figure 7.28**: Macrographs with embedded longitudinal microstrain profiles measured at different depths; **a)** laser weld 7 kW and 1 m min^{-1}; **b)** laser weld 7 kW 6 m min^{-1}*

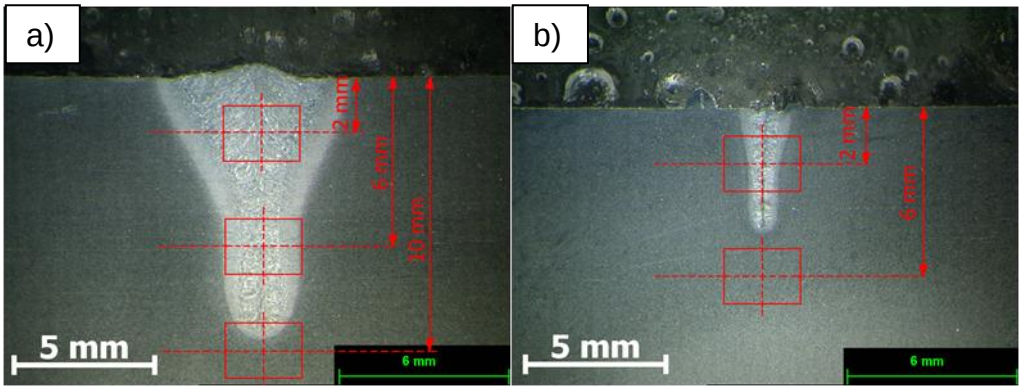

***Figure 7.29**: Macrographs with embedded position of gauge volume form surface for laser welding with 7 kW and two different travel speeds: **a)** 1 m min^{-1}; **b)** 6 m min^{-1}.*

In Fig.7.30 the longitudinal strains across the depth in the weld centreline is presented. It is confirmed that in the case of weld with 10 mm of depth of penetration the magnitude of the tensile strain is stable throughout the depth. Unlike in the case of deep weld, the magnitude of the tensile peak in the weld with 4 mm depth of penetration, drops suddenly after the gauge volume was placed below 4 mm from the surface.

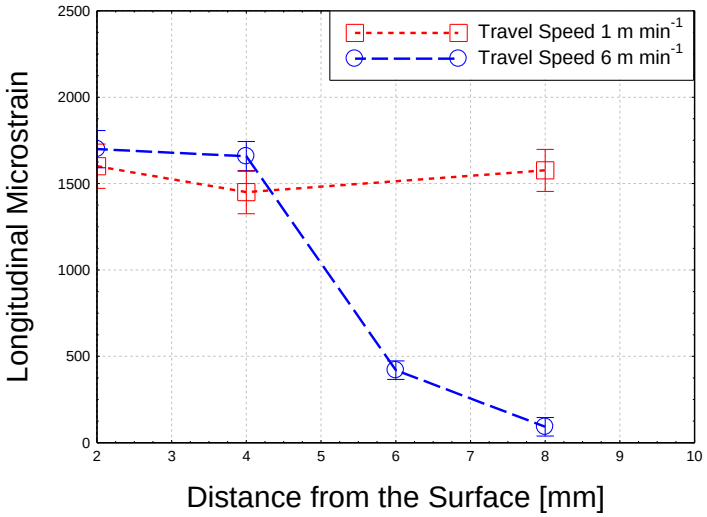

***Figure 7.30**: Measurement of longitudinal residual strain through the depth for 7 kW laser welding with different travel speeds of 1 m min^{-1} and 6 m min^{-1}.*

The effect of weld width on the accuracy of measurement of the residual strains was investigated. It can be seen on macrographs in Fig.7.31 that in the case of autogenous laser welds with 7 kW power and 0.63 mm beam diameter, the weld width became smaller than the gauge volume as the welding speed exceeded 3 m/min. The longitudinal micro-strains of related samples are shown in Fig.7.32. It is demonstrated that, in spite of the weld width being smaller than the gauge volume, the resolution during the residual strain measurement was high enough to distinguish these welds from one another. Note that in the vicinity of the fusion zone the gauge volume was translated with 1 mm intervals during the measurement of residual strains. This provided the overlap of the gauge volume and ensured sufficient resolution. The widths of the tensile peaks in Fig.7.32 clearly decrease with increasing travel speed. The sample corresponding to 8 m/min travel speed in this figure is the shallowest among all the presented in this chapter.

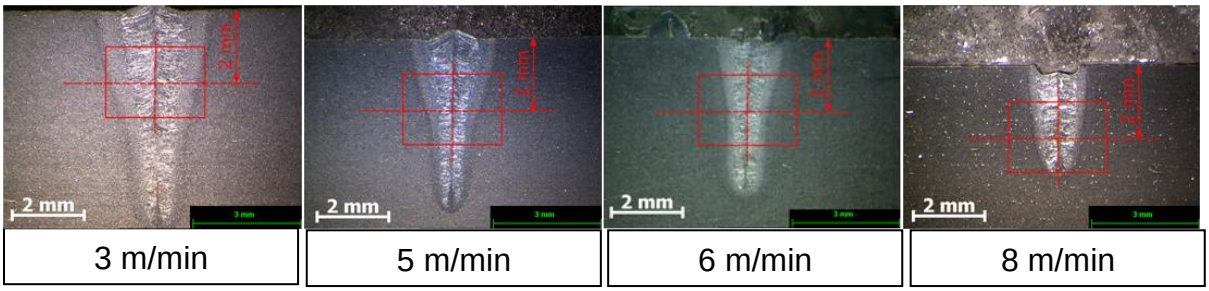

***Figure 7.31**: Size of gauge volume with respect to width of laser welds achieved at 7 kW of power and different travel speeds.*

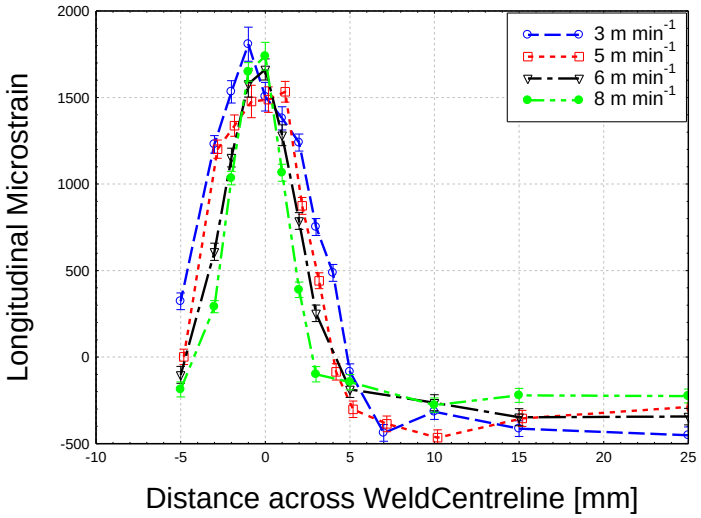

***Figure 7.32**: Comparison of longitudinal microstrains of laser welds at 7 kW and two different travel speeds: 6 m min^{-1} and 8 m min^{-1}*

7.6.2. Heat transfer coefficient

The comparison of two processes, the laser welding with 7 kW power and the hybrid welding with 7 kW power presented in Section 7.4, was carried out with the assumption of total heat transfer between heat sources and workpiece. In this section the difference in the absorbed energy between the laser welding and the hybrid laser/TIG welding with the same applied energy is evaluated.

7.6.2.1. Methodology

The evaluation of transfer efficiency of laser welding and hybrid laser welding, using thermocouples, was carried out. To avoid a direct influence of a thermocouple by the arc column in the hybrid laser welding, the temperature readings at a distance of 15 mm from the weld centreline, indicated as TC 4 in Fig.7.1 were acquired. Then the absorbed energy were calculated as the integrals over the time-temperature curves.

7.6.2.2. Results

In Fig.7.33 the comparison of thermal cycles of laser welding and hybrid laser welding with the same heat inputs of 420 J/mm (7 kW, 1 m/min) are shown. A higher temperature suggesting a higher transfer efficiency of the autogenous laser welding, as compared to the laser/TIG is evident. A similar can be concluded from Fig.7.34 at a lower heat input of 70 J/mm (7 kW, 6 m/min). In both cases the recorded temperature field for 7 kW hybrid welding is higher than for 4 kW laser welding.

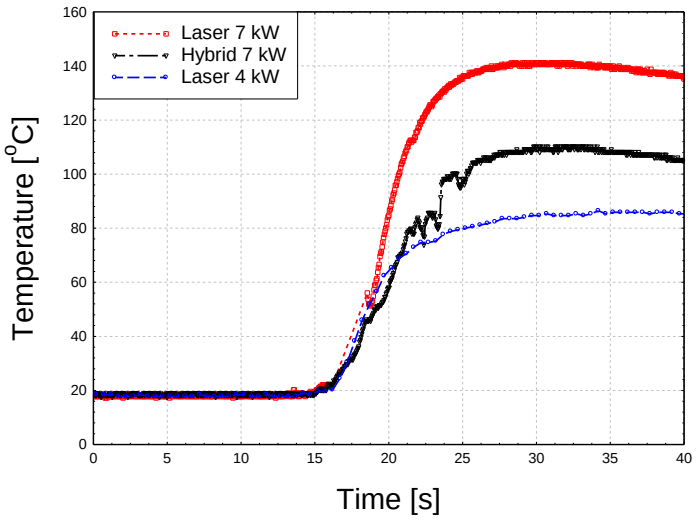

***Figure 7.33**: Comparison of thermal cycles between: laser welding with 7 kW of power, laser welding with 4 kW of power and hybrid welding with 7 kW of overall power (4 kW laser + 3 kW TIG); at a constant travel speed of 1 m min^{-1} (measured 15 mm from weld centreline).*

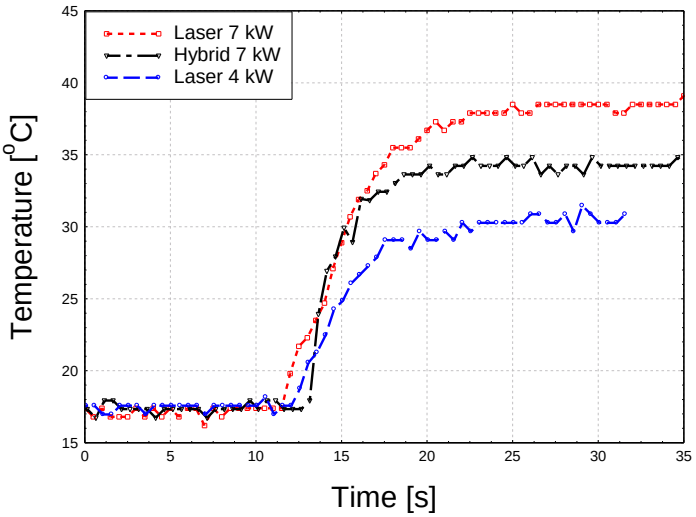

***Figure 7.34**: Comparison of thermal cycles between: laser welding with 7 kW of power, laser welding with 4 kW of power and hybrid welding with 7 kW of overall power (4 kW laser + 3 kW TIG); at a constant travel speed of 6 m min^{-1} (measured 15 mm from weld centreline).*

The integrated absorbed energy from the time-temperature curves for other conditions are compared in Fig.7.35. The red curve with squares refers to the laser welding with 7 kW power. Since this process exhibited the highest temperatures in Fig.7.33 and Fig.7.34 among the compared processes, all processes were normalised with respect to the laser welding with 7 kW of power. This normalised difference shown in Fig.7.35 allows for a relative comparison of the absorbed energies between the processes. It can be seen that for the same applied heat input the hybrid process transferred less energy to the material by 20% than the laser welding. Fig.7.35 shows that a significant portion of TIG energy must have been absorbed by the workpiece since the temperature field of the hybrid process is higher than the temperature field of 4 kW laser welding.

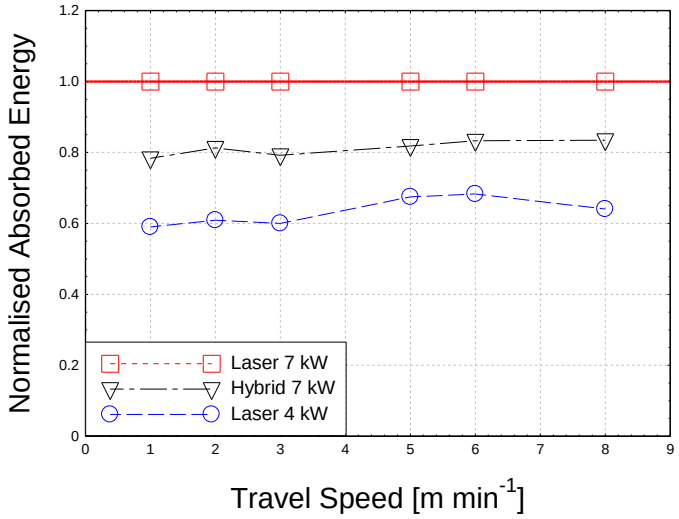

***Figure 7.35**: Normalised absorbed energy as a function of travel speed for laser welding with 7 kW and hybrid welding with 7 kW of overall power (4 kW laser + 3 kW TIG) and 4 kW laser welding.*

7.7. Residual stress

In the previous experiments the residual strains were analysed only in the longitudinal direction, which should give an indication of the residual stresses of the compared processes. To investigate if the residual strains are proportional to the residual stresses, the measurement of strains in three principal directions were carried out. Three selected welds from the previously investigated processes were used in this experiment. This allowed for a calculation of residual stresses.

7.7.1. Methodology

Residual strains were measured in three principal directions, longitudinal, normal and transverse (Fig.7.4) using neutron diffraction. The gauge volume was placed 2 mm below the top surface. The following samples were analysed: 7 kW laser welds achieved with 1 m/min (420 J/mm) and 6 m/min (70 J/mm) travel speeds, as well as 7 kW hybrid weld achieved with 1 m/min travel speed (420 J/mm). A Young modulus of 200 GPa and a Poisson's ratio of 0.3 were used for the calculation of residual stresses. The residual stresses in the principal directions, longitudinal, normal and

transverse (σ_L, σ_N, σ_T) were calculated from the residual strains (ε_L, ε_N, ε_T) according to Equation 7.4 [430]:

$$\begin{vmatrix} \sigma_L \\ \sigma_N \\ \sigma_T \end{vmatrix} = \frac{E}{(1+\nu)(1-2\nu)} \cdot \begin{vmatrix} (1-\nu) & \nu & \nu \\ \nu & (1-\nu) & \nu \\ \nu & \nu & (1-\nu) \end{vmatrix} \cdot \begin{vmatrix} \varepsilon_L \\ \varepsilon_N \\ \varepsilon_T \end{vmatrix} \qquad 7.4$$

The residual strains were calculated from Equation 7.1 using the average stress free reference lattice parameter a_0 (Equation 7.1).

7.7.2. Results

The residual strains in three principal directions of laser welds with heat inputs of 420 J/mm and 70 J/mm, as well as the hybrid weld with 420 J/mm heat input are shown in Fig.7.36, Fig.7.37 and Fig.7.38 respectively. It can be seen that the tensile strains in the longitudinal direction exhibit the highest magnitude, whilst the other strains (normal and transverse) are much smaller. The normal residual strains show a similar behaviour in all cases, however, the strains in the transverse direction exhibit significant differences between the welding processes. The transverse strains in both welds with heat inputs of 420 J/mm are mostly compressive, whilst in the case of laser weld with 70 J/mm heat input the transverse strain is tensile.

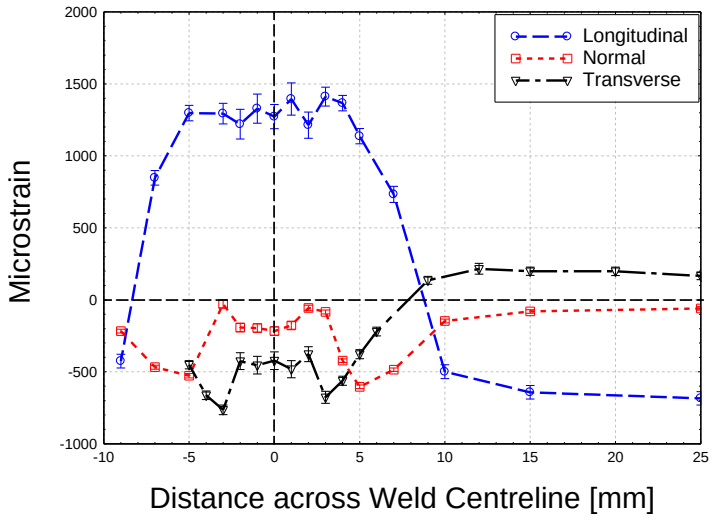

***Figure 7.36**: Residual strain in three directions for laser welding with 420 J mm^{-1} heat input (7 kW and 1 mmin^{-1}).*

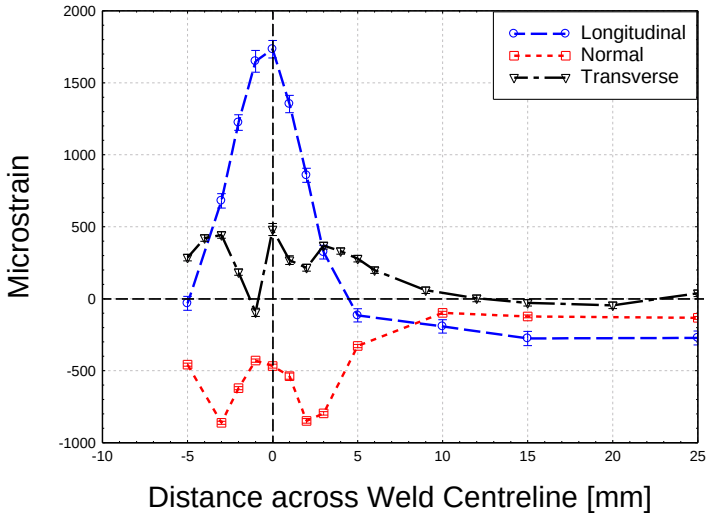

***Figure 7.37**: Residual strain in three directions for laser welding with 70 J mm^{-1} heat input (7 kW and 6 m min^{-1}).*

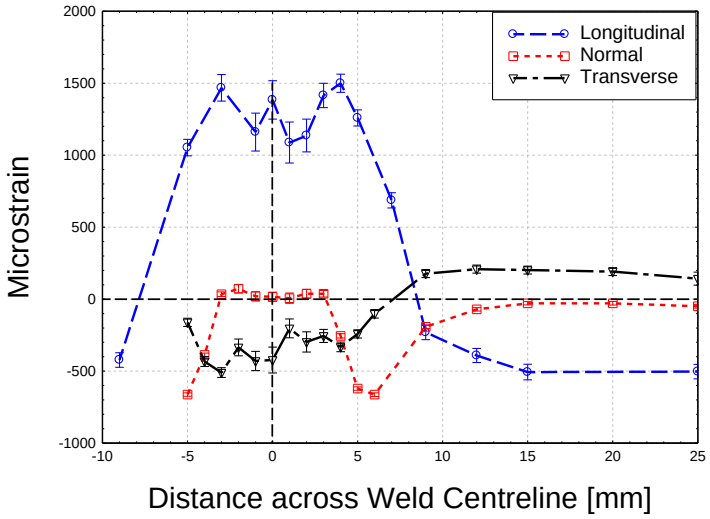

***Figure 7.38**: Residual strain in three directions for hybrid welding with 420 J mm^{-1} heat input (7 kW total = 4 kW laser + 3 kW TIG; 1 m min^{-1}).*

The residual strains in three directions were applied into Equation 7.4 to calculate the residual stresses. A comparison of the longitudinal residual stresses between all three specimens is shown in Fig.7.39. The magnitudes and the widths of the tensile peaks of both welds achieved with 420 J/mm heat inputs are the same. In contrast, in the case of laser weld achieved with 70 J/mm heat input the width of the tensile peak

is lower, but the magnitude is higher by 200 MPa, as compared to both welds with heat inputs of 420 J/mm.

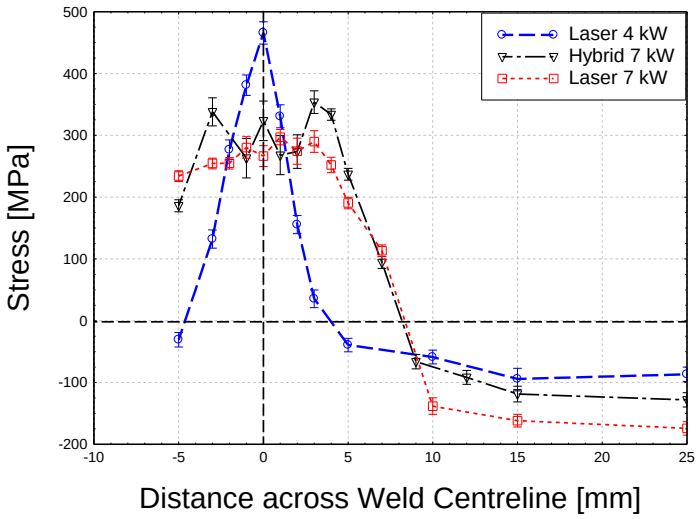

***Figure 7.39**: Residual stress in longitudinal direction across the weld centreline: 7 kW laser welding at 1 m min^{-1} (420 J mm^{-1}), 7 kW laser welding at 6 m min^{-1} (70 J mm^{-1}), and 7 kW hybrid welding at 1 m min^{-1} (420 J mm^{-1}).*

7.8. Discussion

7.8.1. Joining efficiency in laser welding

Every welding process has its optimum operating conditions, where the energy is efficiently utilised. It was shown in Fig.7.5 (page 195) that the joining efficiency initially increases with increasing interaction time and then after reaching a maximum tends to decrease again. This can be explained by the fact that initially the depth of penetration also increases with increasing energy density (product power density and interaction time) from the melting threshold. Since at short interaction time range there is only a little melt around the keyhole, the depth of penetration increases relatively faster than the weld width, hence the aspect ratio of depth to width increases in this range. However, at a certain interaction time, where the drilling rate is maximised, but the melt pool is still small, the maximum joining efficiency is

achieved. At this point the laser energy is efficiently utilised for depth of penetration and the maximum aspect ratio of depth to width is reached. The maximum joining efficiency is obtained at a point where the heat transfer into the bulk material is minimised, but the process is sufficient to maintain a high depth of penetration. After this point, a further increase of energy density by increasing interaction time, results in an increase of melting rate along with the propagation of depth of penetration. When the process conditions for a given material are beyond the optimum interaction time the rate of increase of weld width becomes faster than the rate of increase of depth of penetration. In other words, the amount of molten metal increases and thus the aspect ratio of depth to width and the joining efficiency decrease, despite the continuous increase of energy density and depth of penetration.

For every combination of power density and beam diameter there is an optimum interaction time at which the maximum joining efficiency occurs. The joining efficiency is independent of the power density, as long as there is a sufficient amount of energy for deep penetration. It was shown in Fig.7.6 (page 195) that at long interaction times the joining efficiency was independent of the power densities. However, below a certain interaction time the joining efficiency of laser welding with a power density of 0.64 MW/cm^2 became much lower, as compared to the laser welding with power densities of 1.6 MW/cm^2 and 2.6 MW/cm^2. This implies that the combination of power density of 0.64 MW/cm^2 with a beam diameter of 0.63 mm provided insufficient energy to maintain weld with a high aspect ratio as the interaction time decreased below 12 ms. This is attributed to the threshold energy density for the keyhole regime discussed in Section 5.9.1.

The same trend was apparent when different beam diameters were compared either at a constant power density (Fig.7.7 page 196) or at a constant power factor (Fig.7.8). At long interaction times the beam diameter did not affect the joining efficiency. However, as the interaction time reduced below approximately 10 ms, a better joining efficiency was achieved with a smaller beam diameter (Fig.7.7 and Fig.7.8). The same power factor achieved with a smaller beam diameter, on one hand, may lead to a severe spatter and low fit-up tolerance, but on the other hand, at short interaction times it requires lower heat input for a particular depth of penetration. Therefore, at short interaction times a smaller beam diameter leads to a higher joining efficiency and a lower distortion. In contrast, at high and medium

interaction times a larger beam diameter will provide the same joining efficiency as a small one, but with better properties.

The way the energy is utilised for depth of penetration is additionally dependent on the thermal properties of material. In Fig.7.9 (page 197) different materials, low carbon steel, stainless steel and aluminium alloy were compared. For the same welding conditions, the aluminium alloy resulted in a greater depth of penetration and hence a greater joining efficiency, as compared to the stainless steel and low carbon steel. This is consistent with findings from Section 5.6, in which the difference in depth of penetration between the alloys was attributed to the difference in recoil pressure and viscosity. Macrographs from Fig.7.11 (page 198) confirmed a slight difference in depth of penetration between the materials. Furthermore, the aluminium alloy exhibited a three times greater melting efficiency than both steels for the same conditions in Fig.7.10 (page 198). This is attributed to the lower melting temperature and the higher thermal diffusivity of aluminium, as compared to both steels. The fact that the melting efficiency of both steels was almost constant in the entire range of interaction time suggests a constant rate of utilisation of energy for melting. This also implies that the amount of molten metal increases proportionally with increasing heat input, whereas the joining efficiency specifies the ratio between the energy used for depth of penetration and melting. In addition, the aluminium alloy experienced a significant variation of melting efficiency with the interaction time in Fig.7.10 (page 198). This indicates a more dynamic behaviour in aluminium, as compared to both steels. A lower melting efficiency at both extremes of interaction time could result from variation of absorption and strong convection within the melt pool.

7.8.2. Comparison of laser welding with laser hybrid welding

Laser welding is characterised by a high energy density with a low heat input, which promotes welds with high aspect ratios and joining efficiencies. The joining efficiency of the hybrid process is much lower, as compared to the autogenous laser welding. This was demonstrated in Fig.7.12 (page 200). This graph can be better understood by analysing the macrographs from Fig.7.13 (page 201). The depth of penetration of the hybrid process with 7 kW of overall power was the same as the depth of penetration of the laser welding with 4 kW of power. This means that the extra heat

from the arc source in the hybrid process did not contribute to the depth of penetration, but a wide heat source resulted in a larger weld width. The depth of penetration of the laser welding with 7 kW of power was almost double, that of the hybrid welding for the same overall input power. At the same time the melting area of 7 kW laser welding was also greater (Fig.7.14 page 201). This is attributed to a lower heat transfer from the heat source to the workpiece in the hybrid welding than in the laser welding.

The residual strain analysis from Fig.7.15 and Fig.7.16 (pages 202-203) revealed that the strain generation is minimised when the joining efficiency is maximised. The integrated area under the longitudinal tensile strain peak decreased with increasing travel speed in Fig.7.16. This is important for all applications because this integrated peak area is proportional to the plastic deformation, which occurs during thermal cycle and which results in distortion. As the travel speed increases (interaction time reduces) at a constant power, the amount of heat absorbed be the workpiece decreases, causing a decrease of residual tensile strain and distortion. However, the depth of penetration also reduces with increasing travel speed.

Therefore it is more useful, in terms of welding applications, to compare different welding processes at the parameters, which are necessary to obtain a particular depth of penetration. This was demonstrated on macrographs in Fig.7.17 (page 204). The best quality and the lowest sensitivity to the fit-up tolerance were obtained in the hybrid process (Fig.7.17c). However, the hybrid weld exhibited the highest residual strain among all three processes (Fig.7.18 page 204). The width of the tensile strain domain was the smallest in the case of 7 kW laser weld. The integrated area under the tensile strain domain of 7 kW autogenous laser weld was lower by 50%, as compared to 7 kW hybrid weld. This corresponds to the reduction of tensile strain in laser welding by 50%, as compared to hybrid process for the same depth of penetration.

The required heat input per unit of depth of penetration, plotted in Fig.7.19 (page 205), demonstrates the difference between the processes. The data are also summarised in Table 7.1. Since the arc in the hybrid process did not contribute to the depth of penetration, this process was the least efficient. Comparing both laser processes, the laser welding with 7 kW of power needed much less energy for a

given depth of penetration than the laser welding with 4 kW of power. The high laser power (high power density and specific point energy), in this case, enabled the increase of welding speed (reduction of interaction time), leading to the reduction of heat input and residual strain as a result. The laser welding with 4 kW of power required much lower travel speed in order to achieve 6 mm of depth of penetration, which resulted in a relatively high heat input and residual strain. Only at shallow depths of penetration the joining efficiency of 4 kW laser process approached the efficiency of 7 kW laser process, because the heat inputs were similar (Fig.7.19).

***Table 7.1**: Parameters of different processes required for 6 mm depth of penetration*

Process	Laser power [kW]	Travel speed [m/min]	Arc voltage [V]	Arc current [A]	Arc power [kW]	Total heat input [J/mm]	Joining efficiency [mm^2/kJ]
LASER 4 kW	4	1	-	-	-	240	25
LASER 7 kW	7	3	-	-	-	140	43.2
HYBRID 7kW	4	1	13.23	224	2.96	420	12.6

The choice of welding parameters for a given depth of penetration depends on the application requirements. The hybrid process gives a wide weld with good fit-up tolerance but also results in a larger residual strain field that could lead to issues with distortion. If the residual strains need to be minimised then a higher laser power (higher power density) should be used. Also smaller beam diameters help minimise heat input at low interaction times, but often with deterioration of quality.

Hybrid laser welding is often selected over the autogenous laser welding due to the extremely high cooling rates of the laser welding, which often lead to undesired microstructures. The additional energy from the arc source in the hybrid process can reduce the cooling rate, which should prevent from hard phases in carbon steels appearing. However, it was demonstrated in Fig.7.20 (page 206) that the autogenous TIG welding had a limited ability to reduce the cooling rate and the resultant hardness. At a travel speed of 2 m/min a similar magnitude of the hardness profile was achieved in laser welding (120 J/mm) and in hybrid laser welding (210 J/mm). The higher heat input of the hybrid welding, as compared to the laser welding with 4

kW of power, resulted only in a narrower distribution of hardness, without any major effect on the maximum value. The width of the hardness profiles in Fig.7.20 was directly proportional to the heat input. A similar effect was observed at faster travel speeds (Fig.7.21 page 206). This shows that the extra energy from the arc in hybrid welding has limited ability to reduce the cooling rate at fast travel speeds. Therefore the maximum hardness of 4 kW laser process was only insignificantly higher than both 7 kW processes, whereas the widths of the profiles were the same for all the processes, indicating very low heat inputs in general. The thermal cycles of the corresponding welds (Fig.7.22 page 207) confirmed very low temperatures. The maximum temperatures recorded at a distance of 5 mm from the weld centreline for 7 kW laser welding and 7 kW hybrid welding were approximately 350^{o}C. Note that the achieved temperature profiles were insufficient to calculate the cooling rates inside the fusion zones. Even though a higher peak temperature in the parent metal might be the indication of a lower cooling rate in the fusion zone, which could suggest a lower cooling rate in the hybrid welding in comparison to 4 kW laser welding. However, very low temperatures in general, recorded at such a close distance (5 mm from the weld centrelines) indicate high cooling rates for all investigated processes. Also the comparison of all three processes at the conditions required to achieve the same depth of penetration, made in Fig.7.23 (page 208) exhibited the same magnitude of the hardness. The difference in heat input, in this case, affected only the width of the hardness distribution without any major influence on its magnitude.

Therefore, it can be concluded that the energy of the arc source in hybrid welding is insufficient to significantly reduce the cooling rate and hardness induced by laser. This is in contrast with results presented in the literature [420]. However, majority of studies on hybrid laser welding were carried out with a MIG process as a secondary source. Thus the discrepancy can result from additional elements from the filler wire, which used in hybrid welding prevent from hard phases forming. Furthermore, the cooling rate and hardness may be reduced if arc sources with much higher heat inputs are used or thinner materials are welded.

7.8.3. Comparison of different materials

The comparison of residual strains in low carbon steel and stainless steel in Fig.7.24 (page 209) showed no major differences in the magnitude of the strain peaks between the materials. Also the integrated area under the longitudinal tensile strain, which corresponds to distortion, was similar for both materials at a travel speed of 1 m/min (Fig.7.25 page 209). In contrast, at a higher travel speed of 2 m/min, a larger area under the strain domain was exhibited in stainless steel. This will lead to a slightly larger distortion in stainless steel, as compared to low carbon steel. The difference can be attributed to the lower thermal diffusivity of stainless steel, which maintains the high temperature at a given point inside the material for a longer period of time.

7.8.4. Evaluation of errors in residual strain measurement

The fact that the same gauge volume (2x2x2 mm^3) placed at the same distance from the surface (2 mm) was used for all welds with various depths of penetration, could lead to a systematic error. Particularly in welds with shallow depths, a part of the gauge volume could reach below the fusion zone in the parent metal, whilst scanning across the weld. It was shown in Fig.7.26 (page 211) that in the case of weld with a depth of penetration of 10 mm the magnitude of the tensile peak did not change as the gauge volume moved further into depth. The only difference between the measurements on different depths was in the width of the tensile strain peak domain. A first reason of reducing the tensile strain domain, as the gauge volume moves towards the bottom of the workpiece, can be attributed to the shape of the fusion zone. It was shown on macrograph in Fig.7.28(a) that typical laser welds exhibit the widest bead near the surface, which then gets narrower in lower parts. This corresponds to less plastic deformation in the lower parts of the weld. A second reason can be attributed to the fact that at a distance of 10 mm below the top surface a significant part of the gauge volume was scanning below the fusion zone, hence averaging the plastic deformation between the weld and the parent metal.

In an analogous experiment carried out on a weld with 4 mm depth of penetration (Fig.7.27 page 211) no clear tensile peak was apparent at a depth below 4 mm from the top surface. Thus it can be concluded that in order to acquire an unambiguous

measurement of the magnitude of the tensile strain, at least a half of the gauge volume has to reach the weld zone. However, for an accurate analysis of the plastic deformation, measured as the integrated area under the tensile peak domain, the entire gauge volume has to be within the fusion zone. This was also apparent on the distribution of the longitudinal tensile strain through the thickness in Fig.7.30 (page 213). Despite only the half of the gauge volume being within the weld metal at a distance of 4 mm below the surface of the specimen with 4 mm depth of penetration, still the valuable measurement of the tensile peak was achieved. This implies that a minimum depth of penetration, at which at least a half of the gauge volume was within the fusion zone for this particular set-up, as being 2 mm. But to accurately evaluate the tensile strain domain the depth of penetration should not be lower than 3 mm. The minimum depth of penetration among all the analysed welds in this chapter was 3 mm (Fig.7.31 page 214).

In a similar way the weld width can affect the residual strain measurement, particularly when the fusion zone is narrower than the gauge volume. It was shown on macrographs in Fig.7.31 (page 214) that at these conditions the weld width became narrower than the gauge volume, as the travel speed exceeded 3 m/min and then stayed constant down to 8 m/min. The longitudinal tensile residual strains of the corresponding welds (Fig.7.32 page 214) demonstrated that the tensile peak could be still distinguished. It was shown that despite the welds being narrower than the size of the gauge volume, the measured residual strains were different. This means that the measurement resolution was sufficient to distinguish the analysed welds. The low intervals of the translation of the gauge volume across the welds centres lines, which was down to 1 mm, used during the neutron diffraction experiment, accounted for this high resolution. Such a low intervals resulted in overlapping of the scanned area and ensured a higher resolution than might be from 2x2x2 mm^3 gauge volume. The weld in Fig.7.31 (page 214) indicated as 8 m/min was the narrowest among all the analysed samples in this study.

7.8.5. Estimation of transfer efficiency

Since a universal value of the transfer efficiency for laser and TIG processes, which would be suitable for such a wide range of parameters, used in this chapter, does not

exist, the applied heat input was simply used in this study. It is anticipated that some parts of laser and TIG energy get dissipated due to radiation, vaporisation, reflection and other losses, such as conduction in the tungsten electrode in TIG process. The rate of all different losses can change with welding conditions, thus in order to accurately measure the absorbed energy a calorimetric test of every case would have to be carried out. Instead a relative estimation of the absorbed energy, based on a thermal history was performed in this study. To exclude the influence of the distribution and size of the heat source on the temperature distribution the thermocouples were placed at a distance of 15 mm from the weld centreline. In Fig.7.33 and in Fig.7.34 (pages 215-216) a comparison of the temperature fields between the laser welding and the hybrid laser welding for the same applied heat input was shown. A lower temperature recorded for the hybrid welding is indication of a lower absorbed energy of this process, as compared to the laser welding. The integral of the time-temperature curve is proportional to the absorbed energy and was used for a relative comparison of the transfer coefficients between the processes. The hybrid welding resulted in a lower energy absorbed by 20% than the autogenous laser welding for the same applied heat input (Fig.7.35 page 217). However, the integrated temperature field of the hybrid welding was between that of 4 kW and 7 kW laser welding, which implies that a significant part of the heat from the TIG source was absorbed. Even though this is not a quantitative measurement, the promising is the fact that the difference between the laser and the hybrid welding was consistent at all travel speeds. This is also consistent with the comparison of melting rates between the processes from Fig.7.14 (page 201). The melting rate of the hybrid welding was approximately 20% lower, as compared to the laser welding with the same applied heat input.

7.8.6. Residual stress

The measurements of residual strains in three principal directions (Fig.7.36 to Fig.7.38 pages 218-219) confirmed that the majority of plastic deformation in laser welds occurs in the longitudinal direction. It was shown that laser welding with 420 J/mm heat input (Fig.7.36) and hybrid welding with heat input of 420 J/mm (Fig.7.38) had similar distribution of strains, whilst laser welding with 70 J/mm heat input was clearly different. Unlike in both 420 J/mm processes the transverse residual strain of

the weld made with 70 J/mm heat input exhibited a much more complex case. Also the comparison of longitudinal stresses, calculated from the residual strains (Fig.7.39 page 220) indicated unexpected effects. The process with the lowest heat input resulted in the highest magnitude of the tensile stress. This can be attributed to two different phenomena. First, a shallow depth of penetration, much lower than the plate thickness, achieved with this low heat input, could result in a much more complicated stress distribution. Second more likely, the measurement error due to the variation of microstructure could also be significant in this case. It is well known that the residual stress field in welded joints can vary significantly due to the variation of microstructure across the weld [431]. Thus to exclude such effects from the analysis of residual strains, a reference stress-free sample has to be measured from different parts of a weld. This enables for evaluation of zero level stresses in different regions of a weld, such as fusion zone and heat affected zone, as well transition layers, which accounts for stresses only due to the heat effects. Since in this case the parent metal measurement was used for the determination of stress-free reference sample, there might be inaccuracy in the residual stresses achieved in Fig.7.39 in Section 7.7. Particularly in samples achieved with low heat inputs, where the fast cooling rates could result in hard microstructures. However, for the measurement of the tensile strain domain (area under the tensile peak), which was of the main interest in this study, the error attributed with the inaccurate stress-free reference sample is less significant. Therefore the presented results do not give quantitative information regarding the residual stress but a relative comparison of different processes in terms of plastic strain, which is proportional to distortion.

Chapter 8. Fit-up tolerance

The maximum gap that can be accommodated by a welding process, referred to as a fit-up tolerance, is an important criterion determining its usefulness in many applications. This is particularly the case in laser welding, where a narrow heat source can easily pass between the joined components, if the gap exceeds the beam diameter, which is usually less than 1 mm. Such narrow gaps require high accuracy of machining and alignment of joined components, which increase the costs of pre-welding processes. Additionally, distortion may cause misalignment during fabrication. Therefore, the traditional MIG processes are frequently preferable even for the price of lower productivity. The hybrid laser/MIG process is often seen as a compromise between the high speed of laser welding and the good fit-up tolerance of arc-based welding processes.

The fit-up tolerance of laser and laser hybrid process is investigated in this chapter. It is evaluated if the hybrid welding provides better conditions for welding of butt-joints than autogenous laser welding. Furthermore, to extend this approach, a tandem MIG process (multiple wire system) is used simultaneously with the laser to increase the deposition rate, as compared to the standard hybrid welding. The maximum ability of laser/MIG hybrid and laser/tandem MIG hybrid to join large gaps is determined. Both processes are investigated with respect to the requirements of pipe industry. The main objective is to achieve a suitable welding process for the seam tack welding during the pipe manufacturing process. For such an application a high processing speed and good fit-up tolerance are required.

8.1. Experimental set-up

The laser system and the arc sources used for hybrid and hybrid tandem arc welding, as well as more details regarding the filler wire and general set-up are shown in Chapter 3. For autogenous laser welding two focusing lenses with focal lengths of 150 mm and 300 mm were used. These lenses resulted in beam diameters at the

focal points of 0.37 mm and 0.75 mm respectively. All the hybrid and hybrid tandem arc welds were carried out using a focusing lens with 250 mm focal length, resulting in a beam diameter of 0.6 mm. Different beam diameters in the case of hybrid and hybrid tandem arc welding were achieved by appropriate defocusing of the beam (focal point above the surface).

The arc sources in the hybrid and hybrid tandem arc welding were operated in a synergic pulse mode, in which the welding parameters are automatically adjusted to a primary selected wire feed speed. To tune the stability of the process and allow for the spray metal transfer, the arc length correction parameter was used as a fine adjustment. The power of the arc source was calculated by averaging the instantaneous current and voltage according to Equation 3.2 in Section 3.9.

Behaviour of the melt pool was examined using a Phantom VR 0608 high speed imaging camera with a tele-macro lens. The melt pool was illuminated with a green diode light delivered through an optical fibre. To enable only the green light coming into the camera a narrow band green filter was used.

Low carbon steel (S355) having 250 mm length and 12 mm thickness with different bevels and joint configurations was used, as shown in Table 8.1. The edges of the plates were machined to ensure consistent gap conditions. All samples were tack-welded on both ends prior to welding, to maintain the appropriate gap. Auxiliary start and stop plates were used at both ends of the specimens, to allow for the utilisation of entire length of the specimens. In some cases 4 mm thick low carbon steel plates, referred to as backing plates, were placed under the bevels to support the molten metal. The welds were investigated in terms of consistency, shape and defects.

***Table 8.1**: Weld preps used in this chapter.*

Butt-weld with diverging gap (0–2 mm or 0–7 mm)	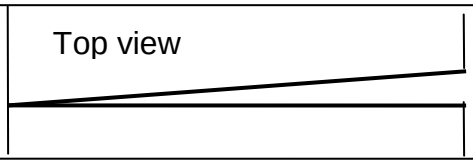
X-prep zero gap	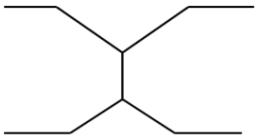
X-prep (2, 3 or 5 mm) horizontal gap	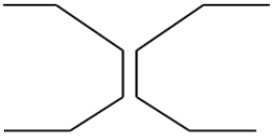
X-prep misaligned X-prep misaligned with 2 mm gap	
X-prep 2 mm horizontal gap + vertical misalignment	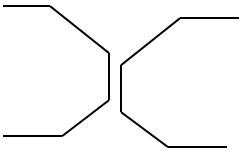
Laser tilted off side Laser and arc off side	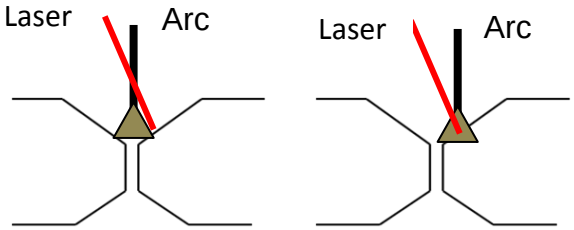

8.2. Fit-up tolerance of autogenous laser welding

It is anticipated that the fit-up tolerance of laser welding mainly depends on the melt pool size, which in autogenous laser welding is mainly controlled by the interaction time. Since the interaction time can be changed either by the beam diameter or the travel speed, both effects are investigated in this section.

8.2.1. Methodology

The autogenous laser butt-welds in zero gap configuration were carried out. Two beam diameters of 0.37 mm and 0.75 mm and travel speeds of 0.5 m/min and 3

m/min were used. The beam diameters were achieved by changing the optical set-up of the laser head. The laser energy was adjusted for every combination of travel speed and beam diameter in order to achieve a constant depth of penetration of 6 mm. The welds were compared in terms of width of the beads.

In the next experiment the fit-up tolerance of the laser welding with two different beam diameters of 0.37 mm and 0.75 mm was investigated using a workpiece with a diverging gap (0-2 mm), as shown in Table 8.1. The experiments were carried out with travel speeds ranging from 0.5 m/min to 3 m/min. The laser power was appropriately adjusted for every combination of travel speed and beam diameter to achieve a depth of penetration of 6 mm. The welding process was commenced at the zero-gap end of the plate to establish a stable process and terminated at the wide-gap end. A position at which the process collapsed with no melting evident was considered as the limit of the fit-up. An example is shown in Fig.8.1. Any thin depositions of molten metal apparent below the top surface, particularly at fast travel speeds, were attributed to the acceleration-dragged metal and ignored.

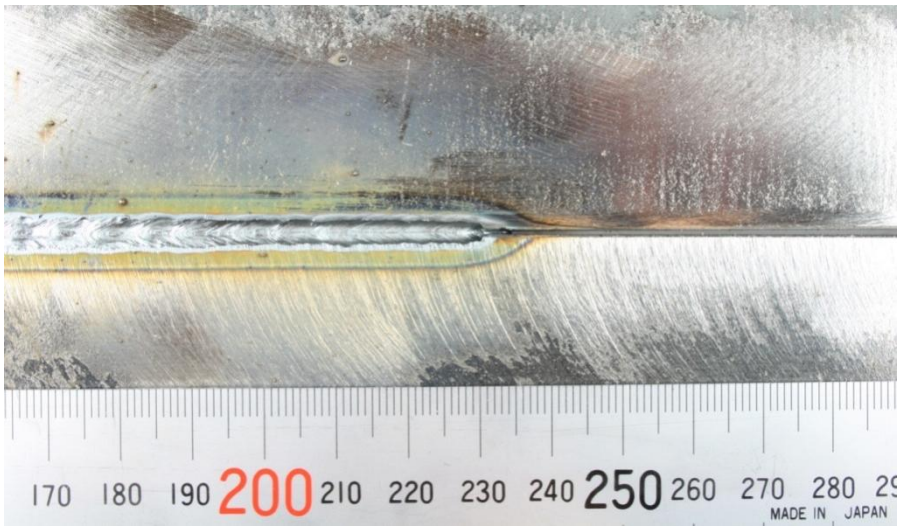

***Figure 8.1**: Maximum gap bridging ability of laser welding at 0.5 m min^{1} travel speed of and 0.75 mm beam diameter studied on diverging gap from 0 mm to 2 mm.*

8.2.2. Results

High speed images of autogenous laser butt-welds with zero-gap configuration are shown in Fig.8.2 and Fig.8.3. It can be seen that the beam diameter has limited effect

on the width of laser welds. Only at faster travel speeds a larger melt pool was achieved with a bigger beam diameter, as shown in Fig.8.3 for a travel speed of 3 m/min. Note that a higher energy was required to achieve the same depth of penetration as the beam diameter increased. Apart from the undercut apparent in case of a smaller beam diameter, it seems that at this conditions the width of the top bead is not affected by the beam diameter. The main difference is that the welds achieved with a larger beam diameter exhibit wider thermal affected zones at all travel speeds. The weld widths for other conditions are summarised in Fig.8.4 and Table 8.2. It is evident in Fig.8.4 that despite the interaction time with a bigger beam diameter being as twice as high, compared to a smaller beam diameter, the difference between the weld widths is very small. Only at higher travel speeds a bigger beam diameter resulted in a wider weld bead. The macrographs of the corresponding welds were shown in Fig.6.3 in Section 6.2.2 (page 164).

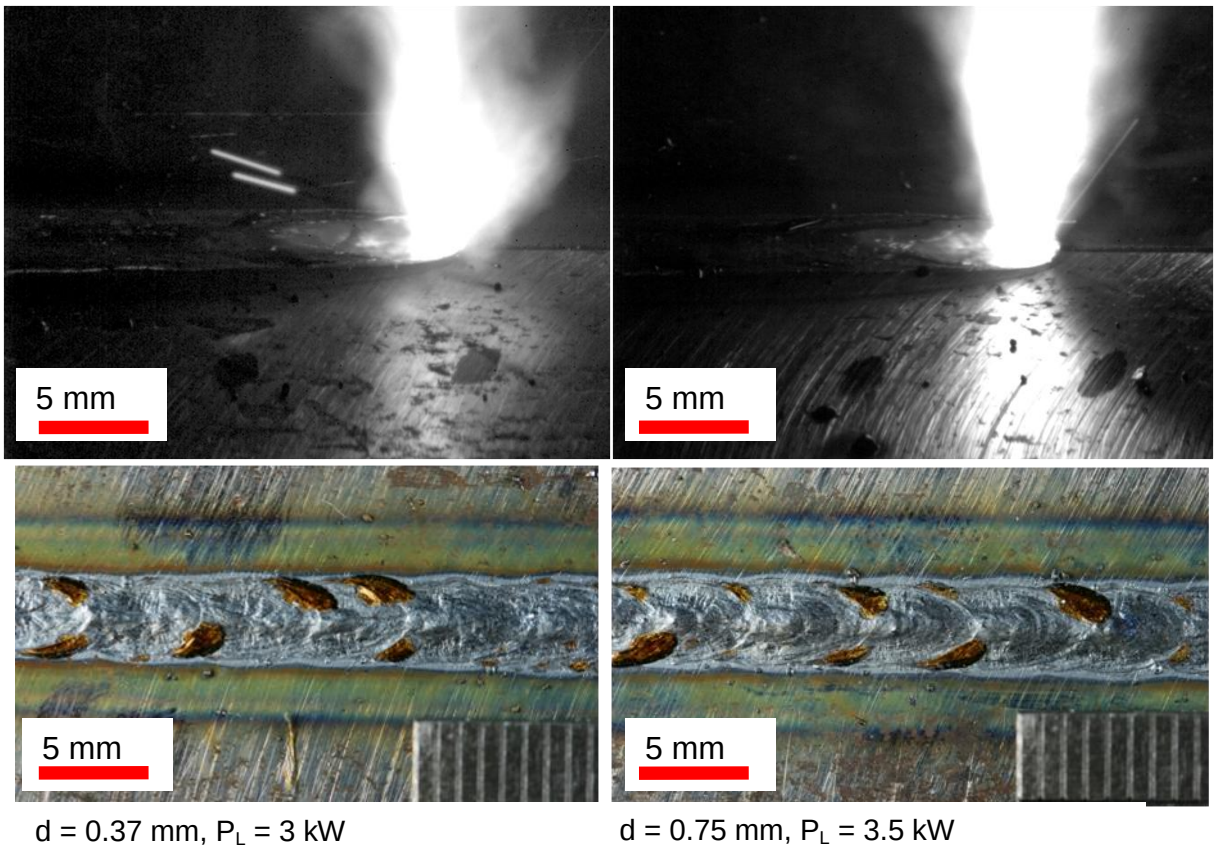

d = 0.37 mm, P_L = 3 kW d = 0.75 mm, P_L = 3.5 kW

***Figure 8.2**: Autogenous laser butt-welds on zero-gap configuration at 0.5 m min^{-1} travel speed and combinations of parameters for 6 mm of depth of penetration.*

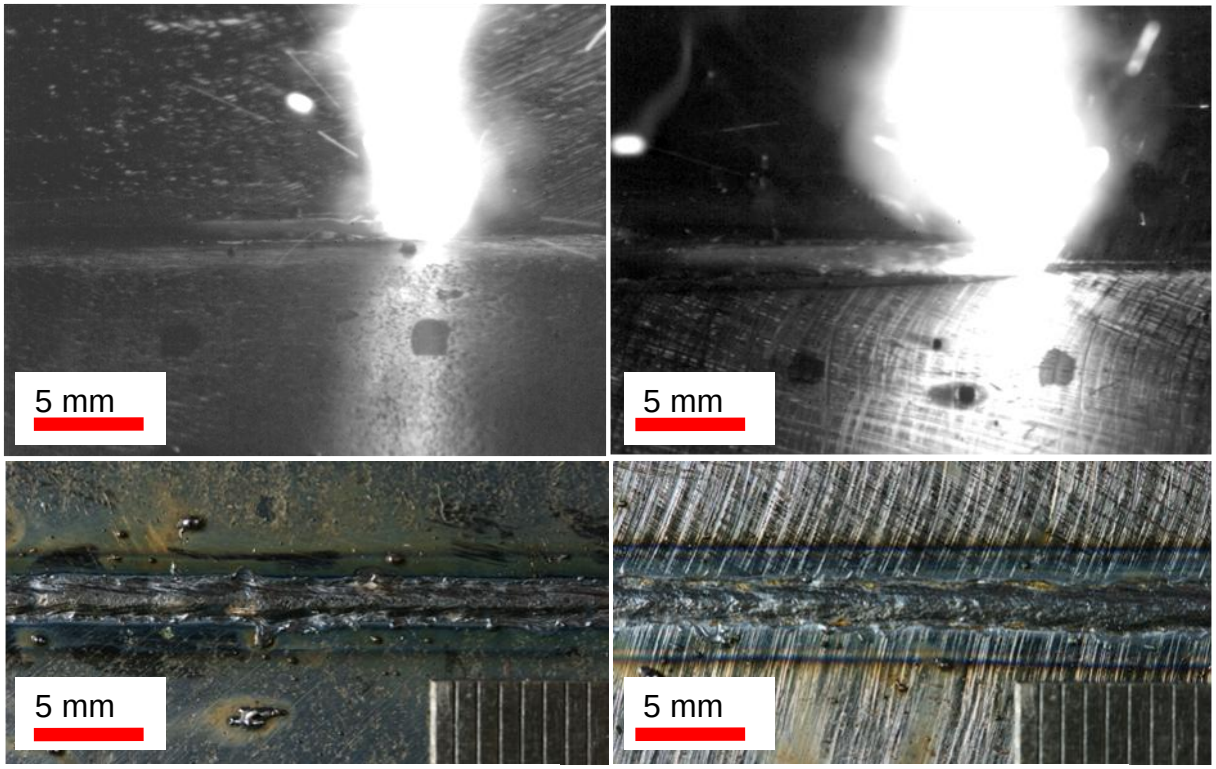

d = 0.37 mm, P_L = 6 kW d = 0.75 mm, P_L = 7.5 kW

***Figure 8.3**: Autogenous laser butt-welds on zero-gap configuration at 3 m min^{-1} travel speed and combinations of parameters for 6 mm of depth of penetration.*

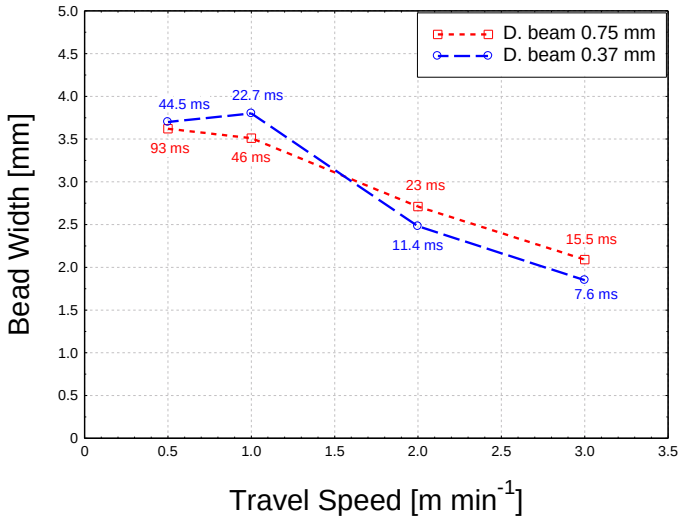

***Figure 8.4**: Width of the top bead as a function of beam diameter and travel speed (effect of interaction time)*

***Table 8.2**: Parameters used for investigation of the effect of beam diameter on the width of the weld bead.*

	d = 0.37 mm					d = 0.75 mm				
v	P_L	q_P	τ_i	E_{SP}	Width	P_L	q_P	τ_i	E_{SP}	Width
[m/min]	[kW]	[MWcm^2]	[ms]	[J]	[mm]	[kW]	[MW/cm^2]	[ms]	[J]	[mm]
0.5	3	2.8	44.5	133	3.7	3.5	0.5	93	325	3.6
1	4	3.7	22.7	91	3.8	5	1.13	46	232	3.5
2	5	4.65	11.4	57	2.5	6	1.36	23	138	2.7
3	6	5.58	7.6	45.6	1.85	7.5	1.7	15.5	116	2.1

The maximum gap that can be accommodated by the autogenous laser welding, obtained from butt-joints with diverging gaps form 0 mm to 2 mm, is shown in Fig.8.5. It can be seen that a bigger beam diameter provides a better fit-up tolerance. In both cases the fit-up tolerance deteriorates marginally with increasing travel speed. The maximum gap bridging ability exhibits very little dependence on the travel speed. For both beam diameters an increase of the travel speed from 0.5 m/min to 3 m/min corresponds to a decrease of interaction time by a factor of six, whilst an increase of beam diameter form 0.37 mm to 0.75 mm corresponds to an increase of interaction time by approximately a factor of two. However, the effect of beam diameter is more significant than the travel speed. It is interesting to notice that the maximum fit-up tolerance of the process with a bigger beam diameter approaches the diameter of the beam on the surface, whereas in case of a smaller beam diameter the tolerance is greater than the actual size of the beam on the surface. In general the fit-up tolerance of laser welding is of the order of beam diameter on the surface.

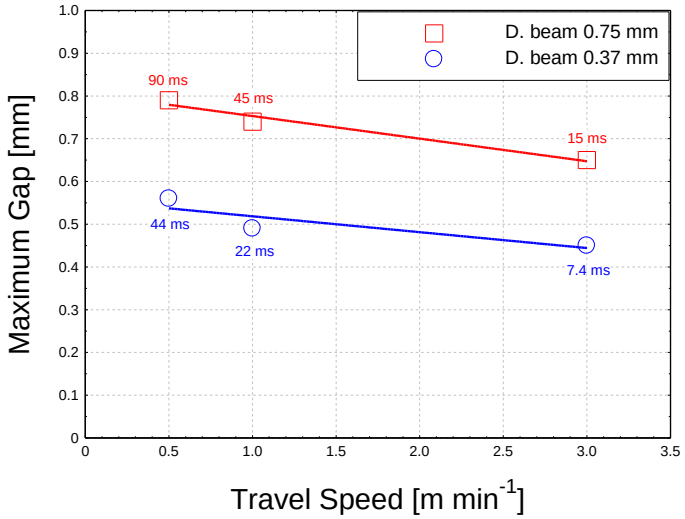

***Figure 8.5**: Maximum gap bridging ability as a function of travel speed for two beam diameters 0.37 mm and 0.75 mm and conditions required for 6 mm depth of penetration (based on diverging gap 0-2 mm).*

8.3. Interactions between laser and arc

8.3.1. Methodology

A focusing lens with a focal length of 250 mm, resulting in 0.6 mm beam diameter in the focal point, was used. This optical set-up provided optimum conditions of the beam diameter and the sufficient working distance between the optics and the workpiece. First, a parametric study of the hybrid welding on bead-on-plate welds was carried out. The influence of contact-tip-to-workpiece-distance (CTWD) of MIG, laser energy, arc energy and leading source selection on the bead profile were examined. All welds were performed with the laser beam at the focal point (focused on the surface).

As the analogy to the laser single arc hybrid welding, a similar parametric study of the hybrid tandem arc welding on bead-plate-welds was carried out. Depending on the orientation of the filler wires relatively to the welding direction in the tandem arc process, they are referred to as longitudinal or transverse configuration of wires. Pictures of both configurations can be found in Section 3.9.3. A CTWD of 14 mm was used for all laser tandem arc hybrid welds.

8.3.2. Results

8.3.2.1. Parametric study of hybrid laser welding

The effect of contact-tip-to-workpiece-distance (CTWD) on the weld profile is shown in Fig.8.6. The welds become deeper and more slender at the bottom, whilst the top beads flatten down with increasing CTWD. However, it was found that when the CTWD was increased beyond 20 mm the arc became too aggressive, resulting in undercut of the toe. Despite the manufacturer recommended CTWD of 19 mm the most suitable value for this work was found to be 17 mm.

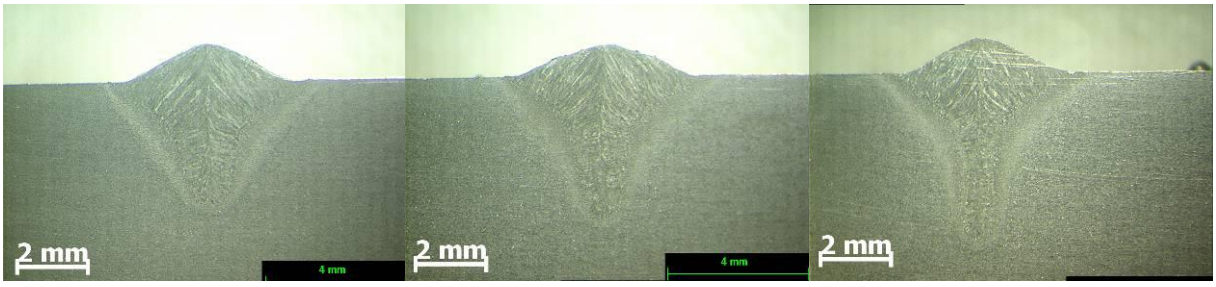

CTWD = 12 mm,	CTWD = 14 mm,	CTWD = 18 mm,
P_{Al} = 7.3 kW (237 A, 27 V)	P_{Al} = 8 kW (235 A, 29.6 V)	P_{Al} = 7.5 kW (213 A, 30 V)

***Figure 8.6**: Effect of CTWD on bead shape (P_L = 5 kW, d = 0.6 mm, v = 4 m min^{-1}, WFS = 13 m min^{-1} and laser leading configuration).*

The flexibility of the hybrid welding is illustrated in Fig.8.7 and Fig.8.8.The depth of penetration is mainly controlled by the laser energy, whilst the deposition rate depends on the wire feed speed of the arc source. An interesting effect is shown in Fig.8.9. A wider top bead and a lower depth of penetration are achieved with the laser leading configuration, compared to the arc leading configuration. A similar effect is shown in Fig.8.10 for a lower wire feed speed. In Fig.8.11 MIG welds without the laser are shown at two welding directions. The same trend as in the hybrid welding is apparent. Note that there was a difference in the incidence angles of the torch, relatively to the workpice, between the laser leading and the arc leading directions, which was shown in Fig.3.12 in Section 3.9.2. In the laser leading configuration the torch was in 30° push position, whilst in the laser leading the torch was in 30° pull position.

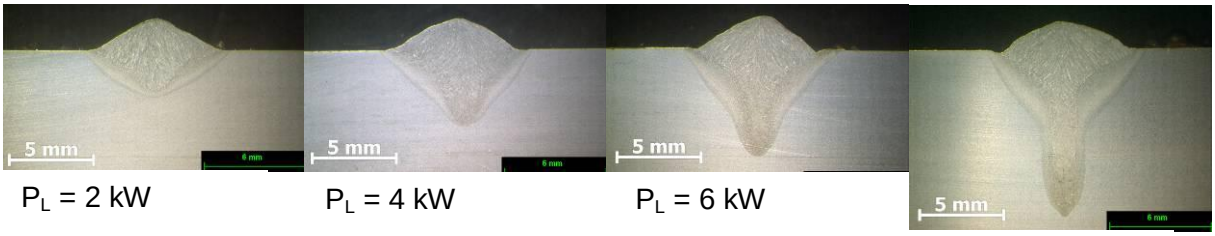

P_L = 2 kW P_L = 4 kW P_L = 6 kW P_L = 8 kW

***Figure 8.7**; Effect of laser power on bead profile (WFS = 15 m min^{-1}, v = 1.5 m min^{-1}, d = 0.6 mm, laser leading, CTWD = 17 mm).*

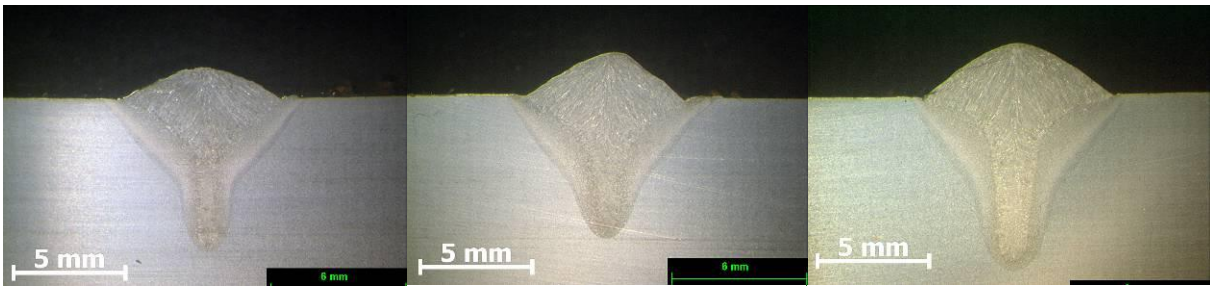

WFS = 10 m/min, P_{AI} = 6.4 kW (184 A, 29 V)
WFS = 15 m/min, P_{AI} = 7.9 kW (248 A, 28 V)
WFS = 20 m/min, P_{AI} = 10.3 kW (314 A, 30 V)

***Figure 8.8**: Effect of wire feed speed on bead shape (P_L = 6 kW, v = 1.5 m min^{-1}, d = 0.6 mm, laser leading, CTWD = 17 mm).*

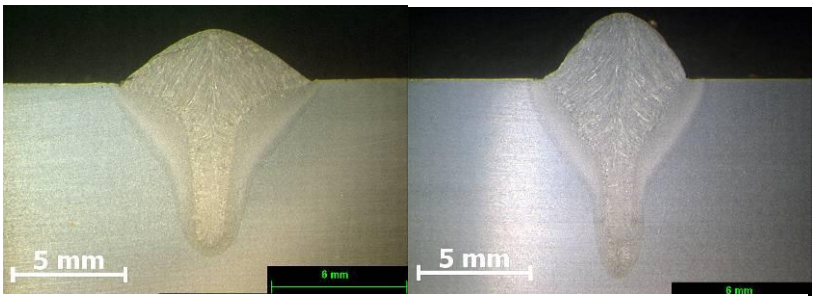

Laser leading P_{AI} = 10.3 kW (314 A, 30 V)
Arc leading P_{AI} = 10.5 kW (323 A, 30.1 V)

***Figure 8.9**: Effect of leading source on bead shape at WFS = 20 m min^{-1} (P_L = 6 kW, v = 1.5 m min^{-1}, d = 0.6 mm, and CTWD = 17 mm).*

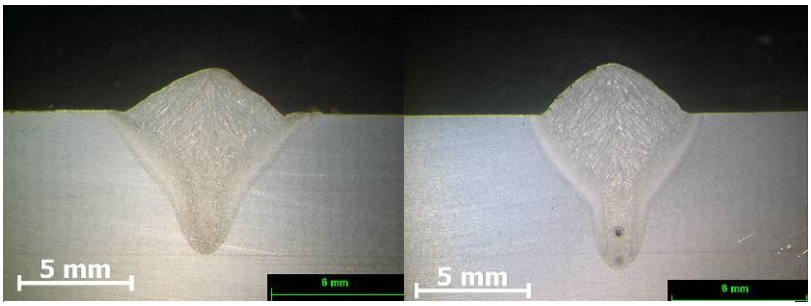

Laser leading
P_{AI} = 7.9 kW (248 A, 28 V)

Arc leading
P_{AI} = 8 kW (237 A, 29 V)

***Figure 8.10**: Effect of leading source on bead shape at WFS = 15 m min^{-1} (P_L = 6 kW, v = 1.5 m min^{-1}, d = 0.6 mm, and CTWD = 17 mm).*

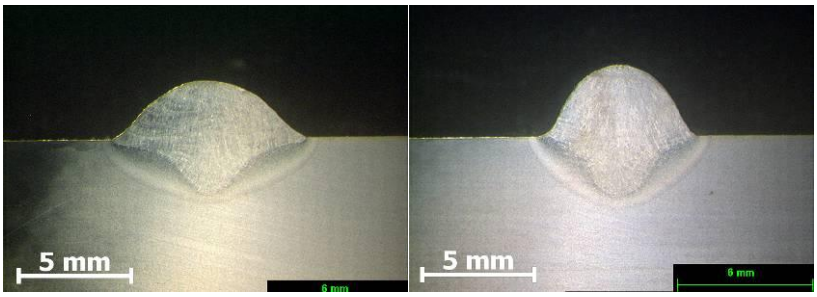

Arc pushing

Arc pulling

***Figure 8.11**: Effect of inclination angle of MIG torch on bead shape (WFS = 15 m min^{-1}, v = 0.8 m min^{-1} and CTWD = 17 mm).*

A comparison of MIG and laser welding separately, as well as in hybrid configuration is shown in Fig.8.12. It is evident that MIG pulling or pushing configuration does not affect the depth of penetration, but only the shape of the bead. The depth of penetration provided by the laser exceeds the depth of MIG welding by few times. Thus in hybrid welding with MIG pushing the depth of penetration is exactly the same as in the case of autogenous laser welding. However, in hybrid welding with MIG torch pulling, the depth of penetration is slightly improved, as compared to the laser welding only.

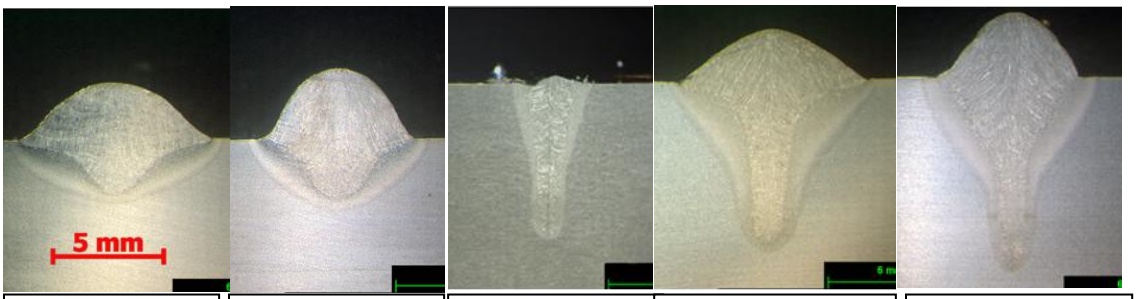

MIG only Pushing	MIG only Pulling	Laser only	Hybrid MIG pushing	Hybrid MIG pulling

***Figure 8.12**: Effect of laser-arc interaction on depth of penetration in hybrid welding.*

8.3.2.2. Parametric study of laser tandem arc hybrid welding

Similarly as in the hybrid welding with a single arc, the shape of the bead and the depth of penetration in the tandem arc hybrid welding can be controlled fairly independent, by adjusting the laser energy or wire feed speed, as shown in Fig.8.13 and Fig.8.14. However, the characteristic for the laser welding bead shape, with the narrow neck at the bottom, is only apparent with high laser energies. This is attributed to a large amount of molten metal from both filler wires that the laser has to cope with. Thus, as shown in Fig.8.14 the weld becomes more uniform as the wire feed speed increases However, as a consequence, the heat input increases rapidly with increasing wire feed speed.

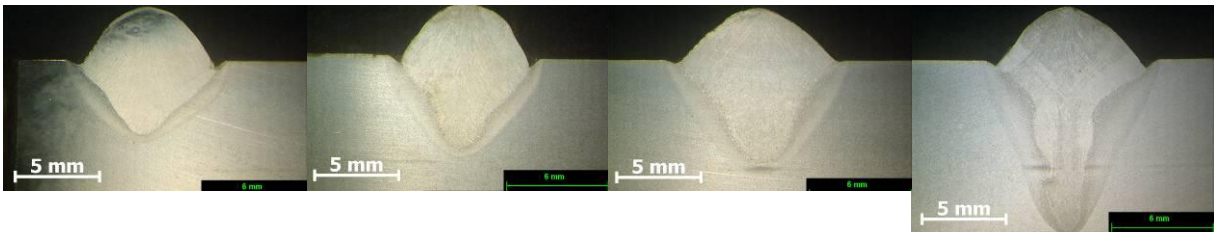

P_L = 2 kW, P_{AI} = 18.5 kW	P_L = 4 kW, P_{AI} = 14.6 kW	P_L = 6 kW, P_{AI} = 16.6 kW	P_L = 8 kW, P_{AI} = 15.4 kW

***Figure 8.13**: Effect of laser energy on bead shape in tandem MIG hybrid welding (WFS = 2x 15 m min^{-1}, v = 1.5 m min^{-1}, d = 0.6 mm, laser leading and transverse arcs).*

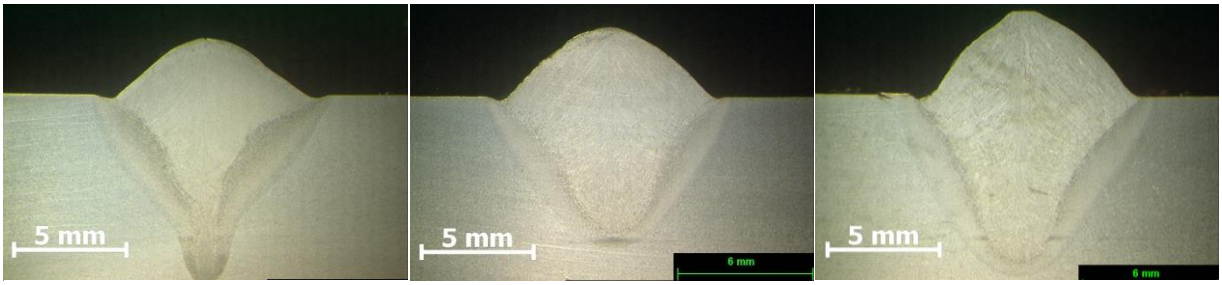

WFS = 2 x 10 m/min, P_{AI} = 11 kW, (175 A, 24 V; 186 A, 24 V)	WFS = 2 x 15 m/min, P_{AI} = 16.6 kW, (242 A, 27.8 V; 252 A, 29.2 V)	WFS = 2 x 20 m/min, P_{AI} = 20.3 kW, (316 A, 28.8 V; 328 A; 28.8 V)

***Figure 8.14**: Effect of wire feed speed on bead shape in tandem MIG hybrid welding (P_L = 6 kW, d = 0.6 mm, v = 1.5 m min^{-1}, laser leading and transverse arcs).*

The effect of leading source on the bead shape also has an important effect, as shown in Fig.8.15. A significant reduction of the weld width and increase of the depth of penetration by approximately 5 mm can be observed with the arc leading configuration, as compared to the laser leading case. Note that the higher depth of penetration was achieved, despite a slightly lower power of the arc source. It can be also seen in Fig.8.15 that the depth of penetration with the arc leading configuration is greater than the laser welding only, whilst the hybrid welding with the laser leading exhibits a slightly shallower welds than in the laser welding. Considering the width of the top bead, the laser leading configuration seems to be more beneficial for bridging wide gaps.

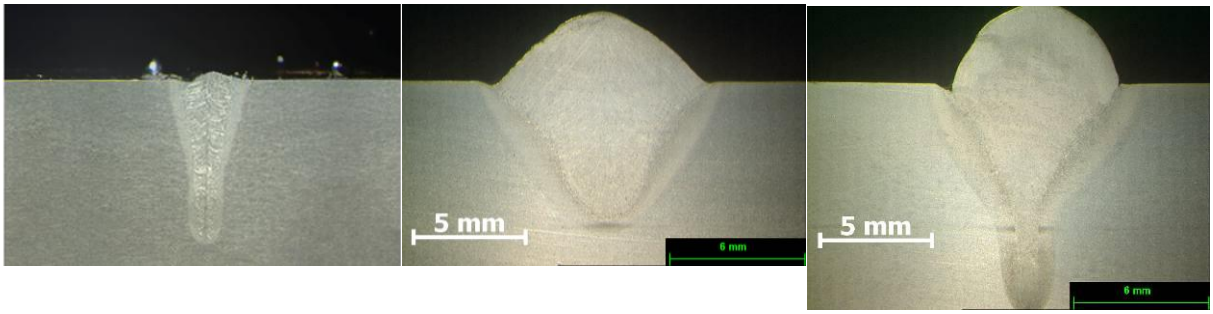

Laser only	Laser leading P_{AI} = 16.6 kW, (242 A, 27.8 V; 252 A, 29.2 V)	Arc leading P_{AI} = 14.6 kW, (244 A, 24.8 V; 257 A; 24.4 V)

***Figure 8.15**: Effect of leading source on bead shape in tandem MIG hybrid welding (WFS = 2x15 m min^{-1}, P_L = 6 kW, v = 1.5 m min^{-1}, d = 0.6 mm, transverse arcs).*

In Fig.8.16 a comparison of laser/MIG hybrid and laser/tandem MIG hybrid for the same overall wire feed speed of 20 m/min is shown. The welds have similar dimensions, but the hybrid tandem arc one exhibits a less uniform shape. The melting areas of hybrid welding and hybrid tandem, measured from the macrographs are 30 mm^2 and 35 mm^2 respectively.

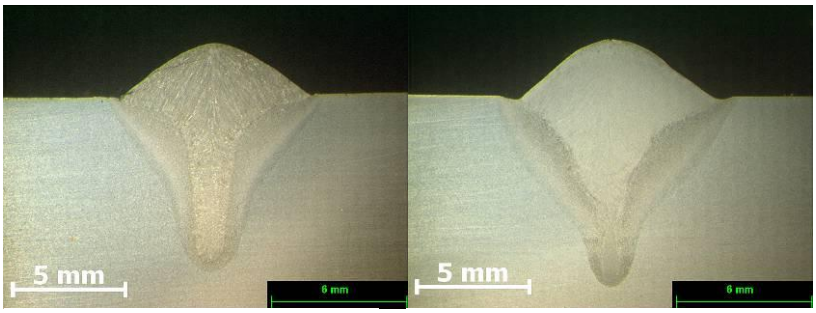

Hybrid with single arc	Hybrid with tandem arc
P_{Al} = 10.3 kW	P_{Al} = 11 kW
WFS = 20 m min^{-1}	WFS = 2x10 m min^{-1}

***Figure 8.16**: Comparison of hybrid single MIG and hybrid tandem MIG processes for the same overall wire feed speed of 20 m min^{-1} (P_L = 6 kW, d = 0.6 mm, v = 1.5 m min^{-1}).*

The importance of laser beam on the uniformity of the weld bead is shown in Fig.8.17. The picture presents an example of top bead produced by the tandem MIG process without the laser at a travel speed of 1.5 m/min. The unstable bead shape and characteristic humps, despite depositing a significant amount of filler metal are evident. Note that unlike usually used in tandem welding, the transverse configuration of filler wires was mostly used in this chapter. It can be seen that a 1.5 m/min travel speed can be considered as a maximum limit for tandem MIG welding with the transverse configuration of filler wires, unless a laser beam is added.

***Figure 8.17**: Picture of top bead achieved with tandem MIG welding without laser beam at 1.5 m min^{-1} travel speed (WFS = of 2x15 m min^{-1}, transverse configuration of wires).*

8.4. Fit-up tolerance of laser single arc hybrid welding

It was shown that the maximum gap between the joined plates that could be bridged by the autogenous laser welding was less than 0.8 mm. To increase the fit-up tolerance the hybrid welding process is utilised. As was shown previously the fit-up tolerance of laser welding is primarily dependent on the beam diameter on the surface and then is also slightly dependent on the size of the melt pool. In this part the influence of filler wire is investigated.

8.4.1. Methodology

The fit-up tolerance of hybrid welding on different bevel configurations (Table 8.1) was investigated. A CTWD of 17 mm and a maximum possible wire feed speed of 20 m/min (1 mm diameter of wire) were used. All the hybrid single arc butt-welds were carried out with the laser leading configuration. Some welds were performed with the laser beam being out of focus (positive defocusing) to provide greater beam diameters.

8.4.2. Results

The fit-up tolerance of the hybrid welding was initially investigated using a butt-weld with a diverging gap from 0 mm to 2 mm, similarly as in the case of laser welding. Unlike in the autogenous laser welding, the 2 mm gap was insufficient to collapse the hybrid laser process, as shown in Fig.8.18.

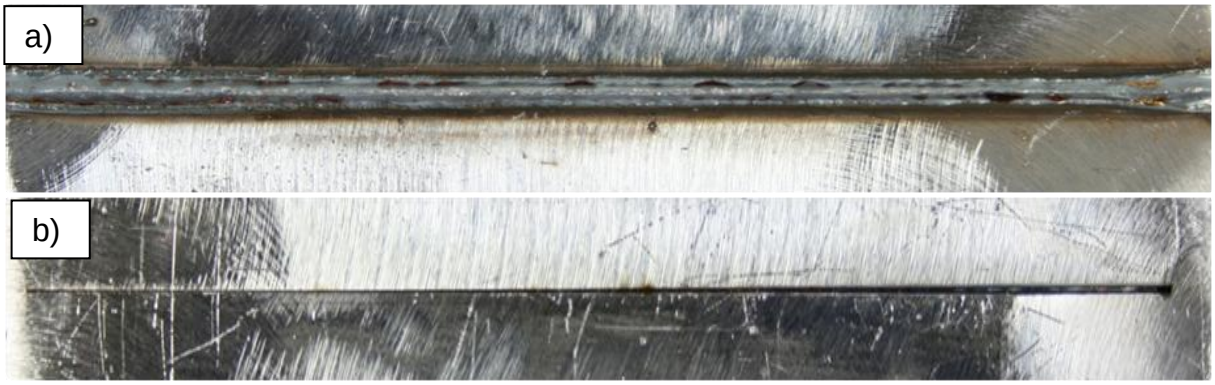

***Figure 8.18**: Hybrid laser single MIG welding in butt-weld configuration with diverging gap 0-2 mm (v = 3 m min^{-1}, WFS = 20 m min^{-1}, P_L = 6 kW, d = 0.6 mm);* ***a)** top bead;* ***b)** bottom side.*

The effect of gap on the bead shape at a constant deposition rate is shown in Fig.8.19. It can be seen in Fig.8.19(a) that the laser energy was insufficient to fully penetrate the plates and the majority of filer metal was deposited at the top of the X-prep, when no gap was apparent. In contrast, as the gap increased to 2 mm, the majority of metal was deposited in the space between the plates, as shown in Fig.8.19(b). The lack of fusion, due to insufficient beam diameter of the laser, which was not able to melt both edges is apparent. Unfortunately the weld was not consistent over the entire length of the workpiece and the process collapsed completely in a further part, which is shown in Fig.8.22.

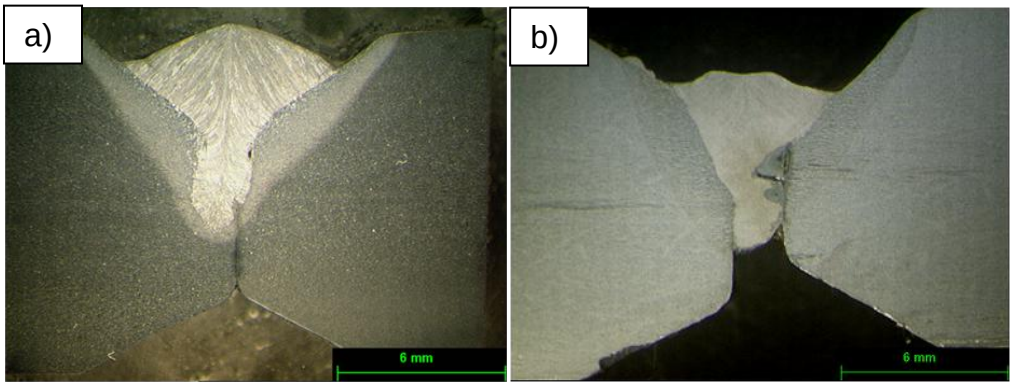

***Figure 8.19**: Effect of gap on butt-weld with X-prep configuration (v = 1.5 m min^{-1}, WFS = 20 m min^{-1}, P_L = 4 kW, d = 0.6 mm, q_p = 1.4 MW cm^{-2}, τ_i = 24 ms, E_{SP} = 96 J);* ***a)** no gap;* ***b)** 2 mm horizontal gap.*

In Fig.8.20 a tack weld with the zero gap configuration, carried out at a travel speed of 4 m/min is shown. In general the weld exhibits a reasonably good appearance for the tack welding application, despite a significant lack of penetration. In contrast, the lack of penetration disappeared completely in case of misaligned bevel, as shown in Fig.8.21. The opened top, in this example, provided enough gap for the filler metal and laser beam to reach the bottom of the joint, whilst the closed bottom prevented the liquid metal from sagging. Thus a successful joint could be achieved at a fairly fast travel speed of 5 m/min.

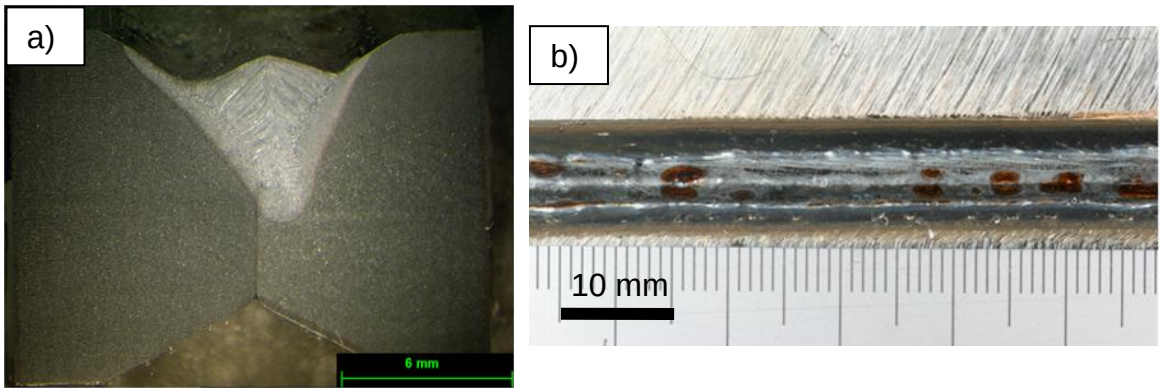

***Figure 8.20**: Butt-weld on X-prep with zero gap configuration (v = 4 m min^{-1}, WFS = 20 m min $^{-1}$, P_L = 8 kW, d = 0.6 mm, q_p = 2.8 MW cm^{-2}, τ_i = 9 ms, E_{SP} = 72 J); **a)** macrograph; **b)** top bead.*

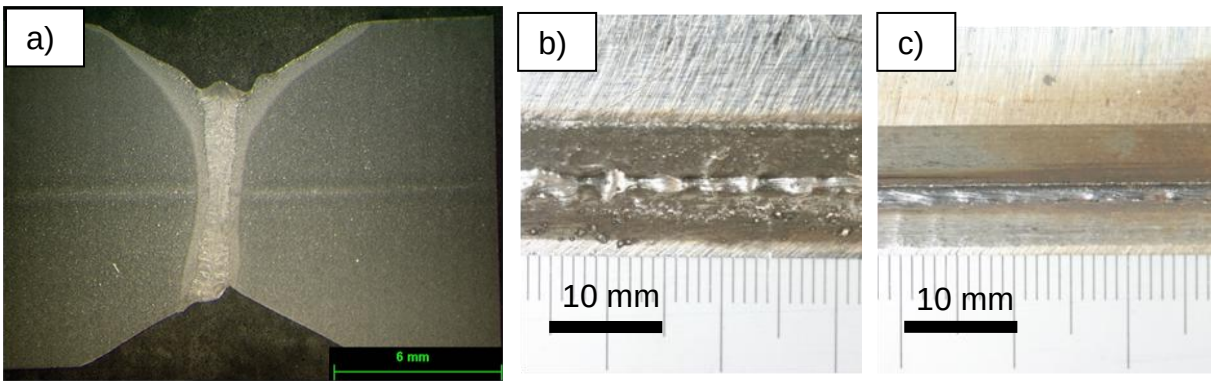

***Figure 8.21**: Butt-weld on misaligned X-prep configuration (v = 5 m min^{-1},WFS = 20 m min $^{-1}$, P_L = 8 kW, d = 0.6 mm, q_p = 2.8 MW cm^{-2}, τ_i = 7.2 ms, E_{SP} = 58 J); **a)** macrograph; **b)** top bead.*

The standard hybrid laser welding process failed to weld a joint with a horizontal gap of 2 mm, as shown in Fig.8.22. Unlike in the misaligned bevel (Fig.8.21), here there was not enough force to hold the deposited metal against gravity and therefore a significant part of the joint was not bridged. The same gap could be, however, bridged when the power density of the laser beam was significantly reduced by increasing the beam diameter. As shown in Fig.8.23 a successful weld could be achieved with a beam diameter of 1.8 mm and the arc conditions kept the same. A similar effect could be obtained by focusing the laser beam off-axis from the weld centreline, on one of the edges of the bevel. The weld presented in Fig.8.24 also exhibits good appearance.

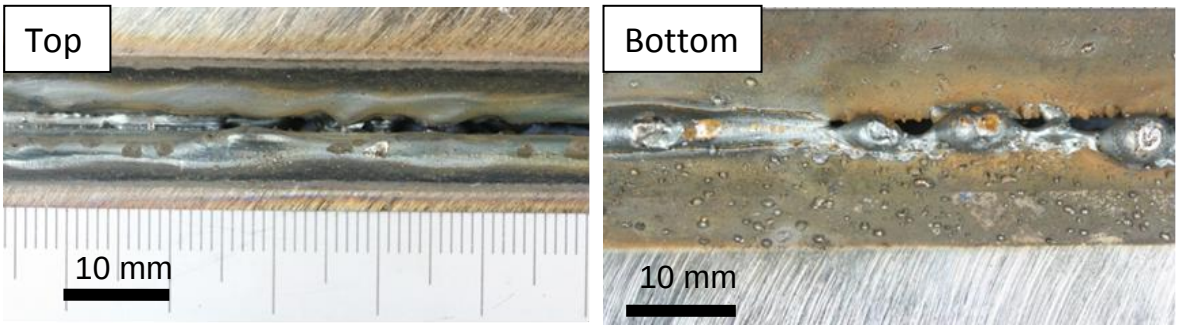

***Figure 8.22**: Butt-weld on X-prep with 2 mm horizontal gap configuration (v = 1.5 m min^{-1}, WFS = 20 m min $^{-1}$, P_L = 4 kW, d = 0.6 mm, q_p = 1.4 MW cm^{-2}, τ_i = 24 ms, E_{SP} = 96 J).*

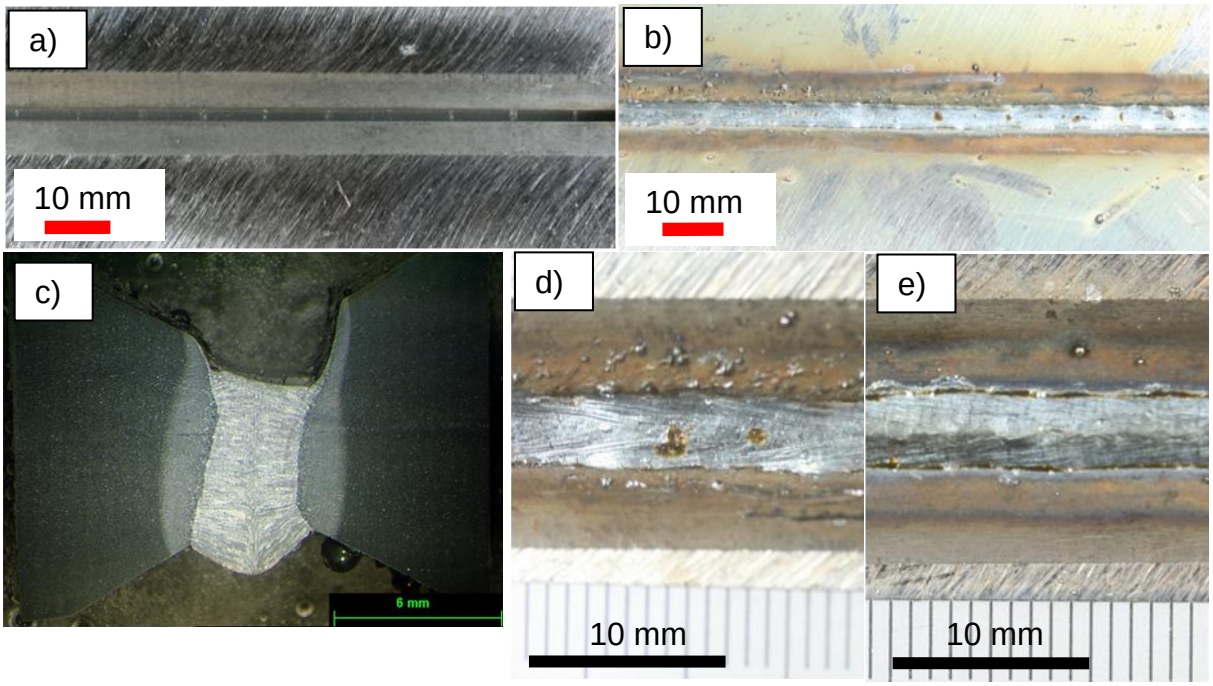

***Figure 8.23**: Butt-weld on X-prep with 2 mm horizontal gap configuration (v = 1.5 m min^{-1}, WFS = 20 m min $^{-1}$, P_L = 5 kW, d = 1.8 mm (defocused by 17 mm), q_p = 0.2 MW cm^{-2}, τ_i = 72 ms, E_{SP} = 360 J); **a)** before welding; **b)**, **d)** top bead; **c)** macrograph; **e)** root face.*

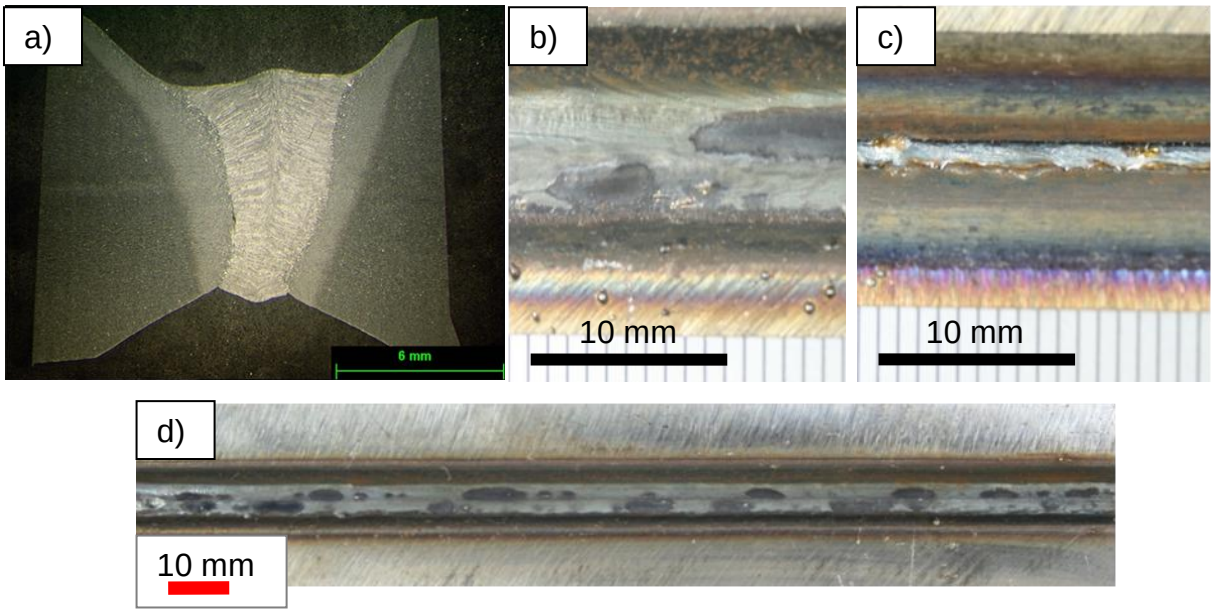

***Figure 8.24**: Butt-weld on X-prep with 2 mm horizontal gap configuration (v = 1.5 m min^{-1}, WFS = 20 m min $^{-1}$, P_L = 5 kW, d = 0.6 mm, laser beam tilted by 5° off-side, q_p = 1.8 MW cm^{-2}, τ_i = 24 ms, E_{SP} = 120 J); **a)** macrograph; **b)**, **d)** top bead; **c)** root face.*

8.5. Fit-up tolerance of laser/tandem MIG hybrid process

To improve the fit-up tolerance farther beyond 2 mm and perhaps enable an increase of travel speed, in the next experiment a tandem arc process is combined with the laser. The aim is to investigate if the gap bridging ability can be improved further by increasing the deposition rate of the filler metal.

8.5.1. Methodology

A focusing lens with a focal length of 250 mm, resulting in 0.6 mm beam diameter in the focal point was used. To achieve bigger beam diameters, various out of focus positions were used. The tandem arc process was operated in a synergic mode and the arc length correction parameter was adjusted to achieve a stable spray metal transfer. A CTWD of 14 mm was used. The fit-up tolerance of hybrid tandem MIG welding was investigated on different bevel configurations (Table 8.1). All the hybrid tandem arc butt-welds were carried out in the laser leading configuration.

8.5.2. Results

8.5.2.1. Diverging gap

As the analogy to the autogenous laser welding and the hybrid laser welding, the fit-up tolerance using a butt-joint with a diverging gap was initially investigated. Unlike in previous cases, a gap diverging from 0 mm to 7 mm was used. The results for a travel speed of 1.5 m/min and a wire feed speed of 2x15 m/min are shown in Fig.8.25. It can be seen that the process collapsed as the gap exceeded approximately 4 mm, despite the fact that the relatively wide separation distance between both wires was sufficient to melt both edges of the bevel, almost until the end. The top bead seems to be unchanged i.e. without any sign of undercut until the gap does not exceed 2 mm. The ability to bridge gaps did not increase with increasing wire feed speed further to 2x25 m/min, as shown in Fig.8.26.

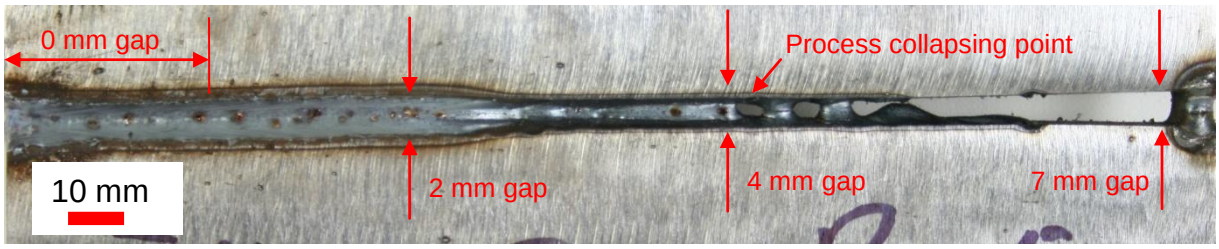

***Figure 8.25**: Maximum gap bridging ability of tandem MIG hybrid welding on butt-weld with diverging gap 0-7 mm with WFS = 2x15 m min^{-1} (v = 1.5 m min^{-1}, P_L = 5 kW, d = 0.6 mm, transverse configuration of wires).*

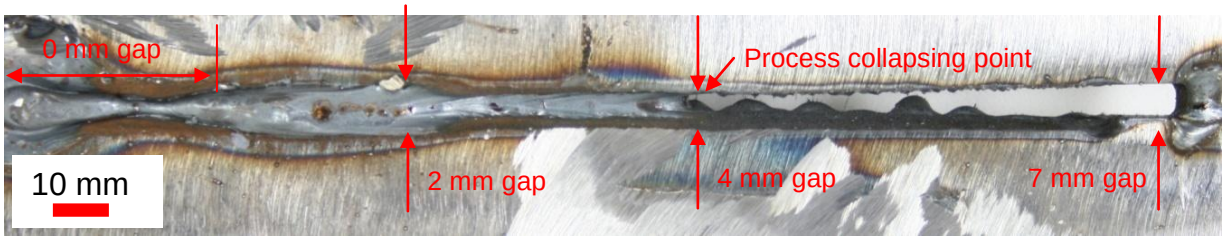

***Figure 8.26**: Maximum gap bridging ability of tandem MIG hybrid welding on butt-weld with diverging gap 0-7 mm with WFS = 2x25 m min^{-1} (v = 1.5 m min^{-1}, P_L = 5 kW, d = 0.6 mm, transverse configuration of wires).*

8.5.2.2. Zero gap and not square bevel

The effect of different configurations of filler wires on the bead shape in X-prep with zero gap is shown in Fig.8.27. It can be seen that a wire feed speed of 2x20 m/min provided more than sufficient amount of filler metal to weld this joint at 1.5 m/min travel speed. A marginally wider and more uniform weld profile with the transverse configuration of wires is apparent, compared to the longitudinal one. In both cases the instantaneous powers of the arcs were similar.

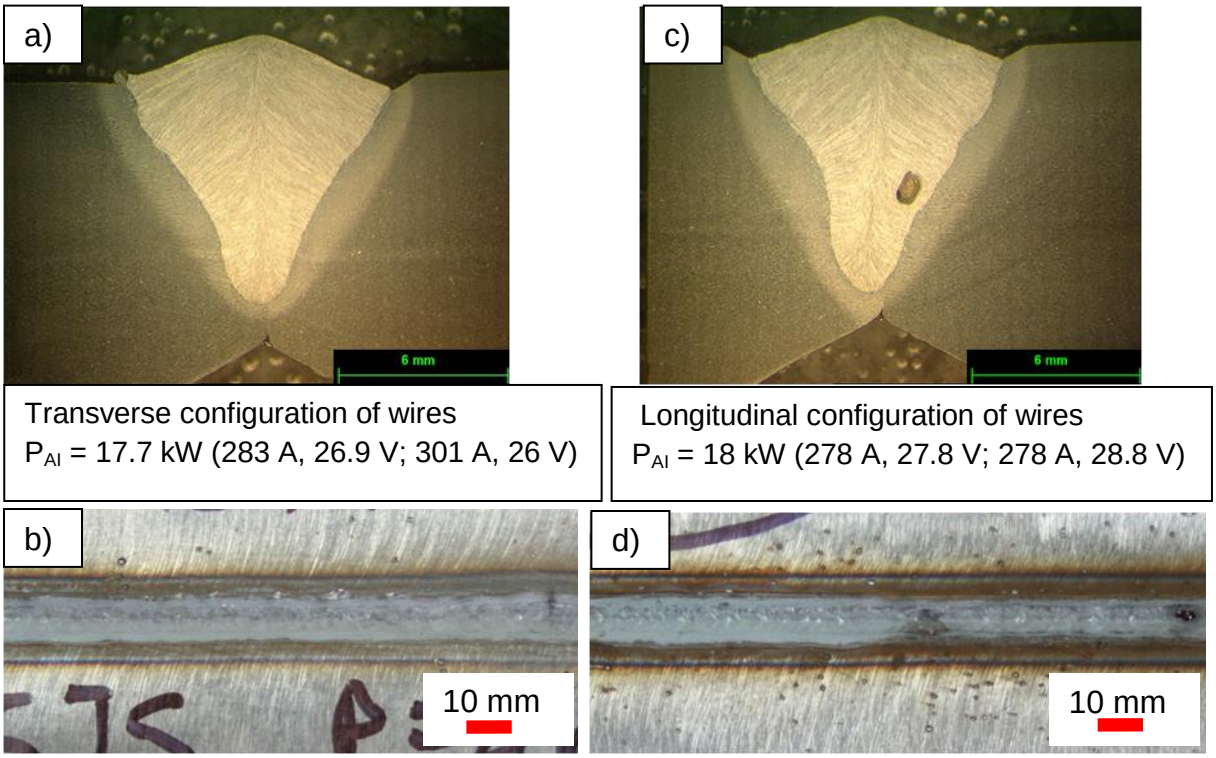

***Figure 8.27**: Effect of arc configuration on butt-weld with X-prep zero gap (v = 1.5 m min^{-1}, WFS = 2x20 m min $^{-1}$, P_L = 4 kW, d = 0.6 mm, q_p = 1.4 MW cm^{-2}, τ_i = 24 ms, E_{SP} = 96 J); **a)**, **b)** macrograph and top bead for transverse configuration of wires; **c)**, **d)** macrograph and top bead for longitudinal configuration of wires.*

In Fig.8.28 a hybrid laser tandem arc weld in a butt-joint at a travel speed of 4 m/min is shown. The top bead exhibits an inconsistent transition between the weld and the parent metal, due to lack of wet-ability. It can be seen that the majority of laser energy was focused in the middle of the bead to provide the depth of penetration, rather than to spread the filler metal. This demonstrates that the travel speed of the hybrid tandem arc welding cannot be much more increased than in the single arc hybrid welding process, despite the larger amount of filler metal.

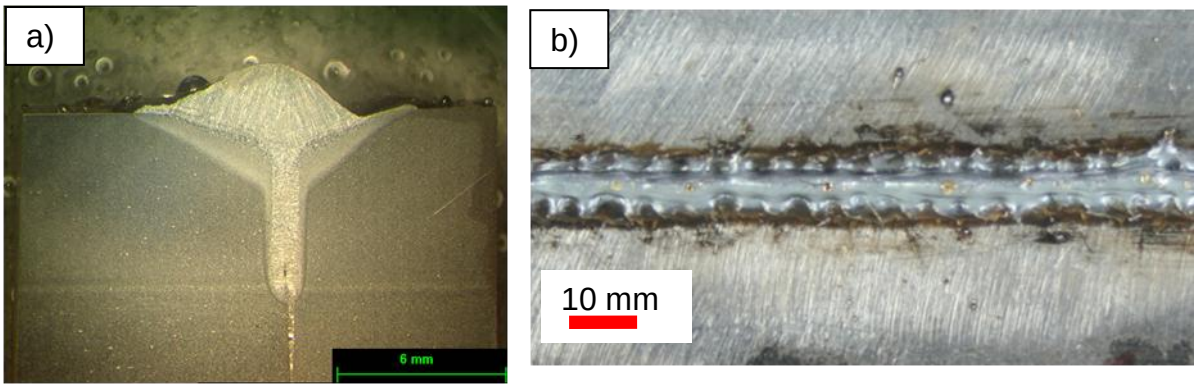

***Figure 8.28**: Butt-weld with zero gap configuration (v = 4 m min^{-1}, WFS = 2x20 m min $^{-1}$, P_{AI} = 14.1 kW, P_L = 7 kW, d = 0.6 mm, q_p = 2.5 MW cm^{-2}, τ_i = 9 ms, E_{SP} = 63 J, transverse configuration of wires); **a)** macrograph; **b)** top bead.*

It was shown in Section 8.4 that using larger beam diameters could improve the bead quality of the hybrid laser welding. A similar effect is observed in the hybrid laser tandem process. In Fig.8.29 a tack weld in X-prep with a misaligned bevel is presented. The large beam diameter of 1.8 mm provided a nice surface finish at this high travel speed of 4 m/min. However, this weld exhibits a significant lack of penetration, due to the low power density of 0.2 MW/cm^2, despite the incompletely closed bevel design. Alternatively, in Fig.8.30 the depth of penetration is increased by increasing the power density to 0.6 MW/cm^2. This was achieved by reducing the beam diameter from 1.8 mm to 1.2 mm. Furthermore, it is shown in Fig.8.31 that the excessive wire feed speed does not improve the quality and depth of penetration of the joint. The relatively high wire feed speed of 2x25 m/min resulted in a convex reinforcement, which is not particularly beneficial.

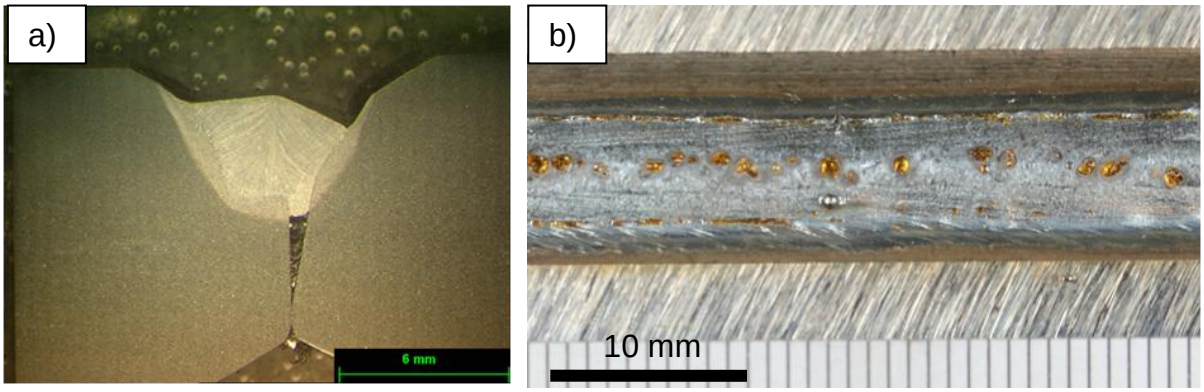

***Figure 8.29**: Butt-weld on misaligned X-prep configuration (v = 4 m min^{-1},WFS=2x15 mmin $^{-1}$, P_{Al} = 11.8 kW, P_L = 5 kW, d = 1.8 mm (defocused by 17 mm), q_p = 0.2 MW cm^{-2}, τ_i = 27 ms, E_{SP} = 135 J, transverse configuration of wires); **a)** macrograph; **b)** top bead.*

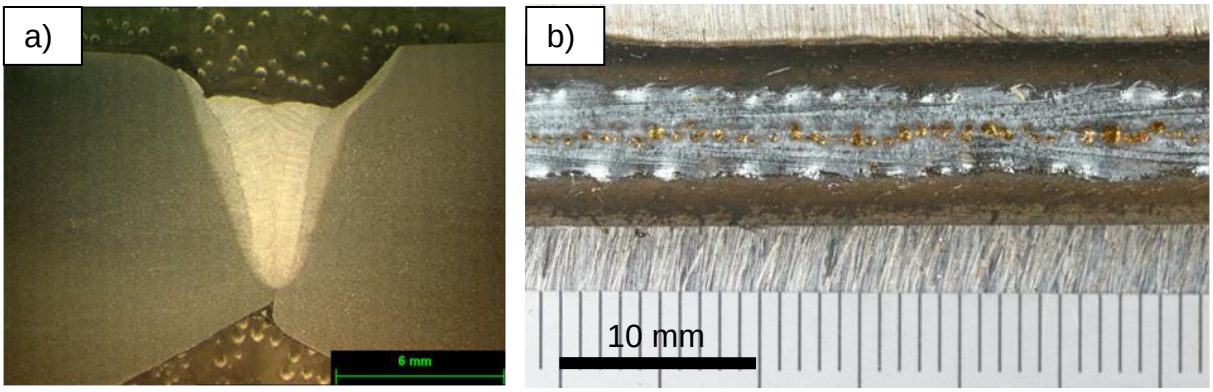

***Figure 8.30**: Butt-weld on misaligned X-prep configuration (v = 5 m min^{-1},WFS=2x20 mmin $^{-1}$, P_{Al} = 16 kW, P_L = 7 kW, d = 1.2 mm (defocused by 10 mm), q_p = 0.6 MW cm^{-2}, τ_i = 14 ms, E_{SP} = 101 J, transverse configuration of wires); **a)** macrograph; **b)** top bead.*

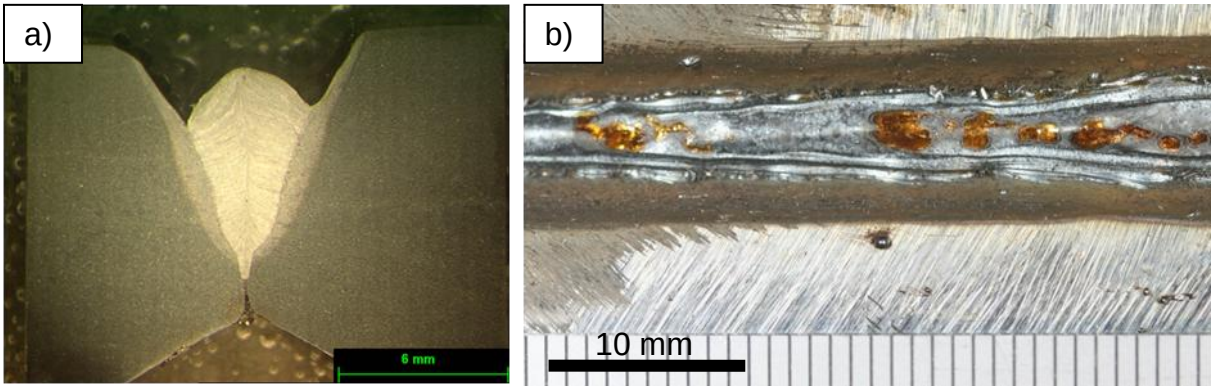

***Figure 8.31**: Butt-weld on misaligned X-prep configuration (v = 4 m min^{-1},WFS=2x25 mmin $^{-1}$, P_{Al} = 21.1 kW, P_L = 7 kW, d = 1.2 mm (defocused by 10 mm), q_p = 1.6 MW cm^{-2}, τ_i = 18 ms, E_{SP} = 126 J, transverse configuration of wires); **a)** macrograph; **b)** top bead.*

8.5.2.3. 2 mm horizontal gap

It was shown in Section 8.4 that the real difficulties in the hybrid laser welding with a single arc emerged when the gap significantly increased. In Fig.8.32 an example of unsuccessful joint in a bevel with 2 mm horizontal gap bevel, using a tandem arc hybrid laser welding is shown. The joint exhibits an inconsistent bead and excessive amount of metal in the root face. This implies that the large amount of filler metal is not sufficient to bridge large gaps. It was possible, however, to improve the gap bridging ability by focusing the laser beam off-axis on the edge of the bevel, as shown in Fig.8.33. Note that the gap was bridged despite using a small beam diameter of 0.6 mm and a high power density of 1.8 MW/cm^2. A further step was taken in Fig.8.34. In this case the laser beam, as well as the tandem torch was focused on the edge of the bevel. This enabled for an accommodation of this gap at 3 m/min travel speed. To be able to place both filler wires on one the edges of the bevel, the longitudinal configuration of filler wires was used. It can be seen in Fig.8.34 that despite the asymmetric bead, due to the strong electromagnetic force from the arc, the achieved joint is consistent.

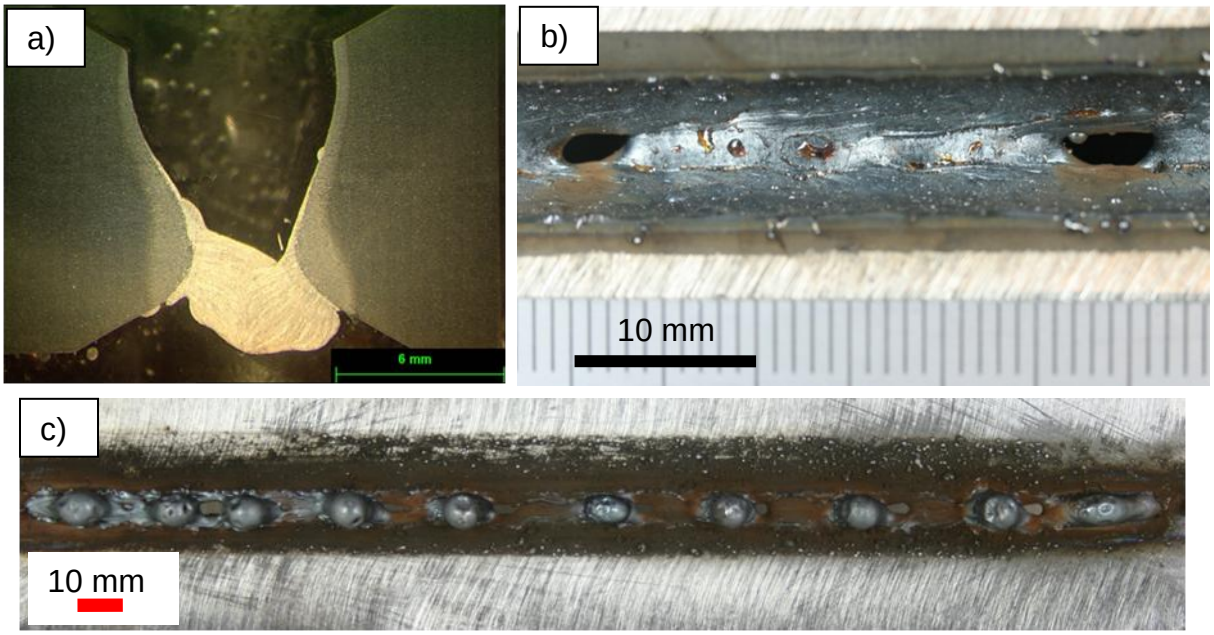

***Figure 8.32**: Butt-weld on X-prep with 2 mm horizontal gap configuration (v = 1.5 m min^{-1}, WFS = 2x20 m min^{-1}, P_{Al} = 18.2 kW, P_L = 5 kW, d = 0.6 mm, q_p = 1.8 MW cm^{-2}, τ_i = 24 ms, E_{SP} = 120 J, transverse configuration of wires); **a)** macrograph; **b)** top bead; **c)** root face.*

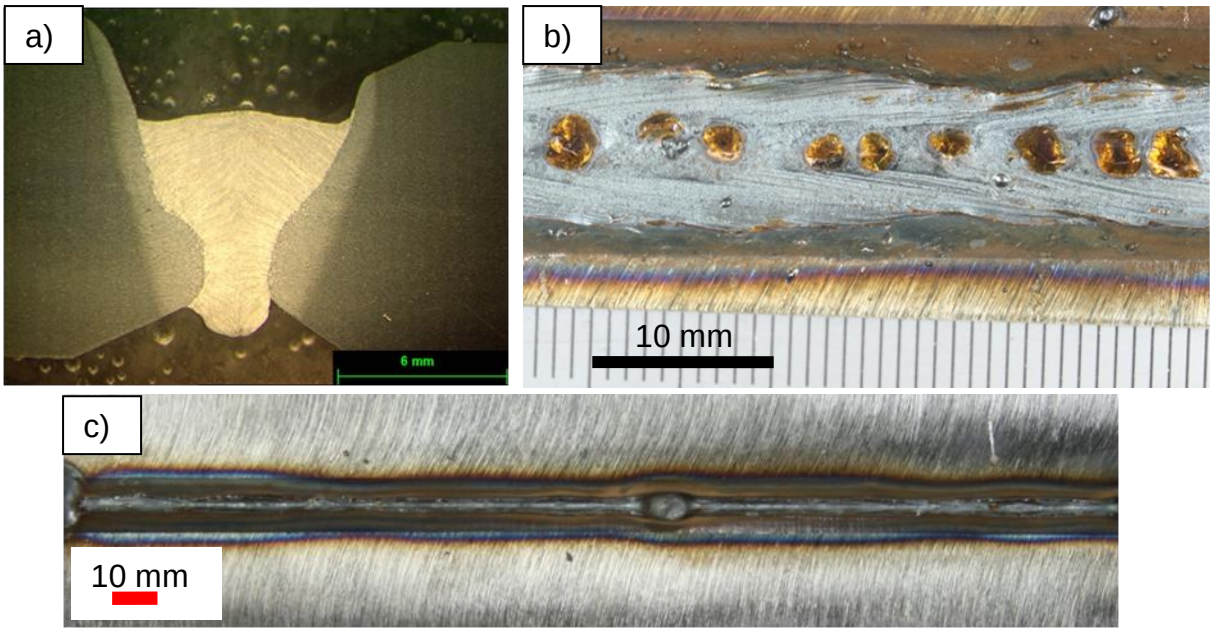

***Figure 8.33**: Butt-weld on X-prep with 2 mm horizontal gap configuration (v = 1.5 m min^{-1}, WFS = 2x20 m min $^{-1}$, P_{Al} = 16.5 kW, P_L = 5 kW, d = 0.6 mm, q_p = 1.8 MW cm^{-2}, τ_i = 24 ms, E_{SP} = 120 J, transverse configuration of wires, laser tilted off side); **a)** macrograph; **b)** top bead; **c)** root face.*

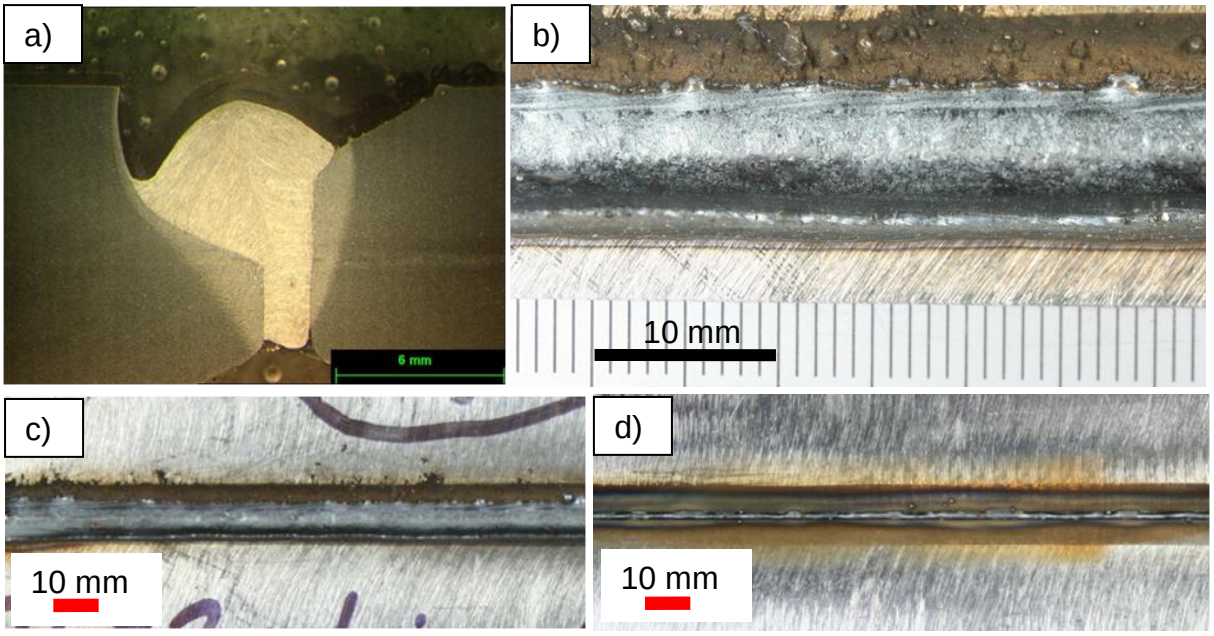

***Figure 8.34**: Butt-weld on X-prep with 2 mm horizontal gap configuration (v = 3 m min^{-1}, WFS = 2x25 m min $^{-1}$, P_{Al} = 21.4 kW, P_L = 5 kW, d = 0.6 mm, q_p = 1.8 MW cm^{-2}, τ_i = 12 ms, E_{SP} = 60 J, longitudinal configuration of wires, laser and arc off side); **a)** macrograph; **b)**, **c)** top bead; **d)** root face.*

To have a reference point a backing plate, which supported the molten metal at the bottom, was used on some of the bevels. In Fig.8.35 such an example with 2 mm gap is shown. The backing bar enabled a consistent joint with a good surface to be achieved at 3 m/min travel speed. Unfortunately the backing bar could not be separated from the workpiece after welding.

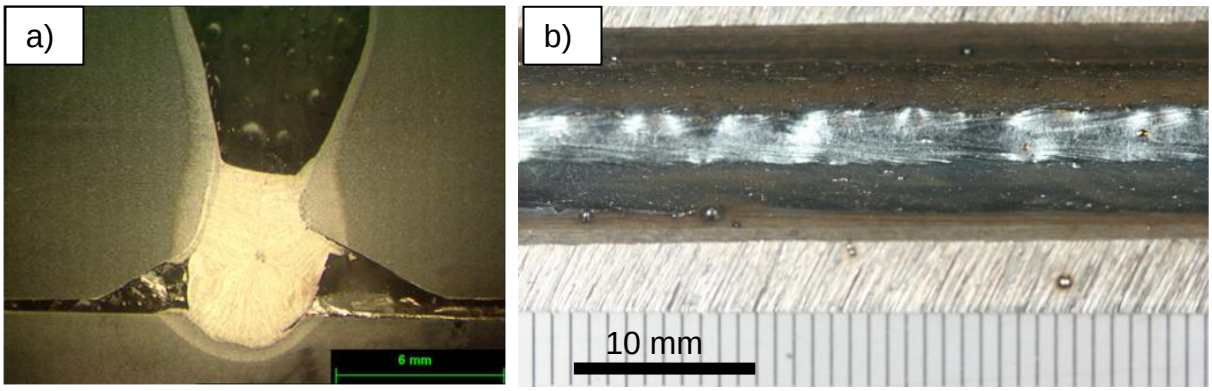

***Figure 8.35**: Butt-weld on misaligned X-prep with 2 mm horizontal gap configuration with backing plate (v = 3 m min^{-1}, WFS = 2x20 m min $^{-1}$, P_{AI} = 17.2 kW, P_L = 7 kW, d = 1.2 mm (defocused by 10 mm), q_p = 0.6 MW cm^{-2}, τ_i = 24 ms, E_{SP} = 168 J, transverse configuration of wires); **a)** macrograph; **b)** top bead.*

8.5.2.4. 3 mm and 5 mm horizontal gap

As demonstrated in Fig.8.36 the tandem arc hybrid welding failed to bridge a joint with 3 mm horizontal gap, despite using a defocused laser beam. It can be observed that the majority of filler metal was deposited just on one side of the bevel. In contrast, focusing the laser beam on one of the edges of the bevel significantly improved the bridging ability, as shown in Fig.8.37. This prevented the filler metal form severe sagging. There is evidence of disturbed integrity of the joint in two points, but in general it was possible to bridge this gap. As a comparison in Fig.8.38 the same joint configuration with a backing plate is presented. The improved surface quality and joint consistency is apparent. Fig.8.39 shows that the tandem torch with a medium wire feed speed provided enough metal for a tack joint with 5 mm horizontal gap at 1.5 m/min travel speed.

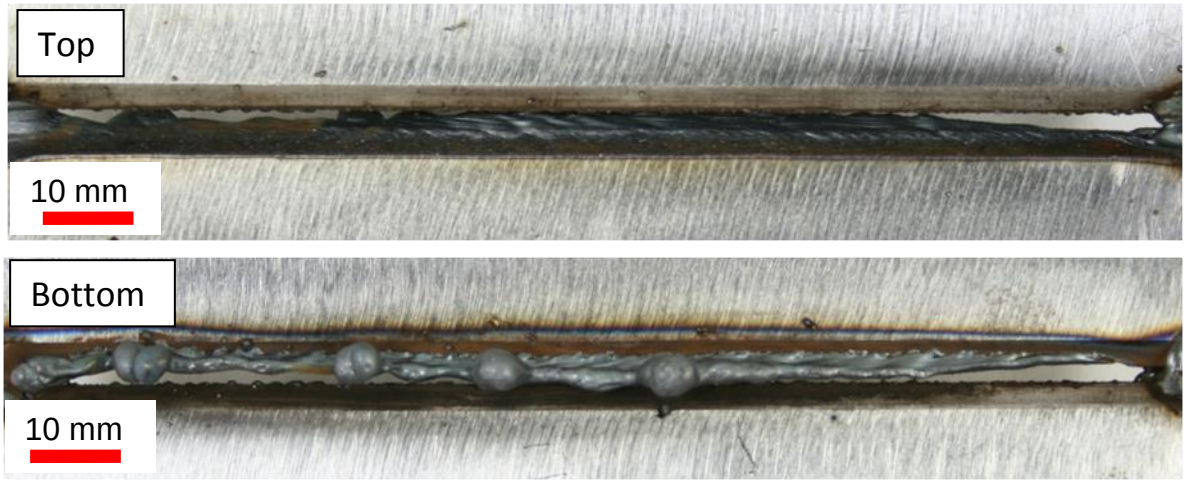

***Figure 8.36**: Butt-weld on X-prep with 3 mm gap configuration (v = 1.5 m min^{-1}, WFS = 2x15 m min $^{-1}$, P_L = 5 kW, d = 1.2 mm (defocused by 10 mm), q_p = 0.4 MW cm^{-2}, τ_i = 48 ms, E_{SP} = 240 J, transverse configuration of wires); **a)** macrograph; **b)** top bead*

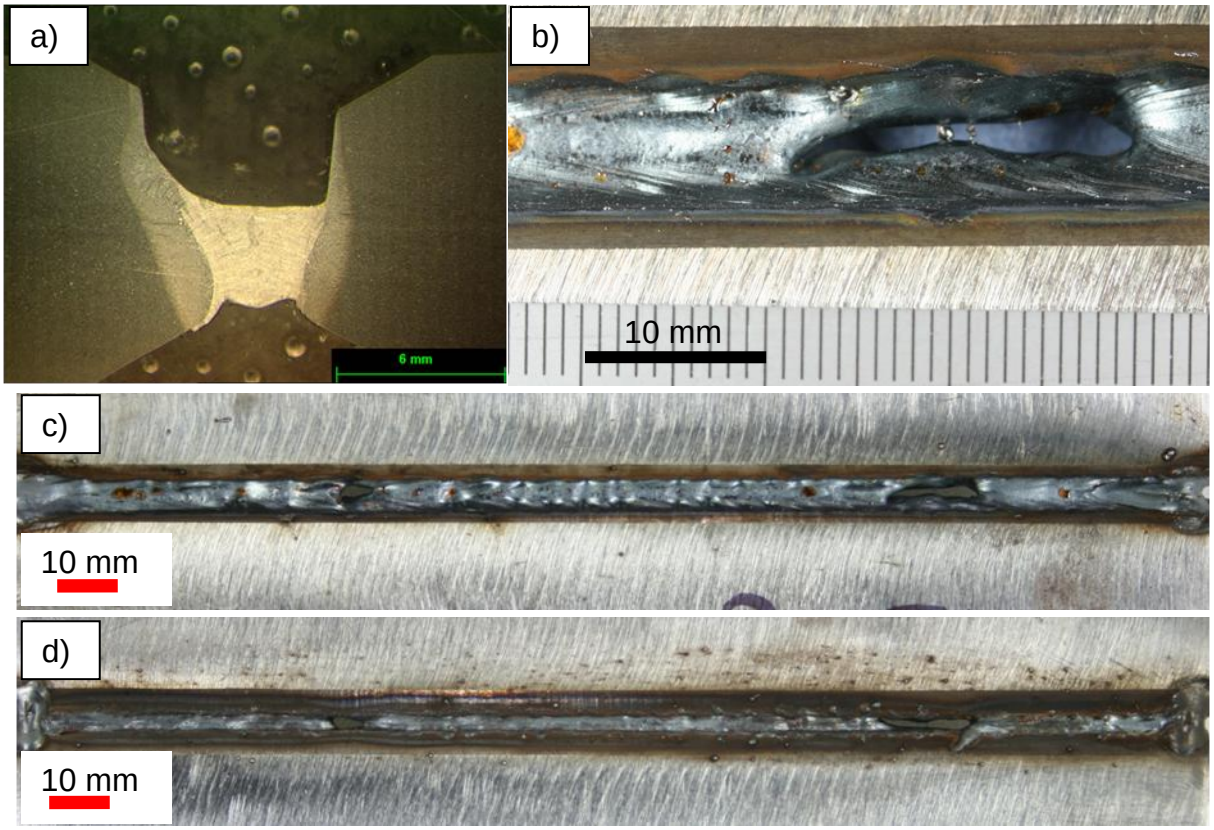

***Figure 8.37**: Butt-weld on X-prep with 3 mm horizontal gap configuration (v =1.5 m min^{-1}, WFS = 2x15 m min $^{-1}$, P_{AI} = 15.7 kW, P_L = 5 kW, , d = 1.2 mm (defocused by 10 mm), q_p = 0.4 MW cm^{-2}, τ_i = 48 ms, E_{SP} = 240 J, laser tilted off side, transverse configuration of wires); **a)** macrograph; **b)**, **c)** top bead; **d)** root face.*

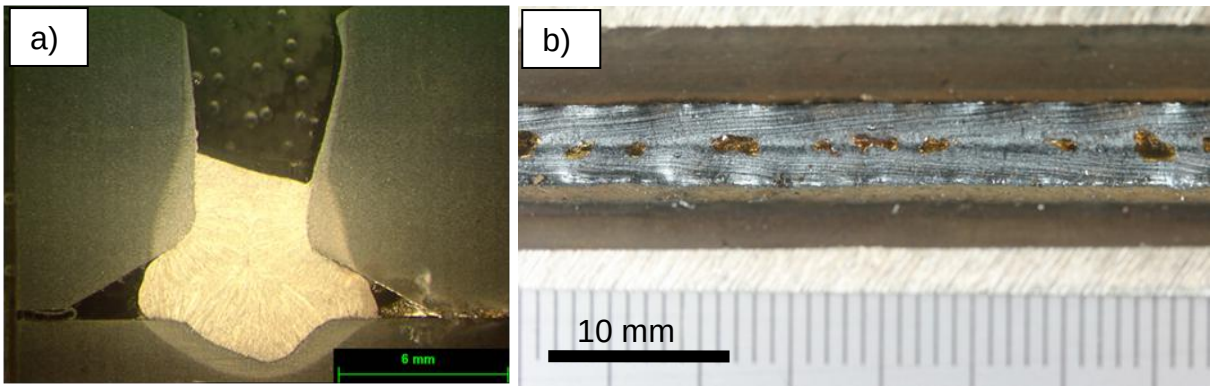

***Figure 8.38**: Butt-weld on misaligned X-prep with 3 mm horizontal gap configuration with backing plate (v = 3 m min^{-1}, WFS = 2x30 m min $^{-1}$, P_{Al} = 25.7 kW, P_L = 7 kW, d = 1.2 mm (defocused by 10 mm), q_p = 0.6 MW cm^{-2}, τ_i = 24 ms, E_{SP} = 168 J, transverse configuration of wires); **a)** macrograph; **b)** top bead.*

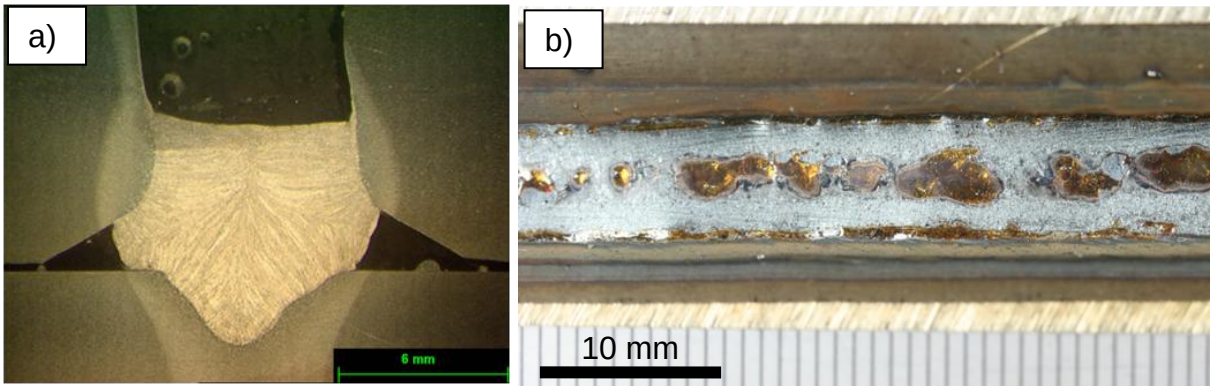

***Figure 8.39**: Butt-weld on misaligned X-prep with 5 mm horizontal gap configuration with backing plate (v = 1.5 m min^{-1}, WFS = 2x18 m min $^{-1}$, P_L = 7 kW, d = 1.2 mm (defocused by 10 mm), q_p = 0.6 MW cm^{-2}, τ_i = 48 ms, E_{SP} = 336 J, transverse configuration of wires); **a)** macrograph; **b)** top bead.*

8.6. Discussion

8.6.1. Fit-up tolerance of laser welding

The fit-up tolerance is determined by many factors, such as the ability of the heat source to melt both edges, the amount of metal to fill the gap, as well as the sufficient force to support the liquid metal against gravity. The importance of each of these aspects changes depending on the conditions of the gap. The ability of autogenous

laser welding to create a joint, in case of perfectly fitted edges, is only dependent on the amount of molten metal available to form the joint. It was shown in Fig.8.2 and Fig.8.3 (pages 235-236) the bead width is almost independent of the beam diameter. Although it was shown in Section 5.6 that the depth of penetration is mainly dependent on the power density and specific point energy, whilst the interaction time controls the weld width, the effect of interaction time is, however, evident only at constant power density and specific point energy. When the other interaction parameters are changed simultaneously the effect is not so clear. The increase of beam diameter in Fig. 8.4 (page 236) did not have as strong effect on the weld width as the reduction of travel speed, despite the interaction time being equally dependent on both. However, an increase of travel speed at a constant laser power and beam diameter results in an increase of interaction time and specific point energy at the same time. Thus a larger beam diameter requires a greater specific point energy to achieve the same depth of penetration, as compared to a smaller beam diameter. This was also evident in the width of the heat affected zone on the surface, presented in Fig.8.2 and Fig.8.3. The width of the heat affected zone increases with increasing beam diameter, as a result of greater specific point energy. Thus because the amount of molten metal in autogenous laser welding is determined by all the interaction parameters, not only the interaction time, therefore the effect of interaction time on weld width in Fig.8.4 was not clear.

The beam diameter becomes important when the gap between the joined components exceeds the size of the heat source. This was shown in Fig.8.5 (page 238) on a butt-weld with a diverging gap from 0 to 2 mm. The effect of beam diameter on the fit-up tolerance seemed to be stronger than the effect of travel speed. The effect was quite different to that discussed previously from Fig.8.4 (page 236). This ambiguity might result from the character of the gap. The diverging in this case, provides some space enabling for the establishment of the stable melt pool at the initial stage, before encountering the actual gap. This enhances the gap bridging ability of the process, as compared to the continuous gap case. In addition, the measured fit-up tolerance from the diverging gap could be unrealistically high due to the acceleration-dragged molten metal, which moves the molten metal further towards the extended gap. In reality i.e. with a continuous gap the laser beam would pass through the gap and the molten metal would not have a chance to occur. This

questions the validity of these types of tests with diverging gaps in investigation of the fit-up tolerance. On the other hand, it is quite intuitive that the greater the beam diameter the larger the melt pool and thus the better ability to bridge gaps. Therefore a better fit-up should be achieved with greater beam diameters on the surface.

In general the fit-up tolerance of laser welding is of the order of beam diameter on the surface. In order to avoid undercut on the surface, the addition of filler metal is necessary when the gap exceeds beyond 0.5 mm.

8.6.2. Interactions between laser and arc

A fairly easy way of increasing the gap bridging ability, whilst maintaining the benefits of high power density of the laser is using the hybrid laser/MIG process. A high level of flexibility, allowing an independent control of the shape and the depth of penetration of the bead, is one of the main benefits of hybrid welding. The depth of penetration is mainly determined by the laser, whilst the bead shape is determined by the arc source. This was shown in Fig.8.7 to Fig.8.8 (page 240). Additionally, the process is sensitive to the selection of leading source. A greater depth of penetration was achieved with the arc leading configuration (Fig.8.9 and Fig.8.10 pages 240-241). In this case the laser interacts with the surface already molten by the arc, hence its absorption increases. On the other hand, a wider bead achieved with the laser leading can be attributed to the improved wet-ability. In this configuration the filler metal is deposited on the hot surface, previously preheated by the laser beam. In addition, the angle of the MIG torch relatively to the welding direction is also critical in determining the bead shape. It was shown in Fig.8.11 (page 241) that in the laser leading configuration the arc torch is was the push position, whilst in the arc leading the torch was in the pull configuration, which significantly affected the arc conditions.

Even though the depth of penetration in the hybrid welding is mainly determined by the laser source, the increased depth of penetration of the hybrid laser welding, as compared to the autogenous laser welding, owing to different synergic effects, was reported in the literature [321, 322, 329]. Macrographs in Fig.8.12 (page 242) revealed that in the hybrid welding with the laser leading configuration the depth of penetration was the same as in the case of laser welding. Alternatively in the arc leading configuration, the depth of penetration of the hybrid welding was slightly

greater than one in the laser welding. This can be attributed to three different effects. First, the increased absorption of the laser beam due to the preheating of the workpiece by the arc. Second, the pre-melting effect of the workpice by the arc, which reduces the effective thickness of the plate that has to be penetrated by the laser beam, could account for the improved depth of penetration. Finally, the arc pressure acting on the surface could significantly contribute to the drilling force, in particular with currents exceeding 300 A.

The effect of improved depth of penetration of hybrid welding, as compared to laser welding, was more profound in hybrid tandem arc welding in Fig.8.15 (page 243). The difference of 5 mm in depth of penetration between the laser leading and the arc leading is striking. The depth of penetration of the hybrid tandem arc welding with laser leading configuration was even lower than in the laser welding. This implies that due to the large amount of molten metal the keyhole induced by the laser was disturbed. The laser beam had to cope with such a large amount of molten metal, leading to the lower depth of penetration than in the autogenous laser welding. This was also demonstrated in hybrid tandem arc welding in Fig.8.14 (page 243), where much more laser energy was required to maintain the characteristic for laser welding bead shape. All welds in this figure with laser power up to 6 kW exhibited the MIG-like weld shape and only after increasing the laser power to 8 kW the keyhole shape emerged. Since in the laser leading configuration, the MIG torch was pushing the molten metal against the keyhole propagation direction, it could easier disturb the keyhole. In the arc leading configuration, on the other hand, the MIG torch was depositing the filler metal according to the welding direction, leading to a more stable deposition of filler metal and resulting in a more stable keyhole. In addition a more uniform weld profile of the single arc hybrid welding than the tandem arc hybrid welding for the same overall deposition rate, presented in Fig.8.16 implies a higher arc pressure in the case of single arc. This underlines the influence of arc pressure on the depth of penetration in laser/MIG hybrid welding.

The voltage of the arc source is also important. It was shown in Fig.8.6 (page 239) the bead shape becomes flatter and wider as the voltage increases. However, an excessive voltage leads to strong arcs and results in undercut of the toe. Also right parameters of the arc source are necessary for a spatter-free stable metal transfer. For instance a low voltage results in a short circuiting and may lead to a generation of

spatter. Thus the main requirement from the arc characteristics is a spatter-free metal transfer.

The stabilisation effect of arc by the laser beam is commonly known in the literature [15, 309, 313, 317]. In the standard tandem MIG welding two wires are in the longitudinal configuration with one wire following another along the welding direction. This allows different parameters to be set-up on each wire, for instance to provide more depth of penetration with the leading wire and a wider bead shape with the trailing wire. However, in this study two wires were in the transverse direction side by side. This on one hand, increased the fit-up tolerance and made it easier for the laser to approach the wires, but on the other hand, the stability of the arcs was slightly reduced. This was demonstrated in Fig.8.17 (page 244) where the tandem source was used without the laser at a travel speed of 1.5 m/min. Although the tandem welding with faster speeds was reported in the literature [432, 433], but for the transverse configuration of wires 1.5 m/min travel speed was found to be limited. Nevertheless in the tandem arc laser hybrid welding the transverse configuration was found to be stable even at faster speeds, due to the extra heat from the laser. The advantage of this configuration was exhibited in Fig.8.25 (page 251). The filler metal was deposited on both edges of the specimen until the gap width exceeded approximately 6 mm. The two configurations compared in Fig.8.27 (page 252) showed a better performance of the transverse configuration, mainly due to the easier access of the laser beam to the arc interaction zone.

8.6.3. Fit-up tolerance of laser single arc hybrid welding

The laser MIG hybrid welding has much better ability to bridge gaps than the laser welding, mainly due to the additional metal from the filler wire. It was shown in Fig.8.18 (page 246) that the process did not collapse on the diverging gap even at 3 m/min travel speed, which is impressive in comparison to the autogenous laser welding from Fig.8.1 (page 234). Even though the fit-up tolerance studied on the gradually increasing gaps is greater than when bridging continuous gaps, due to the fact that the process has time to establish stable conditions before encountering the gap, however, its gives a rough estimate.

The situation becomes complicated when the gap between the joined components changes randomly during welding. The gap can have detrimental effect on the process if the same conditions are maintained. It was shown in Fig.8.19 (page 246) that for a zero gap configuration the amount of filler metal was sufficient to achieve a sufficient reinforcement at a travel speed of 1.5 m/min. As a matter of fact, the laser energy was insufficient to provide a full penetration, but it could be increased if required. Alternatively, in case of 2 mm gap (Fig.8.19b) more laser energy would result in joint failure because of sagging of the molten material. Thus a successful tack weld on a zero-gap configuration could be achieved with a travel speed up to 4 m/min (Fig.8.20 page 247). The only limitation from increasing travel speed further was the limitation of the deposition rate from the arc source and the laser power if more depth of penetration would be required. In contrast, a misaligned bevel configuration presented in Fig.8.21 (page 247) was found to be very beneficial. The opened top allowed the filler metal and the laser beam to access the bottom of the bevel, whilst the closed bottom supported the molten metal from dropping. Thus this configuration provided the best conditions, in terms of quality and productivity with the current welding system. In order to achieve more reinforcement on the top a more powerful MIG power source would have to be used.

A detrimental effect of gravity on the filler metal and fit-up tolerance was demonstrated in Fig.8.22 (page 248). A higher wire feed speed in this case was found to even decrease the fit-up tolerance, due to the increased arc pressure. Similarly, the laser beam can interact with the deposited metal and disturb the bridging ability, due to the strong recoil pressure. The results from Fig.8.23 and Fig.8.24 (page 249) imply that correctly selected parameters of laser are the key factor in the gap bridging ability of the hybrid welding. A larger beam diameter provided good conditions to bridge large gaps. The reduced power density in this case mitigated the recoil pressure, whilst the high laser power provided sufficient specific point energy to spread the filler metal and to keep the arc stable. Note that the beam diameter was smaller than the gap. Alternatively, focusing the laser beam off-side on one of the edges of the bevel, without changing the beam diameter, also resulted in reducing the downward force, as demonstrated in Fig.8.24 (page 249). It seems like universal parameters suitable for different gap conditions do not exist. A high power density of the laser is necessary in narrow gaps to achieve a required

depth of penetration. In contrast, larger gaps require strict control of the power density to avoid sagging of the deposited metal. The off-set of the laser beam without changing the power density can be also applied if combined with an appropriate seam tracking system, which would monitor the gap in front of the welding process.

8.6.4. Fit-up tolerance of laser tandem arc welding

Use of a tandem MIG hybrid welding was found to be an easy way of increasing the deposition rate, without applying an excessively high arc pressure, attributed with high currents, if the wire feed speed of a single MIG would be further increased. It was shown in Fig.8.13 and Fig.8.14 (pages 242-243) that the depth of penetration and the bead shape in laser/tandem MIG hybrid can be controlled fairly independent by altering the parameters of laser and arc, similarly to the hybrid welding with a single arc. The only difference is that more laser energy is required to significantly increase depth of penetration in the tandem process, due to the fact that the laser beam has to cope with a larger amount of filler metal.

The initial evaluation of fit-up tolerance using a bevel with a diverging gap revealed a promising performance of the laser/tandem MIG process (Fig.8.25 page 251). In this case the process collapsed totally only when the horizontal gap exceeded 4 mm. The benefit from the additional amount of filler metal is clearer when comparing Fig.8.27 (page 252) with Fig.8.19 (page 246). The objective of this paragraph was to investigate if the fit-up tolerance could be improved only by increasing the amount of filler metal. It turned out that the extra metal is advantageous as long there is enough supporting force against gravity, as in the case of misaligned bevel (Fig.8.30 page 254). In comparison with the single arc hybrid welding from Fig.8.21 (page 247), the benefit from the extra metal in the tandem arc hybrid is evident. Note that the weld presented in Fig.8.30 was achieved at a travel speed of 5 m/min. However, a further increase of wire feed speed resulted in an undesired bead shape, due to the effect of arc pressure (Fig.8.31 page 254). Also the energy required from the laser beam to spread the molten metal uniformly and provide a consistent bead increases with increasing the amount of filler metal. This was demonstrated on a butt-weld in Fig.8.28 (page 253). The bead shape exhibited the characteristic for insufficient wet-ability wrinkles, despite the high power density of the laser beam used. The highly

focused laser energy, in this case, was mainly utilised for the depth of penetration. To overcome this problem a larger beam diameter can be used. In examples in Fig.8.29 and Fig.8.30 (page 254) the bead shape was controlled by varying the laser parameters, which confirms the versatility of the hybrid welding process.

The superior performance of the laser/tandem MIG process over the single MIG laser hybrid welding diminished as the separation between the plates increased to 2 mm. It was demonstrated in Fig.8.32 (page 255) that the joint was not continuous and most of the metal solidified under the bevel. This proves that the sufficient force to support the molten metal against gravity is the most important factor in bridging large gaps. Having experience from the previous tests with the single arc hybrid welding, the same trick with focusing the laser beam on one of the edges of the bevel was also used in the tandem arc hybrid welding. A fairly consistent joint was achieved in an example in Fig.8.33 (page 256). However, a large amount of filler metal resulted in a more convex root face, as compared to the single arc hybrid welding from Fig.8.23 (page 249). Nevertheless this solution improves the fit-up tolerance. By off-setting not only the laser beam, but also the arc source, the continuous joint on a bevel with 2 mm gap could be achieved, even at a travel speed of 3 m/min (Fig.8.34 page 256). Note that in this case the arcs were in the longitudinal configuration. To have a reference point the same bevel was welded with an additional support of the backing plate, as demonstrated in Fig.8.35 (page 257). The combined energy from laser and tandem MIG melted the edges and enlarged the gap, thus almost entire metal was deposited on the backing plate. This demonstrates that the proper selection of welding parameters is crucial even with sufficient supporting force for molten metal.

The standard laser tandem MIG hybrid welding process failed to create a joint as the gap between the plates increased to 3 mm (Fig.8.36 page 258). However, using the same conditions but focusing the laser beam off-side, on one of the edges of the bevel, changed the situation drastically. Apart from two defects, a successful joint on this large gap was shown in Fig.8.37 (page 258). These defects could be perhaps avoided if a higher wire feed speed or shielding gas at the root were used. A comparison between the tandem arc hybrid welding and the single arc hybrid welding demonstrates that the fit-up tolerance of the tandem arc hybrid welding increased only from 2 mm to 3 mm. The data from the fit-up tolerance study are summarised in Table 8.3. It is shown that the laser source is critical in determining the fit-up

tolerance, as long as the arc source provides a sufficient amount of filler metal. In general large beam diameters are beneficial, due to the low power density and recoil pressure. It is believed that using wider beam diameters than the gaps or using the twin spot welding should be beneficial in improving the gab bridging ability, but only if a sufficient supporting force for the molten metal is provided at the bottom. Otherwise there is a potential risk of the excessive melting and sagging. The present results imply that in the case of tack applications the laser beam is mainly used to spread the molten metal, rather than to directly melt the edges. Therefore a wider beam diameter on the surface than the gap width was found to be unnecessary in this case.

***Table 8.3**: Comparison of fit-up tolerance between different welding processes.*

Process	Laser welding		Hybrid single MIG			Hybrid tandem MIG	
Beam diameter [mm]	d = 0.37	d = 0.75	d = 0.6	d = 0.6 off side	d = 1.8	d = 0.6	d = 0.6 off side
Gap [mm]	0.5 mm	0.7 mm	< 2 mm	2 mm	2 mm	< 2 mm	3 mm

Finally, to demonstrate an alternative way of supporting the molten metal, the backing plates were used. The examples showed in Fig.8.38 and Fig.8.39 (page 259) suggest that the tandem source used here, provided enough metal to accommodate a gap of 5 mm at a travel speed of 1.5 m/min or a gap of 3 mm at a travel speed of 3 m/min. This demonstrates that more effort should be taken towards increasing the upward force for the molten metal rather than towards increasing the deposition rate. Even though a usefulness of such backing plates in real applications is doubtful, but there are other methods of increasing the upward force of the molten metal, such as by increasing the surface tension or using a negative polarity MIG welding. The surface tension can be also increased effectively by using a shielding gas at the root face.

Chapter 9. Critical discussion

This project looked into some of the most common issues related to the hybrid laser welding. These include:

- poor data transferability between the laser systems with different beam diameters,
- lack of welding parameters, which uniquely specify the achieved weld beads,
- insufficient data on the robustness of the process, required by industry.

It has been found that the new solid state laser sources, such as the fibre laser provide good stability, in terms of delivered output laser power and beam diameter. Although a shift of the focal point, due to the heat effects on the optical components, referred to as a focus shift, has been identified, but as long as the correct optical set-up for a particular application is used and the optics is in clean conditions, its effect on the achieved weld bead is negligible. It has been found that the natural fluctuations of keyhole, in partially penetrated welds, can cause more variations of depth of penetration and weld shape than the focus shift, as shown in Fig.9.1. The focus shift becomes problematic in case of contaminated optics or optics with large optical magnifications.

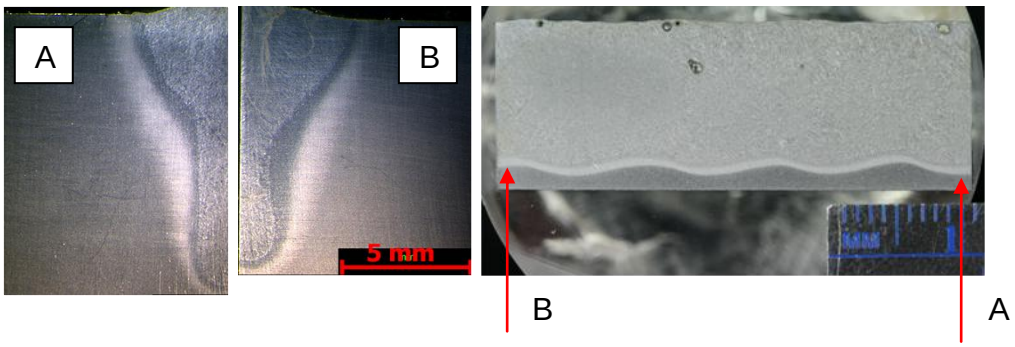

***Figure 9.1**: Effect of keyhole fluctuations on bead shape in partially penetrated weld for 1 m min^{-1} travel speed of and 8 kW power.*

The study of basic laser material interaction parameters have shown that the laser welding can be characterised by parameters, which describe the energy conditions on the surface, such as the average power density, interaction time and specific point energy. These simple parameters are independent of the laser system, meaning that they can be calculated based on system parameters, such as beam diameter on the surface, laser power and travel speed, for any laser process. This allows for the comparison of laser results between different laser systems with different beam diameters.

It has been demonstrated that depth of penetration in keyhole regime is primarily determined by the power density and the specific point energy, whilst the weld width is determined by the interaction time, as shown in Fig.9.2. These parameters provide a unique characterisation of the laser welding, which is different from the laser power or the heat input, where a particular combination of heat input can lead to different welds due to the effect of beam diameter. This means that a particular combination of power density, interaction time and specific point energy will lead to a particular weld with a particular depth of penetration and shape, which will be unique for these parameters.

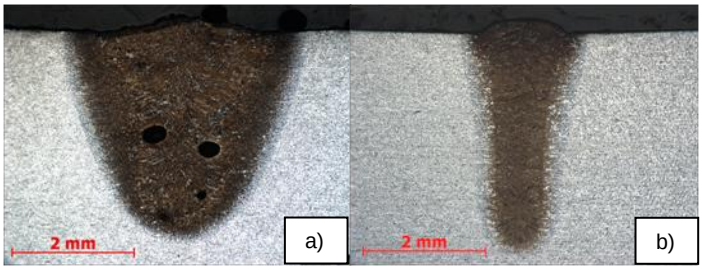

***Figure 9.2**: Macrographs at constant power density of 1.6 MWcm^{-2} and specific point energy of 60 J: **a)** interaction time of 38 ms (P_L = 1.8 kW, v = 0.68 m min^{-1}, d = 0.38 mm); **b)** interaction time of 8 ms (P_L = 7.6 kW, v = 5.9 m min^{-1}, d = 0.78 mm).*

The basic laser material interaction parameters enabled us to understand some phenomena related to the beam diameter. As shown in Fig.9.3 all of the interaction parameters change simultaneously, whilst changing the beam diameter on the surface. Thus when the laser beam is defocused for instance, the power density decreases, but the interaction time and the specific point energy increase. The

compensating effect of specific point energy for the drop of power density explains the large depth of focus, which is observed experimentally in many welding situations. It also shows that since the depth of penetration is controlled by the power density and the specific point energy, the use of small beam diameters does not always lead to great depths of penetration, which is commonly believed. In such cases the power density increases but the specific point energy decreases with decreasing beam diameter, which depending on the conditions may even lead to a reduction of depth of penetration as a net result.

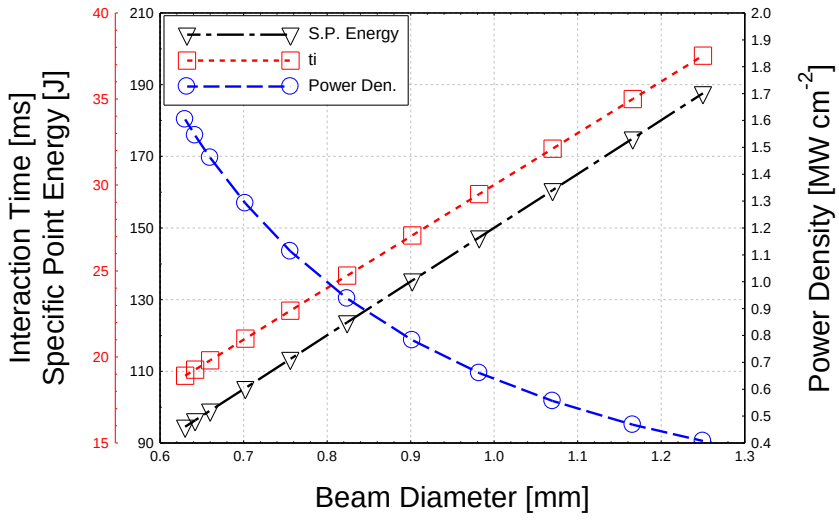

***Figure 9.3**: Simultaneous variation of interaction parameters with beam diameter at 2 m min^{-1} travel speed of and 5 kW power.*

The experimental findings imply that during defocusing or any other case when the beam diameter on the surface varies, the achieved welds are determined by the basic laser material interaction parameters. Thus the same weld depths can be achieved with random combinations of the system parameters (laser power, travel speed and beam diameter) if they provide the same power density and specific point energy. It has been demonstrated that this is independent of the intensity distribution profile or the divergence angle of the laser beam. The same depth of penetrations and weld widths, as with top-hat beams, were achieved with Gaussian beams. This justifies the use of the average power density and the maximum interaction time, as being sufficient for characterisation of laser welding.

Since the basic laser material interaction parameters, discussed above, all change simultaneously with the beam diameter, control of which is usually user-independent to a certain extent, it is desired to have a simpler approach. Thus a system of parameters, allowing achievement of a particular weld on different laser systems with different beam diameters has been developed. The power factor, which is the product of power density and beam diameter, together with the interaction time enable the user to achieve a given depth of penetration, independent of the beam diameter, as shown in Fig.9.4.

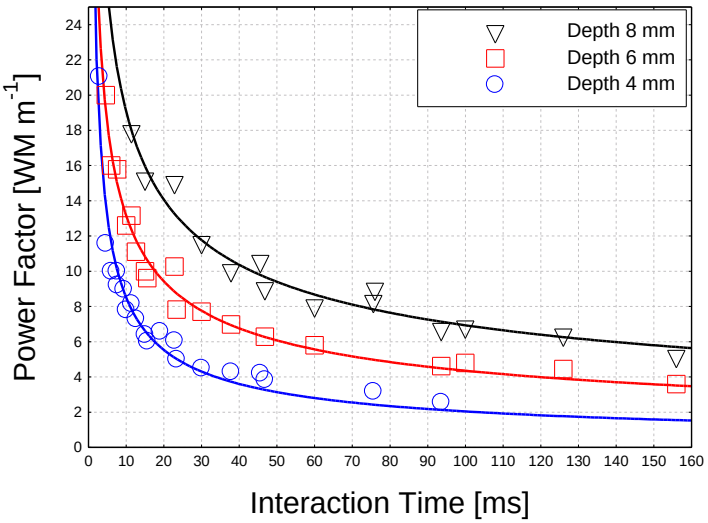

***Figure 9.4**: Required power factor for depths of penetration of 8 mm, 6 mm and 4 mm as a function of interaction time (range of beam diameters 0.38 mm to 0.78 mm).*

The improvement of data transferability between the laser systems can be potentially achieved. A new approach for selection of welding parameters has been demonstrated. Instead of selecting the welding parameters based on the limits of the laser system, in this case the parameters are selected based on quality/productivity criteria. The interaction time, which determines the weld width, microstructure and other properties, is primarily selected and then, depending on a required depth of penetration, an appropriate power factor is selected based on Fig.9.4. These parameters provide the laser system-independent conditions to achieve a particular weld. These parameters can be transferred into the system parameters and applied on a particular laser system, as shown in Fig.9.5. The bigger the beam diameter the

greater the laser power has to be provided in order to achieve the required power factor. This model enables the user to estimate the properties of the laser system, in terms of laser power and beam diameter, needed for a particular application.

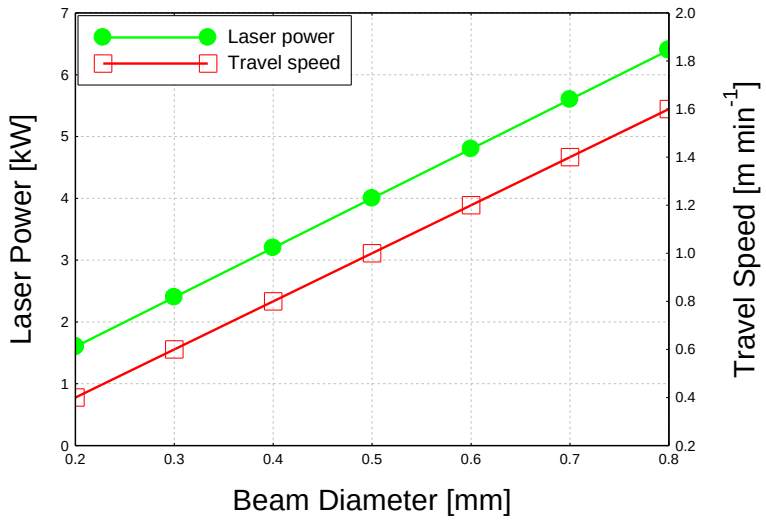

***Figure 9.5**: Dependence of laser power and travel speed required for 30 ms interaction time and 8 MW/m power factor with beam diameter.*

The power factor model can be also used to predict the parameters of hybrid laser welding, with an assumption that the depth of penetration is determined mainly by the laser beam, whilst the arc provides the filler metal for the reinforcement, which has been shown to be the case.

To evaluate the hybrid laser welding, in terms of residual stress and distortion, the joining efficiency parameter has been studied. It has been shown that for every process and a given material there are the most optimum conditions that will ensure a maximum utilisation of the heat for the creation of the joint. The maximum joining efficiency corresponds to the conditions where the conduction heat losses are minimised and the energy is efficiently utilised to form the joint. In laser welding this leads to welds with a maximum aspect ratio of depth to width, as shown in Fig.9.6. This is mainly dependent on the interaction time. At excessively short interaction times there is not enough energy to form a sufficient joint, whereas at long interaction times the conduction of the heat increases the size of the melt pool and the joining efficiency is low.

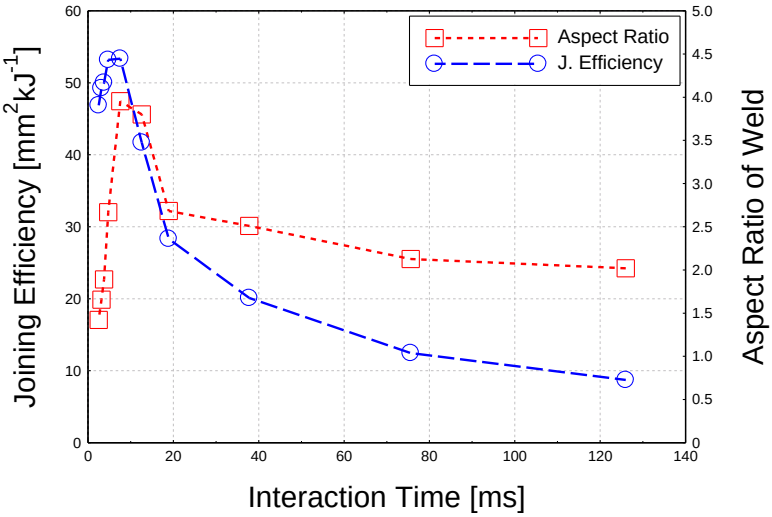

***Figure 9.6**: Joining efficiency and aspect ratio of a weld as a function of interaction time at 1.6 MW cm^{-2} power density of and 0.63 mm beam diameter.*

It has been shown that the residual strains, which are proportional to the residual stress, are minimised when the joining efficiency is maximised. The longitudinal residual stress is the main factor determining welding distortions, which are considered to be one of the main issues in welding technology. The joining efficiency allows different welding processes to be compared, in terms of their ability to accommodate a particular component, considering at the same time the level of residual stress and thus distortion induced by this process. The comparison of autogenous laser welding with hybrid laser/TIG welding have revealed that the laser welding requires much less energy to weld the same component with a given thickness, as compared to the hybrid welding, which is shown in Fig.9.7.

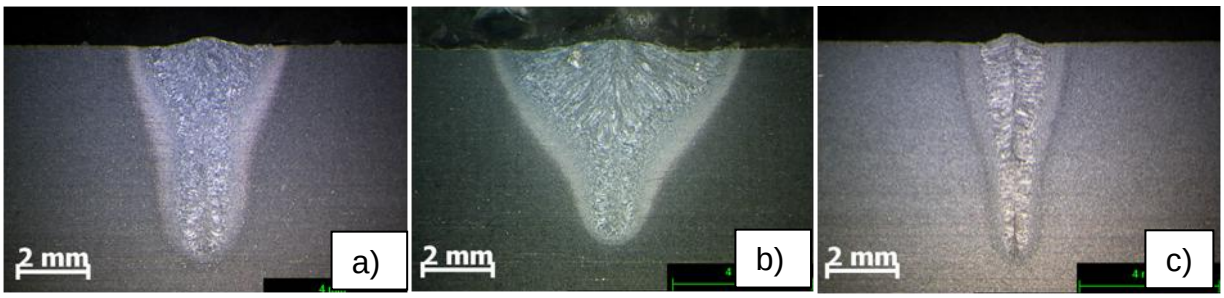

***Figure 9.7**: Macrographs for combination of parameters required for 6 mm depth of penetration: **a)** laser welding 4 kW, 1m min^{-1} (240 J mm^{-1}); **b)** hybrid welding 7 kW, 1 m min^{-1} (420 J mm^{-1}); **c)** laser welding 7 kW, 3 m min^{-1} (140 J mm^{-1})*

Therefore, the laser welding will provide less residual stress and distortion, but the hybrid process will ensure better tolerance to fit-up. Thus if the tolerance to fit-up is the main requirement then the hybrid laser welding should be selected, but for the price of greater distortion, as compared to the laser welding.

The industrial study from the evaluation of the gab bridging ability of hybrid laser welding have indicated three important factors affecting the fit-up tolerance. First, a sufficient amount of molten metal is critical to form a joint. Second, an adequate upward force at the bottom needs to be provided to support the molten metal against gravity. Finally, a sufficiently wide heat source, which allows both edges to be melted, has to be provided. This condition is not as critical in tack welding applications as in butt-welding of thick sections. The tandem MIG process (twin wire system) has been found to provide the best combination of high deposition rate with a relatively low plasma pressure, as compared to a single wire system. The lack of upward force for molten metal has been found to be the most challenging difficulty in bridging large gaps. Using lasers with large beam diameters in hybrid laser welding is beneficial for the improvement of fit-up tolerance, due to a low power density and a high specific point energy, which reduces the downward forces and enlarges the melt pool.

The hybrid laser/tandem MIG process studied in this project has been found to be capable of producing high speed joints for tack-weld application with welding speeds of the order of 5 m/min in case of misaligned bevels (Fig.9.8) or at 1.5 m/min with horizontal gaps up to 3 mm.

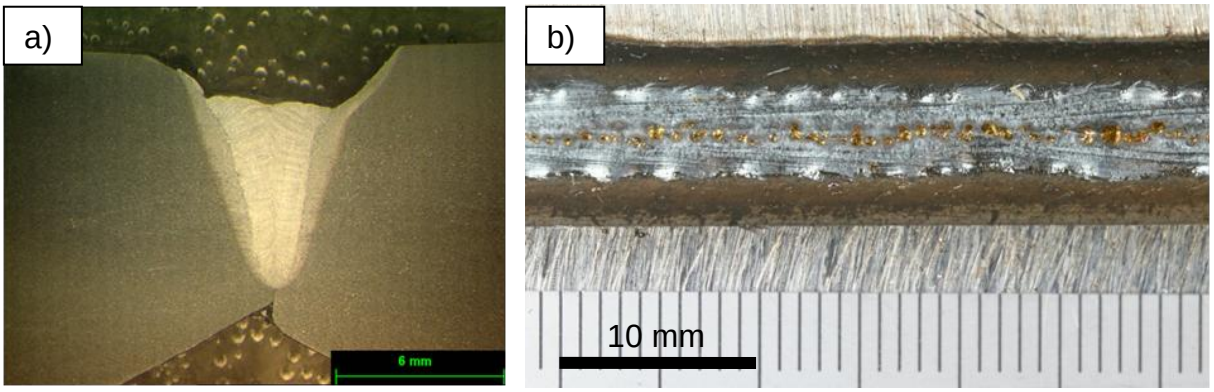

***Figure 9.8**: Butt-weld on misaligned X-prep configuration at a travel speed of 5 m min^{-1} at wire feed speed of 2 x 20 m min $^{-1}$; **a)** macrograph; **b)** top bead.*

Chapter 10. Conclusions and potential for future work

10.1. Conclusions

By investigating the laser welding process using laser material interaction parameters a deep understanding have been obtained and some phenomena explained. From the work presented in this thesis the following can be concluded:

- Three parameters are suitable to characterise the laser welding process, which are power density, interaction time and specific point energy. The depth of penetration is determined by power density and specific point energy, whilst the width of the bead is controlled by interaction time.
- Effect of beam diameter at constant power and travel speed can be explained by the changes of laser material interaction parameters. The saturation of depth of penetration that is eventually reached when decreasing beam diameter at constant power and travel speed is caused by the decrease of specific point energy.
- By studying the effect of beam divergence at constant laser material interaction parameters it has been shown that in the range of beam diameters from 0.38 mm to 0.78 mm the divergence has negligible effect on depth of penetration and weld shape.
- A new parameter, power factor has been developed, which combined with interaction time allows us to specify deep penetration laser welding process independent of the beam diameter. This allows for:
    - Transfer of the process between different laser systems with different beam diameters;
    - Development of process specifications for application requirements.
- For the same depth of penetration achieved with laser and hybrid laser welding the peak residual strains are the same but the widths of the tensile peaks are wider in case of hybrid welding.

- For the same heat input the integrated area under the tensile residual strain in hybrid and laser welding are the same. However, the weld beads are different. The laser weld is deeper and narrower, compared to the hybrid weld.
- Fit-up tolerance of laser welding is in order of beam diameter and did not exceed 1 mm, as compared to 2 mm in case of hybrid welding and 3 mm in case of tandem MIG hybrid welding.
- As expected the hybrid process is much more tolerant to the variation of gap than the laser process. However, to achieve the maximum benefit a careful selection of the processing conditions needs to be made. In particular:
    - High laser power density should be avoided, because it forces metal to flow downwards, which results in sagging;
    - High overall energy is advantageous, since it improves wetting and melting of joined faces.
- An important issue of laser hybrid process is insufficient amount of filler metal. Use of tandem MIG welding has been found to be beneficial because it allows high deposition rate with a relatively low current on each wire.
- The practical limit of fit-up tolerance for any conditions in this study was approximately 2-3 mm.
- The depth of penetration in hybrid laser welding is controlled by the laser, whilst the bead shape is controlled by the arc. There is some increase of depth of penetration with the arc leading configuration. The bead profile is strongly dependent whether MIG torch is pushing or pulling, as in conventional MIG welding.

10.2. Potential for future work

- Although the potential of power factor model has been presented, but a full study on a wider range of beam diameters and output powers, as well as various materials would be required to assess its feasibility in real applications;
- A further step in the utilisation of the power factor model would include a development of an algorithm or a software, which would provide welding parameters based on input data, such as required width and depth of penetration, material, shielding gas etc;
- A calorimetric study of laser absorption of laser welding with different beam diameters at a constant power density and interaction time would be required to fully investigate some effects;
- The application study of hybrid laser welding and tandem MIG hybrid laser welding should be further extended, to investigate mechanical properties;
- Also the benefits of using large beam diameters on the fit-up tolerance in hybrid laser welding of thick section butt-welds should be exploited;
- The optimisation of MIG conditions allowing for a stable metal transfer with high deposition rates, suitable for hybrid laser welding should be carried out. In particular the benefits of MIG welding with the negative polarity on the electrode in hybrid welding should be investigated.

References

1. Ion, J.C., *Laser processing of engineering materials*. 2005, Oxford UK: Elsivier.
2. Lancaster, J.F., *The physics of welding*. 2nd edition ed. 1986: Pergamon Press.
3. Martukanitz, R.P., *A critical review of laser beam welding*, in *Proceedings of SPIE - The International Society for Optical Engineering*. 2005: San Jose, CA. p. 11-24.
4. Dilthey, U. and A. Wieschemann, *Prospects by combining and coupling laser beam and arc welding processes, International Institute of Welding, IIW Doc. XII-1565-99*. 1999.
5. Magee, K.H., V.E. Merchant, and C.V. Hyatt, *Laser assisted gas metal arc weld characteristics*, in *Proceedings of International Congress on Applications of Laser and Electro-Optics, ICALEO* 1990, Laser Institute of America: Boston, USA. p. 382-399.
6. Hayashi, T., et al., *High power CO_2 laser-MIG hybrid welding process for increased gap tolerance - Hybrid weldability of thick steel plates with square groove (report I).* Yosetsu Gakkai Ronbunshu/Quarterly Journal of the Japan Welding Society, 2003. **21**(4): p. 522-531.
7. Fujinaga, S., et al., *Improvements of welding characteristics of aluminum alloys with YAG laser and TIG arc hybrid system*, in *Proceedings of SPIE - The International Society for Optical Engineering*, I. Miyamoto, et al., Editors. 2002: Osaka. p. 301-306.
8. Biffin, J., et al., *Enhancing the Performance of Industrial Lasers with a Plasma Arc*, in *ASM Proceedings of the International Conference: Trends in Welding Research*, J.M. Vitek, et al., Editors. 1998: Pine Mountain, GA. p. 492-497.
9. Biffin, J.R. and R.P. Walduck, *Plasma arc augmented laser welding (PALW)*, in *Proceedings of 2nd European Conference on Joining Technology, EUROJOIN 2*. 1994: Firence, Italy. p. 295-304.
10. Boellinghaus, T. and H. Schobbert, *Nd:YAG laser plasma powder hybrid welding of austenitic stainless steels*, in *ASM Proceedings of the International Conference: Trends in Welding Research*. 2002: Phoenix, AZ. p. 453-458.
11. Seyffarth, P. and I.V. Krivtsun, *Laser-arc processes and their applications in welding and material treatment* Vol. Welding and Allied Processes volume 1. 2002, London CRC Press Taylor & Francis Group.
12. Seyffarth, P., B. Anders, and J. Hoffmann, *Combined laser beam arc welding - a high efficiency welding technology*, in *Proceedings of The International Conference on the Joining of Materials*. 1997. p. 120.
13. Ribic, B., R. Rai, and T. DebRoy, *Numerical simulation of heat transfer and fluid flow in GTA/Laser hybrid welding.* Science and Technology of Welding and Joining, 2008. **13**(8): p. 683-693.
14. Ribic, B.D., et al., *Arc-laser interactions and heat transfer and fluid flow in hybrid welding*, in *ASM Proceedings of the International Conference: Trends in Welding Research* 2009: Pine Mountain, GA. p. 313-320.
15. Steen, W.M. and M. Eboo, *Arc augmented laser welding.* Metal construction, 1979. **11**(7): p. 332-335.

16. O'Neill, B., et al., *High power high brightness industrial fiber laser technology*, in *Proceedings of 23rd International Congress on Applications of Laser and Electro-Optics, ICALEO*. 2004: San Francisco, CA.
17. *www.ipgphotonics.com*. 2011.
18. Paschotta, R., *Encyclopedia of Laser Physics and Technology, online access at: www virtual library* 2011.
19. Vollertsen, F. and C. Thomy, *Welding with fiber lasers from 200 to 17000 W*, in *Proceedings of 24th International Congress on Applications of Lasers and Electro-Optics, ICALEO* 2005: Miami, FL. p. 254-263.
20. Kittel, S. and F. Dausinger. *Welding with brilliant lasers: Prospects and limitations*. in *Proceedings of SPIE - The International Society for Optical Engineering*. 2010. San Francisco, CA.
21. Petring, D., et al., *The relevance of brightness for high power laser cutting and welding*, in *Proceedings of 27th International Congress on Applications of Lasers and Electro-Optics, ICALEO*. 2008: Temecula, CA. p. 95-103.
22. Beyer, E., B. Brenner, and L. Morgenthal, *Laser beam application with high power fiber lasers*, in *Proceedings of SPIE - The International Society for Optical Engineering*. 2007: Gmunden.
23. Seefeld, T. and B. O'Neill, *Cutting and welding with the new high brightness lasers.* The Laser User, 2008. **50**: p. 32.
24. Gobel, G., B. Brenner, and E. Beyer, *New application possibilities for fiber laser welding*, in *Proceedings of 26th International Congress on Applications of Lasers and Electro-Optics, ICALEO* 2007: Orlando, FL. p. 102.
25. Howse, D.S., R.J. Scudamore, and G.S. Booth, *The evolution of Yb fibre laser/MAG hybrid processing for welding of pipelines*, in *Proceedings of the International Offshore and Polar Engineering Conference*. 2005: Seoul. p. 90-95.
26. Salminen, A., H. Piili, and T. Purtonen, *The characteristics of high power fibre laser welding.* Proceedings of the Institution of Mechanical Engineers, Part C: Journal of Mechanical Engineering Science, 2010. **224**(5): p. 1019-1029.
27. Salminen, A., J. Lehtinen, and P. Harkko, *The effect of welding parameters on keyhole and melt pool behavior during laser welding with high power fiber laser*, in *Proceedings of 27th International Congress on Applications of Lasers and Electro-Optics, ICALEO*. 2008: Temecula, CA. p. 354-363.
28. Katayama, S., et al., *Weld penetration and phenomena in 10 kW fiber laser welding*, in *Proceedings of 26th International Congress on Applications of Lasers and Electro-Optics, ICALEO* 2007: Orlando, FL. p. 353.
29. Weberpals, J. and F. Dausinger, *Fundamental understanding of spatter behavior at laser welding of steel*, in *Proceedings of 27th International Congress on Applications of Lasers and Electro-Optics, ICALEO*. 2008: Temecula, CA. p. 364-373.
30. Weberpals, J. and F. Dausinger, *Influence of inclination angle on spatter behavior at welding with lasers of strong focusability*, in *Proceesings of 26th International Congress on Applications of Lasers and Electro-Optics, ICALEO* 2007: Orlando, FL. p. 858-865.
31. Wedel, B., *Focusing high brightness lasers special requirements on laser processing heads*, in *Proceedings of 26th International Congress on Applications of Lasers and Electro-Optics, ICALEO* 2007: Orlando, FL. p. 83.
32. Abt, F., A. Heß, and F. Dausinger, *Focusing high-power, single-mode laser beams.* Photonics Spectra, 2008. **42**(5): p. 78.

33. Bautze, T. and K. Diepold. *Review of fundamental aspects of focal shift effects and countermesaures*. in *Proceedings of 4th Pacific International Conference on Applications of Lasers and Optics, PICALO*. 2010. Wuhan.
34. De Lange, D.F., J.T. Hofman, and J. Meier, *Optical characteristics of Nd:YAG optics and distortion at high powers*, in *Proceedings of 24th International Congress on Applications of Lasers and Electro-Optics, ICALEO*. 2005: Miami, FL. p. 745-754.
35. Marten, O., et al., *The characterisation of focusing system for high power lasers with high beam quality.* Laser+Photonik, 2009: p. 60-64.
36. Reitemeyer, D., et al., *Cover glass influence on high power fibre laser induced focus shift*, in *Proceedings of 28th International Congress on Applications of Lasers and Electro-Optics, ICALEO*. 2009: Orlando, FL. p. 751-758.
37. Penano, J., et al., *Optical quality of high power laser beams in lenses*. 2008, Naval Research Laboratory: Washington DC.
38. Bisson, J.F. and H. Sako, *Suppression of the focal shift of single-mode laser with a miniature laser processing head.* Journal of Laser Micro/Nanoengineering 2009. **4**(3): p. 170-176.
39. Kogel-Hollacher, M., et al., *Solution for lasers with high brightness - a deeper look into processing heads for welding and cutting*, in *Proceedings of 28th International Congress on Applications of Lasers and Electro-Optics, ICALEO*. 2009: Orlando, FL. p. 146-150.
40. Rummel, S., G. Herrit, and A. Hedges, *Comparison of 1 micron transmissive optical materials for high power lasers*, in *Proceedings of 29th International Congress on Applications of Lasers and Electro-Optics, ICALEO* 2010: Anaheim, CA. p. 21-25.
41. Reitemeyer, D., T. Seefeld, and F. Vollertsen, *Online focus shift measurement in high power fiber laser welding*, in *Proceedings of 29th International Congress on Applications of Lasers and Electro-Optics, ICALEO* 2010: Anaheim, CA. p. 13-20.
42. Zhang, X., et al., *High-power fiber laser welding of thick steel at low welding speed*, in *Proceedings of 26th International Congress on Applications of Lasers and Electro-Optics, ICALEO* 2007: Orlando, FL. p. 850.
43. Verhaeghe, G. and P. Hilton, *The effect of spot size and laser beam quality on welding performance when using high-power continuous wave solid-state lasers*, in *Proceedings of 24th International Congress on Applications of Lasers and Electro-Optics, ICALEO*. 2005: Miami, Fl. p. 264-271.
44. Kawahito, Y., et al., *High-power fiber laser welding and its application to metallic glass Zr55Al10Ni5Cu30.* Materials Science and Engineering B: Solid-State Materials for Advanced Technology, 2008. **148**(1-3): p. 105-109.
45. Weberpals, J., *Influence of the focus diameter in laser welding with thin disk laser*, in *Proceedings of Lasers in Manufacturing*. 2005: Munich, Germany. p. 39.
46. Kessler, B., *Welding results - IPG Photonics marketing materials, Burbach, Germany*. 2006-2008.
47. Zhang, W., C.H. Kim, and T. DebRoy, *Heat and fluid flow in complex joints during gas metal arc welding - Part II: Application to fillet welding of mild steel.* Journal of Applied Physics, 2004. **95**(9): p. 5220-5229.
48. Weberpals, J., et al., *The role of strong focusability on the welding process*, in *Proceedings of 25th International Congress on Applications of Laser and Electro-Optics, ICALEO*. 2006: Scottsdale, AZ.

49. Weberpals, J., et al., *Role of strong focusability on the welding process.* Journal of Laser Applications, 2007. **19**(4): p. 252-258.
50. Hugel, H., *New solid-state lasers and their application potentials.* Optics and Lasers in Engineering, 2000. **34**(4-6): p. 213-229.
51. Thomy, C., T. Seefeld, and F. Vollertsen, *High-power fibre lasers - Application potentials for welding of steel and aluminium sheet material.* Advanced Materials Research, 2005. **6-8**: p. 171-178.
52. Wandera, C., et al. *Cutting of stainless steel with fiber and disk laser*. in *Proceedings of 25th International Congress on Applications of Laser and Electro-Optics, ICALEO*. 2006. Scottsdale, AZ.
53. Petring, D., P. Abels, and E. Beyer, *The absorption distribution as a variable property during laser beam cutting*, in *Proceedings of 7th International Congres on Applications of Lasers and Electro Optics, ICALEO* 1988: Santa Clara, CA. p. 293-302.
54. Petring, D., *Application-oriented modeling of laser beam cutting for computer-assisted process optimisation, PhD Thesis*. 1994, Aachen University: Aachen, Germany.
55. Mahrle, A. and E. Beyer, *Theoretical aspects of fibre laser cutting.* Journal of Physics D: Applied Physics, 2009. **42**(17).
56. Wandera, C., A. Salminen, and V. Kujanpaa, *Inert gas cutting of thick-section stainless steel and medium-section aluminum using a high power fiber laser.* Journal of Laser Applications, 2009. **21**(3): p. 154-161.
57. Wandera, C. and V. Kujanpaa, *Characterization of the melt removal rate in laser cutting of thick-section stainless steel.* Journal of Laser Applications, 2010. **22**(2): p. 62-70.
58. Olsen, F., *An evaluation of the cutting potential of different types of high power lasers*, in *Proceedings of 25th International Congress on Applications of Laser and Electro-Optics, ICALEO*. 2006: Scottsdale, AZ. p. 188-196.
59. Weberpals, J., F. Dausinger, and H. HĂĽgel, *Welding characteristics with lasers of high focusability*, in *Proceedings of SPIE - The International Society for Optical Engineering*. 2007: Gmunden.
60. Weberpals, J., C. Deininger, and F. Dausinger, *Application potential of laser with strong focusability*, in *Proceedings of 2nd Pacific International Conference on Applications of Laser and Optics, PICALO* 2006: Melbourne, VIC. p. 27-31.
61. Gahan, B.C., *New high-power fiber laser enables cutting edge research.* Laser Technology, Winter, 2004: p. 29-31.
62. *LIA Handbook of Laser Material Processing*, ed. J.F. Ready. 2001, Orlando, USA: Laser Institute of America.
63. Katayama, S. and Y. Kawahito, *Interpretation of laser weld penetration and welding phenomena.* Zhongguo Jiguang/Chinese Journal of Lasers, 2009. **36**(12): p. 3160-3166.
64. Ono, M., K. Nakada, and S. Kosuge, *Investigation on CO_2 laser-induced plasma.* Yosetsu Gakkai Ronbunshu/Quarterly Journal of the Japan Welding Society, 1992. **10**(2): p. 31-37.
65. Matsunawa, A., J.D. Kim, and S. Katayama, *Spectroscopic studies on laser-induced plume of aluminum alloys*, in *Proceedings of International Congress on Applications of Lasers and Electro-Optics ICALEO*. 1995: San Diego, USA. p. 719-728.
66. Katayama, S., Y. Kawahito, and M. Mizutani, *Collaboration of physical and metallurgical vewpoints for understanding and process development of laser*

welding, in *Proceedings of International Congress on Applications of Lasers and Electro-Optics ICALEO* 2007: Orlando, USA. p. 360-369.
67. Mahrle, A. and E. Beyer, *Hybrid laser beam welding - Classification, characteristics, and applications.* Journal of Laser Applications, 2006. **18**(3): p. 169-180.
68. Matsunawa, A. and T. Ohnawa, *Beam-plume interaction in laser materials processing.* Transactions of J W R I, 1991. **20**(1): p. 9-15.
69. Hansen, F. and W.W. Duley, *Attenuation of laser radiation by particles during laser materials processing.* Journal of laser applications, 1994. **6**(3): p. 137-143.
70. Tsubota, S., et al., *Development of 10 kW class YAG laser welding technology*, in *Proceedings of International Congress on Applications of Lasers and Electro-Optics, ICALEO* 2000: Dearborn, MI. p. 219-229.
71. Lacroix, D., G. Jeandel, and C. Boudot, *Solution of the radiative transfer equation in an absorbing and scattering Nd:YAG laser-induced plume.* Journal of Applied Physics, 1998. **84**(5): p. 2443-2449.
72. Greses, J., et al., *Laser-vapour interaction in high-power cw Nd:YAG laser welding*, in *Proceedings of 22nd International Congress on Applications of Laser and Electro-Optics, ICALEO*. 2003: Jacksonville, FL.
73. Greses, J., et al., *Plume attenuation under high power Nd:yttritium-aluminum-garnet laser welding.* Journal of Laser Applications, 2004. **16**(1): p. 9-15.
74. Olivier, C.A., P.A. Hilton, and J.D. Russel, *Materials processing with a 10 kW Nd:YAG laser facility*, in *Proceedings of 18th International Congress on Applications of Lasers and Electro-Optics, ICALEO*. 1999: San Diego, USA. p. 233-241.
75. Verhaeghe, G. and B. Dance, *An assessment of the welding performance of high-brightness lasers and a comparison with in-vacuum electron beams*, in *Proceedings of 27th International Congress on Applications of Lasers and Electro-Optics, ICALEO*. 2008: Temecula, CA. p. 406-414.
76. Paulini, J. and G. Simon, *Theoretical lower limit for laser power in laser-enhanced arc welding.* Journal of Physics D: Applied Physics, 1993. **26**(9): p. 1523-1527.
77. Ming, G., Z. Xiaoyan, and H. Qianwu, *Effects of gas shielding parameters on weld penetration of CO_2 laser-TIG hybrid welding.* Journal of Materials Processing Technology, 2007. **184**(1-3): p. 177-183.
78. Rao, Z.H., et al., *Modeling of the transport phenomena in GMAW using argon-helium mixtures. Part II - The metal.* International Journal of Heat and Mass Transfer, 2010. **53**: p. 5722-5732.
79. *www.ophiropt.com.* 2011.
80. *www.lambdaphoto.co.uk.* 2011.
81. *www.primes.de.* 2011.
82. Boulanger, P., et al., *An absolute calorimeter for high power CO2 laser.* Journal of Physics E: Scientific Instruments, 1973. **6**(6): p. 559-560.
83. Preston, J.S., *A radiation thermopile for cw and laser pulse measurement.* Journal of Physics E: Scientific Instruments, 1971. **4**(12): p. 969-972.
84. ISO11554:2006, *Optics and photonics - Lasers and laser-related equipment - Test methods for laser beam power, energy and temporal characteristics.* 2006.
85. *PRIMES GmbH Product Catalogue available at: www.primes.de*.

86. Fuerschbach, P.W., et al., *Development and evaluation of an in-situ beam measurement for spot welding lasers.* Welding Journal (Miami, Fla), 2004. **83**(5): p. 154-S.
87. ISO11146-1:2005, *Lasers and laser related equipment - Test methods and beam properties ratios - Part 1: Stigmatic and simple astigmatic beams.* 2005.
88. ISO11146-2:2005, *Lasers and laser related equipment - Test methods and beam properties ratios - Part 2: General astigmatic beams*
89. ISO/TR11146-3:2004, *Lasers and laser related equipment - Test methods and beam properties ratios - Part 3: Intrinsic and geometrical laser beam classification, propagation and details of test methods* 2004.
90. Green, L., *Pitfalls of beam profilling.* SPIE OE Mag., 2002. **2**(3): p. 48.
91. Ready, J.F., K. Nagarathnam, and J. Mazumder, *Beam Profilers*, in *LIA Handbook of Laser Materials Processing* J.F. Ready, Editor. 2001. p. 149-151.
92. *Handbook of Optical and Laser Scanning* ed. G.F. Marshall. 2004, New York: Marcel Dekker, INC.
93. *Fundamentals of beam profiling and measurement, Materials of CVI Melles Griot available at: www.cvimellesgriot.com.* 2011.
94. O'Connell, R.M. and R.A. Vogel, *Abel inversion of knife-edge data from radially symmetric pulsed laser beams.* Applied Optics, 1987. **26**(13): p. 2528-2532.
95. Skinner, D.R. and R.E. Whitcher, *Measurement of the radius of a high-power laser beam near the focus of a lens.* Journal of Physics E: Scientific Instruments, 1972. **5**(3): p. 237-238.
96. Firester, A.H., M.E. Heller, and P. Sheng, *Knife-edge scanning measurement of subwavelength focused light beams.* Applied Optics, 1977. **16**(7): p. 1971-1974.
97. Khosrofian, J.M. and B.A. Garetz, *Measurement of a Gaussian laser beam diameter through the direct inversion of knife-edge data.* Applied Optics, 1983. **22**(1): p. 3406-3410.
98. Fan, K.C., et al., *Development of a high-precision straightness measuring system with DVD pick-up head.* Measurement Science and Technology, 2003. **14**(1): p. 47-54.
99. Rabczuk, G., M. Sawczak, and G. Sliwinski, *Diagnostic instrument for measurements of a high power CO2 laser beam*, in *Proceedings of SPIE - The International Society for Optical Engineering*. 2000, Society of Photo-Optical Instrumentation Engineers: Szczecin-Swinoujscie, Pol. p. 212-218.
100. Essien, M. and P.W. Fuerschbach, *Beam characterization of a materials processing CO_2 laser.* Welding Journal (Miami, Fla), 1996. **75**(2): p. 47-s.
101. *PRIMES GmbH Materials: Calculation of Laser Beam Parameters for Focus Monitor, Beam Monitor and Micro Spot Monitor*.
102. Wright, D., *Beam widths of a diffracted laser using four proposed methods.* Optical and Quantum Electronics, 1992. **24**(9): p. S1129-S1135.
103. ISO11146-2:2005, *Lasers and laser related equipment - Test methods and beam properties ratios - Part 2: General astigmatic beams.* 2005.
104. Ahmed, N., *New developments in advanced welding*. 2005: CRC Press.
105. Steen, W.M., *Laser material processing*. 2003, New York: Springer Verlag.
106. Zhou, J., H.L. Tsai, and P.C. Wang, *Transport phenomena and keyhole dynamics during pulsed laser welding.* Transactions of the ASME, 2006. **128**(July 2006): p. 680.

107. Rosenthal, D., *Mathematical theory of heat distribution during welding and cutting.* Weld Journal (Miami Fla), 1941. **20**.
108. Rykalin, N.N. and A.V. Nikolaev, *Welding arc heat flow.* Welding in the World, 1971. **9**(3/9): p. 112-132.
109. Friedman, E., *Thermodynamic analysis of the welding process using the finite element method.* ASTM Transactions; Journal of Pressure Vessel Technology, 1975: p. 206.
110. Carslaw, H.S. and J.C. Jaeger, *Conduction of Heat in Solids* 1967: Oxford University Press.
111. Jouvard, J.M., K. Girard, and O. Perret, *Keyhole formation and power deposition in Nd:YAG laser spot welding.* Journal of Physics D: Applied Physics, 2001. **34**(18): p. 2894-2901.
112. Kawahito, Y., M. Mizutani, and S. Katayama, *High quality welding of stainless steel with 10 kW high power fibre laser.* Science and Technology of Welding and Joining, 2009. **14**(4): p. 288-294.
113. Jin, X., L. Li, and Y. Zhang, *A study on fresnel absorption and reflections in the keyhole in deep penetration laser welding.* Journal of Physics D: Applied Physics, 2002. **35**(18): p. 2304-2310.
114. Jin, X., L. Li, and Y. Zhang, *A heat transfer model for deep penetration laser welding based on an actual keyhole.* International Journal of Heat and Mass Transfer, 2003. **46**(1): p. 15-22.
115. Solana, P. and G. Negro, *A study of the effect of multiple reflections on the shape of the keyhole in the laser processing of materials.* Journal of Physics D: Applied Physics, 1997. **30**(23): p. 3216-3222.
116. Fujinaga, S., et al., *Direct observation of keyhole behaviour during pulse modulated high-power Nd:YAG laser irradiation.* Journal of Physics D: Applied Physics, 2000. **33**(5): p. 492-497.
117. Olfert, M. and W.W. Duley, *Holographic interferometry of isotherms during laser drilling of fused quartz.* Journal of Physics D: Applied Physics, 1996. **29**(5): p. 1140-1145.
118. Dowden, J., et al., *A keyhole model in penetration welding with a laser.* Journal of Physics D: Applied Physics, 1987. **20**(1): p. 36-44.
119. Fuerschbach, P.W., *Measurement and prediction of energy transfer efficiency in laser beam welding.* Welding Journal (Miami, Fla), 1996. **75**(1): p. 24-s.
120. Fuerschbach, P.W. and G.R. Eisler, *Effect of very high travel speeds on melting efficiency in laser beam welding.* Journal of Materials and Manufacturing, 1999. **108**.
121. Fuerschbach, P.W. and D.O. MacCallum, *Variation of laser energy transfer efficiency with weld pool depth*, in *Proceedings of 14th International Congress on Applications of Lasers and Electro-Optocs, ICALEO* 1995: San Diego, USA. p. 493-497.
122. Schneider, M., et al., *Measurement of laser absorptivity for operating parameters characteristic of laser drilling regime.* Journal of Physics D: Applied Physics, 2008. **41**(15).
123. Norris, J.T., et al., *Development of a time-resolved energy absorption measurement technique for laser beam spot welds.* Welding Journal (Miami, Fla), 2010. **89**(4): p. 75s-81s.
124. Fabbro, R., M. Hamadou, and F. Coste, *Metallic vapor ejection effect on melt pool dynamics in deep penetration laser welding.* Journal of laser applications, 2004. **16**(1): p. 16-19.

125. Sudnik, W., et al., *Numerical simulation of weld pool geometry in laser beam welding.* Journal of Physics D: Applied Physics, 2000. **33**(6): p. 662-671.
126. Semak, V.V., et al., *Melt pool dynamics during laser welding.* Journal Physics D: Applied Physics, 1995. **28**: p. 2443-2450.
127. Kroos, J., et al., *Dynamic behaviour of the keyhole in laser welding* Journal of Physics D: Applied Physics, 1993. **26**: p. 481-486.
128. Andrews, J.G. and D.R. Atthey, *Hydrodynamic limit to penetration of a material by a high-power beam.* Journal of Physics D: Applied Physics, 1976. **9**(15): p. 2181-2194.
129. Amara, E.H. and R. Fabbro, *Modelling of gas jet effect on the melt pool movements during deep penetration laser welding.* Journal of Physics D: Applied Physics, 2008. **41**(5).
130. Petring, D., *Basic description of laser cutting*, in *LIA Handbook of Laser Material Processing*. 2001, Laser Institute of America nad Magnolia Publishing Orlando, USA.
131. Schulz, W., et al., *On laser fusion cutting of metals.* Journal of Physics D: Applied Physics, 1987. **20**(4): p. 481-488.
132. Kaplan, A., *Model of deep penetration laser welding based on calculation of the keyhole profile.* Journal of Physics D: Applied Physics, 1994. **27**(9): p. 1805-1814.
133. Ki, H., P.S. Mohanty, and J. Mazumder, *Multiple reflection and its influence on keyhole evolution.* Journal of laser applications, 2002. **14**(1): p. 39-45.
134. Cho, J.H. and S.J. Na, *Implementation of real-time multiple reflection and Fresnel absorption of laser beam in keyhole.* Journal of Physics D: Applied Physics, 2006. **39**(24): p. 5372-5378.
135. Fabbro, R. and K. Chouf, *Dynamical description of the keyhole in deep penetration laser welding.* Journal of laser applications, 2000. **12**(4): p. 142-148.
136. Milewski, J.O. and M.B. Barbe, *Modeling and analysis of laser melting within a narrow groove weld joint.* Welding Journal (Miami, Fla), 1999. **78**(4): p. 109s-115s.
137. Lee, J.Y., et al., *Mechanism of keyhole formation and stability in stationary laser welding.* Journal of Physics D: Applied Physics, 2002. **35**(13): p. 1570-1576.
138. Weber, R., et al., *Effect of radial and tangential polarization in laser material processing.* Physics Procedia, 2011. **12**: p. 21-30.
139. Fabbro, R., *Dynamic approach of the keyhole and melt pool behavior for deep penetration Nd-Yag laser welding*, in *AIP Conference Proceedings*. 2008: Edmonton, Alberta, Canada. p. 18-24.
140. Fabbro, R., et al., *Study of keyhole behaviour for full penetration Nd-Yag CW laser welding.* Journal of Physics D: Applied Physics, 2005. **38**(12): p. 1881-1887.
141. Niziev, V.G. and A.V. Nesterov, *Influence of beam polarization on laser cutting efficiency.* Journal of Physics D: Applied Physics, 1999. **32**(13): p. 1455-1461.
142. Sudnik, W., D. Radaj, and W. Erofeew, *Computerized simulation of laser beam welding, modelling and verification.* Journal of Physics D: Applied Physics, 1996. **29**(11): p. 2811-2817.
143. Mazumder, J., H. Ki, and P.S. Mohanty, *Role of recoil pressure, multiple reflections, and free surface evolution during laser keyhole welding*, in

Proceedings of 21st International Congress on Applications of Lasers and Electro-Optics, ICALEO. 2002: Scottsdale, AZ. p. 11.
144. Matsunawa, A., J.D. Kim, and S. Katayama, *Porosity formation in laser welding* in *Proceedings of 16th International Congres on Applications of Lasers and Electro-Optics ICALEO*. 1997: San Diego, USA. p. 73-82.
145. Katayama, S., et al., *Formation mechanism and reduction method of porosity in laser welding of stainless steel*, in *Proceedings of 16th International Congres on Applications of Lasers and Electro-Optics ICALEO*. 1997: San Diego, USA. p. 83-92.
146. Arata, Y., et al., *Dynamic behavior of laser welding and cutting*, in *Proceedings of 7th International Coference on Electron and Ion Beam Science and Technology*. 1976. p. 111-128.
147. Shannon, M.A., *A simplified cavity analysis for estimating energy coupling during laser ablation and drilling of solids - Theory.* Applied Surface Science, 1998. **127-129**: p. 218-225.
148. Kayukov, S.V. and A.A. Gusev, *Influence of the laser beam parameters on the depth and efficiency of the melting of metals by pulsed laser radiation.* Kvantovaya Elektronika, 1996. **23**(8): p. 714.
149. Kayukov, S.V. and A.A. Gusev, *Influence of the aperture angle on the efficiency of the melting of steel by millisecond laser pulses.* Quantum Electronics, 2000. **30**(4): p. 337-341.
150. Petring, D., *Calculable laser cutting*, in *Proceedings of the Fiftth International WLT-Conference on Lasers in Manufacturing* 2009: Munich. p. 209-214.
151. Powell, J., et al., *Fibre laser cutting of thin section mild steel: An explanation of the 'striation free' effect.* Optics and Lasers in Engineering, 2011. **49**: p. 1069-1075.
152. Venkatakrishnan, K. and B. Tan, *Interconnect microvia drilling with a radially polarized laser beam.* Journal of Micromechanics and Microengineering, 2006. **16**(12): p. 2603-2607.
153. Graf, S., et al., *Enhanced melt pool stirring in welding with dynamic polarised laser beam.* Science and Technology of Welding and Joining, 2010. **15**(3): p. 208-212.
154. Meier, M., V. Romano, and T. Feurer, *Material processing with pulsed radially and azimuthally polarized laser radiation.* Applied Physics A: Materials Science and Processing, 2007. **86**(3): p. 329-334.
155. Zaitsev, A.V., et al., *Numerical analysis of the effect of the TEM_{00} radiation mode polarisation on the cut shape in laser cutting of thick metal sheets.* Quantum Electronics, 2005. **35**(2): p. 200-204.
156. Niziev, V.G., *Theory of CW laser beam cutting.* Laser Physics, 1993. **3**: p. 629-635.
157. Bardin, F., et al., *Process control of laser conduction welding by thermal imaging measurement with a color camera.* Applied Optics, 2005. **44**(32): p. 6841-6848.
158. Benzinger, T.H. and C. Kitzinger, *Direct calorimetry by means of the gradient principle.* The Review of Scientific Instruments 1949. **20**(12): p. 849-860.
159. Katayama, S., Y. Kawahito, and N. Matsumoto, *Laser absorption in high-power fiber laser welding of stainless steel and aluminum alloy (Invited presentation)*, in *Proceedings of 4th Pacific International Conference on Applications of Lasers and Optics, PICALO*. 2010: Wuhan, China.

160. Sakamoto, H., T. Iwase, and K. Shibata, *Effect of twin spot beam arrangement on energy coupling during welding - Study of twin spot Nd:YAG laser welding of aluminum alloys (rep. 3).* Yosetsu Gakkai Ronbunshu/Quarterly Journal of the Japan Welding Society, 2003. **21**(4): p. 501-506.
161. Cremers, D.A., G.K. Lewis, and D.R. Korzekwa, *Measurement of energy deposition during pulsed laser welding.* Welding Journal 1991. **70**(7).
162. Sharp, D.H., *An overview of Rayleigh-Taylor instability.* Physica D, 1984. **12**: p. 3-18.
163. Fuerschbach, P.W. and G.R. Eisler, *Effect of laser spot weld energy and duration on melting and absorption.* Science and Technology of Welding and Joining, 2002. **7**(4): p. 241-246.
164. Kim, T.H. and J.G. Kim, *Process efficiency and multiple absorption of a laser beam during bead-on plate welding of steels by a CO_2 laser.* Journal of Materials Science Letters, 1992. **11**(18): p. 1263-1265.
165. Perret, O., P. Naudy, and M. Bizouard, *Two experimental methods to understand keyhole formation in pulse Nd:YAG laser welding*, in *Proceedings of SPIE - The International Society for Optical Engineering*. 2000, Society of Photo-Optical Instrumentation Engineers: Osaka, Jpn. p. 778-787.
166. Weston, J., *Surface related features of laser welding of aluminium alloys.* ISIJ International, 2000. **40**(SUPPL.).
167. Hess, A., et al., *Forced deep-penetration welding with low-power second-harmonic assistance of cw copper welding with 1 um wavelength*, in *Physics Procedia*. 2010: Erlangen. p. 29-36.
168. Hess, A., et al., *Benefits from combining laser beams with different wavelengths (green and IR) for copper welding*, in *Proceedings of 29th International Congress on Applications of Lasers and Electro-Optics, ICALEO*. 2010: Anaheim, CA. p. 540-546.
169. Otte, F., U. Stute, and A. Ostendorf, *Micro welding of electronic components with 532 nm laser radiation*, in *Proceedings of SPIE - The International Society for Optical Engineering*. 2007: San Jose, CA.
170. Moon, J.H., et al., *Melting characteristics of metals by combined laser beams with different wavelengths.* Journal of Laser Applications, 2003. **15**(1): p. 37-42.
171. Mys, I. and M. Geiger, *Use of pre-pulse in laser spot welding of materials with high optical reflection*, in *Proceedings of SPIE - The International Society for Optical Engineering*, I. Miyamoto, et al., Editors. 2003: Munich, Germany. p. 314-318.
172. Rosenthal, D., *The theory of moving source of heat and its application to metal treatment* Transaction ASME, 1946. **43**(11): p. 849-866.
173. Steen, W.M., et al., *A point and line source model of laser keyhole welding* Journal of Physics D: Applied Physics, 1988. **21**: p. 1255-1260.
174. Kaplan, A.F.H., *Surface processing with non-Gaussian beam.* Applied Physics Letters, 1997. **70**(2): p. 246-266.
175. Resch, M. and A.F.H. Kaplan, *Heat conduction modelling of laser welding.* Lasers in Engineering, 1998. **7**(3-4): p. 229-240.
176. Pavelic, V., et al., *Experimental nad computed temperature histories in Gas Tungsten-Arc Welding of thin plates.* Welding Journal, 1969. **48**(7): p. 295s-305s.

177. Eagar, T.W. and N.S. Tsai, *Temperature fields produced by traveling distributed heat sources.* Welding Journal (Miami, Fla), 1983. **62**(12): p. 346-355.
178. Goldak, J., A. Chakravarti, and M. Bibby, *A new finite element model for welding heat sources.* Metallurgical Transactions B, 1984. **15**(2): p. 299-305.
179. Goldak, J. and M. Akhlaghi, *Computational welding mechanics*. 2005: Springer.
180. Bibby, M., J. Goldak, and G.Y. Shing, *Model for predicting the fusion and heat affected zone sizes of deep penetration welds.* Canadian Metallurgical Quarterly, 1985. **24**(1): p. 101-105.
181. Christensen, N., L.V. Davies, and K. Gjermundsen, *Distribution of temperatures in arc welding.* British Welding Journal, 1965. **12**: p. 54-75.
182. Bag, S., A. Trivedi, and A. De, *Development of a finite element based heat transfer model for conduction mode laser spot welding process using an adaptive volumetric heat source.* International Journal of Thermal Sciences, 2009. **48**(10): p. 1923-1931.
183. He, X., P.W. Fuerschbach, and T. DebRoy, *Heat transfer and fluid flow during laser spot welding of 304 stainless steel.* Journal of Physics D: Applied Physics, 2003. **36**(12): p. 1388-1398.
184. Zhang, W., et al., *Modeling of heat transfer and fluid flow during gas tungsten arc spot welding of low carbon steel.* Journal of Applied Physics, 2003. **93**(5): p. 3022-3033.
185. Solana, P., P. Kapadia, and J. Dowden, *Surface depression and ablation for a weld pool in material processing: A mathematical model.* Journal of laser applications, 2000. **12**(2): p. 63-67.
186. Cho, J.H. and S.J. Na, *Three-dimensional analysis of molten pool in GMA-laser hybrid welding.* Welding Journal (Miami, Fla), 2009. **88**(2): p. 35s-43s.
187. Bedenko, D.V., O.B. Kovalev, and I.V. Krivtsun, *Simulation of plasma dynamics in a keyhole during laser welding of metal with deep penetration.* Journal of Physics D: Applied Physics, 2010. **43**(10).
188. Boran, K., *Laser gas assisted melting and thermal efficiency analysis.* Lasers in Engineering, 2008. **18**(3-4): p. 187-202.
189. Zhiryakov, B.M., et al., *Influence of hydrodynamic perturbation on laser evaporation of metals with a phase interface.* Soviet journal of quantum electronics, 1983. **13**(6): p. 763-766.
190. Schauer, D.A., W.H. Giedt, and S.M. Shintaku, *Electron beam welding cavity temperature distributions in pure metals and alloys.* Welding Journal (Miami, Fla), 1978. **57**(5): p. 127s-133s.
191. Anisimov, S.I., *Vaporisation of metal absorbing laser radiation* Sov. Phys. JETP, 1968. **27**.
192. Von Allmen, M., *Laser drilling velocity in metals.* Journal of Applied Physics, 1976. **47**(12): p. 5460-5463.
193. Solana, P., et al., *Time dependent ablation and liquid ejection processes during the laser drilling of metals.* Optics Communications, 2001. **191**(1-2): p. 97-112.
194. Semak, V. and A. Matsunawa, *The role of recoil pressure in energy balance during laser materials processing.* Journal of Physics D: Applied Physics, 1997. **30**(18): p. 2541-2552.
195. Semak, V.V., B. Damkroger, and S. Kempka, *Temporal evolution of the temperature field in the beam interaction zone during laser material*

processing. Journal of Physics D: Applied Physics, 1999. **32**(15): p. 1819-1825.
196. Ganesh, R.K., et al., *A model for laser hole drilling in metals.* Journal of Computational Physics, 1996. **125**(1): p. 161-176.
197. De Lange, D.F., A. Schoonderbeek, and J. Meijer, *Melt ejection during laser drilling*, in *Proceedings of 23rd International Congress on Applications of Laser and Electro-Optics, ICALEO*. 2004: San Francisco, CA.
198. Colegrove, P., et al. *Evaluation of a drilling model approach to represent laser spot microwelding*. in *Trends in Welding Research, Proceedings of the 8th International Conference* 2008.
199. Colegrove, P., et al., *Evaluation of a drilling model approach to represent laser spot microwelding*, in *Trends in Welding Research,ASM Proceedings of the 8th International Conference 2008* S.A. David and T. DebRoy, Editors. 2009: Pine Mountain, GA. p. 303-312.
200. Batteh, J.J., M.M. Chen, and J. Mazumder, *A stagnation flow analysis of the heat transfer and fluid flow phenomena in laser drilling.* Journal of Heat Transfer, 2000. **122**(4): p. 801-807.
201. Basu, S. and T. DebRoy, *Liquid metal expulsion during laser irradiation.* Journal of Applied Physics, 1992. **72**(8): p. 3317-3322.
202. Chun, M.K. and K. Rose, *Interaction of high-intensity laser beams with metals.* Journal of Applied Physics, 1970. **41**(2): p. 614-620.
203. Uchiumi, S., et al., *Penetration and welding phenomena in YAG laser-MIG hybrid welding of aluminum alloy*, in *Proceedings of 23rd international congress on applications of lasers and electro-optics, ICALEO*. 2004: San Francisco, CA.
204. Anisimov, S.I. and A. Rakhmatulina, K, *The dynamics of the expansion of a vapor when evaporated into a vacuum.* Sov. Phys. JETP, 1973. **37**(3): p. 441-444.
205. Knight, C.J., *Theoretical modeling of rapid surface vaporization with back pressure.* AIAA journal, 1979. **17**(5): p. 519-523.
206. Zhao, J.R., S.B. Zhang, and D. D.Sun, *Research of a new welding technique double heat source laser-arc, IIW Doc., No. XII-1187-90*. 1990. p. 375-390.
207. Xiao, R.S., et al., *Hybrid Nd: YAG laser beam welding of aluminum in addition with an electric current*, in *Proceedings of SPIE - The International Society for Optical Engineering*. 2005: San Jose, CA. p. 195-201.
208. Wei, P.S. and J.Y. Ho, *Energy considerations in high-energy beam drilling.* International Journal of Heat and Mass Transfer, 1990. **33**(10): p. 2207-2217.
209. Chen, X. and H.X. Wang, *A calculation model for the evaporation recoil pressure in laser material processing.* Journal of Physics D: Applied Physics, 2001. **34**(17): p. 2637-2642.
210. Solana, P., et al., *Analytical model for the laser drilling of metals with absorption within the vapour.* Journal of Physics D: Applied Physics, 1999. **32**(8): p. 942-952.
211. Mazumder, J. and W.M. Steen, *Heat transfer model for cw laser material processing.* Journal of Applied Physics, 1980. **51**(2): p. 941-947.
212. Von Allmen, M., et al., *Absorption phenomena in metal drilling with Nd-lasers.* IEEE Journal of Quantum Electronics, 1978. **QE-14**(2): p. 85-88.
213. Ducharme, R., et al., *Laser welding of thin metal sheets: an integrated keyhole and weld pool model with supporting experiments.* Journal of Physics D: Applied Physics, 1994. **27**(8): p. 1619-1627.

214. Gao, Z., Y. Wu, and J. Huang, *Analysis of weld pool dynamic during stationary laser-MIG hybrid welding.* International Journal of Advanced Manufacturing Technology, 2009. **44**(9-10): p. 870-879.
215. Rai, R., et al., *A convective heat-transfer model for partial and full penetration keyhole mode laser welding of a structural steel.* Metallurgical and Materials Transactions A: Physical Metallurgy and Materials Science, 2008. **39**(1): p. 98-112.
216. Wang, H., Y. Shi, and S. Gong, *Effect of pressure gradient driven convection in the molten pool during the deep penetration laser welding.* Journal of Materials Processing Technology, 2007. **184**(1-3): p. 386-392.
217. Amara, E.H., R. Fabbro, and F. Hamadi, *Modeling of the melted bath movement induced by the vapor flow in deep penetration laser welding.* Journal of Laser Applications, 2006. **18**(1): p. 2-11.
218. Mizutani, M. and S. Katayama, *Keyhole behavior and pressure distribution during laser irradiation on molten metal*, in *Proceedings of 22nd International Congress on Applications of Laser and Electro-Optics, ICALEO*. 2003: Jacksonville, FL.
219. Knorovsky, G.A. and D.O. MacCallum, *Recoil force measurements during pulsed Nd:YAG laser spot welds*, in *Proceeding of Internationl Congress on Applications of Lasers and Electro-Optics ICALEO*. 2003: Jacksonville, FL.
220. Katayama, S., et al., *Pulsed YAG laser spot welding under microgravity*, in *Proceedings of SPIE - The International Society for Optical Engineering*. 2000, Society of Photo-Optical Instrumentation Engineers: Osaka, Jpn. p. 96-103.
221. Moon, D.W. and E.A. Metzbower, *Laser beam welding of aluminum alloy 5456.* Welding Journal (Miami, Fla), 1983. **62**(2).
222. Cieslak, M.J. and P.W. Fuerschbach, *On the weldability, composition, and hardness of pulsed and continuous Nd:YAG laser welds in aluminum alloys 6061,5456, and 5086.* Metallurgical Transactions B, 1988. **19**(1): p. 319-329.
223. Khan, P.A.A. and T. Debroy, *Alloying element vaporization and weld pool temperature during laser welding of AISI 202 stainless steel.* Metallurgical Transactions B, 1984. **15**(4): p. 641-644.
224. Block-Bolten, A. and T.W. Eagar, *Metal vaporization from weld pools.* Metallurgical Transactions B, 1984. **15**(3): p. 461-469.
225. Zhao, L., et al., *Influence of oxygen on weld geometry in fibre laser and fibre laser-GMA hybrid welding.* Science and Technology of Welding and Joining, 2011. **16**(2): p. 166-173.
226. Schuocker, D., *Interaction between high power laser beams and matter*, in *High power lasers in production and engineering*. 1999, Imperial College Press: London. p. 183-210.
227. Bohren, C.F. and D.R. Huffman, *Absorption and scattering of light by small particles*. 2010, New York: Whiley-Interscience.
228. Dowden, J., *The onset and absorption of ionisation in the vapour for laser keyhole welding.* International Journal for the Joining of Materials, 2001. **13**(4): p. 85-90.
229. Ingle, J.D.J. and S.R. Crouch, *Spectrochemical analysis*. 1988, New Jersey: Prentice Hall.
230. Zhao, H. and T. DebRoy, *Macroporosity free aluminum alloy weldments through numerical simulation of keyhole mode laser welding* Journal of Physics, 2003. **93**(12): p. 10089-10096.

231. Rai, R., et al., *Heat transfer and fluid flow during keyhole model laser welding of tantalum, Ti-6Al-4V, 304L stainless steel and vanadium.* Journal Physics D: Applied Physics, 2007. **40**: p. 5753-5766.
232. Peebles, H.C. and R.L. Williamson, *The role of the metal vapor plume in pulsed Nd:YAG laser welding on aluminium 1100*, in *Proceedings of LAMP'87*. 1987. p. 19-24.
233. Lacroix, D., G. Jeandel, and C. Boudot, *Spectroscopic characterization of laser-induced plasma created during welding with a pulsed Nd:YAG laser.* Journal of Applied Physics, 1997. **81**(10): p. 6599-6606.
234. Mueller, R.E., et al., *Real time optical spectral monitoring of laser welding plumes*, in *Proceeding of International Congress on Applications of Lasers and Electro-Optics ICALEO*. 1999: San Diego, CA.
235. Greses, J., et al., *Spectroscopic studies of plume/plasma in different gas environments*, in *Proceedings of 20th International Congress on Applications of Lasers and Electro-Optics, ICALEO* 2001: Jacksonville, FL.
236. Kawahito, Y., et al., *Characterisation of plasma induced during high power fibre laser welding of stainless steel.* Science and Technology of Welding and Joining, 2008. **13**(8): p. 744-748.
237. Zel'dovich, Y.B. and R.Y. P., *Physics of shock waves and high-temperature hydrodynamic phenomena*. 1966, New York, (reprinted by Dover, 2002): Academic Press.
238. Michalowski, A., et al., *Plume attenuation under high power Yb:YAG laser material processing* in *Proceedings of the Fourth International WLT-Conference on Lasers in Manufacturing* 2007: Munich, Germany. p. 357-361.
239. Liu, L. and X. Hao, *Study of the effect of low-power pulse laser on arc plasma and magnesium alloy target in hybrid welding by spectral diagnosis technique.* Journal of Physics D: Applied Physics, 2008. **41**(20).
240. Bibik, O.B., V.N. Brodyagin, and Y.P. Pokladov, *Peculiarities of interaction of laser irradiation and welding electric arc in application to combined laser-arc welding process.* Fizika i khimija obrabotki materialov, 1990. **2**: p. 95-98.
241. Hu, B. and I.M. Richardson, *Absorption of laser energy by a welding arc*, in *Proceedings of 22nd International Congress on Applications of Laser and Electro-Optics, ICALEO*. 2003: Jacksonville, FL.
242. Matsunawa, A., et al., *Porosity formation and solidification cracking in laser welding*, in *Proceedings of Taiwan International Welding Conference'98 on Technology Advancements and New Industrial Applications in Welding*. 1998. p. 47.
243. Brajdic, M., et al., *In situ measurement of plasma and shock wave properties inside laser-drilled metal holes.* Measurement Science and Technology, 2008. **19**(10).
244. Raizer Yu, P., *Heating of a gas by a powerful light pulse.* Sov. Phys. JETP, 1965. **21**: p. 1009.
245. Kononenko, T.V., et al., *Comparative study of the ablation of materials by femtosecond and pico-or nanosecond laser pulses.* Quantum Electronics, 1999. **29**(8): p. 724-728.
246. Tokarev, V.N., et al., *Suppression of laser plasma melting side walls in laser drilling high aspect ratio microvias*, in *Proceedings of 29th International Congress on Applications of Lasers and Electro-Optics, ICALEO*. 2010: Anaheim, CA. p. 966-975.

247. Schellhorn, M. and H. Buelow, *CO laser deep-penetration welding: a comparative study to CO_2 laser welding*, in *Proceedings of SPIE - The International Society for Optical Engineering*, L. Bohn Willy and H. Huegel, Editors. 1995, Society of Photo-Optical Instrumentation Engineers: Friedrichshafen, Germany. p. 664-669.
248. Gebhardt, F.G., *High power laser propagation.* Applied Optics, 1976. **15**(6): p. 1479-1493.
249. Gerritsen, C.H.J. and C.A. Olivier, *Optimisation of plasma/plume control for high power Nd:YAG laser welding of 15mm thickness C-Mn steels*, in *ASM Proceedings of the International Conference: Trends in Welding Research*. 2002: Pheonix, Arizona. p. 465-470.
250. Fabbro, R., et al., *Experimental study of the dynamical coupling between the induced vapour plume and the melt pool for Nd-Yag CW laser welding.* Journal of Physics D: Applied Physics, 2006. **39**(2): p. 394-400.
251. Klein, T., M. Vicanek, and G. Simon, *Forced oscillations of the keyhole in penetration laser beam welding.* Journal of Physics D: Applied Physics, 1996. **29**(2): p. 322-332.
252. Golubev, V.S., *Laser welding and cutting: Recent insights into fluid-dynamics mechanisms*, in *Proceedings of SPIE - The international Society for Optical Engineering*. 2002: Moscow. p. 1-15.
253. Metzbower, E.A., *Keyhole formation.* Metallurgical Transactions B, 1993. **24**(5): p. 875-880.
254. Matsunawa, A. and V. Semak, *The simulation of front keyhole wall dynamics during laser welding.* Journal of Physics D: Applied Physics, 1997. **30**(5): p. 798-809.
255. Limmaneevichitr, C. and S. Kou, *Experiments to simulate effect of Marangoni convection on weld pool shape.* Welding Journal (Miami, Fla), 2000. **79**(8).
256. Fabbro, R. and K. Chouf, *Keyhole modeling during laser welding.* Journal of Applied Physics, 2000. **87**(9 I): p. 4075-4083.
257. Chakraborty, N., *Thermal transport regimes and effects of prandtl number in molten pool transport in laser surface melting processes.* Numerical Heat Transfer; Part A: Applications, 2008. **53**(3): p. 273-294.
258. Jaidi, J. and P. Dutta, *Modeling of transport phenomena in a gas metal arc welding process.* Numerical Heat Transfer; Part A: Applications, 2001. **40**(5): p. 543-562.
259. Mahrle, A. and J. Schmidt, *The influence of fluid flow phenomena on the laser beam welding process.* International Journal of Heat and Fluid Flow, 2002. **23**(3): p. 288-297.
260. Robert, A. and T. Debroy, *Geometry of laser spot welds from dimensionless numbers.* Metallurgical and Materials Transactions B: Process Metallurgy and Materials Processing Science, 2001. **32**(5): p. 941-947.
261. Ye, X.H. and X. Chen, *Three-dimensional modelling of heat transfer and fluid flow in laser full-penetration welding.* Journal of Physics D: Applied Physics, 2002. **35**(10): p. 1049-1056.
262. He, X., T. DebRoy, and P.W. Fuerschbach, *Alloying element vaporization during laser spot welding of stainless steel.* Journal of Physics D: Applied Physics, 2003. **36**(23): p. 3079-3088.
263. Dowden, J., *Interaction of the keyhole and weld pool in laser keyhole welding.* Journal of laser applications, 2002. **14**(4): p. 204-207.

264. Gu, H. and W.W. Duley, *A statistical approach to acoustic monitoring of laser welding.* Journal of Physics D: Applied Physics, 1996. **29**: p. 556-560.
265. Klein, T., et al., *Oscillations of the keyhole in penetration laser beam welding.* Journal of Physics D: Applied Physics, 1994. **27**(10): p. 2023-2030.
266. Jan, R., R.R. Howell, and R.P. Martukanitz, *Optimising the parameters for laser beam welding of aluminium-lithium alloy 2195*, in *Proceedings of the 4th International Conference on Trends in Welding Research* 1996, ASM p. 329-334.
267. Simon, G., U. Gratzke, and J. Kroos, *Analysis of heat conduction in deep penetration welding with a time-modulated laser beam.* Journal of Physics D: Applied Physics, 1993. **26**(5): p. 862-869.
268. Klemens, P.G., *Heat balance and flow conditions for electron beam and laser welding.* Journal of Applied Physics, 1976. **47**(5): p. 2165-2174.
269. Hohenberger, B., et al., *Laser welding with Nd:YAG multi-beam technique*, in *Proceedings of International Congress on Applications of Lasers and Electro-Optics, ICALEO* 1999, Laser Institute of America: San Diego, USA. p. 167-176.
270. Matsunawa, A., et al., *Dynamics of keyhole and molten pool in high power CO_2 laser welding*, in *Proceedings of SPIE - The International Society for Optical Engineering*. 2000: Osaka. p. 34-45.
271. Seto, N., S. Katayama, and A. Matsunawa, *Porosity formation mechanism and suppression procedure in laser welding of aluminum alloy.* Yosetsu Gakkai Ronbunshu/Quarterly Journal of the Japan Welding Society, 2000. **18**(2): p. 243-255.
272. Tsukamoto, S., et al., *Formation mechanism and suppression of welding defects in 20 kW CO_2 laser welding*, in *ASM Proceedings of the International Conference: Trends in Welding Research*. 2002: Phoenix, AZ. p. 459-464.
273. Williams, K., et al., *On laser welding meltpool dynamics*, in *Proceedings of the International Conference on Applications of Lasers and Electro-Optics ICALEO*. 1993: Orlando, FL.
274. Schroll, R.D., et al., *Liquid transport due to light scattering.* Physical Review Letters, 2007. **98**(13).
275. Shenkenberg, D.L., *Laser-induced fluid flow.* Photonics Spectra, 2007. **41**(5): p. 46-47.
276. Mueller, R.E., J. Bird, and W.W. Duley, *Laser drilling into an absorbing liquid.* Journal of Applied Physics, 1992. **72**(2): p. 551-556.
277. Antonov, A.A. and G.I. Kozlov, Kvantovaya Elektronika, 1987. **4**(N6): p. 747-753.
278. Cybulski, A. and Z. Mucha, *Laser keyhole in liquids.* Welding International, 1997. **11**(3): p. 212-220.
279. Kawahito, Y., et al., *Effect of weakly ionised plasma on penetration of stainless steel weld produced with ultra high power density fibre laser.* Science and Technology of Welding and Joining, 2008. **13**(8): p. 749-753.
280. Seto, N., S. Katayama, and A. Matsunawa, *High-speed simultaneous observation of plasma and keyhole behavior during high power CO_2 laser welding: Effect of shielding gas on porosity formation.* Journal of Laser Applications, 2000. **12**(6): p. 245-250.
281. Cho, M.H., et al., *Laser weld keyhole dynamics*, in *ASM Proceedings of the International Conference: Trends in Welding Research*. 2002: Phoenix, AZ. p. 112-117.

282. Arata, Y., N. Abe, and T. Oda, *Fundamental phenomena in high power CO_2 laser (report II) - vacuum welding* Transactions of JWRI (Japanese Welding Research Institute), 1985. **14**(2): p. 17-22.
283. Karhu, M., T. Jokinen, and V. Kujanpaa, *Welding experiments using vacuum enviroment with Nd:YAG-laser*, in *Proceedings of 22nd International Congress on Applications of Laser and Electro-Optics, ICALEO*. 2003: Jacksonville, FL.
284. Brown, C.O. and C.M. Banas, *High-power laser beam welding in reduced-pressure atmospheres.* Welding Journal (Miami, Fla), 1986. **65**(7): p. 48-53.
285. Meier, J.W., *Electron beam welding at various pressures.* Metallurgical Society Conference Proceedings, 1966. **51**(1): p. 505-533.
286. Song, W., et al., *Study on vacuum laser cladding.* Jiguang Jishu/Laser Technology, 1997. **21**(4): p. 243-245.
287. Katayama, S., et al., *Effect of vacuum on penetration and defects in laser welding.* Journal of Laser Applications, 2001. **13**(5): p. 187-192.
288. Ono, M., K. Nakada, and S. Kosuge, *Effect of ambient pressure and gas on penetration depth and laser-induced plasma behavior.* Yosetsu Gakkai Ronbunshu/Quarterly Journal of the Japan Welding Society, 1992. **10**(2): p. 9-14.
289. Verwaerde, A., R. Fabbro, and G. Deshors, *Experimental study of continuous CO_2 laser welding at subatmospheric pressures.* Journal of Applied Physics, 1995. **78**(5): p. 2981-2984.
290. Reisgen, U., S. Olschok, and S. Longerich, *Laser beam welding in vacuum - A comparison with electron beam welding.* Welding and Cutting, 2010. **9**(4): p. 224-230.
291. Abe, Y., et al., *Deep penetration welding with high power laser under vacuum*, in *Proceedings of 29th International Congress on Applications of Lasers and Electro-Optics, ICALEO* 2010: Anaheim, CA. p. 648-653.
292. Carlson, K.W., *The role of heat input in deep penetration laser welding*, in *Proceeding of the International Conference on Applications of Lasers and Electro-optics ICALEO' 85*, C. Albright, Editor. 1985. p. 49.
293. Gregson, V., *Laser data welding*, in *The industrial laser handbook*, D. Belforte and M. Levitt, Editors. 1988, Penn Well Pub. Co. p. 13-15.
294. Mannik, L. and S.W. Brown, *A relationship between laser power, penetration depth and welding speed in the laser welding of steels.* Journal of Laser Applications, 1990. **2**(3&4).
295. Swift-Hook, D.T. and A.E.F. Gick, *Penetration welding with lasers.* Welding Journal (Miami, Fla), 1973. **52**(11): p. 492s-499s.
296. Lankalapalli, K.N., J.F. Tu, and M. Gartner, *A model for estimating penetration depth of laser welding processes.* Journal of Physics D: Applied Physics, 1996. **29**(7): p. 1831-1841.
297. Leong, K.H., et al., *Threshold laser beam irradiances for melting and welding.* Journal of laser applications, 1997. **9**(5): p. 227-231.
298. Ion, J.C., *Laser processing diagrams*, in *Laser Processing of Engineering Materials*. 2005, Elsevier: Oxford. p. 178-187.
299. Tzeng, Y.F., *Process characterization of pulsed Nd:YAG laser seam welding.* International Journal of Advanced Manufacturing Technology, 2000. **16**(1): p. 10-18.
300. Steen, W.M., *Laser material processing - An overview.* Journal of Optics A: Pure and Applied Optics, 2003. **5**(4): p. S3-S7.

301. McBride, R., et al., *Modelling and calibration of bending strains for iterative laser forming.* Journal of Physics D: Applied Physics, 2005. **38**(22): p. 4027-4036.
302. Jebbari, N., et al., *Thermal affected zone obtained in machining steel XC42 by high-power continuous CO_2 laser.* Optics and Laser Technology, 2008. **40**(6): p. 864-873.
303. Kerstens, N.F.H., I.M. Richardson, and B.T.J. Stoop, *High power diode laser welding of AA2024 and AISI316L*, in *Proceedings of 24th International Congress on Applications of Lasers and Electro-Optics, ICALEO*. 2005: Miami, FL.
304. Triantafyllidis, D., L. Li, and F.H. Stott, *Investigation of the effects of nonconventional beam geometries in laser surface treatment of ceramics: Experimental analysis.* Journal of laser applications, 2006. **18**(3): p. 267-274.
305. Ashby, M.F. and K.E. Easterling, *The transformation hardening of steel surfaces by laser beams-I. Hypo-eutectoid steels.* Acta Metallurgica, 1984. **32**(11): p. 1935-1937,1939-1948.
306. Xie, J. and A. Kar, *Laser welding of thin sheet steel with surface oxidation.* Welding Journal (Miami, Fla), 1999. **78**(10): p. 343-s.
307. Von Allmen, M. and A. Blatter, *Laser-beam interactions with materials, 2nd edition*. 1998, Berlin: Springer.
308. Yang, T.Y.B., et al., *Absorption of laser light in overdense plasmas by sheath inverse bremsstrahlung.* Physics of Plasmas, 1995. **2**(8): p. 3146-3154.
309. Tusek, J. and M. Suban, *Hybrid welding with arc and laser beam.* Science and Technology of Welding and Joining, 1999. **4**(5): p. 308-311.
310. Chandel, R.S., *Electrode melting and plate melting efficiencies of submerged arc welding and gas metal arc welding.* Materials Science and Technology, 1990. **6**(8): p. 772-777.
311. Stute, U., R. Kling, and J. Hermsdorf, *Interaction between electrical arc and Nd: YAG laser radiation.* CIRP Annals - Manufacturing Technology, 2007. **56**(1): p. 197-200.
312. Seyffarth, P. and I.V. Krivtsum, *Laser-arc processes and their applications in welding and material treatment. Welding and allied processes*. Vol. volume 1. 2002, London: CRC Press Taylor & Francis Group.
313. Diebold, T.P. and C.E. Albright, *Laser-GTA welding of aluminum alloy 5052.* Welding Journal (Miami, Fla), 1984. **63**(6): p. 18-24.
314. Devletian, J.H., *Arc-augmented laser welding of aluminum*. 1988, Welding Research Council: New York.
315. Gornyi, S.G., V.A. Lopota, and V.D. Redozubov, *Examination of the electrical characteristics of the arc in laser-arc welding.* Welding International, 1990. **36**(1): p. 474-476.
316. Naito, Y., S. Katayama, and A. Matsunawa, *Keyhole behavior and liquid flow in Molten Pool during laser-arc hybrid welding*, in *Proceedings of SPIE - The International Society for Optical Engineering*. 2002: Osaka. p. 357-362.
317. Ono, M., et al., *Development of laser-arc hybrid welding.* NKK Technical Review, 2002(86): p. 8-12.
318. Chen, Y.B., et al., *Experimental study on welding characteristics of CO_2 laser TIG hybrid welding process.* Science and Technology of Welding and Joining, 2006. **11**(4): p. 403-411.
319. Hu, B. and G. Ouden, *Synergetic effects of hybrid laser/arc welding.* Science and Technology of Welding and Joining, 2005. **10**(4): p. 427-431.

320. Kim, Y.P., N. Alam, and H.S. Bang, *Observation of hybrid (cw Nd:YAG laser+MIG) welding phenomenon in AA 5083 butt joints with different gap condition.* Science and Technology of Welding and Joining, 2006. **11**(3): p. 295-307.
321. Liu, L. and X. Hao, *Improvement of laser keyhole formation with the assistance of arc plasma in the hybrid welding process of magnesium alloy.* Optics and Lasers in Engineering, 2009. **47**(11): p. 1177-1182.
322. Gao, M., X.Y. Zeng, and Q.W. Hu, *Effects of welding parameters on melting energy of CO_2 laser-GMA hybrid welding.* Science and Technology of Welding and Joining, 2006. **11**(5): p. 517-522.
323. Gureev, D.M., A.E. Zaikin, and A.B. Zolotarevsky, *Method of laser-arc material processing and its application.* Transactions of the Physical Institute of the USSR Academy of Science, Moscov, Nauka, 1989. **198**: p. 41-61.
324. Dilthey, U., *Capabilities of welding processes and their automation potential with a view to the year 2000*, in *Proceedings of the IIW Asian Pacific Welding Congress*. 1996: Manukau City, New Zeland. p. 65-81.
325. Ono, M., et al., *Welding properties of thin steel sheets by laser-arc hybrid welding: laser focused arc welding*, in *Proceedings of LAMP 2002, Laser Advance Materials Processing, High Temperature Society of Japan*. 2002. p. 396.
326. Dilthey, U., F. Lueder, and A. Wieschemann, *Process-technical investigations on hybrid technology laser beam-arc welding* in *Proceedings of the 6th Int. Conference on Welding and Melting by Electron and Laser Beams*. 1998: Toulon, France. p. 417-424.
327. Shinn, B.W., D.F. Farson, and P.E. Denney, *Laser stabilisation of arc cathode spots in titanium welding.* Science and Technology of Welding and Joining, 2005. **10**(4): p. 475-481.
328. Steen, W.M., *Arc augmented laser processing of materials.* Journal of Applied Physics, 1980. **51**(11): p. 5636-5641.
329. Liming, L., W. Jifeng, and S. Gang, *Hybrid laser-TIG welding, laser beam welding and gas tungsten arc welding of AZ31B magnesium alloy.* Materials Science and Engineering A, 2004. **381**(1-2): p. 129-133.
330. Kutsuna, M. and L. Chen, *Interaction of both plasmas in CO_2 laser - MAG hybrid welding of carbon steel*, in *Proceedings of SPIE - The International Society for Optical Engineering*, I. Miyamoto, et al., Editors. 2002: Osaka. p. 341-346.
331. Hu, B. and G. den Ouden, *Laser induced stabilisation of the welding arc.* Science and Technology of Welding and Joining, 2005. **10**(1): p. 76-81.
332. Miller, R. and T. Debroy, *Energy absorption by metal-vapor-dominated plasma during carbon dioxide laser welding of steels.* Journal of Applied Physics, 1990. **68**(5): p. 2045-2050.
333. Zhao, G.Y., M. Dassanayake, and K. Etemadi, *Numerical simulation of a free-burning argon arc with copper evaporation from the anode.* Plasma Chemistry and Plasma Processing, 1990. **10**(1): p. 87-98.
334. Etemadi, K. and E. Pfender, *Impact of anode evaporation on the anode region of a high-intensity argon arc.* Plasma Chemistry and Plasma Processing, 1985. **5**(2): p. 175-182.
335. Akbar, S. and K. Etemadi, *Impact of copper vapor contamination on argon arcs.* Plasma Chemistry and Plasma Processing, 1997. **17**(2): p. 251-262.

336. Hsu, K.C., K. Etemadi, and E. Pfender, *Study of the free-burning high-intensity argon arc.* Journal of Applied Physics, 1983. **54**(3): p. 1293-1301.
337. Albright, C.E., *Method and apparatus for initiating, directing and constricting electrical discharge arcs*. United States Patent Nr. US 6482077 B1: USA.
338. Berger, O., A. Englhard, and U. Prank. *Development of the LGS-GMA welding process*. in *Proceedings of the Fifth International WLT-Conference on Lasers in Manufacturing*. 2009. Munich, June 2009.
339. Walters, C.T. and A.H. Clauer, *Transient reflectivity behavior of pure aluminum at 10.6 micrometers.* Applied Physics Letters, 1978. **33**(8): p. 713-715.
340. Ujihara, K., *Reflectivity of metals at high temperatures.* Journal of Applied Physics, 1972. **43**(5): p. 2376-2383.
341. Williams, S.W., G. Scott, and N.J. Calder, *Direct diode laser welding of aerospace alloys.* LaserOpto, 2001. **33**: p. 50-54.
342. Morgan, S.A. and S.W. Williams, *Hybrid laser conduction welding* in *Proceedings of 55th Annual Assembly of International Institute of Welding* 2002, 24-28 June: Copenhagen, Denmark.
343. Matsuda, J., et al., *TIG or MIG arc augmented laser welding of thick mild steel plate.* Joining & materials, 1988. **1**(1): p. 31-34.
344. Campana, G., et al., *The influence of arc transfer mode in hybrid laser-MIG welding.* Journal of Materials Processing Technology, 2007. **191**(1-3): p. 111-113.
345. Gao, M., et al., *Weld microstructure and shape of laser-arc hybrid welding.* Science and Technology of Welding and Joining, 2008. **13**(2): p. 106-113.
346. Li, Z., et al., *A study of the radiation of a Nd:YAG laser-MIG hybrid plasma.* Optics and Laser Technology, 2010. **42**(1): p. 132-140.
347. Ono, M., et al., *Laser-arc hybrid welding of thin steel sheets.* Quarterly J. Japan Welding Society, 2003. **21**(4): p. 515-521.
348. Kelly, S.M., et al., *Examination of the process efficiency during hybrid laser-arc welding.* Materials Science and Technology, 2005. **3**: p. 69-76.
349. Cho, Y. and S.J. Na. *Temperature measurement of laser arc hybrid welding plasma*. in *Proceedings of 22nd International Congress on Applications of Laser and Electro-Optics, ICALEO*. 2003. Jacksonville, FL.
350. Cho, Y.T., W.I. Cho, and S.J. Na, *Numerical analysis of hybrid plasma generated by Nd:YAG laser and gas tungsten arc.* Optics and Laser Technology, 2010. **43**(3): p. 711-720.
351. Sugino, T., et al., *Fundamental study on welding phenomena in pulsed laser-GMA hybrid welding*, in *Proceedings of 24th International Congress on Applications of Lasers and Electro-Optics, ICALEO* 2005: Miami, FL. p. 108-116.
352. Schilf, M., et al., *Some aspects of arc stability in GMA-laser-hybrid welding*, in *Proceedings of the Second International WLT-Conference on Lasers in Manufacturing* 2003: Stuttgart, Germany. p. 171-175.
353. Fellman, A., A. Salminen, and V. Kujanpaa, *A study of the molten filler material movements during CO_2-laser-MAG hybrid welding* in *Proceedings of the Third International WLT-Conference on Lasers in Manufacturing* 2005: Munich p. 171-176.
354. Huang, Y. and Y.M. Zhang, *Laser-enhanced GMAW.* Welding Journal (Miami, Fla), 2010. **89**(9).

355. Song, G. and Z. Luo, *The influence of laser pulse waveform on laser-TIG hybrid welding of AZ31B magnesium alloy.* Optics and Lasers in Engineering, 2011. **49**: p. 82-88.
356. Liu, L. and X. Hao, *Phase matching mode between laser pulse and TIG arc in hybrid welding process.* IEEE Transactions on Plasma Science, 2010. **38**(12 PART 2): p. 3375-3379.
357. Cantin, G.M.D. and J.A. Francis, *Arc power and efficiency in gas tungsten arc welding of aluminium.* Science and Technology of Welding and Joining, 2005. **10**(2): p. 200-210.
358. Essers, W.G. and R. Walter, *Heat transfer and penetration mechanisms with GMA and plasma-GMA welding.* Welding Journal (Miami, Fla), 1981. **60**(2): p. 37. s-42. s.
359. Kim, Y.S., D.M. McEligot, and T.W. Eagar, *Analysis of electrode heat transfer in GMAW.* Welding Journal, 1991: p. 20s-31s.
360. Tsao, K.C. and C.S. Wu, *Fluid flow and heat transfer in GMA weld pools.* Welding Journal, 1988: p. 70s-75s.
361. Zacharia, T., A.H. Eraslan, and D.K. Aidun, *Modeling of non-autogenous welding.* Welding Journal, 1988: p. 18s-27s.
362. Wu, C.S. and L. Dorn, *Computer simulation of fluid dynamics and heat transfer in full-penetrated TIG weld pools with surface depression* Computational Materials Science 1994. **2**: p. 341-349.
363. Zhou, J. and H.L. Tsai, *Investigation of mixing and diffusion processes in hybrid spot laser-MIG keyhole welding.* Journal of Physics D: Applied Physics, 2009. **42**(9).
364. Zhou, J., H.L. Tsai, and P.C. Wang, *Effects of electromagnetic force on melt flow and weld shape in laser keyhole welding*, in *Proceedings of 23rd International Congress on Applications of Laser and Electro-Optics, ICALEO*. 2004: San Francisco, CA.
365. Nielsen, S.E., et al., *Hybrid welding of thick section C/Mn steel and aluminium, International Institute of Welding, IIW document, XII 1731-02* 2002, .
366. Nilsson, K., H. Engstrom, and A. Kaplan, *Influance of butt- and T-joint preparation in laser arc hybrid welding, International Institute of Welding, IIW, Copenhagen, Denmark, Doc. XII-1732-02*. 2002.
367. Zhou, J., H.L. Tsai, and P.C. Wang, *Investigation of mixing phenomena in hybrid laser-MIG keyhole welding*, in *Proceedings of 23rd International Congress on Applications of Laser and Electro-Optics, ICALEO*. 2004: San Francisco, CA.
368. Bonss, S., B. Brenner, and E. Beyer, *Hybrid welding with CO_2 and diode laser* Industrial Laser User, 2000. **21**: p. 26-28.
369. Kristensen, J.K., *Laser welding in ship building - a challenge to research and development for more than a decade*, in *Proceedings of 7th International Aachen conference on high productivity joining processes*. 2001: Aachen, Germany. p. 447.
370. Russell, J.D., *Laser weldability of C-Mn steels.* Welding in the World, 2000. **44**(6): p. 19-24.
371. Glumann, C., et al., *Welding with combination of two CO_2 lasers*, in *Proceedings of the International Congress on Application of Lasers and Electro-Optics ICALEO*. 1993, LIA: Orlando, FL. p. 672-681.
372. Hsu, R., A. Engler, and S. Heinemann, *The gap bridging capability in laser tailored blank welding*, in *Proceedings of the International Congress on*

Application of Lasers and Electro-Optics ICALEO. 1998: Orlando, FL. p. 255-231.
373. Xie, J., *Dual beam laser welding.* Welding Journal (Miami, Fla), 2002. **81**(10): p. 223/S-230/S.
374. Trautmann, A. and M.F. Zaeh, *Hybrid bifocal laser welding of aluminum*, in *Proceedings of 24th International Congress on Applications of Lasers and Electro-Optics, ICALEO* 2005: Miami, FL. p. 153.
375. Dawes, C.J., *Laser welding of sheet metal fabrications - Process improvements*, in *Proceeding of the International Conference on Applications of Lasers and Electro-optics ICALEO*, C. Albright, Editor. 1985: The Welding Institute, UK. p. 73.
376. Rubben, K., H. Mohrbacher, and E. Leirman, *Advantages of using an oscillating laser beam for the production of tailored blanks*, in *Proceedings of SPIE - The International Society for Optical Engineering*, L.H.J.F. Beckmann, Editor. 1997: Munich. p. 228-241.
377. Coste, F., R. Fabbro, and L. Sabatier, *Application of vision to laser welding: Increase of operating tolerances using beam-oscillation and filler-wire*, in *Laser Institute of America, Proceedings of Laser Processing Conference, ICALEO*. 1997: San Diego, CA, USA. p. 83.
378. Bagger, C., et al., *Closing the weld gap with laser/MIG hybrid welding process*, in *Proceedings of 9th Conference on Laser Material Processing in the Nordic Countries, NOLAMP*. 2003: Trondheim, Norway. p. 113-124.
379. Staufer, H., *Laser hybrid welding for industrial applications*, in *Proceedings of SPIE - The International Society for Optical Engineering*. 2007: Gmunden.
380. Petring, D., et al. *Investigation and applications of laser-arc hybrid welding from thin sheets up to heavy section components*. in *Proceedings of 22nd International Congress on Applications of Lasers and Electro-Optics, ICALEO*. 2003. Jacksonville, FL.
381. Pace, D.P., K.L. Kenney, and D.L. Galiher, *Laser assisted arc welding of ultra high strength steels*, in *ASM Proceedings of the International Conference: Trends in Welding Research*. 2002: Phoenix, AZ. p. 442-447.
382. Wieschemann, A., H. Keller, and U. Dilthey, *Development of laser-GMA hybrid- and hydra welding processes for shipbuilding.* Welding Research Abroad, 2002. **48**(11): p. 10-15.
383. Petring, D., C. Fuhrman, and R. Poprawe, *Progress in laser-MAG hybrid welding of high-strength steels up to 30 mm thickness*, in *Proceedings of 26th International Congress on Applications of Lasers and Electro-Optics, ICALEO* 2007: Orlando, FL. p. 300.
384. Shi, G. and P. Hilton, *A comparison of the gap bridging capability of CO_2 laser and hybrid CO_2 laser MAG welding on 8mm thickness C-Mn steel plate.* Welding in the World, 2005. **49**(9 SPEC. ISS.): p. 75-87.
385. Chae, H., et al., *The effect of process parameters on the gap bridging capability for CO_2 laser-GMA hybrid welding*, in *Proceedings of 24th International Congress on Applications of Lasers and Electro-Optics, ICALEO* 2005: Miami, FL. p. 169-173.
386. Gongqi, S. *Laser and hybrid laser MAG welding of thick section C-MN steel*. in *Proceedings of International Forum on Welding Technologies in Energy Engineering* 2005. Shanghai, China, 21-23 September 2005.

387. Staufer, H., *High productivity by using laser-GMAW- and laser-tandem-hybrid-processes for thick plates.* Welding in the World, 2005. **49**(9 SPEC. ISS.): p. 66-74.
388. El Rayes, M., C. Walz, and G. Sepold, *The influence of various hybrid welding parameters on bead geometry.* Welding Journal (Miami, Fla), 2004. **83**(5): p. 147-S.
389. Abe, N., et al., *High speed welding of thick plates using a laser-arc combination system.* Transactions of JWRI (Japanese Welding Research Institute), 1997. **26**(1): p. 69-75.
390. Fellman, A. and V. Kujanpa¨a¨, *The effect of shielding gas composition on welding performance and weld properties in hybrid CO_2 laser-gas metal arc welding of carbon manganese steel.* Journal of Laser Applications, 2006. **18**(1): p. 12-20.
391. Northcote, D., *Shielding gases for GMA welding of steels.* Australian Welding Journal, 1975. November/December: p. 37-42.
392. Naito, Y., M. Mizutani, and S. Katayama, *Effect of oxygen in ambient atmosphere on penetration characteristics in single yttrium-aluminum-garnet laser and hybrid welding.* Journal of Laser Applications, 2006. **18**(1): p. 21-27.
393. Tani, G., et al., *The influence of shielding gas in hybrid laser-MIG welding.* Applied Surface Science, 2007. **253**(19): p. 8050-8053.
394. Zhao, L., et al., *Influence of welding parameters on distribution of wire feeding elements in CO_2 laser GMA hybrid welding.* Science and Technology of Welding and Joining, 2009. **14**(5): p. 457-467.
395. Chae, H.B., et al., *The effect of shielding gas composition in CO_2 laser-gas metal arc hybrid welding.* Proceedings of the Institution of Mechanical Engineers, Part B: Journal of Engineering Manufacture, 2008. **222**(11): p. 1315-1324.
396. Heiple, C.R. and J.R. Roper, *Mechanism for minor element effect on GTA fusion zone geometry.* Welding Journal (Miami, Fla), 1982. **61**(4): p. 97. s-102. s.
397. Lu, S.P., et al., *Effect of oxygen content in He-O_2 shielding gas on weld shape in ultra deep penetration TIG.* Science and Technology of Welding and Joining, 2007. **12**(8): p. 689-695.
398. Mills, G.S., *Fundamental mechanisms of penetration in GTA welding.* Weld J (Miami Fla), 1979. **58**(1).
399. Mills, K.C., et al., *Marangoni effects in welding.* Philosophical Transactions of the Royal Society A: Mathematical, Physical and Engineering Sciences, 1998. **356**(1739): p. 911-925.
400. Naito, Y., et al., *Effect of ambient atmosphere on penetration geometry in laser and hybrid welding*, in *Proceedings of 23rd International Congress on Applications of Laser and Electro-Optics, ICALEO*. 2004: San Francisco, CA.
401. Coste, F., et al. *Laser and hybrid welding of high strength steel. Application to pressure vessel manufacturing*. in *Proceedings of 24th International Congress on Applications of Lasers and Electro-Optics, ICALEO*. 2005. Miami, FL.
402. Norrish, J., *Gas metal arc welding*, in *Advanced welding processes*. 1992, Woodhead Publishing
403. Suban, M. and J. Tušek, *Dependence of melting rate in MIG/MAG welding on the type of shielding gas used.* Journal of Materials Processing Technology, 2001. **119**(1-3): p. 185-192.

404. Tusek, J., *Mathematical modelling of melting rate in arc welding with a triple-wire electrode.* Journal of Materials Processing Technology, 2004. **146**(3): p. 415-423.
405. Park, Y.S., et al., *Study on the welding variables according to off-set and separation using hybrid laser welding* in *Proceedings of the Third International WLT-Conference on Lasers in Manufacturing* 2005: Munich. p. 199-202.
406. Nakamura, T., K. Hiraoka, and S. Zenitani, *Improvement of MIG welding stability in pure Ar shielding gas using small amount of oxygen and coaxial hybrid solid wire.* Science and Technology of Welding and Joining, 2008. **13**(1): p. 25-32.
407. Dyberg, P., A.F.H. Kaplan, and J. Zachrisson, *On the influence of metal cored wire composition on the laser hybrid welding process*, in *Proceedings of 26th International Congress on Applications of Lasers and Electro-Optics ICALEO* 2007: Orlando, FL. p. 277.
408. Williams, S.W. and A. Steuwer, *Residual stress in friction stir welding* in *Friction stir welding from basics to applications* D.e.a. Lohwasser, Editor. 2010, Woodhead Publishing Ltd.: Cambridge. p. 215-244.
409. Masubuchi, K., *Analysis of welded structures : residual stresses, distortion and their consequences*. 1980, Oxford: Pergamon. xi,642p.
410. Radaj, D., *Heat effects of welding : temperature field, residual stress, distortion*. 1992: Springer. xxii, 348p.
411. Williams, S.W. and A. Steuwer, *Residual stress in friction stir welding*, in *Friction stir welding. From basics to applications*, D. Lohwasser and Z. Chen, Editors. 2010, Woodhead Publishing Limited: Cambridge UK. p. 215-244.
412. Lindgren, L.E., *Numerical modelling of welding.* Computer Methods in Applied Mechanics and Engineering, 2006. **195**(48-49): p. 6710-6736.
413. Lindgren, L.E., *Computational welding mechanics : thermomechanical and microstructural simulations* 2007: Woodhead.
414. Altenkirch, J., et al., *Mechanical tensioning of high-strength aluminum alloy friction stir welds.* Metallurgical and Materials Transactions A: Physical Metallurgy and Materials Science, 2008. **39**(13): p. 3246-3259.
415. Altenkirch, J., et al., *Residual stress engineering in friction stir welds by roller tensioning.* Science and Technology of Welding and Joining, 2009. **14**(2): p. 185-192.
416. Brust, F.W.a.K., D. S., *Processes and mechanisms of welding residual stress and distortion, chapter 8: Mitigating welding residual stress and distortion*. 2005: Woodhead Publishing in Materials.
417. Price, D.A., et al., *Distortion control in welding by mechanical tensioning.* Science and Technology of Welding and Joining, 2007. **12**(7): p. 620-633.
418. Vinokurov, V.A., *Mechanical aspect of stress relieving by heat and non-heat treatment. In Stress Relieving Heat Treatments of Welded Steel Constructions.* 1987, Sofia, Bulgaria.
419. Soete, W., *Measurement and relaxation of residual stresses.* Welding Journal, 1949. **28**(8): p. 354s-364s.
420. Colegrove, P., et al., *Welding process impact on residual stress and distortion.* Science and Technology of Welding and Joining, 2009. **14**(8): p. 717-725.
421. Assuncao, E., et al., *Characterisation of residual stress state in laser welded low carbon mild steel plates produced in keyhole and conduction mode.* Science and Technology of Welding and Joining, 2011. **16**(3): p. 239-243.

422. Joseph, A., et al., *Measurement and calculation of arc power and heat transfer efficiency in pulsed gas metal arc welding.* Science and Technology of Welding and Joining, 2003. **8**(6): p. 400-406.
423. Ream, S., et al., *Zinc sulfide optics for high power laser applications*, in *Proceedings of 26th International Congress on Applications of Lasers and Electro-Optics, ICALEO* 2007: Orlando, FL.
424. Anisimov, S.I., *Evaporation from a cylidrical surface into vacuum.* Sov. Phys. JETP, 1968. **27**: p. 182-183.
425. Weberpals, J., et al., *Influence of the focus diameter in laser welding with thin disk laser.* Proceedings of the 3rd International WLT Conference of Lasers in Manufacturing, 2005: p. 39-42.
426. Beyer, E., et al., *Development and optical absorption properties of a laser induced plasma during CO_2-laser processing*, in *Proceedings of SPIE - The International Society for Optical Engineering*. 1984: Linz, Austria. p. 75-80.
427. Johnson, M.W., L. Edwards, and P.J. Withers, *Engin - A new instrument for engineers.* Physica B: Condensed Matter, 1997. **234-236**: p. 1141-1143.
428. Santisteban, J.R., et al., *ENGIN-X: A third-generation neutron strain scanner.* Journal of Applied Crystallography, 2006. **39**(6): p. 812-825.
429. Larson, A.C. and R.B. von Dreele, *General Structure Analysis System (GSAS), LAUR 86-748*. 1994, Los Alamos National Laboratory, Los Alamos, NM, USA.
430. De Novion, C.H., *The use of neutrons for materials characterization*, in *Analysis of residual stress by diffraction using neutron and synchrotron radiation*, M.E.F.a.A. Lodini, Editor. 2003, Taylor & Francis: New York. p. 3-27.
431. Krawitz, A.D. and R.A. Winholtz, *Use of position-dependent stress-free standards for diffraction stress measurements.* Material Science Engineering A, 1994. **185**: p. 123-130.
432. Arita, H., et al., *Development of advanced 3-electrode MAG high-speed horizontal fillet welding process.* Welding in the World, 2009. **53**(5-6): p. 35-43.
433. Hua, J.X.M., et al., *Research on a high speed welding technology of triple-wire GMAW*, in *Proc. of the Int. Conf. on Advances in Welding Science and Technology for Construction, Energy and Transportation, AWST 2010, held in Conj. with the 63rd Annual Assembly of IIW* 2010. p. 179-184.

Appendixes

I. Material properties and constants used for calculations of recoil pressure in Section 5.5.6.

***Table I.1**: Material properties*

Property	Symbol	Unit	Material		
			S 355	304	7075
Melting temp.	T_m	K	1803	1727	901
Vaporisation temp.	T_v	K	3133	3023	2793
Density	ρ	kg m^{-3}	7800	8000	2800
Specific heat of solid phase	c_{ps}	J kg^{-1} K^{-1}	480	477	850
Latent heat of melting	H_m	J kg^{-1}	2.7 x 10^5	2.73 x 10^5	3.5 x 10^5
Latent heat of vaporisation	H_v	J kg^{-1}	6.1 x 10^6	6.1 x 10^6	1.19 x 10^7
Thermal conductivity of solid	k_s	W m^{-1} K^{-1}	50	15	190
Thermal conductivity of liquid	k_l	W m^{-1} K^{-1}	28	27	80
Thermal conductivity average	k	W m^{-1} K^{-1}	39	21	135
Thermal diffusivity average	α	m^2 s^{-1}	1.04 x 10^{-5}	5.5 x 10^{-6}	5.67 x 10^{-5}
Viscosity	η	m Pas	8	8	1.3
Atomic mass	M_a	kg	9.22 x 10^{-26}	9.18 x 10^{-26}	4.9 x 10^{-26}
Vaporisation constant	B_0	kg m^{-1} s^{-2}	3.9 x 10^{12}	3.9 x 10^{12}	2.05 x 10^{12}

***Table I.2**: Laser parameters and constants*

Property	symbol	unit	value
Laser absorption coefficient	A	-	0.8
Laser power	P_L	W	3000
Power density on surface	q_P	W m^{-2}	2.5 x 10^{8}
Beam radius	r_B	m	2.5 x 10^{-3}
Travel speed	v	m s^{-1}	16.7
Initial temperature	T_0	K	298
Avogadro's number	N_A	mol^{-1}	6.022 x 10^{23}
Boltzmann's constant	k_B	J K^{-1}	1.38 x 10^{-23}
Gas constant	R	J K^{-1} mol^{-1}	8.3

II. Equations used for calculation of surface temperature and recoil pressure in Section 5.5.6

Temperature distribution in the laser interaction point was calculated based on [305]:

$$T(y,z,t)=\frac{AP_L}{v2\pi k\sqrt{t(t+t_0)}}\exp-\frac{1}{4\alpha}[\frac{(z+z_0)^2}{t}+\frac{y^2}{t+t_0}]$$

Where z_0^2 and t_0 where calculated as:

$$z_0^2=(\frac{\sqrt{\pi}}{e})\sqrt{\frac{\alpha r_B}{v}}r_B$$

$$t_0=\frac{r_B^2}{4a}$$

The maximum temperature achieved on the surface at y=0, z=0 is given by:

$$T_{s(\max)}(y=0,z=0)=T_0+\frac{2AP_L}{ve\pi\rho c_{ps}z_0^2}$$

Various definitions of the recoil pressure, according to different authors were used as follows:

- Von Allmen [307]

$$p_r = 0.54 p_0 \exp(H_v \frac{T_s - T_v}{R T_s T_v})$$

- Semak and Matsunava [194]

$$p_r = 0.55 \frac{B_0}{\sqrt{T_s}} \exp(-\frac{M_a H_v}{k_B N_A T_s})$$

- Anisimov [424]

$$p_r = \frac{q_P 1.69}{\sqrt{H_v}} (\frac{b}{1 + 2.2 b^2});$$

$$b^2 = \frac{k_B T_s}{M_a H_v}$$

- Chen [209]

$$p_r = \frac{q_P \alpha (1 - r) - Q_{heat}}{H_v} \sqrt{\frac{\pi k_B T_s}{2 M_a}}$$

$$Q_{heat} = c_{ps} (T - T_0) + H_m$$